TU Delft

Delft University of Technology

Cavity electromechanics using flipped silicon nitride membranes

Peiter, S.R.

DOI
10.4233/uuid:be47e512-c19c-44c8-bba4-28f719e6fb8f

Publication date
2022

Document Version
Final published version

Citation (APA)
Peiter, S. R. (2022). *Cavity electromechanics using flipped silicon nitride membranes*. [Dissertation (TU Delft), Delft University of Technology]. https://doi.org/10.4233/uuid:be47e512-c19c-44c8-bba4-28f719e6fb8f

Important note
To cite this publication, please use the final published version (if applicable).
Please check the document version above.

Copyright
Other than for strictly personal use, it is not permitted to download, forward or distribute the text or part of it, without the consent of the author(s) and/or copyright holder(s), unless the work is under an open content license such as Creative Commons.

Takedown policy
Please contact us and provide details if you believe this document breaches copyrights.
We will remove access to the work immediately and investigate your claim.

This work is downloaded from Delft University of Technology.
For technical reasons the number of authors shown on this cover page is limited to a maximum of 10.

CAVITY ELECTROMECHANICS USING FLIPPED SILICON NITRIDE MEMBRANES

CAVITY ELECTROMECHANICS USING FLIPPED SILICON NITRIDE MEMBRANES

Proefschrift

ter verkrijging van de graad van doctor
aan de Technische Universiteit Delft,
op gezag van de Rector Magnificus Prof.dr.ir. T.H.J.J. van der Hagen,
voorzitter van het College voor Promoties,
in het openbaar te verdedigen op vrijdag 11 februari 2022 om 10:00 uur

door

Sarwan Ruben PEITER

Natuurkundig ingenieur,
Technische Universiteit Delft, Nederland,
geboren te Rotterdam, Nederland.

Dit proefschrift is goedgekeurd door de

promotor: Prof.dr. G.A. Steele
promotor: Prof.dr. L. Kuipers

Samenstelling promotiecommissie:

Rector Magnificus	voorzitter
Prof.dr. G.A. Steele	Technische Universiteit Delft, promotor
Prof.dr. L. Kuipers	Technische Universiteit Delft, promotor

Onafhankelijke leden:

Prof.dr. P. Steeneken	Technische Universiteit Delft
Dr. R. Norte	Technische Universiteit Delft
Prof.dr. A. Mazumdar	Rijksuniversiteit Groningen
Prof.dr. Y. Chu	ETH Zürich
Prof.dr. A. Schliesser	University of Copenhagen
Prof.dr. Y.M. Blanter	Technische Universiteit Delft, reservelid

Keywords: Electromechanics, microwave resonators, silicon nitride membranes, high-Q, cryogenic temperatures.

Printed by: Gildeprint - The Netherlands

Front & Back: Illustration of silicon nitride membrane surrounded by a silicon phononic shield (back) with lumped-element resonator (front).

Copyright © 2022 by S.R. Peiter

Casimir PhD Series, Delft-Leiden 2022-02

ISBN 978-90-8593-513-1

An electronic version of this dissertation is available at
http://repository.tudelft.nl/.

To my parents and brother...
For their endless love and support.
Thank you

Gi mi mama, papa nanga brada...
Fu lobi nanga yepi mi alaten.
Gran tangi

Aan mijn ouders en broertje...
Voor hun eindeloze liefde en steun.
Bedankt

If I cannot do great things,
I can do small things in a
great way.

Martin Luther King Jr.

CONTENTS

Summary **xi**

Samenvatting **xiii**

1 Introduction **1**
1.1 The problem 2
1.2 Brief history of cavity optomechanics 2
1.3 Thesis Outline 7
References 8

2 Theoretical background **11**
2.1 Mechanical resonators 12
2.2 Dynamics of electromechanical system 14
2.2.1 Capacitive coupled electromechanics 14
2.2.2 System Hamiltonian 15
2.2.3 Equations of motion 17
2.2.4 Solution of the linearized Heisenberg-Langevin equations of motion 20
2.2.5 Power spectrum 21
References 25

3 Device Design and Fabrication **27**
3.1 Superconducting lumped element resonators 28
3.1.1 Design 28
3.1.2 Fabrication. 29
3.2 High tensile stress Si_3N_4 membranes 32
3.2.1 Design conditions 32
3.2.2 Fabrication. 33
3.3 Design and Fabricating In-Substrate phononic shields 44
3.3.1 Design 44
3.3.2 Fabrication. 44
3.3.3 Notes on fabricating phononic shields on full wafer 56
References 59

4 Magnetic losses in planar lumped-element superconducting microwave resonators **63**
4.1 Introduction 64
4.2 Stray magnetic field induced losses of LGR 64
4.3 Geometry dependent conduction loss 67
4.4 Including dielectric losses on lumped-element designs in the simulation. . . . 68

4.5 Conclusion . . . 70
4.6 Supplementary information . . . 71
4.6.1 Q-factor estimation in Sonnet . . . 71
4.6.2 Reducing dielectric loss of MGR . . . 72
4.6.3 Measurement of CPW and lumped-element resonator at 15 mK . . . 73
References . . . 75

5 A cryogenic accelerometer from Hz to MHz using a membrane electromechanical cavity 79
5.1 Introduction . . . 80
5.2 Device details . . . 81
5.3 Cavity noise . . . 83
5.4 Displacement sensitivity . . . 85
5.5 Accelerometric sensing . . . 88
5.6 Discussion . . . 91
5.7 Supplementary information . . . 93
5.7.1 Sonnet g_o simulation . . . 93
5.7.2 Flipchip schematic . . . 93
5.7.3 Measurement setup . . . 94
5.7.4 Bare cavity measurement . . . 95
5.7.5 Estimating intra cavity photons N . . . 96
References . . . 98

6 High cooperativity and high-Q mechanics in a flip-chip membrane cavity electromechanical device 101
6.1 Introduction . . . 102
6.2 Device details . . . 103
6.3 OMIT . . . 105
6.4 Mechanical ringdown . . . 106
6.5 Thermal noise . . . 107
6.6 Discussion . . . 110
6.7 Supplementary information . . . 111
6.7.1 Phononic shield design . . . 111
6.7.2 Measurement setup . . . 113
6.7.3 Voigt fit of cavity response . . . 114
6.7.4 Photon number calibration . . . 117
6.7.5 Cavity noise spectrum . . . 119
6.7.6 Full ringdown measurements . . . 120
6.7.7 Mechanical mode temperature estimation . . . 121
References . . . 123

7 Conclusion and Outlook 127
7.1 Low loss lumped element resonator . . . 128
7.2 Broadband cryogenic accelerometer . . . 128
7.3 High-Q cavity electromechanics with SiN membrane and phononic shield . 130
7.4 The next steps... . . . 130
References . . . 134

Acknowledgements **137**

Curriculum Vitæ **143**

List of Publications **145**

SUMMARY

Silicon nitride (SiN) membrane electromechanics have shown to serve as excellent systems for applied research on sensing and transduction applications. Nevertheless, their relatively large mass in combination with high-Q also makes them suitable for more fundamental research, where gravitational effects can be tested on large mass quantum states, an experiment which has been elusive till so far. However, creating long-lived mechanical quantum states can be challenging for numerous reasons. One difficulty arises when integrating these membranes into a microwave circuit. In particular, the degradation of the mechanical resonator quality factor in an unpredictable manner. Another complication is that we often have to deal with a low coupling between the devices, which makes the control aspect of the mechanical resonator tougher.

In this thesis, we present a robust SiN based electromechanical platform that uses a custom-built flipchip tool. It allows for achieving single photon-phonon coupling on the order of Hz and high-Q factors at cryogenic temperatures consistently. In chapter **1**, we introduce the field of optomechanics and the motivations for extending this field to microwave frequencies. In chapter **2**, we provide a detailed derivation of the electromechanical hamiltonian and use the Heisenberg-Langevin equation of motion to derive an analytical expression for the classical cavity field and mechanical amplitudes. After introducing fluctuations operators in the field amplitudes, we are able to obtain an expression for the noise power spectral density using Wiener–Khinchin theorem. In chapter **3**, we give an extensive overview of the design and fabrication methods that we followed to make the electromechanical devices used in our experiments. In chapter **4**, we optimise the shape of a lumped-element resonator that is to be used in our electromechanical system. By simulating with electromagnetic software Sonnet EM, we show that a large loop inductor can negatively impact the resonator quality factor in case a copper platform is located at the bottom of the device. The losses improve tremendously when replacing the loop with a meandered design of the inductor. In chapter **5**, we combine a square SiN membrane with the optimised lumped-element resonator, using the flipchip tool. We show that the electromechanical system offers large enough sensitivity to quantify the vibrations originating from the cryocooler at the mixing chamber stage. This device shows promise to serve as a broadband cryogenic accelerometer. In chapter **6**, we demonstrate that placing the square SiN membrane within a silicon phononic shield significantly enhances the mechanical quality factor and therefore the cooperativity. We also discuss the implications of mechanically induced cavity noise on the measurements. In chapter **7**, we conclude the thesis and present the prospects of overcoming mechanical induced cavity noise that afflicts our measurements using 2 different methods i.e. a mechanical isolation system and microwave noise locking mechanism.

SAMENVATTING

Elektromechanische platformen gebaseerd op siliciumnitride (SiN) membranen worden alom gebruikt voor ultranauwkeurige detectie- en transductie doeleinden. Desalniettemin maakt de relatief grote massa in combinatie met een hoge Q-factor hen ook geschikt voor fundamenteel onderzoek waarbij zwaartekrachtseffecten kunnen worden bestudeerd in quantum systemen, een experiment dat tot nu toe nog niet gerealiseerd is. Dit vergt het creëren van langdurige coherente mechanische kwantumtoestanden. Desondanks kan dit om verschillende redenen een uitdaging zijn. Een moeilijkheid doet zich voor bij het integreren van deze membranen in een microwave circuit. Hierbij degradeert de mechanische resonator Q-factor op een onvoorspelbare wijze. Een andere complicatie is dat we vaak te maken hebben met een lage koppeling tussen de apparaten, wat het coherente besturingsaspect van de mechanische resonator moeilijker maakt.

In dit proefschrift wordt een robuust elektromechanisch platform gepresenteerd dat gebaseerd is op SiN en gebruik maakt van een op maat gemaakte flipchip-tool. Dit maakt het mogelijk om een consistent foton-fononkoppeling in de orde van Hz en hoogwaardige Q-factoren te bereiken op cryogene temperaturen. In hoofdstuk **1** wordt het veld van de optomechanica geintroduceerd en de redenen om dit generaliseren naar microwave frequenties. In hoofdstuk **2** wordt een gedetailleerde afleiding van de elektromechanische hamiltoniaan gegeven en wordt de bewegingsvergelijking van Heisenberg-Langevin gebruikt om een analytische uitdrukking af te leiden voor de klassieke elektromagnetische en mechanische amplitudes. Na het introduceren van operatoren voor fluctuaties, wordt een uitdrukking verkregen voor de spectrale dichtheid van het ruisvermogen met behulp van de Wiener–Khinchin stelling. In hoofdstuk **3** wordt een uitgebreid overzicht van de ontwerp- en fabricagemethoden gegeven, dat is gevolgd om de elektromechanische apparaten te maken die in de experimenten worden gebruikt. In hoofdstuk **4** is de geometrie van een microwave lumped-element resonator geoptimaliseerd die bovendien ingezet zal worden in ons elektromechanische systeem. Door te simuleren met elektromagnetische software Sonnet EM, wordt er aangetoond dat een grote lus vormig spoel een negatieve invloed kan hebben op de Q-factor van de resonator indien zich een koperen platform aan de onderkant van het apparaat bevindt. De verliezen verbeteren enorm wanneer de lus wordt vervangen door een compacte gekronkeld ontwerp van de spoel. In hoofdstuk **5** is een vierkant vormig SiN-membraan gecombineerd met de geoptimaliseerde lumped-element resonator, met behulp van de op maat gemaakte flipchip-tool. Vervolgens wordt gedemonstreerd dat het elektromechanische systeem voldoende gevoeligheid biedt om de vibraties van de cryokoeler op de millikelvin plaat te kwantificeren. Dit apparaat is zeer geschikt om als een breedband cryogene versnellingsmeter te fungeren. In hoofdstuk **6** wordt het vierkante SiN-membraan in een akoestisch schild geplaatst, waardoor de mechanische Q-factor en daarmee de coöperativiteit aanzienlijk verbetert. Daarnaast worden de gevolgen van mechanisch geïnduceerde elektromagnetisch ruis op de metingen besproken. In hoofdstuk **7** wordt het

proefschrift afgesloten en zijn de vooruitzichten gepresenteerd die het overwinnen van mechanisch veroorzaakte elektromagnetisch ruis mogelijk maakt. Er worden 2 methoden voorgesteld, namelijk een mechanisch isolatiesysteem en een FPGA gestuurd feedback systeem.

1

INTRODUCTION

At present, it is without doubt that the field of optomechanics is growing at a fast pace, considering the many unexplored territories of physics that can be accessed using optomechanical platforms. In this chapter, we provide a brief history of cavity optomechanics by highlighting the major achievements within the field. We also mention the existing challenges within quantum mechanics in general and how cavity optomechanics can be utilized to provide new insight into the foundation of quantum mechanics.

1

1.1. THE PROBLEM

A popular statement in physics goes as follows: it is the biggest of problems, it is the smallest of problems. Physicists have developed two separate rulebooks to explain how the universe works. We have general relativity (GR) that elegantly describes gravity which governs the dynamics of big objects such as the orbit of planets, stars, colliding galaxies, the expansion of the universe and so on. Almost every modern electronic device connected to the internet nowadays have built-in GPS systems that account for the earth gravitational field to accurately determine their location. That is the big.

On the other hand, we have quantum mechanics that is well-equipped to determine the dynamics of systems governed by the electrostatic force and the two nuclear forces. For example, the red glow of a heating element as you toast a slice of bread or the radioactive decay of an unstable atom such as uranium, are all phenomena that quantum mechanics can correctly explain. It is undoubtedly the most successful theory that has paved the way to engineer new materials, build quantum computers, ultra-secure communication protocols, creation of lasers, sensing at extraordinary small scales, and we could go on. That is the small.

While the two theories are the pillars of modern physics, they are theories that are formulated differently. The problem now is that both describe reality in a form in which the other cannot, making them incompatible. One of the holy grails of modern physics has been to unify the small and the big with a single formalism, but unfortunately without any success to date. The difficulty lies in the fact that it requires extreme environmental conditions in the lab to have a big and massive object exhibit quantum behaviour. Therefore, the interplay between classical Newtonian mechanics and quantum mechanics has been limited to only theoretical descriptions on the drawing board. In this thesis, we construct an optomechanical platform that can or may provide experimental insights into the effects of gravity in a quantum system.

1.2. BRIEF HISTORY OF CAVITY OPTOMECHANICS

We cannot deny the fact that observing the night sky has given rise to many fields of research within physics. The most famous example is the formulation of Newtonian mechanics in 1687 by Isaac Newton to explain the orbit of the moon around the earth. Nowadays, the principles are Newtonian mechanics are used in construction, automotive industry, aerospace and so forth.

Another groundbreaking observation by studying the night sky was done by Chinese astronomers in 635 AD. They observed that the tail of comets always pointed away from the sun. It was only in the early 17th century when German physicist Kepler made the same observation. His explanation: sunlight pushes away the tail. These were the first speculations that light somehow was able to exert a force on matter. At that time, the idea was still vague and was considered unorthodox. It was Maxwell, a Scottish physicist, who formulated the theoretical framework in which he showed that electromagnetic radiation exerts a pressure upon any surface it is exposed to. This pressure was later measured in 1900 by Russian physicist Pyotr Lebedev [1]. At that time, researchers did not know how to utilize or control the radiation pressure force and the particle nature of light was still widely debated in the physics community. In 1906, Einstein proposed a thought

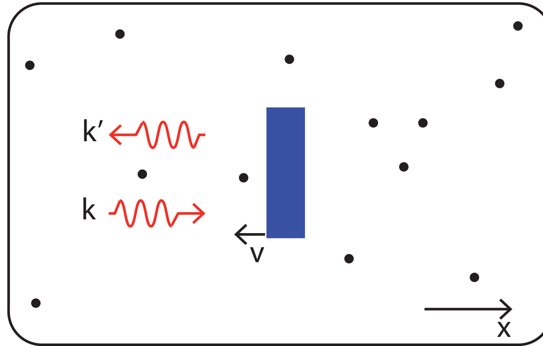

Figure 1.1: Black box containing gas molecules (black dots) and a perfectly reflecting mirror (blue) thermalized at room temperature. Since the mirror wiggles due to constant collision with the gas molecules, the reflected radiation is Doppler shifted and has $k' = k(1 - v/c)$. The momentum transfer is proportional to $k - k'$ and can be considered as an additional force used to damp the motion of the mass, with damping coefficient γ proportional to the laser power.

experiment, shown in Fig.1.1, in order to obtain more insight into the nature of radiation [2].

Here, a moving mechanical oscillator with perfectly reflecting surfaces is kept inside a blackbody cavity filled with gas. The mirror wiggles due to the transfers of energy from gas molecules via collisions. The mirror transfers energy to the radiation field via radiation damping. Here, Einstein concluded that the particle and wave nature of light has to be considered to obtain a complete description for thermal equilibrium between gas, mirror and radiation field. Implicitly came forward that the radiation pressure from the radiation field can also be used to effectively extract kinetic energy from the mirror and therefore dampen its motion. These were very revolutionizing concepts, but in a time with limited technological capacity, was difficult to realize an experiment demonstrating this effect. It was not until late 1967, when Russian physicist, Braginsky, established a concrete theoretical framework of this concept. He explained that the retarded nature of radiation pressure effects of the electromagnetic field in a high-frequency optical cavity consisting of a low-frequency movable mirror, lead to damping or amplification of the movable mirror [3]. This effective interaction between a slow and fast oscillating system is what we call dynamical backaction. A year later, he experimentally demonstrated electromagnetic damping of a mechanical resonator, which was impressive considering that the laser was not invented yet [4]. This laid the early phase of the groundwork of what is now known as cavity optomechanics.

An optomechanical system at its core is an extremely simple optical system as shown in Fig.1.2. It is similar to a Michelson interferometer composed of two mirrors, but in optomechanics, one of the mirrors is able to move freely. The mechanical oscillator i.e. movable mirror, position is coupled with the optical field by the laser radiation pressure force i.e. the force exerted by the photons of the laser. Likewise, the motion of the mirror itself also changes the properties of the optical system. The radiation pressure force is extremely small and for comparison: it will take 7.5 million pocket lasers (1 mW) to hold

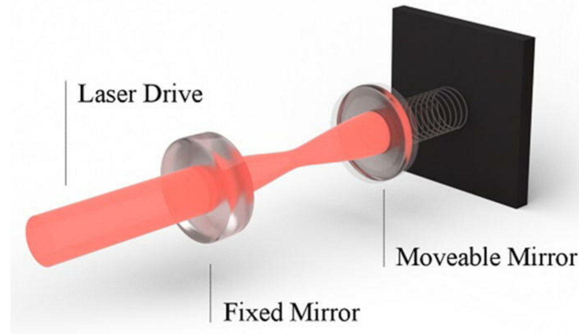

Figure 1.2: A simple cavity optomechanical setup [5]. By allowing one of the mirrors of the Fabry-Perot cavity to move freely, the optical and mechanical degree of freedom can couple in presence of laser light.

up a 2.5 mg mosquito against gravity. A noteworthy fact is that optomechanical effects can be observed in a variety of devices, as shown in Fig.1.3. From pg nanomechanical resonators, dielectric particles, cold atoms to kg mirrors, with lengthscales from nm to m and resonance frequencies from Hz to GHz.

The essence in cavity optomechanics is that we obtain control over the mechanics (cooling and amplification) through the radiation pressure force, and it simultaneously allows us to measure the mechanical motion. Now the question arises: *by how much can the mechanical resonator be cooled, and the accuracy with which we can measure the displacement of the mechanics?*

The answer is that with the right set of optomechanical parameters and laser power, a mechanical resonator can be cooled down to its quantum groundstate. At this point, quantum behaviour start to appear and we need quantum mechanics to describe its dynamics. This then answers our second question, because the accuracy of position measurement is set by the standard quantum limit (SQL) as dictated by quantum mechanics. In certain cases, the accuracy can even surpass the SQL at the cost of losing information of a non commuting observable.

There has been an explosion of interest by researchers that try to harness the radiation pressure force for applications such as ultrasensitive detection, quantum communication, and studies in the foundations of quantum physics. Starting from 2006, the aim within the community was to cool mechanical complaint parts of nano and micro optomechanical systems to their quantum groundstate. In Fig.1.4, we show the progress on this topic and in 2011 researcher finally managed to reach groundstate in both, an optical [7] and microwave system [8]. Achieving groundstate opened doors to perform more advanced experiments, such as engineering mechanical quantum states e.g. Fock states or Schrödinger cat states [9]. The pioneering work of O'Connell *et al.* [10]. was the first to demonstrate a mechanical Fock state, while Palomaki *et al.* [11] went a step further by showing coherent exchange of a single phonon and photon. This was a huge step towards quantum state engineering with mechanical devices. Then in 2015, Wollman *et al.* [12] demonstrated squeezing of mechanical motion below the standard quantum limit as imposed by quantum mechanics. Using squeezed mechanical states is advanta-

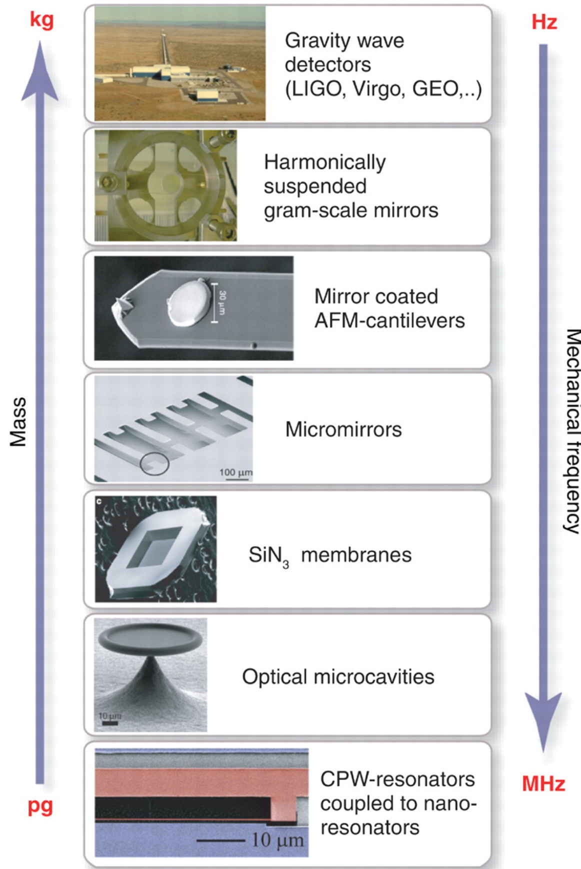

Figure 1.3: Various optomechanical devices that differ in length, mass and resonance frequency [6].

geous for many applications in sensing because it enhances precision measurements by increasing signal-to-noise.

Perhaps the most famous and notable example of optomechanics at work is the laser interferometer gravitational-wave observatory (LIGO), shown also in Fig.1.3 (top). In September 2015, the extreme sensitivities of LIGO detectors made it possible to detect gravitational waves emitted by the collision of two distant black holes [14]. By exploiting an exotic type of light called squeezed light, LIGO is able to detect a change in distance equal to 1/10000th of a proton [15]. Through the rapid development in quantum control techniques, Reed *et al.* [16] demonstrated (2017) coherent transfer of an electromagnetic superposition state (0-1) onto a micron sized metal drum. Not very long after that, in 2018 Riedinger *et al.* [17], was able to entangle two micron size mechanical oscillators separated by 30 cm.

While the technology for quantum state engineering in optomechanics is still in development, already new interesting ideas started to emerge about generating mechani-

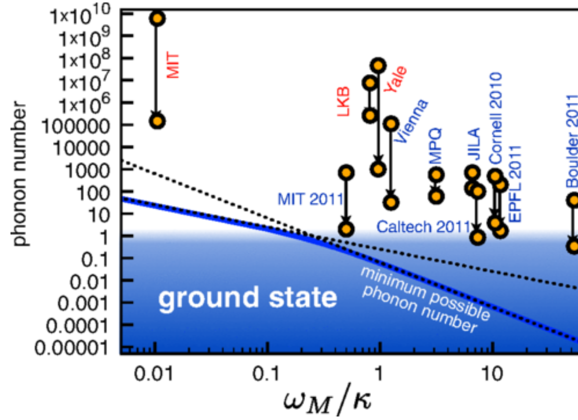

Figure 1.4: Efforts of optomechanical cooling of mechanical resonators to their quantum groundstate by various research groups [13]. Here, the initial and final phonon number of the fundamental mechanical mode is shown. Groundstate cooling was accomplished in 2011 by Ref. [7] and [8].

cal quantum states in optomechanical platforms to study gravity [18, 19]. These systems have a mechanical degree of freedom and their dynamics can be governed by gravity to some degree. The great interest and excitement in these ideas stem from the existing incompatibility between the formulation of quantum mechanics and gravity. In quantum mechanics, time is universal and absolute and thus modelled as an independent variable. However, in Einstein theory of GR, time is considered relative and dynamical. It is inseparably interwoven with the other x, y, z space dimensions into a space-time fabric. This fabric bends in the presence of matter, causing nearby objects to fall (gravity) and time to slow down. This has also been established empirically. Now the confusion: *in quantum mechanics, an object can exist in a superposition of being at two locations at the same time. These effects could give rise to a space-time superposition in which time flows at two different rates, as shown in* Fig.1.5. *Quantum mechanics cannot be used to describe this event accurately, since time is not an operator. Nor can GR because it is a local theory that is deterministic and does not allow for superpositions.*

Excitingly, non-classical mechanical superposition states have already been demonstrated in microwave electromechanical circuits [16], where mass is displaced at multiple locations at the same time. Mechanical Schrödinger cat states are another type of quantum states that can have large uncertainty in position, and here the mass is displaced in space and interferes with itself. Recently, many schemes have been proposed to generate these Schrödinger states in optomechanical platforms [20–22].

At present, no theory can be used to model GR induced deviations of these quantum states, but tentative guesses can still be made estimating time scales on which GR and quantum mechanics may interplay, as well as the consequences of such a situation. Ref. [23] has evaluated different mechanical oscillators on their potential for exploring the interaction between quantum mechanics and GR and obtained an expression for a characteristic timescale. Subsequently, they put forward the system parameters such that the consequences of this situation start to become measurable and found that none of

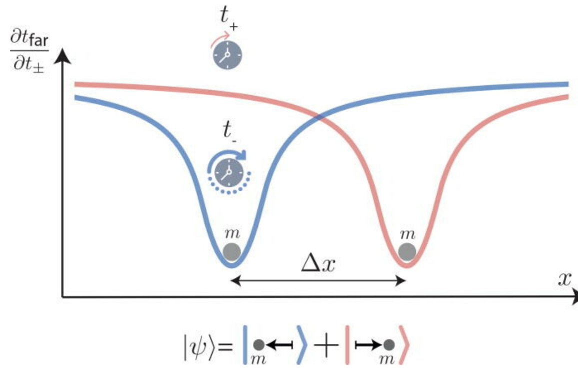

Figure 1.5: A mass m is put in a quantum superposition of two states which are displaced in the opposite direction with Δx. The states evolve with different times i.e. t_- (blue) and t_+ (right) with respect to a reference time frame t_{far} far away from the mass [23]. The notion of having correlated quantum states experiencing different time evolution conflicts with the formalism used to describe quantum mechanics.

the systems mentioned above have sufficient combination of mass and coherence time to probe gravitational effects. In this thesis, we present a high-Q and high coorperativity optomechanical platform that combines a massive SiN membrane with a superconducting lumped-element resonator. This system shows promise for conducting experiments that could provide new and exciting insights in a yet grey area within physics regarding the interplay between quantum mechanics and gravity [23].

1.3. THESIS OUTLINE

Where this chapter has presented an introduction and advances in the field of opto-and electromechanics, the rest of the thesis deals with technicalities of assembling and characterizing an electromechanical system. In **chapter 2**, we start by introducing the electromechanical circuit that we utilized and derive the corresponding coupled equations of motion (EOM). Upon linearizing and solving the EOM, we obtain an analytic expression for the parametrized cavity field amplitudes. The solutions allow us to find an expression for the noise powerspectrum of the joint system as measured with a spectrum analyser. In **chapter 3**, we give tangible meaning to the electromechanical circuit. We discuss the design conditions that both, the mechanical and electrical resonator need to satisfy considering the scope of this thesis. We then continue with a description of the fabrication process that we follow to make these devices. In **chapter 4**, we characterize the electrical circuit to be used in our future electromechanical devices. These circuits are superconducting lumped-element resonators in the GHz-range. Using electromagnetic simulations, we show that the shape of these resonators can be altered to reduce its conductive losses. In **chapter 5**, we have assembled an electromechanical device with the optimized lumped-element resonator and a high tensile stress Si_3N_4 square membrane using a new flipping technique. This device functions as a broadband cryogenic accelerometer that we use to calibrate the mechanical vibrations induced by the cryocooler of the dilution refrigerator. In **chapter 6**, we show that placing the Si_3N_4 membrane within a phononic shield array can significantly reduce mechanical radiation

losses. Upon characterization, the device is disturbed by mechanical noise and poses a challenge to calibrate electromechanical parameters. We nevertheless study the device in presence of mechanical noise and perform OMIT and ringdown measurements. In the laster chapter, we **conclude** the thesis by reflecting on the results and limitations of our architecture.

REFERENCES

[1] P. Lebedew, *Untersuchungen über die druckkräfte des lichtes,* Annalen der Physik **311**, 433 (1901).

[2] A. Einstein, *On the development of our views concerning the nature and constitution of radiation,* Phys. Z **10**, 817 (1909).

[3] V. Braginski and A. Manukin, *Ponderomotive effects of electromagnetic radiation,* Sov. Phys. JETP **25**, 653 (1967).

[4] V. Braginskiĭ, A. B. Manukin, and M. Y. Tikhonov, *Investigation of dissipative ponderomotive effects of electromagnetic radiation,* Soviet Journal of Experimental and Theoretical Physics **31**, 829 (1970).

[5] A. K. Sarma, S. Chakraborty, and S. Kalita, *Continuous variable quantum entanglement in optomechanical systems: A short review,* AVS Quantum Science **3**, 015901 (2021).

[6] T. J. Kippenberg and K. J. Vahala, *Cavity optomechanics: back-action at the mesoscale,* science **321**, 1172 (2008).

[7] J. Chan, T. M. Alegre, A. H. Safavi-Naeini, J. T. Hill, A. Krause, S. Gröblacher, M. Aspelmeyer, and O. Painter, *Laser cooling of a nanomechanical oscillator into its quantum ground state,* Nature **478**, 89 (2011).

[8] J. D. Teufel, T. Donner, D. Li, J. W. Harlow, M. Allman, K. Cicak, A. J. Sirois, J. D. Whittaker, K. W. Lehnert, and R. W. Simmonds, *Sideband cooling of micromechanical motion to the quantum ground state,* Nature **475**, 359 (2011).

[9] D. J. Griffiths and D. F. Schroeter, *Introduction to quantum mechanics* (Cambridge University Press, 2018).

[10] A. D. O'Connell, M. Hofheinz, M. Ansmann, R. C. Bialczak, M. Lenander, E. Lucero, M. Neeley, D. Sank, H. Wang, M. Weides, *et al., Quantum ground state and single-phonon control of a mechanical resonator,* Nature **464**, 697 (2010).

[11] T. Palomaki, J. Harlow, J. Teufel, R. Simmonds, and K. W. Lehnert, *Coherent state transfer between itinerant microwave fields and a mechanical oscillator,* Nature **495**, 210 (2013).

[12] E. E. Wollman, C. Lei, A. Weinstein, J. Suh, A. Kronwald, F. Marquardt, A. A. Clerk, and K. Schwab, *Quantum squeezing of motion in a mechanical resonator,* Science **349**, 952 (2015).

[13] M. Aspelmeyer, T. J. Kippenberg, and F. Marquardt, *Cavity optomechanics,* Reviews of Modern Physics **86**, 1391 (2014).

[14] B. P. Abbott, R. Abbott, T. Abbott, M. Abernathy, F. Acernese, K. Ackley, C. Adams, T. Adams, P. Addesso, R. Adhikari, *et al.*, *Observation of gravitational waves from a binary black hole merger,* Physical review letters **116**, 061102 (2016).

[15] B. Abbott, R. Abbott, R. Adhikari, P. Ajith, B. Allen, G. Allen, R. Amin, S. Anderson, W. Anderson, M. Arain, *et al.*, *Ligo: the laser interferometer gravitational-wave observatory,* Reports on Progress in Physics **72**, 076901 (2009).

[16] A. Reed, K. Mayer, J. Teufel, L. Burkhart, W. Pfaff, M. Reagor, L. Sletten, X. Ma, R. Schoelkopf, E. Knill, *et al.*, *Faithful conversion of propagating quantum information to mechanical motion,* Nature Physics **13**, 1163 (2017).

[17] R. Riedinger, A. Wallucks, I. Marinković, C. Löschnauer, M. Aspelmeyer, S. Hong, and S. Gröblacher, *Remote quantum entanglement between two micromechanical oscillators,* Nature **556**, 473 (2018).

[18] W. Marshall, C. Simon, R. Penrose, and D. Bouwmeester, *Towards quantum superpositions of a mirror,* Physical Review Letters **91**, 130401 (2003).

[19] T. H. Oosterkamp and J. Zaanen, *A clock containing a massive object in a superposition of states; what makes penrosian wavefunction collapse tick?* arXiv preprint arXiv:1401.0176 (2013).

[20] U. Akram, W. P. Bowen, and G. J. Milburn, *Entangled mechanical cat states via conditional single photon optomechanics,* New Journal of Physics **15**, 093007 (2013).

[21] I. Shomroni, L. Qiu, and T. J. Kippenberg, *Optomechanical generation of a mechanical catlike state by phonon subtraction,* Physical Review A **101**, 033812 (2020).

[22] N. E. Abari and M. H. Naderi, *Generation of the mechanical schrödinger cat state in a hybrid atom-optomechanical system,* JOSA B **37**, 2146 (2020).

[23] M. F. Gely and G. A. Steele, *Superconducting electro-mechanics to explore the effect of general relativity in massive superpositions,* arXiv preprint arXiv:2103.12729 (2021).

2

THEORETICAL BACKGROUND

In this chapter, we briefly outline the theory behind our superconducting electromechanical circuit realized via capacitive coupling. First, we model the fundamental mode of the mechanical resonator as an independent harmonic oscillator that is subjected to an external force and derive the mechanical susceptibility. We then couple the mechanical and electrical degree of freedom by capacitively integrating the mechanical oscillator into a superconducting lumped-element resonator. To get the dynamics of the coupled system, we write down and solve the linearized Heisenberg-Langevin equations of motion and obtain solutions for the classical and quantum field amplitudes. By computing the autocorrelation of the fluctuations operators, we obtain a general analytical expression for the noise power spectral density. This is convenient since the power spectrum can be directly measured with a spectrum analyser and allow us to calibrate electromechanical parameters.

The analytical derivations in this chapter have been performed by A. Sanz Mora.

2

2.1. MECHANICAL RESONATORS

In this section we derive an analytical expression for the response function of the fundamental mode of a mechanical resonator when subjected to an external force. A mechanical resonator is a mechanical object that is not infinitely rigid, as assumed and covered in most modern courses on introductory mechanics. The dynamics of a rigid body, when subjected to an external force, can be described by the position of the centre of mass and its orientation with respect to a fixed coordinate system. When the rigidity assumption is omitted, we need to take into account the flexibility of the atomic bonds that gives rise to internal motion. This causes deformation, or strain, of the object. Here, we are not interested in the rigid translation of the object, but only in the strain that occurs within the object. The strength of the atomic bonds also determines the mechanical and electrical properties of the material. The strain is related to the applied force per area (stress) through the stiffness of the material, commonly known as the Young modulus. This relation is known as the Hooke law and is expressed as

$$\overline{\sigma} = \overline{\epsilon} Q \tag{2.1}$$

Here, $\overline{\epsilon}$ and $\overline{\sigma}$ are the strain and normal stress (force per unit area) vector, respectively and Q, the elastic stiffness matrix. If we assume a single degree of freedom, Eq.(2.1) reduces to $\sigma = \epsilon E$. The internal stress-strain relation of a body as described by Eq.(2.1) is analogous to the restoring force of a mass connected to a spring with spring constant k. The equation of motion governing the dynamics of a mass-spring system is given by,

$$M\ddot{x} + \gamma_m \dot{x} - kx = F_{\text{ext}}(t) \tag{2.2}$$

Here, M is the mass and γ_m is the damping rate. It is convenient to study the response of the system in the frequency domain. Therefore, we Fourier transform and rewrite Eq.(2.2) and obtain

$$X(\omega) = \frac{F(\omega)/M}{(\omega^2 - \omega_m^2) - \mathrm{i}\omega\gamma_m} = \chi_m(\omega)\frac{F(\omega)}{M} \tag{2.3}$$

The denominator is considered the inverse susceptibility χ_m^{-1} of the mechanical system and is independent of the external force. The magnitude of the susceptibility can also be regarded as the sensitivity of the mechanical system as a transducer, which relates the external force $F_{\text{ext}}(\omega)$ to mechanical amplitude $X(\omega)$. For a given frequency ω_m, the susceptibility reach a maximum. We call this the mechanical resonance frequency and is defined as $\omega_m = \sqrt{k/M}$ of the mass-spring system. If however the damping γ_m gets too large then, for the system in Eq.(2.2), there is no peak and, hence, no practical resonance.

We define a dimensionless parameter called the quality factor Q, $Q_m = \omega_m/\gamma_m$, which quantifies the number of coherent mechanical oscillations that takes place before its amplitude decreases with e^{π} or by 4%. This definition of the Q factor hold when $Q \gg 1$. For illustrative purposes, we show $|\chi_m(\omega)|^2$ for Q-factors of 10 and 10^5 in Fig.2.1.

At $\omega \ll \omega_m$, the resonator shows a flat frequency response with $|\chi_m(\omega)|^2 \approx 1/\omega_m^4$. The susceptibility at resonance $\omega = \omega_m$ reduces to $|\chi_m|^2 = Q_m^2/\omega_m^4$ and here, the system reaches its maximum sensitivity. Note that the sensitivity on resonance depend linearly on Q and deteriorate with decreasing Q. As the frequency get larger than ω_m, the sensitivity decreases rapidly with ω^2.

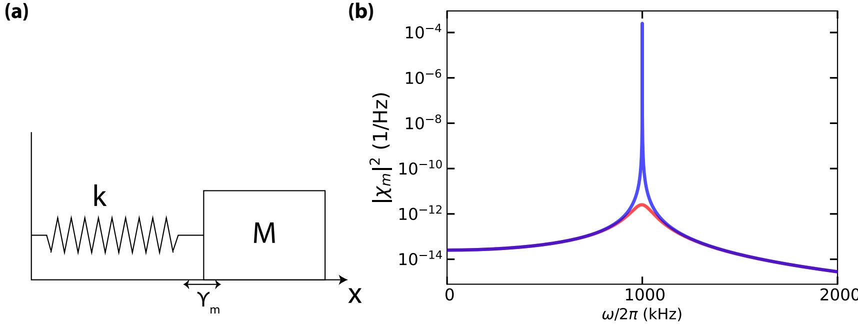

Figure 2.1: **Simple mass-spring analogy of mechanical resonator.** **(a)** Mass-spring model that is used to represent the fundamental mode of a mechanical resonator to first order. The model consists of a mass M connected to a spring with spring constant k and damping rate γ_m. **(b)** The mechanical sensitivity $|\chi_m(\omega)|^2$ for $Q_m = 10, 10^5$ depicted by the red and blue curve, respectively. The mechanical fundamental mode is located at $\omega_m = 2\pi \times 1000$ kHz.

Effective mass

To estimate electromechanical parameters, it is important to carefully calibrate the mass of the mode of interest. Since only a small part of the mechanical mode contributes to the motion [1], we model it as a position measurement of a point with effective mass $\mathrm{m_{eff}}$ that has the same order of magnitude as total mass M. Now we ask ourselves: *what is then the effective mass of the fundamental mode?*

First, we write down the total amplitude displacement of the mechanical resonator that is expressed in the basis formed by the eigenfunctions ξ_n and is given by [2]

$$z(x,t) = \sum_n u_n(t)\xi_n(x) \tag{2.4}$$

Note that $\xi_n(x)$ describes a one-dimensional mode shape for the nth mode of the resonator as a function of position x (for simplicity). The effective mass $\mathrm{m_{eff}}$ can be determined by considering the potential energy for n^{th} mode for a small length $d\mathrm{x}$ with mass element $d\mathrm{m} = \rho A d\mathrm{x}$ and is given with

$$d\mathrm{U} = \frac{1}{2}\rho A\omega_n^2 |u_n(t)\xi_n(x)|^2 d\mathrm{x} \tag{2.5}$$

$$m_{n,\mathrm{eff}} = \rho A \int_x |\xi_n^2(x)| d\mathrm{x} \tag{2.6}$$

assuming ρ is homogenous. The eigenfunctions ξ_n can be viewed as density functions and in case they are orthonormal with $L^{-1}\int_0^L \xi_n^2 \mathrm{dx} = 1$, then $m_{\mathrm{eff}} = M$ [2]. Here, we chose to normalize ξ_n such that the maximum of $|\xi_n|$ is unity. Using this convention, the eigenfunctions are orthogonal, but not orthonormal anymore. For a rectangular membrane and our chosen convention of normalization results in a $m_{\mathrm{eff}} = 0.25$ M and is the same for every mode of the membrane [3]. In the next section we regard the membrane as a rigid plate with $m_{\mathrm{eff}} = 0.25$ M where its dynamics is equivalent to that of the original membrane with mass M. Using other normalization techniques such as

the average displacement ($L^{-1}\int_0^L \xi_n d\mathrm{x} = 1$) will result in a different effective mass. Note that one is free to choose any definition of the displacement amplitude or the effective mass, but choosing one fixes the other, such that the equipartition theorem still holds i.e. $m_{n,\mathrm{eff}}\omega_n^2\langle z_n(t)^2\rangle = k_b T_n$ [4].

2.2. DYNAMICS OF ELECTROMECHANICAL SYSTEM

2.2.1. CAPACITIVE COUPLED ELECTROMECHANICS

We combine the mechanical resonator with an electrical system, of which we are able to measure voltages and currents and hence deduce mechanical observables. These combined systems known as electromechanical circuits, in which the electrical circuit used throughout this research is a superconducting LC resonator. The response of the LC resonator is then parametrized by the displacement of the mechanical resonator. The methods of combing these 2 harmonic oscillators are via (1) inductive coupling [5, 6] or (2) capacitive coupling [7, 8]. Inductive coupling is when the mechanical displacement modulates with magnetic flux of the electrical circuit and therefore its inductance. In a capacitive coupled scheme, the capacitance of the circuit is modulated and in both cases the resonance of the circuit depend on the mechanical amplitude. In this thesis, the emphasis will be on capacitive coupled electromechanical systems, of which we provide the mathematical description.

We characterize the electromechanical circuit sketched in Fig.2.2 in terms of an inductor with inductance L and a capacitor with capacitance $C(x)$, which depends on the distance x between its electrodes. The upper electrode is able to oscillate freely around the equilibrium position x_0, so that the only degree of freedom of mechanical motion is x [9] [1]. The movement of the oscillating electrode will induce a change in capacitance, thereby coupling the mechanical motion of the electrode to the circuit dynamics. This is known as a capacitive coupling. To study the dynamics of our electromechanical circuit, we shall derive the Hamiltonian accounting for such capacitive coupling.

In order to do so, we first need to determine the function $C(x)$. Unfortunately, an explicit form for $C(x)$ is usually hard to determine because the exact shape of the electrodes are yet unknown. However, we do not need to know the exact mode shape since we have reduced the membrane dynamics to a rigid plate with an effective mass. Its motion normalized such that the maximum displacement is unity. Assuming a valid harmonic approximation for the mechanical motion of the moving electrode, we can obtain a good estimation of $C(x)$ by using a Taylor series expansion around x_0.

Keeping terms up to linear order in x, we obtain $C \simeq C_0 + [\partial C/\partial x]_{x_0} x_m$. The resonance

[1] In general, any distortion in the geometry of a capacitor will lead to a change of its stored electrical energy and consequently in an applied stress upon the body that comprises the capacitor. Electrical forces may then deform the very same movable electrode the motion of which we describe through the single mechanical degree of freedom x. Thus, in principle one should account for the electrical energy, as well as the elastic energy, when computing the shape functions and frequencies of the resonant mechanical modes of such movable electrode [9]. However, if mechanical resonance frequencies are way lower than electrical ones, electrical forces will most probably disturb very little the mechanical degrees of freedom that account for the motion of the movable electrode. Each mechanical mode can then be treated independently as a single degree of freedom. Then if x is the coordinate describing the motion of the mode that interests us, we may consider the capacitance to be given by the function $C(x)$.

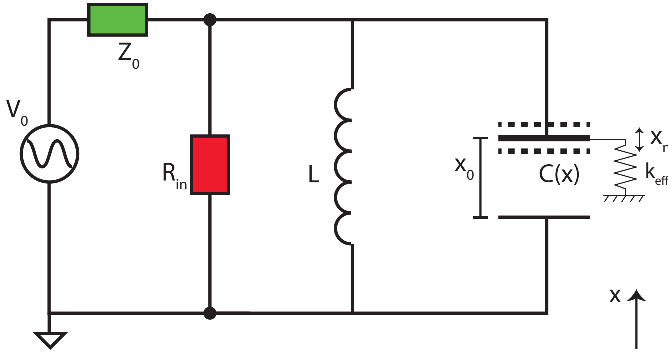

Figure 2.2: Capacitively coupled electromechanical (lumped-element) circuit with inductance L and capacitance C. The upper plate of the capacitor represent the mechanical oscillator and is described as a rigid plate with m_{eff}. Since it is allowed to oscillate freely, the capacitance of the circuit becomes $C \to C(x)$, hence we obtain coupling between the mechanical and electrical degree of freedom. A realistic circuit includes internal and external dissipation with R_{in} (red) and Z_{in} (green), respectively. The circuit is probed with source V_0.

frequency of the LC-oscillator is now approximated with

$$\tilde{\omega}_c(x) = \frac{1}{LC(x)} \simeq \omega_c\Big[1 - \frac{1}{2C_0}\big[\frac{\partial C}{\partial x}\big]_{x=x_0} x_m\Big] \tag{2.7}$$

where $C_0 = C(x_0)$ and $\omega_c = \sqrt{1/LC_0}$ are, respectively, the capacitance and the resonance frequency of the bare circuit (in static equilibrium), and $x_m = x - x_0$ is the displacement amplitude of the harmonically bound electrode. The last approximation in Eq.(2.7) follows from the assumption that a small displacement of the moving electrode results in a small change in capacitance, that is $x_0 \cdot (1/C_0)\partial C/\partial x\big|_{x_0} \ll 1$. More importantly, the expansion above shows that, as a result of the capacitive coupling, the resonance frequency of the LC circuit gets modulated by the amplitude of motion x_m of the movable electrode of the circuit's capacitor. This effect shall then manifest in the power spectrum of a microwave signal reflecting off the circuit. It will do so primarily in the form of sidebands located a mechanical frequency above and below from the signal carrier frequency. To compute noise spectra, we rely on input-output theory under a quantum description of the system Hamiltonian.

2.2.2. SYSTEM HAMILTONIAN

We write down the Hamiltonian that governs the quantum dynamics of the electromechanical circuit. To this end, we follow the usual approach of canonical quantization. We start treating electrical and mechanical variables on an equal footing under the framework of Lagrangian mechanics. Let us first address the description for the electrical degrees of freedom. We shall consider the charge Q flowing across the circuit components as the generalized coordinate. The normal coordinate of the LC-oscillator would then be $\tilde{Q} = Q\sqrt{L}$, and so its corresponding Lagrangian would read $L_{LC} = [\dot{\tilde{Q}}^2 - \tilde{\omega_c}^2(x)\tilde{Q}^2]/2$ [9]. Finally, the Legendre transformation $H_{LC} = \dot{\tilde{Q}}\tilde{\Phi} - L_{LC}$ gives the circuit Hamiltonian with $\tilde{\Phi} = \partial L_{LC}/\partial\dot{\tilde{Q}} = \dot{\tilde{Q}}$ the canonical momentum conjugate of $\tilde{Q}$. Here, we have restricted

ourselves to a non-relativistic description, and so the transformation above is valid. In such case, the following adiabatic picture holds: the energy of the circuit at successive instants of time can be computed as if the movable electrode were at rest[2]. The canonical momentum p_m of the movable electrode of mass m_{eff} is then given by the kinetic momentum $m_{\mathrm{eff}}\dot{x_m}$. We obtain the Hamiltonian H of the joint system by simple adding the Hamiltonian $H_m = p^2/2m_{\mathrm{eff}} + V(x_m)$ of the movable electrode to H_{LC}. Note that we have assumed a harmonic approximation for the motion of the movable electrode, i.e. we employ the harmonic oscillator potential $V(x_m) = m_{\mathrm{eff}}\omega_m^2 x_m^2/2$, and recasting L_{LC} in terms of $\tilde{\Phi}$ in the definition of H_{LC} leads to

$$\begin{aligned} H = H_{LC} + H_m &= \frac{1}{2}\left[\tilde{\Phi}^2 + \tilde{\omega}_c^2(x)\tilde{Q}^2\right] + \frac{p_m^2}{2m_{\mathrm{eff}}} + \frac{1}{2}m_{\mathrm{eff}}\omega_m^2 x_m^2 \\ &\simeq \frac{1}{2}\left[\tilde{\Phi}^2 + \omega_c^2\left[1 - \frac{1}{C_0}\frac{\partial C}{\partial x}\Big|_{x=x_0} x_m\right]^2 \tilde{Q}^2\right] + \frac{p^2}{2m_{\mathrm{eff}}} + \frac{1}{2}m_{\mathrm{eff}}\omega_m^2 x_m^2 \end{aligned} \tag{2.8}$$

To arrive at the expression given by Eq.(2.8), we expanded $\tilde{\omega}_c^2(x)$ up to first order in x_m using equation Eq.(2.7). We now switch to a quantum description by replacing the canonical variables $\tilde{Q}$ and x_m, and its associated conjugate momenta $\tilde{\Phi}$ and p_m, by the corresponding operators $\hat{\tilde{Q}}$, $\hat{x}_m$, $\hat{\tilde{\Phi}}$ and $\hat{p}_m$. These satisfy the commutation relations $[\hat{\tilde{Q}}, \hat{\tilde{\Phi}}] = [\hat{x}_m, \hat{p}_m] = i\hbar$, with all other possible independent commutator pairs equal to zero. We rewrite the Hamiltonian in terms of creation $\hat{A}^\dagger$ and annihilation $\hat{A}$ operators for the LC-oscillator, as well as rescaled position $\hat{X}_m$ and momentum $\hat{Y}_m$ operators for the mechanical resonator,

$$\hat{A} = \sqrt{\frac{1}{2\hbar\omega_c}}\left(\omega_c\hat{\tilde{Q}} + i\hat{\tilde{\Phi}}\right) \tag{2.9}$$

$$\hat{X}_m = \frac{1}{\sqrt{2}}\frac{\hat{x}_m}{x_{\mathrm{zpf}}}, \quad \hat{Y}_m = \frac{1}{\sqrt{2}}\frac{\hat{p}_m}{p_{\mathrm{zpf}}} \tag{2.10}$$

The corresponding commutation relations with the operators defined above are $[\hat{A}^\dagger, \hat{A}] = 1$ and $[\hat{X}_m, \hat{Y}_m] = i$. The Hamiltonian $\hat{H}$ of the quantized electromechanical circuit now reads

$$\begin{aligned} \hat{H}/\hbar = \omega_c[\hat{A}^\dagger\hat{A} + \frac{1}{2}] &+ \frac{\omega_m}{2}[\hat{X}_m^2 + \hat{Y}_m^2] \\ &+ \frac{Gx_{\mathrm{zpf}}}{\sqrt{2}}[\hat{A}^\dagger\hat{A} + \hat{A}\hat{A}^\dagger]\hat{X}_m \\ &+ \frac{Gx_{\mathrm{zpf}}}{\sqrt{2}}[\hat{A}^\dagger\hat{A}^\dagger + \hat{A}\hat{A}]\hat{X}_m \end{aligned} \tag{2.11}$$

The quantities $x_{\mathrm{zpf}} = \sqrt{\hbar/2m_{\mathrm{eff}}\omega_m}$ and $p_{\mathrm{zpf}} = \sqrt{\hbar m_{\mathrm{eff}}\omega_m}/2$ in Eq.(2.9) are, respectively, the zero point uncertainties in the position and momentum of the mechanical resonator i.e. the movable electrode. We define $G = -\omega_c(1/2C_0)\partial C/\partial x\big|_{x_0}$ as the electromechanical frequency shift per unit of displacement, sometimes also referred to as the 'frequency

[2] This adiabatically slow motion of the movable electrode is usually realized if the frequencies of its displacement amplitude x_m are much lower than the resonance frequency of the LC-oscillator [10]

pull parameter'. For systems with $\omega_m \ll \omega_c$, the coupling terms proportional to $\hat{A}^\dagger\hat{A}^\dagger$ and $\hat{A}\hat{A}$ are highly non-resonant. This means that their contribution is negligible [9], since the operating frequencies are around $\sim 2\omega_c$. The response function of the mechanical resonator at these frequencies is very small, and therefore we can safely neglect such coupling terms. With the Hamiltonian at hand, we can proceed to determine the power spectra of the system. The system is ultimately subjected to noise and friction forces that lead to energy dissipation and thermalization. These noise and friction forces are due to interactions of the LC-oscillator and the mechanical resonator with all the other infinitely many modes of their corresponding environments or baths. Using input–output theory, we are able to obtain an analytic expression for the output of the system that is not only coupled but also driven by its environment. Hence, by performing a measurement of the environment, we can deduce the dynamical state of the electromechanical system [11]. In the next section, we derive the input-output relations of the electromechanical circuit.

2

2.2.3. EQUATIONS OF MOTION

For the mechanical resonator we apply input-output theory under a Markov approximation only, while for the microwave resonator we apply input-output theory under both a Markov approximation and a weak coupling or rotating wave approximation (RWA), also known as Born approximation[3]. Finally, we shall distinguish two uncorrelated baths to which the LC-oscillator is coupled to, namely the *internal thermal bath of the resonant circuit itself and the external thermal bath of the transmission line*. We use the latter to coherently drive and read out the dynamical state of the electromechanical circuit. The resulting quantum Heisenberg-Langevin equation of motion for any observable $\hat{O}_{LC}$ of the LC-oscillator reads [12]

$$\begin{aligned}\dot{\hat{O}}_{\mathrm{LC}}(t) = &-\frac{\mathrm{i}}{\hbar}[\hat{O}_{\mathrm{LC}}(t),\hat{H}] - \left(\frac{\kappa}{2}\hat{O}_{\mathrm{LC}}(t) + \sum\sqrt{\kappa_j}\hat{A}_{\mathrm{in},j}(t)\right)[\hat{O}_{\mathrm{LC}}(t),\hat{A}^\dagger(t)] \\ &+\left(\frac{\kappa}{2}\hat{O}^\dagger_{\mathrm{LC}}(t) + \hat{A}^\dagger_{\mathrm{in},j}(t)\right)[\hat{O}_{\mathrm{LC}}(t),\hat{A}(t)]\end{aligned} \tag{2.12}$$

whereas the equivalent equation of motion for an observable $\hat{O}_m$ of the mechanical resonator is

$$\begin{aligned}\dot{\hat{O}}_{\mathrm{m}}(t) = &-\frac{\mathrm{i}}{\hbar}[\hat{O}_{\mathrm{m}}(t),\hat{H}] - \frac{\mathrm{i}}{2Q_m}[[\hat{O}_{\mathrm{m}}(t),\hat{X}_{\mathrm{m}}(t)],\dot{\hat{X}}_{\mathrm{m}}(t)]_+ \\ &-\mathrm{i}\sqrt{2\gamma_{\mathrm{m}}}[\hat{O}_{\mathrm{m}}(t),\hat{X}_{\mathrm{m}}(t)]\hat{Y}_{\mathrm{in}}(t)\end{aligned} \tag{2.13}$$

In Eq.(2.12) and (2.13) above, $\hbar$ is the Planck's constant h divided by 2π and $[\bullet,\bullet]_+$ denotes the anticommutator of two operators. The energy damping rate of the mechanical resonator arising from the interaction with its corresponding thermal bath is γ_{m}. Likewise, $\kappa = \kappa_{\mathrm{IN}} + \kappa_{\mathrm{EX}}$ is the energy damping rate of the LC-oscillator mode and accounts for intrinsic energy dissipation of the resonator, and energy decay due to photons within the LC-oscillator escaping back into the transmission line at a rate κ_{EX}. The internal

[3]The Markov limit assumes that the characteristic evolution time of the system of concern is much greater than the typical correlation time of its corresponding environment. The Born approximation assumes that the system-bath coupling rate is way lower than the system's transition frequencies.

2

and external dissipation κ_j ($j \in \{\mathrm{IN}, \mathrm{EX}\}$) [4] arises from the internal resistor and the external load to which the device is to, e.g. transmission line and source. The operator $\hat{A}_{\mathrm{in},j} = \langle \hat{A}_{\mathrm{in},j} \rangle + \delta \hat{A}_{\mathrm{in},j}$ describes an input stochastic drive onto the LC-oscillator arising from an interaction between the LC-oscillator and thermal bath j with coupling strength $\sqrt{\kappa_j}$. Similarly, the (Hermitian) operator $Y = \langle \hat{Y}_{\mathrm{in}} \rangle + \delta \hat{Y}_{\mathrm{in}}$ describes an input stochastic drive onto the mechanical resonator with strength $\sqrt{\gamma_{\mathrm{m}}}$. The input fields $\hat{A}_{\mathrm{in,IN}}$ and $\hat{Y}_{\mathrm{in}}$ associated with intrinsic dissipation of microwave and mechanical oscillator modes, respectively, are zero mean stochastic forcing terms, $\langle \hat{A}_{\mathrm{in,IN}} \rangle = \langle \hat{Y}_{\mathrm{in}} \rangle$. These forces allow are responsible for bringing such oscillator modes to a statistical equilibrium with the thermal bath. The input field $\hat{A}_{\mathrm{in,EX}} = \alpha_{\mathrm{in}} \exp(-\mathrm{i}\omega_d t) + \delta \hat{A}_{\mathrm{in,EX}}$ is a time dependent coherent drive with $\alpha_{\mathrm{in}} = \langle \hat{A}_{\mathrm{in,EX}} \exp(i\omega_d t) \rangle \neq 0$ and carrier frequency ω_d. We insert this drive through the aforementioned transmission line, and therefore also include its thermal fluctuations $\delta \hat{A}_{\mathrm{in,EX}}$. The output field that exits the resonant circuit is given by [12]

$$\hat{A}_{\mathrm{out}}(t) \equiv \hat{A}_{\mathrm{out,EX}}(t) = \hat{A}_{\mathrm{in,EX}}(t) + \sqrt{\kappa_{\mathrm{EX}}} \hat{A}(t). \tag{2.14}$$

Similar relations follow for the other two output field operators[5]. It can also be shown that, like the input operators, the output operators follow analogous commutation relations as those given in Eq.(2.9). We shall solve the dynamical evolution of $\hat{A}$, $\hat{X}_{\mathrm{m}}$ and $\hat{Y}_{\mathrm{m}}$ using Eq.(2.11) and (2.12) in combination with the quantized Hamiltonian (2.13).

First, we set the energy origin of the whole circuit to the ground state energy of the LC oscillator. This is realized by moving to an interaction picture where Hamiltonian

$$\hat{H}_0/\hbar = \hbar\omega_{\mathrm{c}}/2 \cdot \hat{1}. \tag{2.15}$$

is used. We switch to such interaction picture by means of the unitary operator $\hat{\mathscr{U}}_0 = \exp(\mathrm{i}\hat{H}_0 t/\hbar)$ and the transformed Hamiltonian is given by

$$\begin{aligned} \hat{H} \mapsto \hat{H}_{\mathrm{I}}(t) &= \hat{\mathscr{U}}_0(t)\hat{H}\hat{\mathscr{U}}_0^\dagger(t) + \mathrm{i}\hbar\dot{\hat{\mathscr{U}}}_0(t)\hat{\mathscr{U}}_0^\dagger(t) = \hat{\mathscr{U}}_0(t)\hat{H}\hat{\mathscr{U}}_0^\dagger(t) - \hat{H}_0\hat{\mathscr{U}}_0(t)\hat{\mathscr{U}}_0^\dagger(t) \\ &= \hat{\mathscr{U}}_0(t)\left[\hat{H} - \hat{H}_0\right]\hat{\mathscr{U}}_0^\dagger(t) \end{aligned} \tag{2.16}$$

In the last step of Eq.(2.16) above we use $\hat{H}_0\hat{\mathscr{U}}_0\hat{\mathscr{U}}_0^\dagger = \hat{\mathscr{U}}_0\hat{H}_0\hat{\mathscr{U}}_0^\dagger$, which follows from the fact that $\hat{H}_0$ commutes with $\hat{\mathscr{U}}_0$. The last equality of Eq.(2.16) explicitly shows that, in the new frame, the dynamics of the system is governed by the transformed version of the interaction Hamiltonian $\hat{H} - \hat{H}_0$ in the old frame, hence the use of the subscript I in $\hat{H}_{\mathrm{I}}$. Given that $\hat{H}_0$ is time independent and proportional to the unitary operator $\hat{1}$ of the Hilbert space of the entire electromechanical system, any other operator remains invariant under the frame transformation. Having clarified that, in what follows we will omit the subscript I to keep the notation as compact as possible. Thus, the (**interaction**)

[4] "IN, EX" refer to the internal and external thermal bath of the resonants circuit, while "in" refer to the input drive

[5] Eq.(2.14) is evaluated right at the location where the microwave field abandons the resonant circuit. Given that after interacting with and leaving behind the electromechanical circuit the field propagates freely at a constant speed, evaluating Eq.(2.14) at some distance further away from the exit of the resonant circuit, will yield the same result up to a shift in time.

Hamiltonian in the new frame reads

$$\hat{H}(t)/\hbar = \omega_c \hat{A}^\dagger(t)\hat{A}(t) + \frac{\omega_m}{2}[\hat{X}_m^2(t) + \hat{Y}_m^2(t)] + \frac{Gx_{zpf}}{\sqrt{2}}[\hat{A}^\dagger(t)\hat{A}(t) + \hat{A}(t)\hat{A}^\dagger(t)]\hat{X}_m(t), \tag{2.17}$$

where, as argued in section 2.2.2, we have neglected quadratic terms, proportional to $\hat{A}\hat{A}$ and $\hat{A}^\dagger\hat{A}^\dagger$. The Heisenberg-Langevin equations then read

$$\dot{\hat{A}}(t) = -\left[\mathrm{i}(\omega_c + \sqrt{2}g_0\hat{X}_m(t)) + \kappa/2\right]\hat{A}(t) - \sqrt{\kappa}\hat{A}_{in}(t), \tag{2.18}$$

$$\dot{\hat{X}}_m(t) = \omega_m \hat{Y}_m(t), \tag{2.19}$$

$$\dot{\hat{Y}}_m(t) = -\omega_m\hat{X}_m(t) - \gamma_m\hat{Y}_m(t) - \frac{g_0}{\sqrt{2}}[\hat{A}^\dagger(t)\hat{A}(t) + \hat{A}(t)\hat{A}^\dagger(t)] - \sqrt{2\gamma_m}\hat{Y}_{in}(t), \tag{2.20}$$

where $g_0 = Gx_{zpf}$ and $\hat{A}_{in} = \sqrt{\eta_c}\hat{A}_{in,EX} + \sqrt{1-\eta_c}\hat{A}_{in,IN}$ with $\eta_c = \kappa_{EX}/\kappa$ the circuit's coupling efficiency to its output port (transmission line). We rewrite the equations above in terms of slow varying amplitudes $\hat{a} = \hat{A}\exp(\mathrm{i}\omega_d t)$ and $\hat{a}_{in} = \hat{A}_{in}\exp(\mathrm{i}\omega_d t)$ because the input drive is a fast oscillating field with $\langle\hat{A}_{in}\rangle = \sqrt{\eta_c}\alpha_{in}\exp(-\mathrm{i}\omega_d t)$. We then obtain

$$\dot{\hat{a}}(t) = -\left[-\mathrm{i}(\Delta_0 - \sqrt{2}g_0\hat{X}_m(t)) + \kappa/2\right]\hat{a}(t) - \sqrt{\kappa\eta_c}\alpha_{in} - \sqrt{\kappa}\delta\hat{a}_{in}(t), \tag{2.21}$$

$$\dot{\hat{X}}_m(t) = \omega_m\hat{Y}_m(t), \tag{2.22}$$

$$\dot{\hat{Y}}_m(t) = -\omega_m\hat{X}_m(t) - \gamma_m\hat{Y}_m(t) - \frac{g_0}{\sqrt{2}}[\hat{a}^\dagger(t)\hat{a}(t) + \hat{a}(t)\hat{a}^\dagger(t)] - \sqrt{2\gamma_m}\delta\hat{Y}_{in}(t). \tag{2.23}$$

Here, $\delta\hat{a}_{in} = [\sqrt{\eta_c}\delta\hat{A}_{in,EX} + \sqrt{1-\eta_c}\delta\hat{A}_{in,IN}]\exp(\mathrm{i}\omega_d t)$ and $\Delta_0 = \omega_d - \omega_c$ is the drive cavity detuning.

The classical equations of motion are found by taking the expectation of the operators, which read

$$\langle\dot{\hat{a}}(t)\rangle = -\left[-\mathrm{i}(\Delta_0 - \sqrt{2}g_0\langle\hat{X}_m(t)\rangle) + \kappa/2\right]\langle\hat{a}(t)\rangle - \sqrt{\kappa\eta_c}\alpha_{in}, \tag{2.24}$$

$$\langle\dot{\hat{X}}_m(t)\rangle = \omega_m\langle\hat{Y}_m(t)\rangle, \tag{2.25}$$

$$\langle\dot{\hat{Y}}_m(t)\rangle = -\omega_m\langle\hat{X}_m(t)\rangle - \gamma_m\langle\hat{Y}_m(t)\rangle - \sqrt{2}g_0|\langle\hat{a}(t)\rangle|^2. \tag{2.26}$$

We assume the circuit can settle into a steady state after a sufficiently long time, so that setting time derivatives to zero in the system of Eq.(2.24)–(2.26) above is valid, and, $\langle\hat{\mathcal{O}}(t)\rangle \to \bar{\mathcal{O}}$, where $\hat{\mathcal{O}}$ refers to any operator describing the quantized electromechanical circuit. Thus, one finds

$$\bar{a} = \frac{\sqrt{\kappa\eta_c}\alpha_{in}}{\mathrm{i}(\Delta_0 - \sqrt{2}g_0\bar{X}_m) - \kappa/2} \tag{2.27}$$

$$\bar{X}_m = -\frac{\sqrt{2}g_0}{\omega_m}|\bar{a}|^2 \tag{2.28}$$

$$\bar{Y}_m = 0 \tag{2.29}$$

If we express both the steady state amplitude and the input field amplitude in polar form $\bar{a} = \sqrt{\bar{n}}\exp(\mathrm{i}\bar{\phi})$, $\alpha_{\mathrm{in}} = |\alpha_{\mathrm{in}}|\exp(\mathrm{i}\phi_{\mathrm{in}})$, we then can identify $\bar{n} = \bar{a}^*\bar{a} = |\bar{a}|^2$ with the average number of photons inside the cavity and $\bar{\phi} = \arctan\left(\mathrm{Im}[\bar{a}]/\mathrm{Re}[\bar{a}]\right)$ with the microwave intracavity field phase. From Eq.(2.27) and (2.28) above, we find that these are given by the solution to the following system of algebraic equations

$$\bar{n}\left[(\Delta_0 + 2g_0^2\bar{n}/\omega_{\mathrm{m}})^2 + \kappa^2/4\right] = \kappa\eta_c|\alpha_{\mathrm{in}}|^2, \tag{2.30}$$

$$\bar{\phi} = \phi_{\mathrm{in}} + \arctan\left(2[\Delta_0 + 2g_0^2\bar{n}/\omega_{\mathrm{m}}]/\kappa\right). \tag{2.31}$$

2.2.4. SOLUTION OF THE LINEARIZED HEISENBERG-LANGEVIN EQUATIONS OF MOTION

Linearizing operators around their steady state values, $\hat{a} = \bar{a} + \delta\hat{\hat{a}}$, $\hat{X}_{\mathrm{m}} = \bar{X}_{\mathrm{m}} + \delta\hat{X}_{\mathrm{m}}$, and $\hat{X}_{\mathrm{m}} = \bar{X}_{\mathrm{m}} + \delta\hat{X}_{\mathrm{m}}$, we find the following set of equations for their fluctuations,

$$\delta\dot{\hat{\hat{a}}}(t) = -[-\mathrm{i}\Delta + \kappa/2]\delta\hat{\hat{a}}(t) - \mathrm{i}\sqrt{2}g\exp(\mathrm{i}\bar{\phi})\delta\hat{X}_{\mathrm{m}}(t) - \sqrt{\kappa}\delta\hat{\hat{a}}_{\mathrm{in}}(t), \tag{2.32}$$

$$\delta\dot{\hat{X}}_{\mathrm{m}}(t) = \omega_{\mathrm{m}}\delta\hat{Y}_{\mathrm{m}}(t), \tag{2.33}$$

$$\delta\dot{\hat{Y}}_{\mathrm{m}}(t) = -\omega_{\mathrm{m}}\delta\hat{X}_{\mathrm{m}}(t) - \gamma_{\mathrm{m}}\delta\hat{Y}_{\mathrm{m}}(t) - \sqrt{2}g[\delta\hat{\hat{a}}^\dagger(t)\exp(\mathrm{i}\bar{\phi}) + \delta\hat{\hat{a}}(t)\exp(-\mathrm{i}\bar{\phi})] - \sqrt{2\gamma_{\mathrm{m}}}\delta\hat{Y}_{\mathrm{in}}(t), \tag{2.34}$$

where $g = g_0\sqrt{\bar{n}}$ and we have introduced the effective detuning $\Delta = \Delta_0 + 2g_0^2\bar{n}/\omega_{\mathrm{m}}$. Finally, we can redefine the fluctuating part of the microwave fields so that they lie along the direction given by $\bar{\phi}$, i.e. introduce the operators $\delta\hat{a} = \delta\hat{\hat{a}}\exp(-\mathrm{i}\bar{\phi})$ and $\delta\hat{a}_{\mathrm{in}} = \delta\hat{\hat{a}}_{\mathrm{in}}\exp(-\mathrm{i}\bar{\phi})$. In terms of these rotated amplitude fluctuations we have

$$\delta\dot{\hat{a}}(t) = -[-\mathrm{i}\Delta + \kappa/2]\delta\hat{a}(t) - \mathrm{i}\sqrt{2}g\delta\hat{X}_{\mathrm{m}}(t) - \sqrt{\kappa}\delta\hat{a}_{\mathrm{in}}(t), \tag{2.35}$$

$$\delta\dot{\hat{X}}_{\mathrm{m}}(t) = \omega_{\mathrm{m}}\delta\hat{Y}_{\mathrm{m}}(t), \tag{2.36}$$

$$\delta\dot{\hat{Y}}_{\mathrm{m}}(t) = -\omega_{\mathrm{m}}\delta\hat{X}_{\mathrm{m}}(t) - \gamma_{\mathrm{m}}\delta\hat{Y}_{\mathrm{m}}(t) - \sqrt{2}g[\delta\hat{a}^\dagger(t) + \delta\hat{a}(t)] - \sqrt{2\gamma_{\mathrm{m}}}\delta\hat{Y}_{\mathrm{in}}(t), \tag{2.37}$$

Fourier transforming the equations yields

$$-\mathrm{i}\omega\underline{\delta\hat{a}}(\omega) = -[-\mathrm{i}\Delta + \kappa/2]\underline{\delta\hat{a}}(\omega) - \mathrm{i}\sqrt{2}g\underline{\delta\hat{X}_{\mathrm{m}}}(\omega) - \sqrt{\kappa}\underline{\delta\hat{a}_{\mathrm{in}}}(\omega), \tag{2.38}$$

$$-\mathrm{i}\omega\underline{\delta\hat{X}_{\mathrm{m}}}(\omega) = \omega_{\mathrm{m}}\underline{\delta\hat{Y}_{\mathrm{m}}}(\omega), \tag{2.39}$$

$$-\mathrm{i}\omega\underline{\delta\hat{Y}_{\mathrm{m}}}(\omega) = -\omega_{\mathrm{m}}\underline{\delta\hat{X}_{\mathrm{m}}}(\omega) - \gamma_{\mathrm{m}}\underline{\delta\hat{Y}_{\mathrm{m}}}(\omega) - \sqrt{2}g[\underline{\delta\hat{a}}^\dagger(-\omega) + \underline{\delta\hat{a}}(\omega)] - \sqrt{2\gamma_{\mathrm{m}}}\underline{\delta\hat{Y}_{\mathrm{in}}}(\omega) \tag{2.40}$$

The solution reads

$$\underline{\delta\hat{a}}(\omega) = \mathrm{i}2\sqrt{\kappa}\underline{\chi}_{\mathrm{c}}^*(-\omega;\Delta)\underline{\delta\hat{a}_{\mathrm{in}}}(\omega) - 2\sqrt{2}g\underline{\chi}_{\mathrm{c}}^*(-\omega;\Delta)[\underline{\delta\hat{X}_{\mathrm{m},0}}(\omega) + \underline{\delta\hat{X}_{\mathrm{m,BA}}}(\omega)], \tag{2.41}$$

$$\underline{\delta\hat{X}_{\mathrm{m},0}}(\omega) = \sqrt{2\gamma_{\mathrm{m}}}\underline{\varepsilon_{\mathrm{m}}}(\omega)\underline{\delta\hat{Y}_{\mathrm{in}}}(\omega), \tag{2.42}$$

$$\underline{\delta\hat{X}_{\mathrm{m,BA}}}(\omega) = \sqrt{2\gamma_{\mathrm{m}}}\underline{\varepsilon_{\mathrm{m}}}(\omega)\underline{\delta\hat{Y}_{\mathrm{BA}}}(\omega), \tag{2.43}$$

where,

$$\underline{\delta\hat{Y}}_{\mathrm{BA}}(\omega) = -\mathrm{i}\kappa\sqrt{C/2}[\underline{\chi}_{\mathrm{c}}(\omega;\Delta)\underline{\delta\hat{a}}^{\dagger}_{\mathrm{in}}(-\omega) - \underline{\chi}^{*}_{\mathrm{c}}(-\omega;\Delta)\underline{\delta\hat{a}}_{\mathrm{in}}(\omega)] \tag{2.44}$$

is the dynamical backaction force exerted by the intracavity radiation onto the mechanical resonator with $C = 4g^2/(\kappa\gamma_{\mathrm{m}})$ the so called electromechanical cooperativity. In the Eq.(2.41) and (2.42) above, the cavity and effective mechanical susceptibilities, $\underline{\chi}_{\mathrm{c}}$ and $\underline{\varepsilon}_{\mathrm{m}}$ respectively, are given by

$$\underline{\chi}_{\mathrm{c}}(\omega;\Delta) = \frac{-\mathrm{i}/2}{-\mathrm{i}(\omega-\Delta)+\kappa/2}, \tag{2.45}$$

$$\underline{\varepsilon}_{\mathrm{m}}(\omega) = \frac{\underline{\chi}_{\mathrm{m}}(\omega)}{1-4g^2\underline{\chi}_{\mathrm{m}}(\omega)[\underline{\chi}_{\mathrm{c}}(\omega;\Delta)+\underline{\chi}^{*}_{\mathrm{c}}(-\omega;\Delta)]}, \tag{2.46}$$

where the mechanical susceptibility is

$$\underline{\chi}_{\mathrm{m}}(\omega) = \frac{\omega_{\mathrm{m}}}{\omega^2-\omega_{\mathrm{m}}^2+\mathrm{i}\gamma_{\mathrm{m}}\omega}. \tag{2.47}$$

Note that since $\underline{\chi}^{*}_{\mathrm{m}}(-\omega) = \underline{\chi}_{\mathrm{m}}(\omega)$, it follows that $\underline{\varepsilon}^{*}_{\mathrm{m}}(-\omega) = \underline{\varepsilon}_{\mathrm{m}}(\omega)$. Likewise, it is useful to note that $\underline{\chi}^{*}_{\mathrm{c}}(-\omega;\Delta) = -\underline{\chi}_{\mathrm{c}}(\omega;-\Delta)$.

2.2.5. POWER SPECTRUM

In this section, we describe how the powerspectrum can be derived with the linearized solution of the Heisenberg-Langevin equations and is mostly inspired by [11] and [13]. We define the fluctuations of a real and time varying noisy signal (random process) $V(t)$ as $\delta V(t) = V(t) - \langle V(t)\rangle$, with $\langle\cdot\rangle$ denoting an ensemble average, over the set of possible realizations of V. Then we consider the instantaneous (noise) power of V to be $\delta V^2(t)$, so that the averaged (noise) power of V over a time period $\mathcal{T} > 0$ is given by

$$\lim_{\mathcal{T}\to\infty}\frac{1}{\mathcal{T}}\int_{-\mathcal{T}/2}^{+\mathcal{T}/2}\mathrm{d}t\langle\delta V^2(t)\rangle. \tag{2.48}$$

This power need not have actual units of power. The term 'power' arises from the fact that the averaged power of physical waves (acoustic waves, light waves, etc.), is proportional to the square of the wave's amplitude. More explicitly, the term power as defined in Eq.(2.48) characterizes the noise variance or noise fluctuations of the noisy signal [11]. This follows from the fact that noise has always zero mean, and therefore its mean-square coincides with its variance.

Often, it is useful to know the distribution of the averaged power (the noise variance) of a noisy signal over the frequency spectrum. The function accounting for such distribution is known as the power spectral density, or simply, the power spectrum of the noisy signal. To derive an explicit form of the power spectrum of V we start by introducing the rectangular, window or gate function

$$\mathrm{rect}_{\mathcal{T}}(t) = \begin{cases} 1 & \text{if } -\mathcal{T}/2 < t < \mathcal{T}/2, \\ 0 & \text{if } |t| > \mathcal{T}/2. \end{cases} \tag{2.49}$$

Then, by virtue of the Plancherel theorem, the definition (2.48) above can be rewritten as follows

$$\lim_{\mathcal{T}\to\infty}\frac{1}{\mathcal{T}}\int_{-\mathcal{T}/2}^{+\mathcal{T}/2}\mathrm{d}t\langle\delta V^2(t)\rangle = \lim_{\mathcal{T}\to\infty}\frac{1}{\mathcal{T}}\int_{-\infty}^{+\infty}\mathrm{d}t\langle\delta V_{\mathcal{T}}^2(t)\rangle = \int_{-\infty}^{+\infty}\frac{\mathrm{d}\omega}{2\pi}\left[\lim_{\mathcal{T}\to\infty}\frac{1}{\mathcal{T}}\langle\underline{\delta V}_{\mathcal{T}}^*(\omega)\underline{\delta V}_{\mathcal{T}}(\omega)\rangle\right], \tag{2.50}$$

where $\delta V_{\mathcal{T}} = \mathrm{rect}_{\mathcal{T}}\delta V$, and $\underline{\delta V}_{\mathcal{T}}(\omega) = \mathscr{F}\{\delta V_{\mathcal{T}}(t)\}(\omega) \equiv \int_{-\infty}^{+\infty}\mathrm{d}t\exp(\mathrm{i}\omega t)\delta V_{\mathcal{T}}(t)$ denotes the Fourier transform of $\delta V_{\mathcal{T}}$. The limit within brackets in the integral of the right-hand side of Eq.(2.50) describes precisely how the noise variance of V is distributed over each frequency, and thus defines the power spectrum of V, which we will denote as $\underline{\mathscr{S}}_{VV}(\omega)$. Finally, if we assume that V is a wide-sense stationary random process, i.e., that its mean and autocorrelator are invariants under time translations, such limit can be computed to give the celebrated Wiener-Khintchine theorem [13]

$$\underline{\mathscr{S}}_{VV}(\omega) \equiv \lim_{\mathcal{T}\to\infty}\frac{1}{\mathcal{T}}\langle\underline{\delta V}_{\mathcal{T}}^*(\omega)\underline{\delta V}_{\mathcal{T}}(\omega)\rangle = \int_{-\infty}^{+\infty}\mathrm{d}t\exp(\mathrm{i}\omega t)\mathscr{S}_{VV}(t), \tag{2.51}$$

where $\mathscr{S}_{VV}(t) \equiv \langle\delta V^*(t)\delta V(0)\rangle$ is the autocorrelator of V.

The power spectral density (2.51) can be of great utility, if we are interested in detecting a monochromatic wave amidst noise that we can record. This is also the case in our electromechanical circuit above. The amplitude fluctuations of a noisy signal measured in time domain is proportional to its power (amplitude square) in the frequency domain. To characterize the proportionality factor and further features of such experiment we shall perform some analytical evaluation of the power spectrum of the noisy signal (microwaves in our case). This will require knowledge of time evolved fluctuating observables such as δV, or, alternatively, its Fourier transform. Indeed, the power spectrum of V can also be computed from the Fourier transform of its fluctuations. Expanding δV and its complex conjugate in terms of their corresponding Fourier amplitudes in the autocorrelator $\mathscr{S}_{VV}$, we can recast the last equality of (2.51) as follows [13]

$$\underline{\mathscr{S}}_{VV}(\omega) = \int_{-\infty}^{+\infty}\mathrm{d}t\exp(\mathrm{i}\omega t)\mathscr{S}_{VV}(t) = \int_{-\infty}^{+\infty}\frac{\mathrm{d}\omega'}{2\pi}\langle\underline{\delta V}^*(-\omega)\underline{\delta V}(\omega')\rangle. \tag{2.52}$$

We aspire to characterize the mechanical motion of the movable electrode in our electromechanical circuit via the record of a noisy microwave signal onto which the mechanical motion is imparted. We derived an analytical expression of the microwave power spectral density using the solution of the quantum Heisenberg-Langevin solutions from the previous section. The unsymmetrized power spectral density of the output field reads

$$\underline{S}_{a_{\mathrm{out}}a_{\mathrm{out}}}(\omega) = \underline{S}_{a_{\mathrm{out},0}a_{\mathrm{out},0}}(\omega) + 8\kappa\eta_{\mathrm{c}}g^2|\underline{\chi}_{\mathrm{c}}(\omega;\Delta)|^2\left[\underline{S}_{X_{\mathrm{m},0}X_{\mathrm{m},0}}(\omega) + \underline{S}_{X_{\mathrm{m,BA}}X_{\mathrm{m,BA}}}(\omega)\right] + 2\mathrm{Re}\left[2g\sqrt{2\kappa\eta_{\mathrm{c}}}\underline{\chi}_{\mathrm{c}}(\omega;\Delta)\underline{S}_{X_{\mathrm{m,BA}}a_{\mathrm{out},0}}(\omega)\right]. \tag{2.53}$$

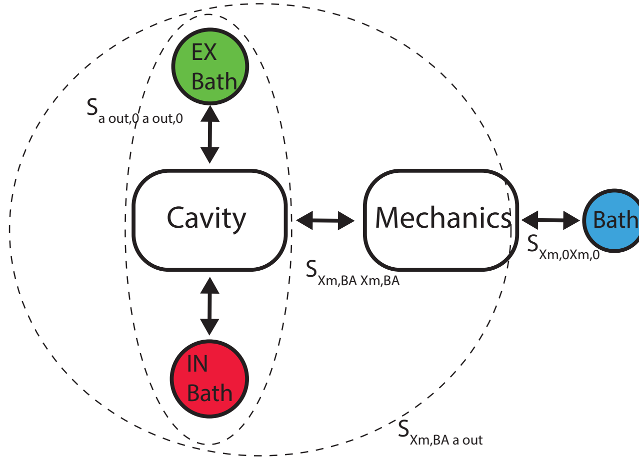

Figure 2.3: Schematic of electromechanical system to illustrate noise spectral density terms in Eq.(2.53).

Here, we have

$$\underline{S}_{a_{\mathrm{out},0}a_{\mathrm{out},0}}(\omega) = \left|1 + \mathrm{i}2\kappa\eta_{\mathrm{c}}\underline{\chi}_{\mathrm{c}}(\omega;\Delta)\right|^2 \bar{n}_{T_{\mathrm{bEX}}} + 4\kappa^2\eta_{\mathrm{c}}(1-\eta_{\mathrm{c}})\left|\underline{\chi}_{\mathrm{c}}(\omega;\Delta)\right|^2 \bar{n}_{T_{\mathrm{bIN}}},$$
$$\underline{S}_{X_{\mathrm{m},0}X_{\mathrm{m},0}}(\omega) = 2\gamma_{\mathrm{m}}|\varepsilon_{\mathrm{m}}(\omega)|^2 \underline{S}_{Y_{\mathrm{in}}Y_{\mathrm{in}}}(\omega);\ \underline{S}_{Y_{\mathrm{in}}Y_{\mathrm{in}}}(\omega) = \frac{\omega}{\omega_{\mathrm{m}}}[\bar{n}_{T_{\mathrm{bm}}}(\omega)+1],\ \underline{S}_{Y_{\mathrm{in}}Y_{\mathrm{in}}}(-\omega) = \frac{\omega}{\omega_{\mathrm{m}}}\bar{n}_{T_{\mathrm{bm}}}(\omega),$$
$$\underline{S}_{X_{\mathrm{m,BA}}X_{\mathrm{m,BA}}}(\omega) = 8\kappa g^2|\varepsilon_{\mathrm{m}}(\omega)|^2\left\{\left[|\underline{\chi}_{\mathrm{c}}(-\omega;\Delta)|^2 + |\underline{\chi}_{\mathrm{c}}(\omega;\Delta)|^2\right]\left[\eta_{\mathrm{c}}\bar{n}_{T_{\mathrm{bEX}}} + (1-\eta_{\mathrm{c}})\bar{n}_{T_{\mathrm{bIN}}}\right] + |\underline{\chi}_{\mathrm{c}}(-\omega;\Delta)|^2\right\},$$
$$\underline{S}_{X_{\mathrm{m,BA}}a_{\mathrm{out}}}(\omega) = \mathrm{i}2g\sqrt{2\kappa\eta_{\mathrm{c}}}\underline{\chi}_{\mathrm{c}}(\omega;\Delta)\varepsilon_{\mathrm{m}}(\omega)\left\{\left[1 + \mathrm{i}2\kappa\eta_{\mathrm{c}}\underline{\chi}_{\mathrm{c}}^*(-\omega;\Delta)\right]\bar{n}_{T_{\mathrm{bEX}}} + \mathrm{i}2\kappa(1-\eta_{\mathrm{c}})\underline{\chi}_{\mathrm{c}}^*(-\omega;\Delta)\bar{n}_{T_{\mathrm{bIN}}}\right\}.$$

The interaction of the electromechanical system with its thermal bath is illustrated in Fig.2.3. The first term $\underline{S}_{a_{\mathrm{out},0}a_{\mathrm{out},0}}(\omega)$ represents the spectral density of the noise that arises from the cavity coupling to its internal and external thermal bath. The second term $\underline{S}_{X_{\mathrm{m},0}X_{\mathrm{m},0}}(\omega)$ come from the noise correlations of the mechanical thermal bath (blue). In case $\hbar\omega_m \ll k_b T$, the term $\underline{S}_{Y_{\mathrm{in}}Y_{\mathrm{in}}}(\omega)$ is not symmetric, since the mechanical creation and annihilation operators do not commute. In the high-temperature limit, however, $\underline{S}_{Y_{\mathrm{in}}Y_{\mathrm{in}}}(-\omega) \simeq \underline{S}_{Y_{\mathrm{in}}Y_{\mathrm{in}}}(\omega)$. The third term $\underline{S}_{X_{\mathrm{m,BA}}X_{\mathrm{m,BA}}}(\omega)$ comes from the backaction that the cavity as detector exert on the mechanical resonator. In general, there will be some correlations between the output and input of the cavity detector i.e. the thermal baths of the cavity and the mechanical resonator. [14]. This is described with the last term $\underline{S}_{X_{\mathrm{m,BA}}a_{\mathrm{out}}}(\omega)$. The terms $\overline{n}_{\mathrm{T_{b_i}}}$ ($i \in \{\mathrm{IN},\mathrm{EX}\}$) are the thermal occupations of the cavity mode due to coupling to the internal and external bath. These approach zero for superconducting GHz resonators at cryogenic temperatures, and therefore the first and last term of Eq.(2.53) are negligible.

Now, the voltage power spectrum displayed in the spectrum analyser is

$$Z_0\mathscr{W}_{\Delta\Omega} \simeq \frac{1}{2\pi}\mathscr{G}_{\mathrm{T}}\hbar\omega_{\mathrm{d}}Z_0 2\Delta\Omega\left[|\alpha_{\mathrm{out}}|^2\pi\delta(\omega-\omega_{\mathrm{d}}) + \underline{S}_{a_{\mathrm{out}}a_{\mathrm{out}}}(\omega-\omega_{\mathrm{d}}) + \bar{n}_{\mathrm{add}} + 1/2\right],$$

with

$$\bar{n}_{\text{add}} = \left(\frac{1}{\eta_l} - 1\right)\frac{1}{2} + \frac{1}{\eta_l}\left(\bar{n}_{\text{A}} + \frac{1}{2}\right),$$

the number of added photons, where $\bar{n}_{\text{A}}$ is the photons added by the low noise amplifier and η_l is the attenuating factor accounting for losses between the output of the electromechanical circuit and the input of the low noise amplifier. The input impedance and the measurement bandwidth are Z_o and $\Delta\Omega$ respectively. $\mathscr{G}_{\text{T}}$ is the total gain from the output of the device to the spectrum analyser. Finally,

$$|\alpha_{\text{out}}|^2 = |\alpha_{\text{in}}|^2 \left|1 - 2\mathrm{i}\underline{\chi}_{\text{c}}^*(0;\Delta)\right|^2$$

is the photon flux at the output of the electromechanical circuit.

REFERENCES

[1] S. Gröblacher, *Quantum opto-mechanics with micromirrors: combining nano-mechanics with quantum optics* (Springer Science & Business Media, 2012).

[2] M. Poot and H. S. van der Zant, *Mechanical systems in the quantum regime,* Physics Reports **511**, 273 (2012).

[3] B. Hauer, C. Doolin, K. Beach, and J. Davis, *A general procedure for thermomechanical calibration of nano/micro-mechanical resonators,* Annals of Physics **339**, 181 (2013).

[4] G. Anetsberger, O. Arcizet, Q. P. Unterreithmeier, R. Rivière, A. Schliesser, E. M. Weig, J. P. Kotthaus, and T. J. Kippenberg, *Near-field cavity optomechanics with nanomechanical oscillators,* Nature Physics **5**, 909 (2009).

[5] G. Via, G. Kirchmair, and O. Romero-Isart, *Strong single-photon coupling in superconducting quantum magnetomechanics,* Physical review letters **114**, 143602 (2015).

[6] I. Rodrigues, D. Bothner, and G. Steele, *Coupling microwave photons to a mechanical resonator using quantum interference,* Nature communications **10**, 1 (2019).

[7] J. D. Teufel, T. Donner, D. Li, J. W. Harlow, M. Allman, K. Cicak, A. J. Sirois, J. D. Whittaker, K. W. Lehnert, and R. W. Simmonds, *Sideband cooling of micromechanical motion to the quantum ground state,* Nature **475**, 359 (2011).

[8] M. Yuan, M. A. Cohen, and G. A. Steele, *Silicon nitride membrane resonators at millikelvin temperatures with quality factors exceeding 108,* Applied Physics Letters **107**, 263501 (2015).

[9] M. Aspelmeyer, T. J. Kippenberg, and F. Marquardt, *Cavity optomechanics: nano- and micromechanical resonators interacting with light* (Springer, 2014).

[10] H. Cheung and C. Law, *Nonadiabatic optomechanical hamiltonian of a moving dielectric membrane in a cavity,* Physical Review A **84**, 023812 (2011).

[11] K. Jacobs, *Quantum measurement theory and its applications* (Cambridge University Press, 2014).

[12] C. Gardiner and P. Zoller, *The quantum world of ultra-cold atoms and light book ii: The physics of quantum-optical devices*, Vol. 4 (World Scientific Publishing Company, 2015).

[13] W. P. Bowen and G. J. Milburn, *Quantum optomechanics* (CRC press, 2015).

[14] A. A. Clerk, M. H. Devoret, S. M. Girvin, F. Marquardt, and R. J. Schoelkopf, *Introduction to quantum noise, measurement, and amplification,* Reviews of Modern Physics **82**, 1155 (2010).

3

Device Design and Fabrication

In this chapter, we present the design considerations and fabrication methods for realizing high-Q microwave resonators and highly stressed Si_3N_4 square membranes. To overcome clamping losses of the membrane and increase mechanical Q, freestanding structures are micromachined in the silicon surrounding the Si_3N_4 membrane and is called a phononic shield. We elaborate on the pitfalls and challenges we encountered during fabrication of these devices and provide suggestions to overcome those.

3.1. SUPERCONDUCTING LUMPED ELEMENT RESONATORS

3.1.1. DESIGN

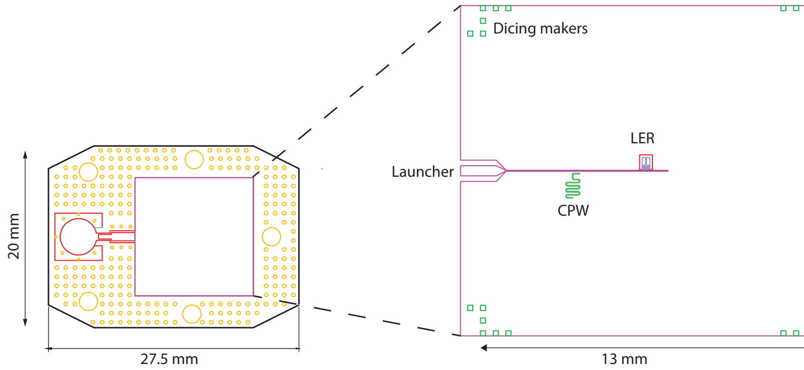

Figure 3.1: Top view of PCB layout (left) with microwave resonators device design (right).

The microwave devices used within the scope of this project, consists of 2 superconducting resonators i.e. co-planar waveguide (CPW) and a lumped-element resonator (LER). Both resonators are coupled to a grounded feedline which means that they are configured in a reflection geometry as shown in Fig.3.1. The LER is the resonator of interest and the CPW serves as a candle resonator. In case we measure no visible response from the LER, it can be challenging to disentangle resonator complications from external ones. The response of the CPW is then used to rule out the possibility of loose connectors within the coaxial lines used to probe the resonator or broken wirebonds.

The lateral dimension of the entire device is 13×13 mm and the LER is situated exactly in the centre of the substrate. Sapphire is used here as substrate, because of its low bulk dielectric loss tangent at cryogenic temperatures $\sim 10^{-8}$, and it is chemically inert [1]. These make it attractive to be used as base material for high-Q superconducting resonators, as these are commonly limited by dielectric losses originating from the dielectric bulk and substrate-metal interface [2]. The metal is chosen to be niobium titanium nitride (NbTiN), because of its high critical temperature $T_c \approx 14.4$ K and low quasiparticle densities at millikelvin temperatures [3, 4]. The microwave device is fixed on copper (Cu) holder with GE varnish. It is an epoxy with excellent thermal conduction and can be removed afterwards with ethanol. A 0.5 mm thick RO4003 printed circuit board (PCB) containing a single smp-connector is also installed with screws on the Cu holder and completely surrounds the microwave device. The PCB has a hexagonal geometry and contains a dozen of vias with $\varnothing = 20$ μm that are distributed over the entire area. The vias connect the upper surface with the bottom such that both planes are held at the same ground potential. The metal used on the PCB is 20 μm thick Cu layer coated with 5 μm Gold/Nickel (Au/Ni). The PCB can be viewed as an adapter that establishes an electrical connection between external measurement instruments and the microwave device.

3.1.2. FABRICATION

In this section, we dive into the fabrication process of the microwave resonators. The crucial steps for achieving high-Q resonators is (1) surface preparation before deposition and (2) to avoid unnecessary processing steps. The latter should not be underestimated because each processing step (cleaning, developing, etching etc.) causes contamination of the device with residues from the environment or the chemical solution it is exposed to. This might not be optically visible, but it is detrimental for the quality factor of the resonators. The wafer preparation and NbTiN deposition (step 1 and 2) are outsourced to Dutch institute for Space Research (SRON), but we nonetheless highlight the fabrication procedure. We continue independently with the fabrication of the microwave resonators at the *Delft Kavli NanoLab* [5] starting from step 3. The processes are depicted in Fig.3.2.

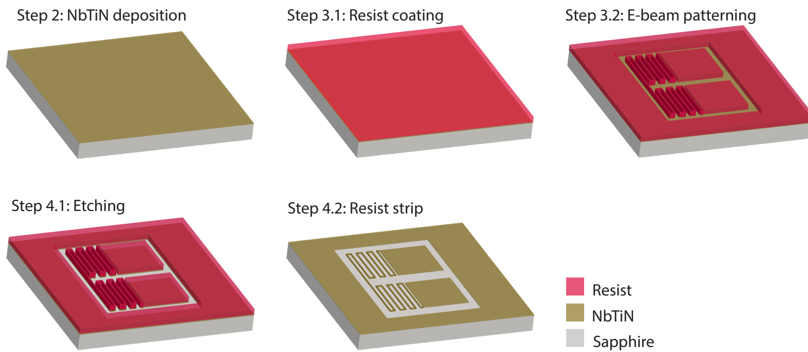

Figure 3.2: The fabrication starts with a 13×13 mm diced sapphire chip that is coated with a 100 nm NbTiN thin film. The colours indicate material type and the fabrication process of the resonators is straightforward with a single exposure step only.

STEP 1: SURFACE PREPARATION

A 4" c-plane sapphire wafer that is doubleside polished (DSP) and 430 μm thick is used as substrate. The substrate is chemically treated first to remove unwanted contaminants. The wafer is immersed face-up in a beaker with phosphoric acid (H_3PO_4) at 110 ^{o}C for 30 minutes. After this time has elapsed, the wafer is immediately rinsed in a de-ionized water (D.I. H_2O) bath at 80 ^{o}C to dissolve the acid. This takes about 30 seconds, after which the wafer is transferred and rinsed in a second D.I. H_2O bath that is at room temperature. Next, the wafer is installed onto a wafer holder and immersed in the quick dump rinser, and we run a 6-minute program. After the program has finished, the wafer is spun dry with 2000 rotation per minute (rpm) while continuously blow-drying the edge with a nitrogen (N_2) gun for 2 minutes. Inspection of the front side of the wafer for micron sized particles is recommended with a high intensity electric torch (10000 lumens). If there are still particles observed on the surface, the wafer needs to be placed again in the quick dump rinser and the program should be repeated until the wafer has zero visible particles.

STEP 2: NBTIN DEPOSITION

Immediately after the surface has been treated, the wafer is transferred within a waferbox to the *LLS801 sputtering machine* (SRON) within 2 minutes. The LLS801 is a refurbished and customized industry-based sputtering machine. The NbTiN is deposited by means of DC magnetron sputtering in the LLS801 located at SRON. A stoichiometric NbTiN film is obtained by using a 99.8% pure $Nb_{0.7}Ti_{0.3}$ target and a continuous N_2 flow to nitrodize the target during the deposition. The metal is applied on the side of the wafer that is appointed as front in the previous step. The final thickness of the metal film is 100 nm and has been characterized to have sheet resistance and kinetic inductance of respectively $R_s = 11\ \Omega$ ($T>T_c$) and $L_k = 1.05$ pH/□ [3]. The deposition parameters used for this deposition can be found in table 3.1. After deposition, the 4" wafer is coated with photoresist to protect the NbTiN film and diced into 13×13 mm single pieces.

3

Machine	Target	Gas	Flow (sccm)	Pressure	RF power	DC voltage	dep. rate (nm/min)
LLS801	$Nb_{0.7}Ti_{0.3}$	Ar/N_2	400/84.7	7 μbar	5000 W	N.A.	N.A

Table 3.1: LLS801 machine settings (SRON) for sputtering NbTiN [3]. This process takes place at room temperature. The T_c for this film is approximately 14.4 K.

STEP 3: PATTERNING

Defining the pattern of the microwave resonators into the NbTiN film is carried out by means of electron beam lithography (E-beam lithography). We first strip the photoresist from the diced sample in a PRS-3000 (positive resist stripper) bath at 80 ^{o}C for 20 minutes. We then transfer the sample to a second fresh PRS-3000 bath at the same temperature. The sample is left in the solution overnight to ensure that the photoresist is dissolved as much as possible. Next, we immerse the sample in an isopropyl alcohol (IPA) solution and perform an ultrasonic clean at the highest power. We blow-dry the chip with a high pressure N_2 gun. Note that the chip is fixed in a holder during cleaning.

Next, we spin ARP6200.13 resist [6] at 4000 rpm on the NbTiN sample followed by a 3-minute bake at 150 ^{o}C on a hotplate. We obtain 400 nm thick resist, enough to serve as a protection mask for etching 100 nm of NbTiN later in the process. We place the sample into the *Raith EBPG-5200* E-beam and use the corners of the sample to determine the centre of the chip with respect to the E-beam holder Faraday cup. We expose the resist with a 110 nm beam and dose of 360 $\mu C/cm^2$. The sample is afterwards developed in a pentyl acetate solution for 1 minute, followed by a 1-minute rinse in a methyl-isobutyl-ketone (MIBK):IPA (1:1) solution to slow down the development. A final 1-minute IPA rinse is carried out to stop the development, and the sample is blown-dry with an N_2 gun. The process is are depicted as step 3.1 and 3.2 in Fig.3.2.

STEP 4: ETCHING

We remove the NbTiN that is exposed after development with a dry reactive plasma in the *Leybold Fluor etcher F3*. In the reactive ion etcher (RIE), the substrate is placed on

the bottom plate of a cylindrical vacuum chamber. The bottom plate serves as a capacitor plate that is electrically isolated from the rest of the chamber. Etching gasses sulfur hexafluoride (SF_6) and oxygen (O_2) enter the vacuum chamber through small inlets and exits through the vacuum pump system. An RF-field at 13.56 MHz is applied to the bottom plate, which ionized the gas mixture [7]. The plasma consists of radicals (F*), ions (F^-, SiF_5^+) and electrons. The positive ions show little response to the oscillation RF-field, while the electron are accelerated and hit the chamber walls and bottom plate. Charge on the bottom plate build up, creating a negative potential. This causes the ions to accelerate down to the substrate. The metal is removed either via physical collision or chemical reaction. In the first, ions have enough kinetic energy to knock off NbTiN atoms from the film. In the second, F* radicals are absorbed on the surface of the metal and undergo a chemical reaction. The product of the chemical reactions are released from the surface through desorption and diffuse back into the main gas flow [8]. Due to the downward motion of the reactive ions, we obtain anisotropic etch profiles with RIE. This etching process takes place at room temperature and an etch rate of approximately 30 nm/min is achieved. The presence of NbTiN is measured during etching with the laser endpoint detection method. In this method, the reflectivity of the surface is measured using a laser. Because the reflectivity of NbTiN is higher than sapphire, the reflected power will drop when the sapphire is exposed. After the sapphire is detected, we overetch the sample for 7 seconds to make sure that no NbTiN is left. Note that the presence of O* radicals in the plasma will etch the resist mask. The resist however is thick enough such that there is still resist left after the etch process has finished. The F3 machine setting are shown in Table3.2.

3

Process	Gas	Flow (sccm)	Pressure	RF power	ΔV
NbTiN etch	SF_6/ O_2	13.5/ 4	6 μbar	150 W	-265 V

Table 3.2: NbTiN etch parameters with Leybold Fluor etcher F3. This process take place at room temperature. We obtain an etch rate of 30 nm/min.

The remaining E-beam resist is stripped off the device using the same procedure as removing the photoresist before patterning, already mentioned above i.e. PRS-3000 bath at 80 ^{o}C for 20 minutes.

3.2. HIGH TENSILE STRESS Si_3N_4 MEMBRANES

3.2.1. DESIGN CONDITIONS

The conditions that the mechanical resonator need to satisfy are: (1) its natural resonance frequency ω_m should be larger than κ such that the electromechanical system is sideband resolved ($\omega_m/\kappa \gg 1$) and (2) large mechanical Q_m such that the inequality $Q_m \cdot f_m > k_b T_m/\hbar$ is satisfied. The latter is the condition for neglecting thermal decoherence over one mechanical period and in combination with (1) indicates that we can groundstate cool the mechanical oscillator to the groundstate [9] over many mechanical oscillations. High stress stoichiometric freestanding Si_3N_4 films on Si substrates have shown to reach these high mechanical quality factors [10, 11], but are also favourable for their high mass. The strikingly large Q_m is not only related to the high tensile stress σ of these thin films, but also on their aspect ratio L/t_f. Here, L and t_f are the window sidelength and film thickness respectively. In Ref. [10], they reported a quadratic scaling of Q_m with respect to L/t_f and measured $Q_m \approx 5 \times 10^7$ for stressed membranes with $\sigma \approx$ 1 GPa and $L/t_f \approx 5 \times 10^4$. The thickness of the Si substrate is 200 μm and is double side polished (DSP) with its crystal plane orientation parallel to the <100>-plane. This specific plane orientation is an important requirement for fabricating freestanding square membranes, and will become clear in the next section.

Determining the dimensions of the square membrane to satisfy condition (1) is straightforward and is calculated with [10],

$$\omega_{mn} = 2\pi\sqrt{\frac{\sigma(m^2+n^2)}{4\rho L^2}} \tag{3.1}$$

Here, the mass density of the SiN film is $\rho = 3180$ kg/m^3 [12] and (n, m) are the indices of the antinodes. We target a mechanical fundamental mode of 1 MHz which translates to a membrane with lateral dimension L$\sim$ 350 μm. The membrane has thickness $t \sim 50$ nm, assuming an in-plane stress $\sigma_x, \sigma_y \approx 1$ GPa. Reducing the thickness to increase the ratio L/t_f poses fabrication challenges because the membranes fracture more easily due to their high stress.

The first 4 mechanical mode shapes are visualized in Fig.3.3 and are obtained by perform a 3D eigenfrequency analysis with a finite element software, COMSOL [13]. Apart from a simple design process, the fabrication of these square membranes are less demanding. In addition to squares, other geometries can also be used to achieve the same mode frequencies and similar Q_m [14], but the fabrication however becomes more tedious and challenging.

For coupling these dielectric mechanical resonators to the lumped-element resonator, the SiN membrane needs to be coated with metal such that the circuit becomes sensitive to miniscule displacement of the membrane. The metal film is also square shaped with similar dimensions as the pads of the lumped-element resonator. This is to increase the participation ratio of the mechanical capacitance. The metal film does not cross the boundary where the SiN membrane is clamped to the Si support, as this result in additional losses and a reduction of Q_m [11]. We have chosen to use 25 nm Al+1%Si as metal, which covers roughly 85% of the membrane area (i.e. $\approx$ 320 μm). Making the metal thicker is detrimental for the electromechanical coupling as this increases the effective

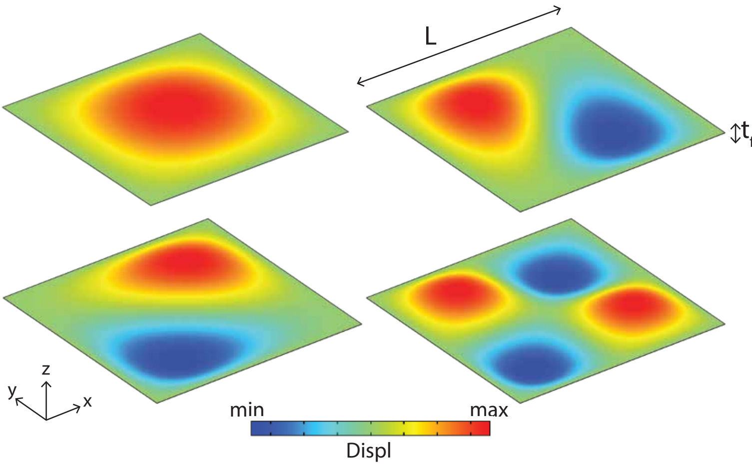

Figure 3.3: A visualization of the first 4 mechanical modes of the membrane. From top-left to bottom-right **(1,1), (1,2), (2,1), (2,2)**. The second and third modes are degenerate and have the same mode frequency.

mass and therefore lowers the single photon-phonon coupling g_0. On the other hand, coating the membrane with a too thin metal results in an increased kinetic inductance that scales with $\sim 1/t^2$ and lowers the power threshold at which the microwave circuit exhibits non-linear duffing response [15].

3.2.2. FABRICATION

The release of highly stressed membranes is a delicate process which need to be optimized through multiple iterations. These thin films are prone to fracture due to their high stress. Although not very complicated, we still decided to outsource this part of the fabrication to an external manufacturer, Norcada Inc.[16]. The devices we receive are 10×10 mm silicon substrates that are 200 μm thick with a 350×350 μm freestanding transparent Si_3N_4 membrane in the middle. The silicon substrates used here have a high resistivity with R> 3500 Ω.cm. The in-plane stress σ of the SiN film is tensile and is estimated to be around 1 GPa, as reported by the company. Below, we highlight some important steps within the fabrication procedure that is followed when creating highly stressed freestanding membranes. The reader should note that we did not actually carry out fabrication steps 1-4, but we describe the processes with equipment available at the *Kavli Nanolab Delft*. We proceed with the fabrication independently, from step 5 and onwards.

STEP 1: SURFACE PREPARATION

Fabrication of high stress Si_3N_4 membranes starts by preparing the surface of a 4" double side polished (DSP) Si wafer that is 200 μm thick with its crystal plane orientated along the <100>-direction. Surface preparation involves a chemical treatment of the substrate carried out in multiple steps to get rid of both, organic and inorganic contaminants, as well as oxides on the surface. The cleaning procedure is called the **RCA method** and

named after the place where it was developed, i.e. *Radio Corporation of America*. We briefly explain the different steps in the RCA procedure [17] below and is summarized in Table 3.3.

- RCA-1: here, organic contaminants from the surface are removed. The chemical solution used is 1 part of 28% ammonia hydroxide (NH_4OH) with 1 part of 30% hydrogen peroxide (H_2O_2) and 5 parts D.I. H_2O. The mixture is heated to 70 ^oC in an au bain-marie. The wafer is immersed in the chemical solution within a teflon holder for 10 minutes. A magnetic steerer need to be used to promote fresh etchant reaching the surface of the wafer. After 10 minutes, the wafer is rinsed twice with fresh D.I. H_2O for 5 minutes continuously.

- RCA-2: here, ionic contaminant are removed from the surface. The solution used consists of 1 part 30% hydrochloric acid (HCl) and 5 parts of D.I. H_2O. This solution is heated in an au bain-marie to 70 ^oC and removed after it has reached the set temperature. Next, 1 part of 30% H_2O_2 is added. The wafer is then immersed in the mixture within a teflon wafer holder for 10 minutes in the mixture and then rinsed twice for 5 minutes with fresh D.I. H_2O continiously.

- Buffered oxide etch (BOE): here, the native oxide on the surface is etched. It involves a buffered oxide etch with 7 parts 40 % ammonium fluoride (NH_4F) and 1 part 49 % HF. We immerse the wafer for 30 seconds in the chemical mixture and thereafter rinse contiously for 5 minutes with D.I. H_2O.

Step	Etch	Name	Mixture volume ratio	Temperature	Time
1	Organic contaminant	RCA-1	NH_4OH:H_2O_2:H_2O (1:1:5)	70 ^oC	10 mins
2	Ionic/metallic contaminant	RCA-2	HCl:H_2O (1:5)	70 ^oC	10 mins
3	Oxide	BOE	NH_4F:HF (7:1)	RT	30s

Table 3.3: Standard cleaning procedure (RCA) of silicon wafer.

STEP 2: LPCVD

After the wafer surface has been treated, it needs to be transferred immediately to a batch type horizontal furnace for depositing stoichiometric Si_3N_4 using the low pressure chemical vapor deposition (LPCVD) process. Preferably within 2 minutes to limit re-oxidation of the Si surface. LPCVD is a conventional method to deposit SiN films and is based on the chemical reaction of dichlorosilane (DCS) and ammonia (NH_3) gas at high temperatures (between 700 and 800 ^oC). The deposition process is a combination of thermal disassociation and chemical reaction of these two reactive gasses. DCS is used as a silicon precursor and NH_3 as a nitrogen precursor. The chemical process is described by [18]

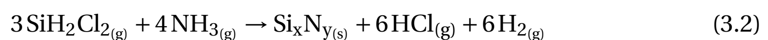

$$3\,SiH_2Cl_{2(g)} + 4\,NH_{3(g)} \rightarrow Si_xN_{y(s)} + 6\,HCl_{(g)} + 6\,H_{2(g)} \tag{3.2}$$

The reaction is usually not balanced and the ratio between Si and N i.e. x/y depends on the actual ratio of the precursor gasses. By varying the ratio of the precursors gasses and

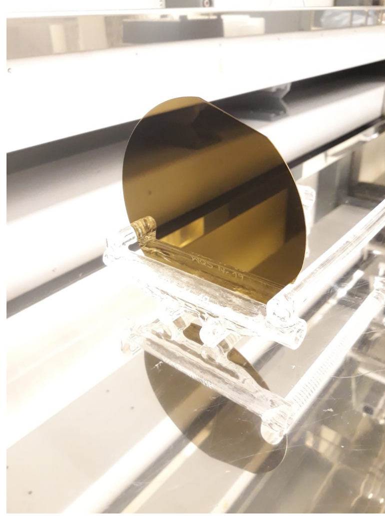

Figure 3.4: Silicon wafer with 50 nm Si_3N_4 in loading arm of the Tempress furnace after LPCVD process has finished. The wafer is unloaded and cools back down to room temperature. The stoichiometric Si_3N_4 film gives the wafer a brown/gold colour.

therefore altering x/y, one obtains either silicon-rich, nitride-rich or stoichiometric films [19]. The mechanical and optical properties of the deposited films change drastically depending on the Si-to-N composition. After the deposition, the SiN film is loaded by a residual mechanical stress that remains in the layer [20]. This is given by

$$\sigma = \sigma_{\text{th}} + \sigma_{\text{i}} \tag{3.3}$$

where the mechanical stress in the film is composed of thermal stress σ_{th} and intrinsic stress σ_{i}. Thermal stress arises from the thermal mismatch between the deposited SiN film and the Si substrate as the sample cools down from process temperature to room temperature. This can be analytically expressed by [21]

$$\sigma_{\text{th}} = \int \frac{E}{1-v}(\alpha_{\text{Si}_3\text{N}_4} - \alpha_{\text{Si}})d\text{T} \tag{3.4}$$

where E is the Young Modulus, v the Poisson constant and α the thermal expansion coefficient. Intrinsic stress on the other hand arises from elongated Si-N bonds as a result of the deposition chemistry of the gasses. Ref. [19] found that high residual stress in SiN films reaching 1 GPa can be achieved for NH_3/DCS ratios between 2 and 20 resulting in a x/y ratio of 0.75. However, the relation between stoichiometry and the degree of stress is yet unclear and still under investigation.

A 50 nm thin stoichiometric Si_3N_4 film can be obtained using the *Tempress TS series* furnace available at the *Kavli Nanolab Delft*. Both sides of the Si wafer will be covered with SiN. The machine settings are presented in Table 3.4. With these parameters, the deposition rate is 4 nm/min with a total deposition time of approximately 12 minutes. The thickness and refractive index of the film can then be measured using the variable

angle *Woollam M-2000 ellipsometer*. A test deposition process is carried out with this furnace, as shown in Fig.3.7 and has yielded a thickness of 48 nm with refractive index of 2. The mechanical stress can be measured with the *Flexus (TOHO) stress meter* that probes the curvature of the wafer. This stress measurement involves 2 steps: a scan of the top surface of the wafer without any film followed by another scan after deposition. The residual stress in the film can be calculated with [22]

$$\sigma = \frac{E\,t_s^2}{6(1-\nu)\,t_f R} \tag{3.5}$$

where E and v are the Young Modulus and Poisson ratio of the substrate, respectively. t_s and t_f are the substrate and film thickness respectively, and R is the average radius measured across the wafer with the stress meter. In order to measure the curvature of the wafer, the film on one side needs to be removed. This can be done with a CHF_3/O_2 RIE. Note that the wafers needed for fabricating free-standing square membranes should have the Si_3N_4 thin film on both sides.

Temperature = 800 ^oC	
Pressure = 250 mTorr	
Gas	Flow (sccm)
NH_3	90
N_2	80
DCS	30
deposition rate = 4 nm/min	

Table 3.4: Tempress furnace parameters for obtaining high tensile stress stoichiometric Si_3N_4 films.

STEP 3: PHOTO-LITHOGRAPHY

After the LPCVD process, a square shaped pattern is defined in the SiN film only on one side of the wafer. This is accomplished by spinning positive photoresist AZ5214 at 4000 rpm on the SiN film followed by a softbake at 110 ^oC for 1 minute on a hotplate. This results in a thick resist layer of 1.4 μm. For convenience, we call this the backside of the wafer, as back-etching in the following step will be facilitated through an opening at this side. Next, square windows are exposed in the photoresist and are slightly bigger than L = 350 μm. This can be performed with the *DMO laser writer* with, for example a 5 μm beam with wavelength of 405 nm and dose of 35 mJ/cm^2. These windows serve as an opening to facilitate back-etching of the Si. The lateral dimensions of the back-etch window need to be greater than the target sidelength of to be realized freestanding membrane. This is because the wet-etch in the following step is not completely anisotropic, i.e. no straight sidewalls. The Si atoms of the different crystal planes have different activation energies for the etching reaction. This causes the <100> and <110> plane to be etched faster than the <111> plane [23]. An angle of 54.7^o with respect to the surface is obtained due to the difference in etch rates, as shown in Fig.3.5. This is compensated by offsetting the dimensions of the back window by $t_s/\tan(54.7^o) \approx 140\,\mu$m. Due to the nature of this etch,

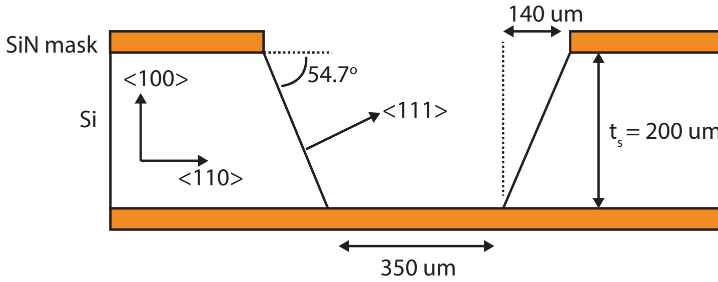

Figure 3.5: Anisotropic wet etch of <100> silicon. The sidewalls are not completely vertical, since the <111>-plane acts as an etch stop. Instead, the walls make an angle of 54.7^{o} w.r.t. the surface and therefore the back-etch window need to be offsetted.

careful thought must be taken when designing a mask as well as ensuring the proper alignment during lithography.

The exposed resist is removed by developing with MF-321 for 2 minutes followed by a continuous flowing D.I. H_2O rinse for 60 seconds. The wafer is dry etched with the *Leybold Fluor etcher F1* to remove the SiN in the developed areas. Here, a CHF_3/O_2 plasma is used for 2 minutes until the bottom Si is exposed. The machine setting to carry out this etch is provided in Table3.5. At last, the resist is stripped with a hot PRS-3000 solution at 80 ^{o}C for 30 minutes, followed by two IPA rinses each 2 minutes and blown-dry with an N_2 gun.

CHF_3	O_2	Pressure	RF Power	Bias voltage
51 sccm	2.5 sccm	9.2 μbar	50W	-520 V
Etch rate = 20 nm/min				

Table 3.5: Leybold Fluor etcher F1 maching setting for etching SiN at room temperature.

STEP 4: KOH

Next, the silicon is removed by means of a wet etch with potassium hydroxide (KOH) to obtain freestanding membranes. This chemical wet etch in which the etch rate depend exponentially on the temperature and concentration of the KOH solution can make it challenging to release a high tensile stress thin Si_3N_4 films without fracturing it. Therefore, a special setup need to employed that consists of a teflon single sided holder and a customized container in which the KOH solution is stored. The container is a cylindrical vessel which contains the 40% KOH solution and has 2 gas inlets, as shown in Fig.3.6a. It is mounted on a heater that is set to 80 ^{o}C and takes roughly 1 hour for the solution to reach this temperature. A magnetic steerer at 60 rpm should be used to promote temperature uniformity in the solution.

The wafer is then placed and fixed on the single sided teflon holder, as shown in Fig.3.6b and thereafter immersed in the etchant. Here, the backside of the wafer is ex-

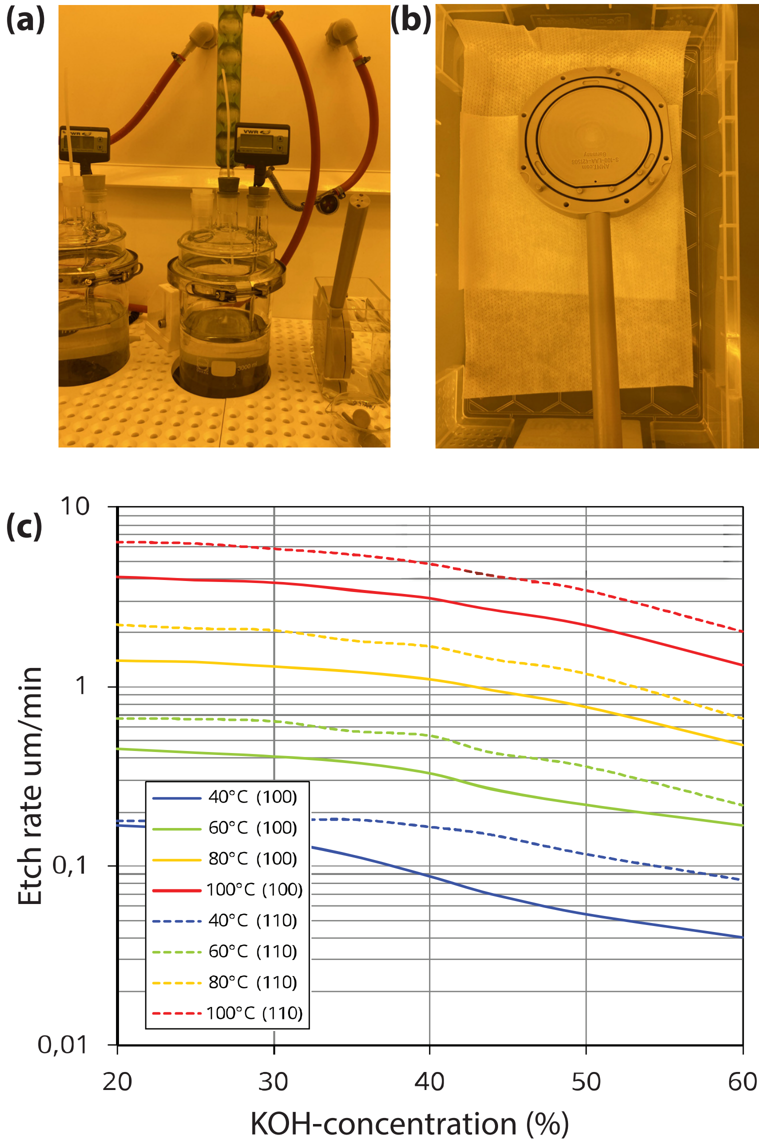

Figure 3.6: **KOH etching setup with etch rate dependency.** **(a)** Reaction vessel that contains 40 % KOH solution. This vessel keeps the KOH concentration constant during long etching periods. **(b)** Single sided teflon holder for etching silicon wafers. With this holder only one side of the wafer is exposed to the etchant, while the other side is protected and forms a cavity. The pressure that builds in this cavity during the etch is released through small vents. **(c)** <100> silicon etch rate at different temperatures and concentrations [23].

posed to etchant, while the edge of the wafer and the frontside is protected against the etchant. The SiN film on the backside serves as a hard mask during etching, such that

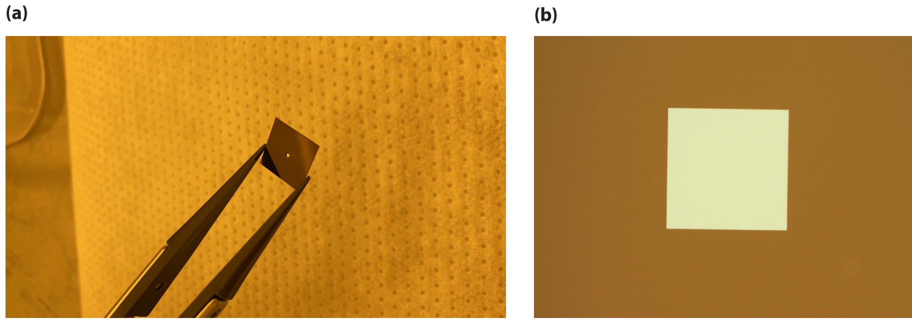

Figure 3.7: **Norcada Si/Si_3N_4 membrane device.** **(a)** Chip as received from Norcada Inc. and has lateral dimensions of 10x10 mm with 200 μm thick silicon substrate. **(b)** A zoom in of the transparent square in the middle of the chip is the free-standing Si_3N_4 film with L = 350 μm and t_f = 50 nm.

only the exposed Si within the square opening is etched only. The selectivity of the etchant to LPCVD Si_3N_4 is 1:49000 with respect to Si [24]. Despite the efforts of keeping the temperature constant and homogenous across the surface of the wafer, it will be difficult to obtain a homogeneous etch rate. This is harmful to the release process of membranes and can be a reason to cause the membrane to fracture.

The etch rate of Si in 40% KOH at 80 ^{o}C is approximately 1 μm/min and is shown in Fig.3.6c. Etching 200 μm can therefore take up to 4 hours. The etch rate is kept constant during this extended amount of time by keeping the concentration of the solution constant. This is automatically taken care of when etching in a reaction vessel. Here, the evaporated H_2O flows out of the vessel through the gas outlet, after which it is condensed back into the solution through the inlet. Not that an increase in KOH concentration lowers the etch rate.

Once the etch has finished and the Si_3N_4 membranes are released, the holder with the wafer need to be removed from the solution and placed immediately in a beaker containing D.I. H2O for 10 minutes. This is crucial as KOH is a viscous fluid and will dry on the wafer if not rinsed with D.I. H_2O. Next, the wafer can be unmounted from the teflon holder and should be immersed in a HCl:H_2O (3:1) solution, twice for 5 minutes each, to remove the remaining potassium atoms. A final flowing D.I. H_2O rinse for 5 minutes should be carried out, after which the wafer can be blown-dry (N_2) and cleaved into single 10x10 mm pieces. The final device should look similar to the ones received from Norcada Inc, as shown in Fig.3.7.

STEP 5: METALLIZATION

Metallization of the membranes is a crucial step for interfacing mechanical devices with microwave circuits in order to achieve electromechanical coupling. There are certain conditions that the metal on the membrane must meet such that the mechanical properties of the Si_3N_4 are perturbed minimally. The three conditions are as follows: (1) it should have neutral stress when deposited on the membrane; (2) it should be of similar density as the SiN dielectric and (3) it should be superconducting at 15 mK.

The **first condition** is satisfied if the stress introduced by the metal is neither compressive or tensile, i.e. neutral. Either of these can be detrimental for the membrane since compressive stress reduces the net stress of the membrane and can cause the membrane to deform thereby altering the mode shapes. A systematic increase in intrinsic damping has been reported in Ref. [25] when 1.5 nm SiO2 layer was deposited on SiN resonators and thereby reducing the effective tensile stress. A too high tensile stress on the other hand increases the load on the membrane and can fracture when it exceeds the ultimate tensile stress (UTS) of Si_3N_4. Therefore, it is a necessity to optimize the deposition process of the metal such that there is additional stress is introduced and the high tensile stress of Si_3N_4 is retained. The **second condition** indicates that the superconducting metal need to be lightweight, because the addition of metal increases the effective mass of the membrane and reduces x_{zpf}. A reduction in x_{zpf} also lowers the single photon-phonon coupling g_0. The mechanical mode frequencies will also decrease due to the added mass of the metal and can deform the mechanical mode shapes. Therefore, a thin and light superconducting metal film is favourable. However, one also needs to take into account the increased kinetic inductance that comes with thin superconducting metals, as it scales inversely with t_f^2. A high kinetic inductance may limit the electromechanical circuit at high input powers, resulting in a Duffing response of the microwave resonator. As already noticeable, the second and third condition are not complementary as a higher g_o is obtained with thinner films, while the kinetic inductance increases with $1/t_f^2$. The microwave resonator circuit is fabricated using 100 nm superconducting NbTiN and it is fairly reasonable to choose the same metal for coating membranes. We have nonetheless investigated the use of two metals i.e. NbTiN and Al+1%Si and in the sections below we elaborate on the fabrication techniques. We deposit 25 nm of each metal with sidelength of 320 μm. The fabrication process is categorized in either a top-down or bottom up approach and is depicted in Fig.3.8.

ALUMINIUM + 1% SILICON

Bottom up We first consider the metallization of the Si_3N_4 using Al+1%Si, which is an aluminium-alloy known for its high fracture strength, almost 5x higher than pure Al (4N) [26]. In the bottom up fabrication process, we first coat the entire substrate with 25 nm Al+1%Si with the *Alliance metal 1 sputtering machine*. The machine settings to obtain a stress-free thin film is given in Table3.6. Before actually sputtering the sample, we have executed a pre-sputter routine of 2 minutes first.

Next, we spin-coat 1.4 μm thick positive photoresist AZ5214 at 4000 rpm followed by a softbake at 90 ^{o}C for 90 seconds on a hotplate. A square with L ≈ 320 μm is exposed by 495 nm (UV) beam with the *DMO laser writer* with dose of 15 mJ/cm^2. Instead of developing the resist, which will open up the exposed area, we perform a post-bake required to promote cross-linking in the exposed area. This is known as an image-reversal technique and allows the resist to be used in negative mode. We perform a second round of flood exposure of the entire resist with a *EVG-620 mask aligner*. We develop the sample in MF-321 (2.1% TMAH) for approximately 6 minutes, and here the developer simultaneously etches the Al+1%Si in the process. Note that most of the metal on the surface is etched away within 3 minutes. However, we are still left with metal at the edges and corner of the substrate since the resist is thicker at those places. We then wait an ad-

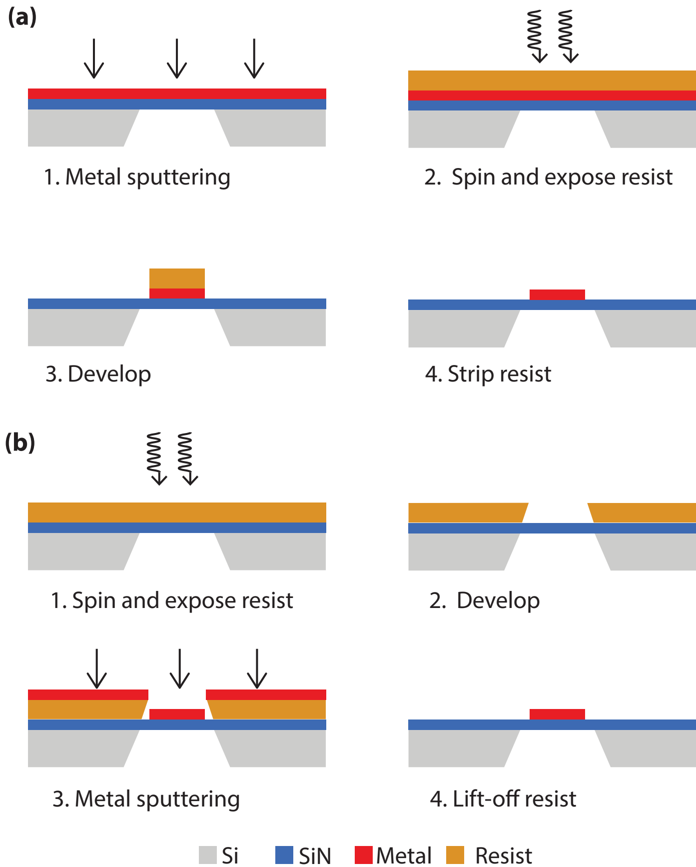

Figure 3.8: Metallizing the Norcada membranes with **(a)** bottom-up or **(b)** top-down approach.

ditional 3 minutes for these to be also removed. After the wet-etch, we are left with an Al+1%Si square island in the middle of the membrane that is covered by the resist mask. As a final step, we strip this resist with a PRS-3000 bath at 80 °C followed by an 2-minute IPA rinse. The sample is blown-dry with N_2 gun at the end. Upon optical inspection, we notice: (1) the square Al+1%Si island is slightly off-centred by 10 μm from the middle of the membrane and (2) the metal square to possesses coarse edges, as shown in Fig.3.9a. The first observation is explained by misalignment when exposing the resist with the laser writer. The corners of the square membrane are used as markers for alignment, and misalignment occur when these corners are not clearly visible through the optical microscope. The coarse edges are due to under etching of the Al+1%Si in MF-321 indicating that developer creeps beneath the resist mask. To solve this problem, one can choose to promote adhesion of the resist to the metal or make use of a thinner resist. The latter reduces the development time and therefore the under etching will be less severe. Note that none of the above-mentioned issues pose any serious threat for the

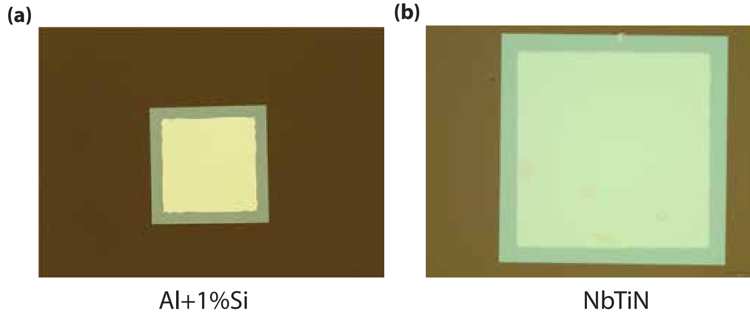

Figure 3.9: **Optical images of metallized Norcada square membranes** with **(a)** Al+1%Si and **(b)** NbTiN using a bottom-up approach. The Al+1%Si metal has coarser edges when compared to NbTiN and is attributed to under etching of Al+1%Si in MF-321 developer. Note that the optical zoom in **(b)** is twice to that used in **(a)**.

subsequent processing steps.

Top down: In the top-down process, the Al+1%Si metal is applied with the lift-off technique. We first spincoat 1.4 um thick positive photoresist AZ5124 (4000 rpm) on the substrate followed by a softbake. We intend to use the resist in its default positive mode, and therefore the baking parameters and exposure differ compared to the bottom-up process. A baking temperature, time and exposure of 110 ^{o}C, 60 seconds and 40 mJ/cm^2 is chosen to comply with a negative sloping resist profile. We follow the same procedure as explained in the previous section by exposing a square with L ~ 320 μm and centred in the middle of the membrane. We develop the sample with MF-321 for 2 minutes to open up the exposed area. We continue with deposition by sputtering 25 nm of Al+1%Si using the same machine and process as stated previously. The last step involves a lift-off, where we strip the unexposed resist with Al+1%Si on top by immersing the sample in n-methyl-2-pyrrolidinone (NMP) solution at 80 ^{o}C followed by an 2-minute IPA rinse. Lastly, the sample is carefully blown-dry with an N_2 gun and a square rectangle of Al+1%Si is visible in the middle of the membrane. The lift-off process is known to work with even lower resist thickness.

NbTiN

The metallization with NbTiN is similar to the bottom-up with Al+1%Si. In the **bottom-up** process, we first sputter NbTiN over the whole substrate with *SuperAJA sputtering machine*. Positive photoresist AZ5214 is used in image reversal mode and is applied, exposed and developed using the same procedure as followed in bottom-up process for Al+1%Si. However, the MF-321 does not etch NbTiN and therefore we remove the NbTiN through a reactive ion etch (RIE) with the *Leybold Fluor etcher F3*. An SF_6/O_2 gas plasma is used to etch away the NbTiN which lasts for 50 seconds. This etch need to be stopped on time since the plasma containing SF_6 also etches SiN and can destroy the membrane. After the etch, we perform an in-situ O_2 plasma ash for to remove the resist mask. The machine settings for this etch are shown in Table 3.2. As a last step, we strip the remaining resist mask by placing our sample in an 80 ^{o}C NMP bath followed by an IPA rinse.

The sample is blown-dry with an N_2 gun.

A wet etch of NbTiN in the bottom up is also possible, but involves more tedious fabrication steps. In Ref. [27], this etch is performed with a mixture of NH_4OH:H_2O_2:H_2O (1:2:5). Therefore, as one has to resort from standard organic photoresist to hydrogen silsesquioxane (HSQ) as the former is known to dissolve fast in the etch mixture. HSQ is a liquid inorganic chemical that is transformed into silicon dioxide (SiO_2) after spinning, baking and exposing it with the E-beam. Parameters such as thickness, baking time, exposure dose and development time of HSQ need to be optimized for it function as a stable hard mask against the etching mixture.

The **top-down** process for NbTiN follows the same procedure as in metallizing the membrane top-down with Al+1%Si.

3

Machine	Target	Gas	Flow (sccm)	Pressure	RF power	DC voltage	dep. rate (nm/min)
Alliance Metal 1	Al+1%Si	Ar	20	3 μbar	100W	312 V	37.5
SuperAJA	$Nb_{0.7}Ti_{0.3}$	Ar	60	100 μbar	100W	N.A.	40

Table 3.6: Alliance metal 1 and SuperAJA machine setting for sputtering Al+1%Si (first row) and NbTiN (second row), respectively. Both process take place at room temperature.

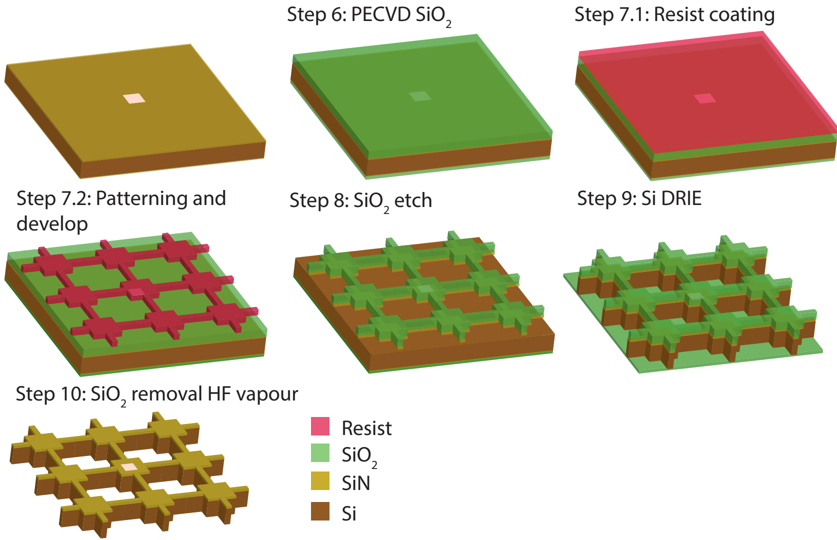

Figure 3.10: The fabrication starts with an Al+1%Si coated Norcada membrane. The end result at each fabrication step portrayed. In step 10, the oxide stoplayer at the back is removed first, followed by the oxide mask on the front.

3.3. DESIGN AND FABRICATING IN-SUBSTRATE PHONONIC SHIELDS

3.3.1. DESIGN

The design of the phononic shield is based on the acoustic crystal developed in Regal Lab [28]. They reported an increase of Q_m when the mechanical resonator is surrounded by periodic mechanical structures. These structures shield the mechanical energy stored in the membrane from its supports and curbs the radiation losses [29, 30], also known as clamping losses. This phononic shield is analogous to a crystal lattice in a metal that gives rise to energybands separated by bandgaps. The same applies for a phononic shield: we obtain energy bands in which a set of phononic modes are forbidden to propagate within the shield. Therefore, we design the shield such that its largest bandgap is centred at the mechanical fundamental mode $\omega_{11} = 2\pi\times$ 1 MHz. This prevents interaction of the mechanical mode with modes of the substrate, effectively resulting in high mechanical quality factors. The design details such as geometry, dimensions and banddiagram of the phononic shield are provided in the supplementary note of chapter 6.

3.3.2. FABRICATION

The process of creating free-standing Si structures within the Si substrate is also commonly known as bulk micro-machining and is a standard operation in CMOS and MEMS processing. To obtain these suspended structures in the substrate, we first apply a hard mask over the entire Si substrate. A pattern is transferred into the hard mask by means of E-beam lithography and plasma dry etching. The unprotected and exposed Si areas are completely removed through a dry etch also known as deep reactive ion etch (DRIE).

DRIE is the most demanding in terms of time and effort as the process needs to be carefully adapted depending on the complexity of the freestanding structures such as aspect ratio, the thickness of the substrate, percentage of exposed Si with respect to the total size of the substrate. Below we elaborate on the details and pitfall of this bulk micromachining fabrication process. We start with a 10x10 mm Si substrate that is 200 μm thick and consist of a freestanding metalized Si_3N_4 membrane in the middle, as is shown in Fig.3.9a. The window has lateral dimensions of 350×350 μm and the Si_3N_4 film is 50 nm thin and coated with 25 nm of Al+1%Si. We have chosen Al+1%Si for its simple fabrication process (fewer steps), its volumetric mass density which is 3x smaller compared to NbTiN and its relative small kinetic inductance at millikelvin temperatures. The fabrication of the phononic shield, starting from step 6 is carried out independently in the *Delft Kavli NanoLab* and is depicted in Fig.3.10.

STEP 6: PECVD SiO_2

The etching gases we will be using for Si etching are SF_6 and C_4F_8 and therefore a hard mask should be resistant against these gases. Silicon dioxide (SiO_2) in general is an attractive candidate to be used as a hard mask due to its high etch selectivity with respect to silicon in plasma of gasses that are mentioned above. Depending on the deposition method of SiO_2, etch selectivities above 1000 have been reported in literature [31] i.e. for every 1000 μm of Si that is etched away, 1 μm of SiO_2 is removed.

We deposit SiO_2 using plasma enhanced chemical vapour deposition (PECVD). This is accomplished with the *Oxford Instruments PlasmaPro 80* machine. PECVD oxide however have selectivities close to 100 [32]. PECVD takes place in a chamber that consists of a conventional parallel plate design and uses a high frequency (13.56 MHz) power source able to generate a plasma of reacting gasses. Our sample is placed on a carrier wafer and transferred to the bottom plate of the chamber and is first heated to 300 ^{o}C. Silane (SiH_4) gas diluted with inert N2 gas and nitrogen dioxide (N_2O) gas are emitted in the chamber and is radicalized and ionized by the RF-field. The Si-ions and O-radicals combine to form SiO_2 and precipitate on the sample.

Note that the membrane sample is surrounded by dummy samples of equal size to effectively increase the size of our device, as shown in Fig.3.11a. This is to improve height uniformity of the SiO_2 across the substrate. By leaving out the dummy samples, we observed a non-uniform height profile across the 10x10 mm Si substrate. It is thinner in the middle and gets thicker by a few hundred nanometres at the edges. This is not ideal since we cannot afford to have a too thin hard mask during Si DRIE in the next step. An earlier than expected removal of the SiO_2 hard mask will start etching the SiN and destroy the membrane.

We cover the front side of the sample with 2.1 μm of SiO_2. The deposition rate is 70 nm/min and the deposition lasts 30 minutes. We also cover the backside with 700 nm SiO_2 with same deposition rate which last for 10 minutes. The SiO_2 on the back serves as an etch-stop layer for Si etching. The thickness of the SiO_2 is determined by means of an ellipsometry measurement with the *Woollam M-2000 ellipsometer*. The machine settings for this deposition are shown in Table3.7.

But one needs to be cautious when depositing PECVD SiO_2 on high stress SiN membranes. We observed membrane buckling up with the naked eye, as shown in Fig.3.11b.

Machine	Gas	Flow (sccm)	Pressure	RF power
Oxford PlasmaPro 80	SiH_4/ N_2O/ N_2	8.5/ 710/ 165	1000 mTorr	20W

Table 3.7: Oxford Instruments PlasmaPro 80 machine settings for depositing PECVD SiO_2. The process takes place with the table temperature set to 300 ^oC. The deposition rate is 70 nm/min.

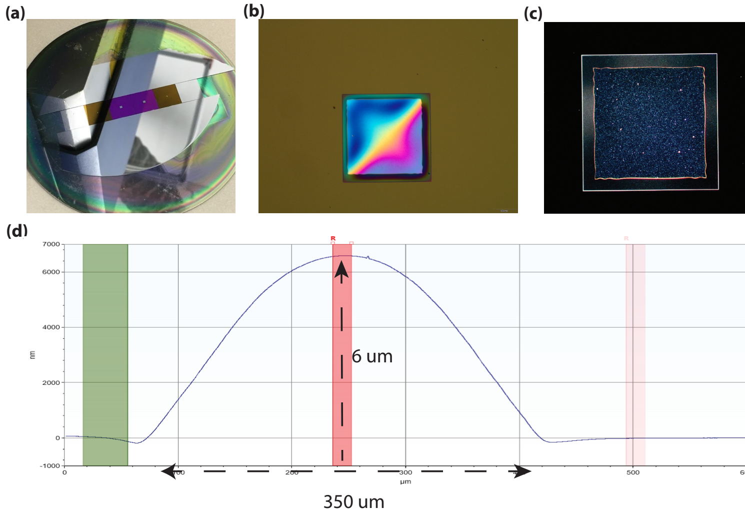

Figure 3.11: **SiO_2 PECVD characterization of the membrane.** **(a)** Membrane samples placed on a 4" Si carrier wafer surrounded by dummy sample of equal thickness. This is to improve the uniformity of the SiO_2 film across the sample. **(b)** Differential interference contrast image taken after PECVD shows the height profile across the membrane and we witness a color gradient indicating that the membrane is buckled due to compressive stress introduced by SiO_2. **(c)** Dark field optical image reveals grains on the metal after PECVD. We suspect these to be chunks SiO_2. **(d)** Height profile of the membrane measured with profilometer shows a step that indicates buckling of the membrane.

The height profile of the membrane with SiO_2 is measured with a *Bruker Dektak XT* profilometer and shown in Fig.3.11d. We witness a hilly profile with peak height of approximately 6 μm that indicate that the membrane is deformed. This buckling can be attributed to the compressive stress that the SiO_2 possesses and has been well documented in Ref. [33]. The compressive stress in the film is dependent on the process conditions in the chamber and thus can be understood from the chemistry of the gasses with respect to temperature, pressure and power. In addition: cooling, venting the chamber and exposing the film to the atmosphere can further alter the stress of the film [34]. This growth induced stress arises during deposition when high energetic atoms or ions bombard the growing film also known as atomic peening [35]. The energetic ions cause atoms to be

incorporated into areas in the growing film which are smaller than the usual atomic volume, resulting in an expansion of the film outwards from the substrate. As the film is not free to relax by expanding in-plane, the entrapped atoms cause macroscopic compressive stress and the membrane therefore buckles up [36].

We provide basic instructions to reduce the residual compressive stress of the SiO_2 film. A simple starting point to obtain stress control of the film is by modifying the reaction gasses flow ratio N_2O/SiH_4 as this will alter the stoichiometry and density of the film. By increasing the SiH_4 gas flow rate, therefore decreasing the aforementioned ratio, results in a monotonic reduction of compressive stress in the SiO_2 films [37]. These are Si rich film, with relative higher refractive index, but caution must be taken when changing the gas ratio. This will increase the deposition rate at the cost of uniformity. Other method for stress control of the film include the addition of a low frequency power source to control the ion energies. Various methods of stress control in SiO_2 film have been investigated quantitatively in Ref. [37].

STEP 7: PATTERNING THE SHIELD

We transfer the pattern of the phononic shield to the SiO_2 hard mask by means of E-Beam lithography. The SiO_2 cannot not be exposed directly to the E-beam, hence we use positive E-beam resist. We spin ARP6200.18 resist at 3000 rpm on the membrane sample followed by a 3-minute bake at 150 ^{o}C on a hotplate. We obtain 900 nm thick resist, enough to serve as a protection mask for etching 2.1 μm SiO_2 later on in the process. Spinning resist should be done carefully with the sample centred in the middle of the chuck as much as possible. If not properly centred, the resist gets deflected upon spinning due to the buckling of the membrane and result in thinner resist coverage over the freestanding film. It will not survive the subsequent etching step due to premature removal of the resist on the membrane. We have a custom-built chuck to mitigate this effect. Its diameter has the same dimension as the lateral size of the membrane sample. This makes it is easier to align the centre of the device with the chuck. After applying resist, we place the sample into the *Raith EBPG5200* E-beam (holder BW0040A) and use the corners of the square membrane to determine the centre of the chip with respect to the E-beam holder Faraday cup. Position A of the holder is always used as this is the closest to the Faraday cup of the holder and leads to better alignment of the pattern with respect to the centre of the device. We expose the resist with a 110 nm beam and dose of 400 $\mu C/cm^2$. The sample is afterwards developed in pentyl acetate solution for 1 minute, followed by a 1-minute MIBK:IPA (1:1) rinse to slow down the development. A final 1-minute IPA rinse is carried out to stop the development, and the sample is blown-dry with a high pressure N_2 gun. The process is depicted as step 7 in Fig.3.10.

STEP 8: SiO_2 REMOVAL

In this step, we define the pattern in the SiO_2 hard mask with an inductively coupled plasma (ICP) dry etch. The ICP etcher is mainly used for its ability to reach relative high etch rates of several hundred nanometres to few microns while still maintaining an anisotropic etch profile.

We start by mounting the 10×10 mm Si/SiN/SiO_2/resist chip at the center of 4" Si carrier wafer. The sample is held in place with 3 miniscule droplets of organic pump

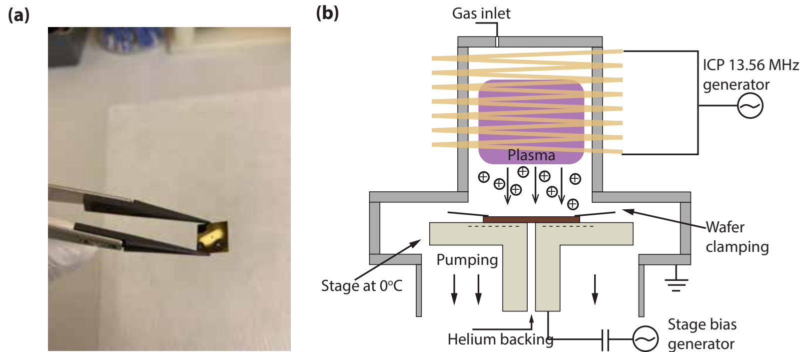

Figure 3.12: **AMS Bosch ICP etch process.** **(a)** Sample preparation with pump oil applied to the backside of membrane sample. **(b)** Illustration of ICP etch process as it takes place in the chamber.

oil on the backside, as shown in Fig.3.11a. The pump oil is originally intended for lubricating turbo pumps but due to its excellent thermal conductance, it can also be used as a thermalization oil. The use of this oil is important because it establishes a thermal path that allows the heat generated during etching to be released to the environment. If not well thermalized, the temperature on the surface of the chip will increase, leading to higher etch rates and lower selectivity between the resist and SiO_2. The sample is therefore moved slightly back and forth such that the oil spreads out evenly on the backside of the sample.

The carrier wafer is loaded into the loadloack of the *AMS Bosch ICP etcher* where it is clamped down and fixed. Helium (He) gas is emitted on the backside of the wafer and functions as an exchange gas to thermalize the sample to 0 ^{o}C before the etching starts. The system will raise a warning stating *"Helium overflow"* if the He flow keeps increasing till its limits are reached. This is usually an indication of a leak and in most cases related to He gas escaping from the backside of the carrier wafer due to misalignment in clamping or a dirty carrier wafer. This issue can be resolved by unloading and cleaning the backside of the carrier wafer with aceton or IPA. The wafer can then be loaded again in the loadlock and repeated until the warning disappears.

The ICP etcher contains 2 independent RF sources: the **first** source is 2 MHz source and responsible for creating a plasma in the chamber. This is done by feeding power to an RF antenna consisting of a large coil. The coil then produces an alternating magnetic field which energizes electrons that aid in ionizing gas molecules C_4F_8 and CH_4, creating a high density plasma. In each cycle of the alternating field, the electrons are accelerated up and down in the chamber, striking the upper walls and the wafer plate in the chamber. Note that the wafer plate is DC isolated from the lower electrode. In contrast to electrons, the ions show little to no response to the RF field. With a **second** 13.56 MHz RF source, we bias the upper walls and the wafer plate of the chamber. Electrons that hit the walls of the chamber are fed to ground and do not change the state of the system. Electrons accumulate on the wafer plate, making the lower electrode negatively charged. The plasma will develop a positive charge due to an absence of negative electrons. The voltage difference ΔV between the electrodes in the chamber that lead to

positive ions to drift toward the wafer plate. These ions collide with the sample and react chemically with SiO_2, but also physically, where they knock off the SiO_2 molecules, as shown in Fig.3.12b. The vertical motion of the ions produce an anisotropic etch profiles. In total, we etch for **6 minutes and 30 seconds** with the etch process split up in 2 steps of equal time. We introduce a wait time of 10 minutes in between for the chamber to cooldown before we proceed with the next step. After the etch is completed, the remaining resist is removed with an in-situ O_2 plasma for 4 minutes. The loadlock is vented and the samples are removed from the 4" Si carrier wafer with ethanol and blown-dried with high pressure N_2 gas. We achieve an etch rate of approximately 350 nm/min for SiO_2 with machine parameters shown in Table3.8, and we estimate the etch rate of ARP 6200.18 to be approximately 100 nm/min.

Process	Gas	Flow (sccm)	Pressure	ICP power	SH power	ΔV	SH height	He cooling
SiO_2 etch	C_4F_8 He CH_4	50 100 10	$4.6{\cdot}10^{-3}$ mbar	2500 W	200 W	23-24.2 V	120 mm	10 mbar/2.8 sccm
Resist O_2 clean	O_2	50	$2.1{\cdot}10^{-2}$ mbar	1000 W	5 W	6 V	200 mm	15 mbar/4.7 sccm

Table 3.8: AMS Bosch ICP machine setting for etching SiO_2. Both process take place at T = 0 ^{o}C. The measured etch rate of SiO_2 is 350 μm/min.

Note that there is a variability in the etch process and the etch rate changes between independent runs. The variability in etch rate is a result of the instability in system parameters. For example, the He flowrate on the backside of the wafer and responsible for wafer temperature control, changes each time the wafer is mounted differently on substrate holder. The location where we attach our chips on the 4" carrier wafer also needs special attention, as etch rate differs across the wafer. The stability of the plasma directly influences the etch rate and depends on the condition of the chamber. An instable plasma can be detected by monitoring the reflected power and ΔV. A much lower etch rate is reached if the reflected power is not able to reach 0 W. A prior 1 hour O_2 plasma clean of the chamber followed by a few minutes of preconditioning is recommended to ensure a stable plasma with 0 W reflected power and minimize etch variability. Therefore, it is of great importance to closely monitor the process parameters during each etching process e.g. bias voltage ΔV, He flow and chamber pressure to achieve consistent etch rates between independent runs. Any deviation from calibrated values may result in different etch rate of the resist and SiO_2. For example, if the carrier wafer is not properly thermalized during the etch process, the sample will heat up resulting in a lower selectivity between SiO_2 and resist. In this case, the sensor will raise an He overflow warning and the process needs to be stopped immediately. Ignoring this warning and continuing the process will cause the resist mask to disappear before the exposed SiO_2 is fully etched, resulting in a thinner SiO_2.

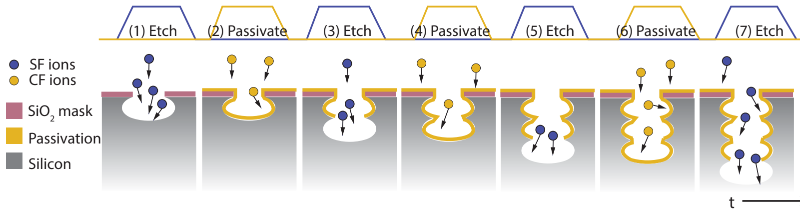

Figure 3.13: Time multiplexed Si DRIE process. The process continiously cycles between silicon etching (SF_6) and passivation (C_4F_8). The etch step is isotropic but is of short duration. In the passivation step, the sidewalls are coated and protected against the subsequent etch steps. The alternation between these steps results in an anisotropic etch profile.

STEP 9: SI DEEP REACTIVE ION ETCH (DRIE)

Si Bulk micromachining is realized with a Bosch process and is commonly used to make high aspect ratio structures in Si [38]. The Bosch process, named after the German company Robert Bosch GmbH which patented the process, is a time division multiplexed plasma etch process that has the capability to achieve high Si-SiO_2 selectivities, good anisotropy control and etch rates up to 10 μm/min in certain circumstances [31].

We prepare the membrane sample for DRIE by attaching them in the centre of a 4" Si carrier wafer with 6 um of thermal SiO_2. The same organic pump oil that was used in step 8 is used as a thermal link between chip and carrier wafer. Here, the location of the oil droplet on the back of the substrate is important and care must be taken when applying this. We place tiny oil droplets at 3 corners on the backside of the Si/SiN/SiO_2 chip and thus away from the square window. We believe that in case the thermalization oil is placed directly beneath the membrane, degassing of the oil in a vacuum environment might cause the membrane to break.

The carrier wafer is placed on the loading arm of *Oxford Instruments PlasmaPro 100 Estrelas* and then transferred automatically into the etching chamber. Here, thermalization is also very important because etching increases the temperature on the surface resulting in non-uniform etch rates as pointed out in step 8. The wafer inside the chamber is cooled to 5 ^{o}C and hereafter He gas is emitted at the backside. The He gas ensures homogenous thermalization during etching, else the sample will heat up resulting in non-uniform etch rates and profiles. A general rule is that the flow should not exceed 10 sccm, else there might be a leak (see step 8).

The Bosch etch process is divided up in cycles, each consisting of 2 steps i.e. etch and deposition. In a complete deposition-etch cycle, the deposition and etch time step are denoted t_d and t_e, respectively, as shown in Fig.3.13. During the deposition step, precursor gas C_4F_8 is emitted in the chamber and is dissociated into ions and radicals species by a strong magnetic field generated with a RF antenna. These undergo polymerization reactions to form a polymeric layer, probably CF, on the surface of the silicon structures. In the next etch, SF_6 gas is used to promote spontaneous Si etching. This etch step consists of the two separate stages. In the first stage of the etch step, the polymer already deposited at the surface is preferentially removed. This process is facilitated by directional ion bombardment. In the second stage, which starts after the polymer de-

posited at the bottom surface is completely removed, F-radicals cause spontaneous and isotropic Si etching by adsorption followed by formation and desorption of volatile products such as SiF_4. Therefore, a complete deposition/etch cycle can be divided into three distinctive but sequential physical stages: polymer deposition stage, polymer removal stage and isotropic Si etching stage.

The etch is started if the temperature of the chamber sidewalls are around **160 ^{o}C**. We witness instabilities in the plasma with colder sidewall temperature. In this case, we execute a 5-minute O_2 plasma clean to raise the temperature of the chamber and the sidewalls. We also precondition the chamber for 100 cycles with a dummy wafer before etching the membrane sample. The execution order of the DRIE process is shown in Table 3.9. This process is illustrated as step 9 in Fig.3.10.

3

Polymerization The substrate is etched through after **773 cycles** and lasts approximately 31 minutes. The sidewall of the free-standing structures are covered by a thin fluor layer that is a by-product from the chemical reactions at the deposition steps, presumably $SiCF_4$. This residue layer is stripped off by running a 5-minute O_2 plasma clean for 2 times, with a wait time of 5 minutes in between. We only start this cleaning process once the chamber has cooled back down to 160 ^{o}C and hereby releasing most of the heat generated during the Bosch process. To prevent the substrate from overheating during the O_2 ash, we keep cooling the backside of the wafer with He gas at 5 ^{o}C. Afterwards, the wafer is transferred from the chamber back to the loadlock and the chips are then carefully removed from the carrier wafer with ethanol. After the samples are separated, we mount them in teflon holder. We then perform a final piranha clean to remove all the organic residues that are still left on the sample i.e. organic pump oil and/or resist. The piranha mixture is created with 3 parts sulfuric acid (H_2SO_4) and 1 part H_2O_2 and is heated up to 100 ^{o}C. The mixture is a highly corrosive and an extremely powerful oxidizer which then removes most of the remaining organic residue. Mixing the 2 chemicals is a highly exothermic process and care must be taken when preparing this mixture i.e. H_2O_2 is poured slowly into H_2SO_4 and not vice versa. The sample is then cleaned for 10 minutes and rinsed twice with flowing D.I. H_2O. They are gently blown-dry with an N_2 gun.

There are several complications that arise when carrying out a Bosch etch process and require special attention. These are highlighted in below.

Aspect ratio dependent etch rate (ARDE) ARDE is a well documented phenomenon that is often observed in Si DRIE with the Bosch process. Here, the etch rate depend on the aspect ratio of the features that are etched. Wider features tend to be etched deeper than narrow ones, indicating a faster etch rate. This is also known as ARDE lag [39] and an example is shown in Fig.3.14a. This raises difficulties if features with different aspect ratios need to coexist in the same pattern. Therefore, we discuss this effect further and provide the reader with suggestions. Many factors contribute to the ARDE lag, but Ref. [40] showed that one factor is the depletions of ions at the bottom of the etched structure. One reason is that the sidewalls capture the ions due to their angular distribution when they enter the trench opening. Electrostatic fields within the trenches also contribute to the depletion of ions since they are deflected when they move through the trench.

Process	Gas	Cycles
Precondition	SF_6 He CHF_3	100 (LF pulsed)
Si etch 1	SF_6 He CHF_3	443 (LF pulsed)
Si etch 2	SF_6 He CHF_3	300 (LF pulsed)
Polymer strip 1	O_2	continuous
Polymer strip 2	O_2	continuous

Table 3.9: Oxford PlasmaPro 100 Estrelas Si DRIE process.

Minimizing ARDE lag, where uniformity in etch rate is achieved independent of the feature sizes can be a tedious and time-consuming task. This requires to find optimum combination of process related parameters e.g. power, deposition, etching gas time, pressure, temperature and many more. Our approach is the opposite: we design the pattern such that the feature to be etched have the size lateral dimension. In this way, we ensure that all the features and trenches are etched simultaneously with the same etch rate.

Notching Another undesirable effect of DRIE etching is known as notching [41]. Notching occurs at the bottom of the trench and can be attributed to charging of the dielectric SiO_2 of the carrier wafer on which the substrate is situated. This is visible as localized undercuts of the Si structures at the bottom Si/SiO_2 interface. Downward accelerated ions are deflected due to charging of the SiO_2 at the bottom. The charging effects do not occur during bulk etch because the silicon substrate is conductive enough to accommodate the current flow within the substrate and prevents any charge separation. However, when the etch front reaches the Si/SiO_2 interface, the insulating SiO_2 is exposed and the conductive current path is broken, allowing charge separation to occur. Due to the different angular distributions of ions and electrons in the plasma, positive ions tend to accumulate at the bottom of the trench, and electrons at the top. The resultant electric field is strong enough to bend the trajectories of arriving ions into the sidewalls of the trench where lateral etching (notching) occurs, as shown in an example in Fig.3.14b. Although harmless for our device, we still mitigate notching by modulating the voltage bias on the wafer holder. Pulsing the substrate electrode bias power with a low frequency source gives the SiO_2 dielectric time to discharge during bias-off-periods [42].

STEP 10: REMOVAL OF SiO_2 HARD MASK

After DRIE, there still remains a few hundred nanometers of SiO_2 on the front side of the chip, assuming a DRIE Si/SiO_2 selectivity of 100. This can be removed with hydrofluoric

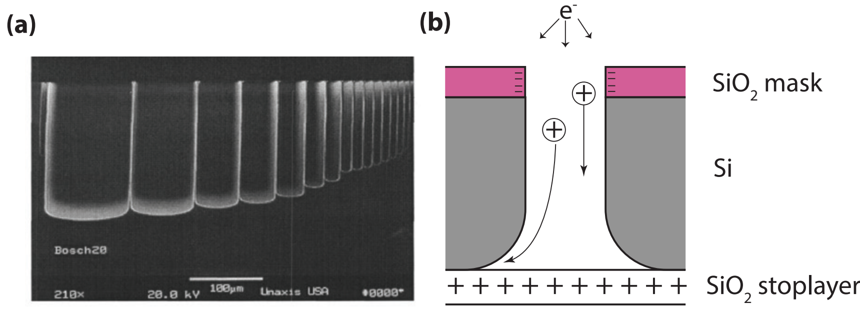

Figure 3.14: **Common DRIE artifacts.(a)** ARDE: the trench depth depend on the aspect ratio of the features. The wider openings are etched deeper compared to the narrow ones [39]. **(b)** Notching: occurs at the bottom of the substrate due to the charging of the SiO_2 stop layer.

acid (HF), but caution is required since this inorganic acid also etches Al+1%Si. Ref. [43] measured an Al etch rate of 2.2 nm/min with HF(79%) and diluting with D.I. H_2O (HF 40%) increases the etch rate to 68 nm/min. Suprisingly, the Al etchrate increases with decreasing HF concentration. HF is a weak acid that dissociates slowly in H^+ and F^- to form H_3O^+ and F^-, but there also remains non-ionized HF molecules. This etch is described via the chemical reaction given by [43]

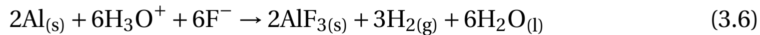

$$2Al_{(s)} + 6H_3O^+ + 6F^- \rightarrow 2AlF_{3(s)} + 3H_{2(g)} + 6H_2O_{(l)} \tag{3.6}$$

Etching of Al in concentrated HF is slower because of an absence of H_3O^+ molecules. Diluting concentrated HF increases $H3O^+$ concentration resulting in faster etch rates of Al. For SiO_2 it is the opposite, because F^- is responsible for the etch and not H_3O^+. The F^- molecules increases proportionally with the HF concentration resulting in faster etch rates for SiO_2. Hence, HF wet etch of the SiO_2 requires careful timing such that the reaction is stopped exactly once the SiO_2 is stripped, else the Al will also be removed. The etching of Si_3N_4 in HF is slow and negligible. Optimizing this process is time-consuming and extremely dangerous involving the use of several test devices and preparing multiple HF solutions in different concentrations. Instead, we use HF vapour (40 %) to etch the SiO_2. HF vapour does not etch or chemically alter the Al+1%Si [44].

This is verified with a test Si substrate (with no SiN) on which we have sputtered 25 nm Al+1%Si. We deposit 700 nm of PECVD SiO_2. We prepare the HF vapour setup by mounting the sample and set the holder temperature to 35 ^oC. The sample is thermalized for 10 minutes before we start the etch process. We etch several samples to calibrate the etch rate of the SiO_2, as shown Fig.3.15a and notice that the etch is not linear in time. The SiO_2 is fully etched after 90 seconds, but we observe residue on the sample and is shown in Fig.3.15b. It does not go away regardless of increasing the etch time. We verify whether the electrical properties of the Al+1%Si are altered due to this residue layer. A 4 point resistance measurement of the Al+1%Si before and after the deposition of PECVD SiO_2 reveals no major difference. It therefore seems that the Al+1%Si is not chemically modified by this residue layer. We currently have no explanation for the origin of this layer. With an electron micrograph inspection, these appear to have grass-like struc-

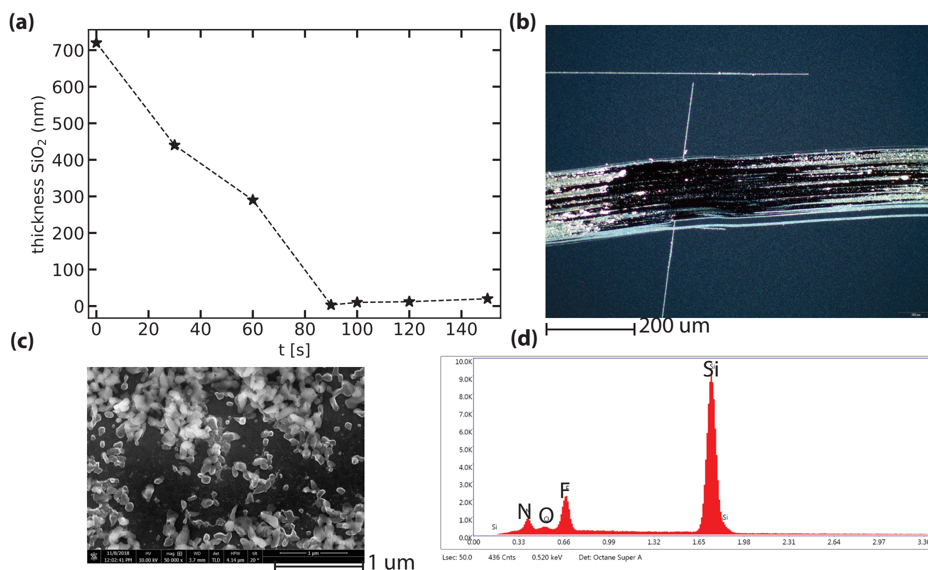

Figure 3.15: **Removal of PECVD SiO_2 with HF vapour.** **(a)** SiO_2 etch in HF vapour at 35 ^{o}C. Each data point is an etched test sample with 700 nm PECVD SiO_2 on a silicon substrate. **(b)** The Si/SiO_2 test chips placed in HF vapour for 90 seconds leave residue behind. The scratch is made with tweezers to improve optical contrast. **(c)** A electron micrograph image shows the residue to possess grass-like structures. **(d)** EDX spectroscopy reveals the presence of Si, F, N and O elements.

tures, as shown in Fig.3.15c. With an energy dispersive X-Ray analyzer (EDX) measurement presented in Fig.3.15d, we find that the residues consists of Si, F, N and O atoms. These seem to vanish if we heat up to sample to 250 ^{o}C on a hotplate for 15 minutes immediately after the HF vapour etch. It has only been carried out on one test sample and can therefore not be regarded as a reliable solution. A quick HF (40% dip) is also able to entirely removes the residue, but it also etch the Al+1%Si.

The SiO_2 on both side of our real sample with free-standing structures is stripped with HF vapour as described above. The oxide is stripped from the back first and subsequently from the front, each taking 90 seconds. At this point, we are still left with the residue that is present on both side of the membrane sample. We immediately mount the chips in a teflon holder. We get rid of this residue layer by a quick dip (< 1 second) of the devices in a 40 % HF solution. The sample is then quickly rinsed with IPA twice for 10 and 30 seconds respectively to stop the etch.

STEP 11: CRITICAL POINT DRYING (CPD)

After the SiO_2 has been stripped, the sample is still mounted in the teflon holder immersed in IPA. The sample now possesses fragile free-standing structures with the square membrane in the middle. We avoid blow-drying as this can damage and break the structures if not done carefully. We instead place the sample with holder in the chamber of the *Leica CPD3* CO_2 critical point dryer (CPD). This critical point dryer is especially useful for drying fragile devices. Before starting the CPD process, we pour IPA into the chamber

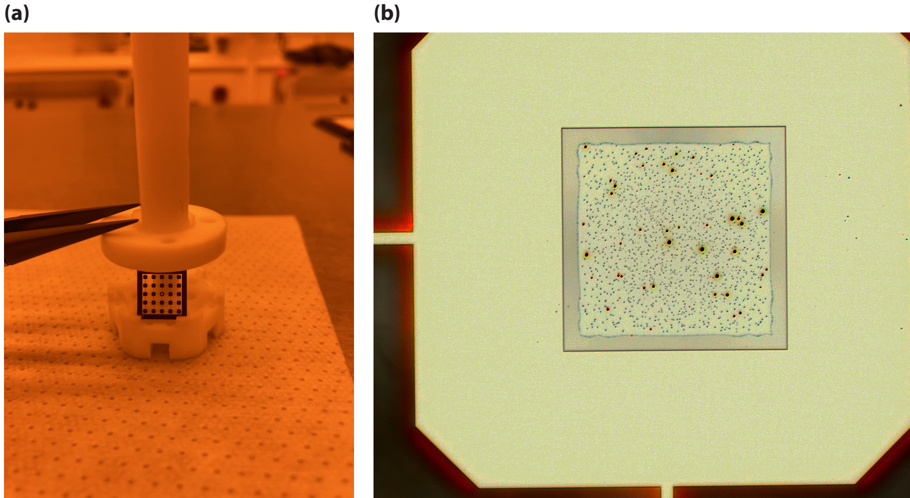

Figure 3.16: **Phononic shield device after CPD**. **(a)** We carefully unscrew the head of the holder and remove the phononic shield, which is then ready to be flipped onto the microwave device. **(b)** Optical image of Al+1%Si film on the SiN membrane contains small crater like structures. Although this is concerning, we found that the mechanical properties of the SiN and electrical properties of the metal are not altered.

until our samples are fully submerged in the liquid. In the CPD machine, the IPA is mixed with liquid CO_2 and by increasing the temperature and pressure, the mixture is brought into a supercritical region that does not cross any phase boundary. The dissimilarity between gas and liquid ceases to exist in this region, and densities of the gas and liquid become equal [45]. The choice for CO_2 is made for its low critical point temperature of 31 ^{o}C. This process removes moisture from the samples in a precise and controlled way and takes roughly 1 hour and 30 minutes. In Fig.3.16a, we show the final device mounted in the custom built teflon holder after CPD. After optical inspection, we notice that the residue layer has vanished, but we instead observe minuscule spots in the Al+1%Si as shown in Fig.3.16b. This raises many questions, but important here is that we found no change in the mechanical properties of the SiN nor the electrical conductivity of the Al+1%Si.

3.3.3. NOTES ON FABRICATING PHONONIC SHIELDS ON FULL WAFER

In this section, we give a suggestion for scaling up the fabrication of the phononic shield to wafer level. The notes here assumes that the wafer already contains freestanding metallized (SiN/Al+1%Si) membranes.

Modifying the fabrication process to produce these phononic shields on an entire 4" Si wafer does not only reduce the overhead time, but also increases the throughput. The large surface of the 4" wafer makes it favourable to use a photoresist as a hard mask against DRIE, instead of SiO_2. Decent adhesion, standard edge beads removal equipment, homogenous height distribution and ability to reach large resist thickness (> 20 μm) are all advantages of using photoresist on 4" wafers compared to single 10×10 mm chips. By using photoresist, we are able to omit the steps that involve SiO_2 processing (step 6-8), as no hard SiO2 mask is needed anymore. Therefore, no additional etch steps are required to open up the SiO_2 hard mask prior to DRIE. Another advantage of processing with photoresist instead of SiO_2 is that we can avoid using extremely dangerous acid HF and replace it with relative less harmful organic chemicals. The latter does not etch or damage the Al+1%Si, but only dissolves the photoresist.

The challenge in using photoresist however are twofold: (1) achieving a proper adhesion to the wafer surface such that the resist film does not peel off during development and (2) determining optimal exposure parameters to obtain straight side walls of the resist after development. We have optimized the process to achieve robust adhesion of the resist and provide further suggestions for determining lithographic parameters. Testing of this process was done on a 200 μm thick 4" double side polished (DSP) Si wafer with 50 nm of LPCVD stoichiometric Si_3N_4. A thick photoresist AZ9260 was chosen as it provides high resolution and superior aspect ratios [46]. To determine the minimum resist mask thickness, we assume a AZ9260-Si selectivity of 25. Note that this selectivity is conservative compared to those reported in Refs. [8, 47]. This then requires a minimum resist thickness of 8 μm to fully etch through the 200 μm Si substrate.

Before applying resist, we prepare the wafer by first heating it to 110 ^{o}C for 10 minutes to dehydrate the surface, followed by an Ozone clean for 20 minutes to further activate the surface to promote adhesion. We immediately transfer the wafer to a spin coater and pour AZ9260 directly from the bottle onto the surface of the wafer. A wait time of 3 minutes is introduced before spinning to ensure that the resist is spread out properly and covers the whole wafer. Spinning takes place at 500 rpm for the first 10 seconds and the remaining 50 seconds at 1100 rpm. This results in a resist thickness of 10 μm. We let the resist rest on the chuck for at least 10 minutes after spinning (1 minute wait per micron). This step is crucial because immediately exposing the wafer to high temperatures causes the solvent at top to evaporate first. The resist hardens and the solvent at the bottom gets trapped by not being able to evaporate. This can lead to complications such as the formation of bubbles during exposure and development. Leaving the sample to rest for a while at room temperature instead smoothens the resist while the solvent gradually evaporates. After this step, we place the wafer on proximity pins that suspends it above the hotplate at a fixed distance and then ramps down the gap slowly until contact is made. The hotplate is set to 110 ^{o}C and baking lasts for 15 minutes.

Before exposure, rehydration of the resist after baking is crucial. It is found that the hydration status of the film has a defining influence on the dissolution behaviour [48].

Films that have had insufficient time to re-hydrate cannot be completely dissolved, even at very high doses and long development times. Rehydration can take several hours depending on the resist thickness and for our case, a rehydration time of at least 3 hours should be taken into account.

After rehydration, the sample is exposed with a *EVG-620 mask aligner* with intensity 9 mW/cm^2 for 75 seconds. This exposure is split in 5 cycles of 15 seconds, with 60 seconds cooldown time between each cycle to prevent excessive heating of the resist. Excessive heating causes nitrogen that exists in the photosensitive substance of the photoresist (diazonaphthoquinone: DNQ) to form bubbles in the resist [49]. This in turn scatter incoming light from the exposure, reducing the light intensity at the bottom of the substrate. In thick film, it makes development difficult because the sidewalls will exhibit crater-like structures. Also, mechanical stress in the resist film due to the N_2 partial pressure can reduce resist adhesion and can lead to cracks.

After exposure, we proceed with development of the resist using 1 part AZ400K and 2 parts D.I. H_2O for 4 minutes and then de-hydrate the resist. De-hydration is done in a vacuum oven below the reflow temperature of the resist i.e. 90 ^oC for 15 minutes. This measure is taken to prevent bubbles forming and bursting in the subsequent heat intensive DRIE step. The resist thus loses its masking function when this occurs.

The last step involves DRIE of the wafer. In this process, it is very important to properly thermalize the wafer during the etch in order to obtain a uniform etch rate across the wafer. This can be challenging considering its large surface. The temperature variation can be as large as 15 ^oC across a 4" wafer when etching at 0 ^oC, as reported by Oxford engineers. To increase the cooling power, we need to increase the He back pressure, but it can cause the wafer to bow and lead to non-uniform etch rates. Hence, an optimum needs to be found between desired wafer cooling while still retaining a flat surface. We therefore increase the wafer holder temperature to 15 ^oC to avoid using high He pressure for cooling the wafer. Note that the wafer is not solely loaded in the loadlock. This is to prevent contamination of the chamber after the Si wafer is etched fully through. It will also expose the He gas that is flowing through the back of the wafer to the main chamber that contains the plasma. The wafer to be etched is therefore placed on a Si carrier wafer first that contains a 6 μm thermal SiO_2 film. The wafers are stacked on top of each other with crystal bond [50], which has excellent adhesive and thermal properties. The crystal bond is a cylindrical crystal stick and is first crushed into grains and dissolved with aceton after which it is poured onto the carrier wafer. We align and place our wafer exactly on top and bake it in a vacuum oven at 90 ^oC for 10 minutes. The 6 μm SiO_2 film on the carrier wafer acts as a stoplayer in the etching process.

Note that we cannot make use of step 9 DRIE process recipe for etching a 4" wafer, but it nonetheless provides a good starting point. The difference is that there is more exposed Si area distributed over the entire wafer that needs to be etched, as is shown in Fig.3.17. The angular distribution of the plasma needs to be adapted to account for this difference and is done through varying system parameters such as power, pressure, gas ratios and time. The interdependencies of all these parameters have been investigated by Ref. [31] and can be followed when adapting the DRIE process to etch an entire 4" Si wafer. Optimizing this etch recipe happens through trial and error. After the etch, the wafers can be separated by immersing both into a PRS-3000 solvent at 80 ^oC for 60

minutes. The individual samples are dried using CPD.

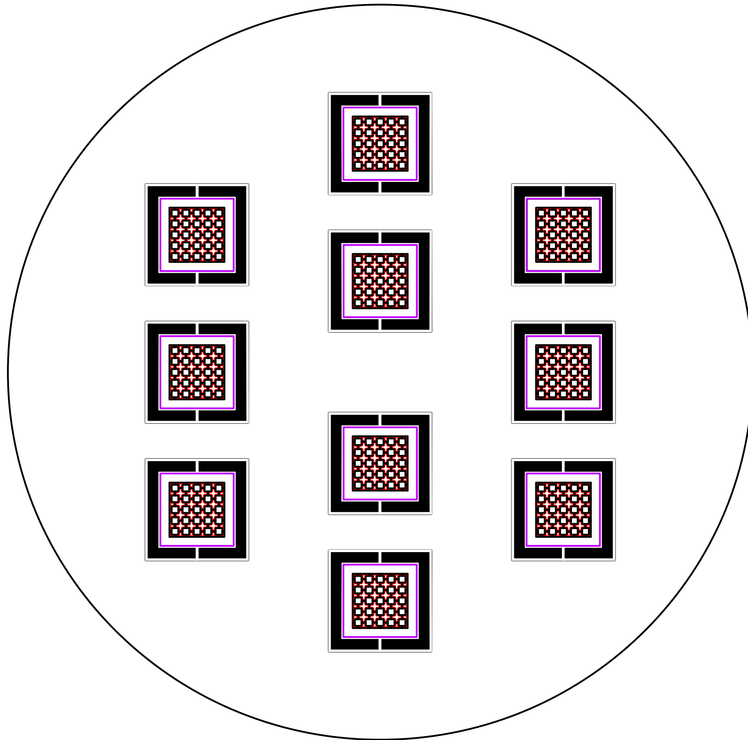

Figure 3.17: Shield design on wafer. A single 4" wafer can be used to fabricate 10 or more phononic shield within a single fabrication run.

REFERENCES

[1] A. Megrant, C. Neill, R. Barends, B. Chiaro, Y. Chen, L. Feigl, J. Kelly, E. Lucero, M. Mariantoni, P. J. O'Malley, *et al.*, *Planar superconducting resonators with internal quality factors above one million,* Applied Physics Letters **100**, 113510 (2012).

[2] D. P. Pappas, M. R. Vissers, D. S. Wisbey, J. S. Kline, and J. Gao, *Two level system loss in superconducting microwave resonators,* IEEE Transactions on Applied Superconductivity **21**, 871 (2011).

[3] D. J. Thoen, B. G. C. Bos, E. Haalebos, T. Klapwijk, J. Baselmans, and A. Endo, *Superconducting nbtin thin films with highly uniform properties over a ∅ 100 mm wafer,* IEEE Transactions on Applied Superconductivity **27**, 1 (2016).

[4] R. Barends, H. Hortensius, T. Zijlstra, J. J. Baselmans, S. Yates, J. Gao, and T. M. Klapwijk, *Noise in nbtin, al, and ta superconducting resonators on silicon and sapphire substrates,* IEEE transactions on applied superconductivity **19**, 936 (2009).

[5] *Kavli nanolab delft,* https://www.tudelft.nl/tnw/over-faculteit/afdelingen/quantum-nanoscience/kavli-nanolab-delft, (Accessed on 07/26/2021).

[6] *Ar-p6200_csar62english_allresist_product-information.pdf,* https://www.allresist.com/wp-content/uploads/sites/2/2020/03/AR-P6200_CSAR62english_Allresist_product-information.pdf, (Accessed on 08/20/2021).

[7] P. M. Kopalidis and J. Jorné, *Modeling and experimental studies of a reactive ion etcher using sf 6/o 2 chemistry,* Journal of the electrochemical society **140**, 3037 (1993).

[8] H. Jansen, H. Gardeniers, M. de Boer, M. Elwenspoek, and J. Fluitman, *A survey on the reactive ion etching of silicon in microtechnology,* Journal of micromechanics and microengineering **6**, 14 (1996).

[9] M. Aspelmeyer, T. J. Kippenberg, and F. Marquardt, *Cavity optomechanics: nano- and micromechanical resonators interacting with light* (Springer, 2014).

[10] S. Chakram, Y. Patil, L. Chang, and M. Vengalattore, *Dissipation in ultrahigh quality factor sin membrane resonators,* Physical review letters **112**, 127201 (2014).

[11] P.-L. Yu, T. Purdy, and C. Regal, *Control of material damping in high-q membrane microresonators,* Physical review letters **108**, 083603 (2012).

[12] *Lpcvd sin (stoichiometric),* http://www.mit.edu/~6.777/matprops/lpcvd_sin2.htm, (Accessed on 01/14/2022).

[13] C. Inc., *Comsol,* (2020).

3

[14] E. Serra, M. Bawaj, A. Borrielli, G. Di Giuseppe, S. Forte, N. Kralj, N. Malossi, L. Marconi, F. Marin, F. Marino, *et al.*, *Microfabrication of large-area circular high-stress silicon nitride membranes for optomechanical applications,* AIP Advances **6**, 065004 (2016).

[15] M. Rösch, *Development of lumped element kinetic inductance detectors for mm-wave astronomy at the IRAM 30 m telescope*, Vol. 12 (KIT Scientific Publishing, 2014).

[16] *Mems chips and lasers for industrial and scientific applications |norcada,* https://www.norcada.com/ (), (Accessed on 07/26/2021).

[17] *Mems device release,* https://engineering.tufts.edu/microfab/documents/SOP_RCA-SC1.pdf (), (Accessed on 09/12/2021).

[18] H. O. Pierson, *Handbook of chemical vapor deposition: principles, technology and applications* (William Andrew, 1999).

[19] P. Pan and W. Berry, *The composition and physical properties of lpcvd silicon nitride deposited with different nh 3/sih2cl2 gas ratios,* Journal of The Electrochemical Society **132**, 3001 (1985).

[20] P. French, P. Sarro, R. Mallée, E. Fakkeldij, and R. Wolffenbuttel, *Optimization of a low-stress silicon nitride process for surface-micromachining applications,* Sensors and Actuators A: physical **58**, 149 (1997).

[21] M. Stadtmüeller, *Mechanical stress of cvd-dielectrics,* Journal of the Electrochemical Society **139**, 3669 (1992).

[22] C. Yang and J. Pham, *Characteristic study of silicon nitride films deposited by lpcvd and pecvd,* Silicon **10**, 2561 (2018).

[23] *Wet-chemical etching of silicon and sio2,* https://www.microchemicals.com/technical_information/silicon_etching.pdf, (Accessed on 09/13/2021).

[24] *Koh-etching-info-2013_v2.pdf,* https://www.nanofab.ualberta.ca/wp-content/uploads/downloads/2016/07/KOH-Etching-Info-2013_V2.pdf, (Accessed on 09/13/2021).

[25] N. Luhmann, A. Jachimowicz, J. Schalko, P. Sadeghi, M. Sauer, A. Foelske-Schmitz, and S. Schmid, *Effect of oxygen plasma on nanomechanical silicon nitride resonators,* Applied Physics Letters **111**, 063103 (2017).

[26] K. Gall, M. Horstemeyer, D. L. McDowell, and J. Fan, *Finite element analysis of the stress distributions near damaged si particle clusters in cast al–si alloys,* Mechanics of Materials **32**, 277 (2000).

[27] X. Wu, J. Long, H. S. Ku, R. Lake, M. Bal, and D. P. Pappas, *Overlap junctions for high coherence superconducting qubits,* Applied Physics Letters **111**, 032602 (2017).

[28] P.-L. Yu, K. Cicak, N. Kampel, Y. Tsaturyan, T. Purdy, R. Simmonds, and C. Regal, *A phononic bandgap shield for high-q membrane microresonators,* Applied Physics Letters **104**, 023510 (2014).

[29] M. Maldovan, *Sound and heat revolutions in phononics,* Nature **503**, 209 (2013).

[30] I. Wilson-Rae, N. Nooshi, W. Zwerger, and T. J. Kippenberg, *Theory of ground state cooling of a mechanical oscillator using dynamical backaction,* Physical review letters **99**, 093901 (2007).

[31] M. J. De Boer, J. G. Gardeniers, H. V. Jansen, E. Smulders, M.-J. Gilde, G. Roelofs, J. N. Sasserath, and M. Elwenspoek, *Guidelines for etching silicon mems structures using fluorine high-density plasmas at cryogenic temperatures,* Journal of microelectromechanical systems **11**, 385 (2002).

[32] S. Gorelick, *Hard masking for silicon etching?* (2019).

[33] L. Nicu, P. Temple-Boyer, C. Bergaud, E. Scheid, and A. Martinez, *Energy study of buckled micromachined beams for thin-film stress measurements applied to sio2,* Journal of micromechanics and microengineering **9**, 414 (1999).

[34] M. Fang, D. Hu, and J. Shao, *Evolution of stress in evaporated silicon dioxide thin films,* Chinese Optics Letters **8**, 119 (2010).

[35] Y. Fan and Z. Zhou, *Atomic peening effect in film sputtering process,* VACUUM SCIENCE AND TECHNOLOGY **16**, 235 (1996).

[36] C. Davis, *A simple model for the formation of compressive stress in thin films by ion bombardment,* Thin solid films **226**, 30 (1993).

[37] K. Mackenzie, D. Johnson, M. DeVre, R. Westerman, and B. Reelfs, *Stress control of si-based pecvd dielectrics,* in *Proceedings of the 207th Electrochemical Society Meeting* (2005) pp. 148–159.

[38] J. Thevenoud, B. Mercier, T. Bourouina, F. Marty, M. Puech, and N. Launay, *Drie technology: from micro to nanoapplications,* Alcatel Micro Machining Systems, ESIEE, no later than , 1 (2011).

[39] S. Lai, D. Johnson, and R. Westerman, *Aspect ratio dependent etching lag reduction in deep silicon etch processes,* Journal of Vacuum Science & Technology A: Vacuum, Surfaces, and Films **24**, 1283 (2006).

[40] H. Jansen, M. de Boer, R. Wiegerink, N. Tas, E. Smulders, C. Neagu, and M. Elwenspoek, *Rie lag in high aspect ratio trench etching of silicon,* Microelectronic Engineering **35**, 45 (1997).

[41] C.-H. Kim and Y.-K. Kim, *Prevention method of a notching caused by surface charging in silicon reactive ion etching,* Journal of Micromechanics and Microengineering **15**, 358 (2004).

[42] F. Laermer and A. Urban, *Challenges, developments and applications of silicon deep reactive ion etching,* Microelectronic Engineering **67**, 349 (2003).

[43] P. Gennissen and P. French, *Sacrificial oxide etching compatible with aluminum metallization,* in *Proceedings of International Solid State Sensors and Actuators Conference (Transducers' 97)*, Vol. 1 (IEEE, 1997) pp. 225–228.

[44] A. Witvrouw, B. Du Bois, P. De Moor, A. Verbist, C. A. Van Hoof, H. Bender, and C. Baert, *Comparison between wet hf etching and vapor hf etching for sacrificial oxide removal,* in *Micromachining and Microfabrication Process Technology VI*, Vol. 4174 (International Society for Optics and Photonics, 2000) pp. 130–141.

[45] I. H. Jafri, H. Busta, and S. T. Walsh, *Critical point drying and cleaning for mems technology,* in *MEMS Reliability for Critical and Space Applications*, Vol. 3880 (International Society for Optics and Photonics, 1999) pp. 51–58.

[46] A. Abbas, P. Supiot, V. Mille, D. Guillochon, and B. Bocquet, *Capillary microchannel fabrication using plasma polymerized tmds for fluidic mems technology,* Journal of Micromechanics and Microengineering **19**, 045022 (2009).

[47] K. Tsujimoto, S. Okudaira, and S. Tachi, *Low-temperature microwave plasma etching of crystalline silicon,* Japanese journal of applied physics **30**, 3319 (1991).

[48] *Rehydration of photoresists,* https://www.microchemicals.com/technical_information/photoresist_rehydration.pdf, (Accessed on 09/15/2021).

[49] *Dry etching with photoresist masks,* https://www.microchemicals.com/technical_information/dry_etching_photoresist.pdf, (Accessed on 09/15/2021).

[50] *Technical data sheet,* https://www.emsdiasum.com/microscopy/technical/datasheet/50400.aspx, (Accessed on 01/14/2022).

4

Magnetic losses in planar lumped-element superconducting microwave resonators

Planar superconducting microwave resonators have a wide range of applications in the field of quantum technologies. A key feature of superconducting resonators is a low intrinsic loss rate, resulting in high quality factors (Q-factors), and understanding and engineering these loss factors is an important process in superconducting resonator development. While a common type of resonator design is based on coplanar waveguides, for some applications, a lumped element design with a large inductor is advantageous. This large inductor, however, leads to the possibility of stray magnetic fields, which could form a source of loss. Here, we numerically model the losses in lumped-element superconducting resonators using a commercial finite element tool, exploring the influence of the inductor geometry on the internal loss. We find that for lump-element design, a large loop inductor can result in stray magnetic fields that induce eddy currents in the copper packaging, which can form a serious limit to the internal quality factor. Our simulation show that replacing this large loop inductor with a meander design mitigates this effect and significantly increases the resonator quality factor, confirmed by measurements on meander-inductor lumped-element devices. Our work illustrates how to account for these magnetic field losses in simulations, and could find applications as well in the simulation of other resonator designs.

This chapter is being prepared for publication as *Magnetic losses in planar lumped-element superconducting microwave resonators.* S.R.Peiter and G.A.Steele

4.1. INTRODUCTION

High-Q resonators are essential components used in quantum computing [1, 2] (QC), optomechanics [3, 4] and many other fields exploiting the tools of circuit quantum electrodynamics (cQED)[5–8]. As an example, the use of these resonators in QC lead to an increase in computation bandwidth [9, 10] or in the case of optomechanics, it provides higher coorperativity, necessary for groundstate cooling [3]. These resonators are made of superconductors, which exponentially suppress ohmic losses at milliKelvin temperatures [11, 12]. Although there are no ohmic losses from the superconducting metal itself at these low temperatures, the resonators are still subjected to dielectric losses, usually by two level systems (TLS) [13, 14]. In recent years, the focus has been to increase Q by reducing the influence of dielectric losses [15] mostly in coplanar waveguides (CPW). A rather successful approach to reduce dielectric losses has been to improve surface preparation protocols in fabrication to minimize parasitic TLS [16, 17]. Therefore, the CPW has been utilized extensively in low loss superconducting experiments. However, in some applications within electromechanics [18, 19] or cQED [20–22], the use of lumped-element resonators with large inductors are more desirable. But in these resonators, the large area inductive element can potentially lead to magnetic or radiation losses [23]. The effect of magnetic losses in high-Q superconducting lumped-element resonators has not yet received much attention in the community. In this letter, we systematically explore the magnitude of magnetic losses in planar superconducting resonators. We find a strikingly large loss rate in large LGR. Using Sonnet simulations, we show that this loss arises from large stray magnetic fields. We use simulations to predict and optimize our resonator geometry and experimentally show an improved loss rate of the optimized resonator we call meandered gap resonator (MGR). All simulations in this chapter were done with Sonnet version 16.54 [24].

4.2. STRAY MAGNETIC FIELD INDUCED LOSSES OF LGR

To investigate magnetic losses in superconducting resonators, we design two GHz-frequency resonators: a $\lambda/4$ co-planar waveguide (CPW) and a loop gap resonator (LGR) positioned closely to a feedline that is shorted at one end, as shown in the inset of Fig.4.1. The design of the $\lambda/4$-CPW starts by first choosing its fundamental mode and then to infer its length l_s with equation [25]

$$f_n(l_s) = \frac{v_p}{\lambda_n} = \frac{c}{\sqrt{\epsilon_{\text{eff}}}} \frac{n}{4l_s} \tag{4.1}$$

Here, ϵ_{eff} is the effective permittivity, taking the waveguide geometry and dielectric constant ϵ_r into account. The fundamental mode of the CPW is chosen to be 6.4 GHz and corresponds to l_s = 1.2 mm. We follow a standard practice of meandering the CPW to save chip area (4 bends). This approach has also shown to reduce radiation losses [26]. The width w of the central conductor and its gap g to the ground plane are chosen such that a characteristic impedance Z_o = 50 Ω is maintained [27]. This condition is satisfied if the ratio $w/(w+2g) \approx 5/11$. In our design, we set $w = 10\ \mu$m and $g = 5\ \mu$m, as Ref. [28] has shown that this parameter combination lead to relatively low losses in presence of a lossy interfacial film between the metal and substrate. We excite TE modes of the CPW by capacitively coupling it to the feedline.

The LGR consists of a loop with diameter D = 1.2 mm and shunted by interdigitated capacitors. The loop wire width w = 5 μm and size of the interdigitated capacitor with respect to the loop is shown in the inset of Fig.4.1. The LGR is surrounded by groundplane which is spaced at a distance of 100 μm. The area within the loop is free from any ground metal. The geometrical inductance and capacitance of the LGR is estimated to be respectively L_g=4.5 nH and C = 110 fF. We place the LGR at the end of the shorted feedline and thus at a current anti-node of the feedline. We can excite modes by inducing currents in the big loop with a magnetic flux generated at this anti-node.

Both resonators including groundplane are assigned the material properties of Niobium titanium nitride (NbTiN) at cryogenic temperatures (15 mK). Below 9K, NbTiN turns into a Type-II superconductor and its impedance turns complex: $Z_s = R_s + j\,\omega\, L_s$. In our case it is valid to assume negligible resistive losses due to low quasi-particle densities at 15 mK, hence we set the surface resistance R_s = 0 [29]. However, kinetic inductance L_s arising from the cooper pairs dynamics at GHz is non-zero and so we set L_s=1.3 pH/sq [30].

The resonators are arranged on a 430 μm thick high-resistivity crystalline Sapphire substrate with R > 3500 Ω.cm. Sapphire and silicon substrates are a standard in superconducting microwave circuits, because of their low dielectric losses with their loss tangent $\tan\delta < 10^{-7}$ and high $\epsilon_r = 10$ [31]. The substrate is mounted on a thick Copper (Cu) block with its electrical conductivity $\sigma = 5.7\times10^{7}$ S/m. Here, we have assumed unity residual resistance ratio (RRR) of Cu, which is the ratio between the electrical resistance measured at 295 K and 4 K (liquid helium).

As the last step, we place the resonator device inside a metal box to suppress power leakage to free space, known as radiation losses [12, 32, 33]. A Cu or Al cover surrounding the top of a device is also common practice in 2D cQED experiments to suppress radiation losses [33, 34]. In our simulation, we assign a lossless metal to the upper and all the side boundaries of the simulation box. The height h_{box} between the subsrate and upper boundary of the simulation box is chosen carefully to prevent boxmodes from appearing. Boxmodes are modes of the enclosed metal box and are detrimental to our circuit as these can cause unwanted loss by coupling to our circuit. The existence of these modes has shown to depreciate the coherency of quantum devices in Refs. [35, 36]. Unfortunately, we cannot get fully rid of these modes as they are inherent to an enclosed metallic box, but we can control its free spectral range by varying h_{box}. By choosing h_{box}=1 mm, the fundamental box mode is shifted above 15 GHz and thus spaced far away from the fundamental mode of the resonators.

A port for exciting and probing the reflection response of the resonators is connected to the feedline with its internal impedance Z_o configured to 50 Ω. The sidewalls of the simulation domain are grounded except at the location where the port makes contact to the feedline. The ground plane metal makes contact with the sidewalls and are therefore held to the same ground potential.

After our device setup and configuration in Sonnet, we perform a wide frequency sweep in the range where the resonance is expected. Once we detect signatures of the fundamental mode, we narrow down the frequency range and increase the number of points. The magnitude of the reflection response of LGR and CPW is shown in Fig.4.1 and is centered around their resonance frequency of respectively 7.2 and 6.8 GHz. On

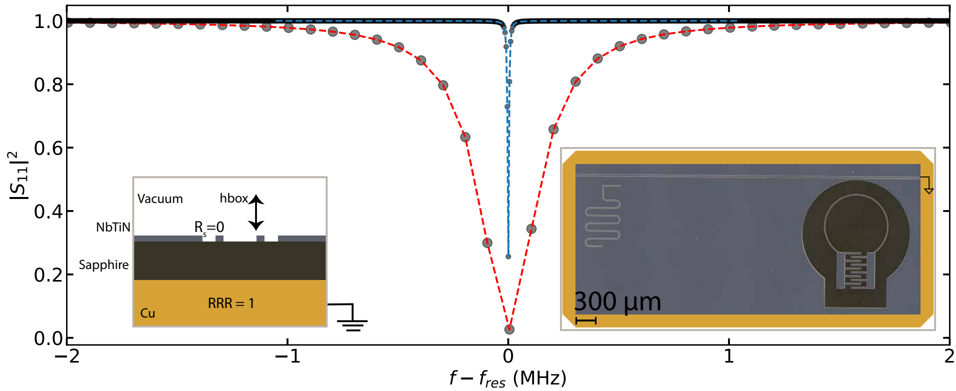

Figure 4.1: **Large simulated losses in loop-inductor lumped-element resonators** Simulation data and corresponding fit of reflection response LGR (red) and CPW (blue) in the presence of a normal Cu surface situated below the substrate. The simulation includes no dielectric losses, nor quasiparticle losses in the superconducting film. The only source of loss are eddy-currents induced in the copper plate below the substrate. The fitting routine is performed with a Lorentzian profile and internal quality factors Q_i are estimated respectively 4.6 $\times 10^4$ and 4.01×10^6. Simulation shows a notable difference in loss between LGR and CPW. **(Inset:left)** Cross-section of simulation box in Sonnet. Layer colouring indicate material. Here, the internal loss come only from the finite conductivity of Cu. The device is enclosed in a grounded lossless metallic box. **(Inset:right)** Top view of NbTiN resonators on a sapphire substrate (grey) configured in a reflection geometry in Sonnet. The CPW is coupled capacitively to the shorted feedline whereas the LGR is coupled inductively and positioned at the end. The substrate is mounted on a thick Cu piece (yellow) and the whole device is placed inside a metal lossless box (grey rectangle)

first observation, we witness a narrow linewidth for the CPW, whereas the LGR is broader and a smaller amount of power is reflected back into the feedline. In order to quantify internal losses between resonators of different frequencies, we use the fitting procedure described in supplementary note 4.6.3 to extract the internal and external losses (κ_i , κ_e) and express it as quality factors Q ($Q_n = \omega/\kappa_n$).

We establish a 100x larger loss rate for the LGR compared to the CPW with internal quality factor of 4.6 $\times 10^4$ and 4.01×10^6 respectively. The losses in the simulation are purely conductive ohmic losses and is a result of stray magnetic fields generated in the resonators, which in turn induce eddy currents at the Cu surface. As the loss for the LGR is notably higher, we make out that the magnetic field generated by the loop is of greater intensity at the Cu surface compared to the CPW. This is attributed to the big loop of the LGR, which is able to sustain high current densities, whereas the electromagnetic field in the CPW is screened by the closely spaced groundplane.

We point out that the simulation shown in Fig.4.1 does not include any sort of dielectric losses. Therefore, the Q_i estimated of the CPW set a lower bound on its internal loss and will decrease more as we increase RRR_{Cu}. Above simulations assume an $RRR_{Cu} = 1$, but ordinary untreated Cu usually has an RRR between 10 and 25 [37]. We have not simulated the loss of the CPW for larger RRR_{Cu}, but we expect it to scale proportionally with $RRR^{0.5}$. NbTiN CPW fabricated and measured at cryogenic temperature have shown $Q_i > 10^6$ [16], which is of the same order of magnitude as our simulation extracted internal quality factors. However, the CPW resonator samples used in the measurement were

limited by the dominant dielectric loss rather than conductive losses.

4.3. GEOMETRY DEPENDENT CONDUCTION LOSS

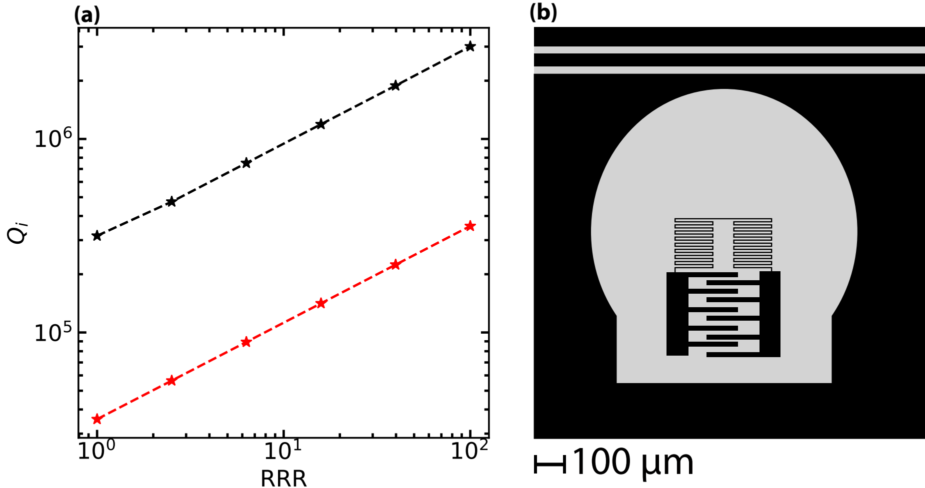

Figure 4.2: **Geometry dependent loss** **(a)** Internal loss dependence on σ_{Cu} for LGR (red) and MGR (black). Untreated regular Cu has RRR between 10 and 25. The MGR shows a 10x improvement in conductive loss compared to the LGR, while conductive losses get reduced as σ_{Cu} is increased. **(b)** Improved the design of MGR by replacing the loop with a meandering inductor, while the ground-plane is unaltered.

As the conductivity σ of Cu increases as we go down to cryogenic temperatures, so will the Q_i of the resonators. We study this dependence for the LGR. Since untreated regular Cu has an RRR ≈ 25, we sweep $\mathrm{RRR}_{\mathrm{Cu}}$ from 1 to 100. The loss dependence of the LGR with σ_{Cu} is shown in Fig.4.2. In this log-log plot, we recognize a linear decrease in loss as RRR is increased. The linearity follows from the Q dependence on the RRR as follows

$$Q \propto \frac{1}{\omega_r R_s C} = \frac{1}{\omega C}\sqrt{\frac{2\sigma_{RT}\mathrm{RRR}}{\mu_r \omega_r}} \tag{4.2}$$

We proceed by modifying the shape of the inductor of the LGR, since it is responsible for the strong magnetic fields at the Cu surface. The loop is replaced by a meandering inductor, where it consists of parallel wires carrying opposing currents with total length of 6.7 mm and pitch $p = 6$ μm. The inductance is estimated to be 4.3 nH, roughly the same as the LGR. The finger capacitor is left untouched, so the capacitance is unchanged. We call this resonator meandering gap resonator (MGR) and is shown in Fig.4.2b. The loss simulation of the MGR (red) in Fig.4.2a. Here, we have determined the internal quality factor Q_i with the procedure described in supplementary note 4.6.1 and it has improved by approximately 10x. We explain this improvement by the fact that opposing current-carrying wires of a meandered inductor have an overall reduced field strength at the bottom of the substrate ($t_{\mathrm{substr}} >> p$), whereas the loop radius R is similar to the thickness of the substrate $t_{\mathrm{substr}} \approx R_{\mathrm{loop}}$. The MGR is more compact than the LGR and occupies less

space on the substrate. Still, the internal losses we simulate for the MGR are superior to the CPWs i.e. $Q_{i_{\mathrm{CPW}}}>Q_{i_{\mathrm{LGR}}}$. The higher internal quality factor of the CPW is a result of the ground plane being closer to the central conductor which screens off the fields generated by the resonator. This effect is also present in the MGR, but to lesser extent compared to the CPW and therefore resulting in larger ohmic dissipation at the Cu.

One approach for minimizing ohmic losses, is by reducing the sheet resistance of the Cu. The frequency dependent sheet resistance R_s is given by [38]

$$R_s = R_{DC}\frac{t}{\delta(1-e^{-t/\delta})} \tag{4.3}$$

Here, R_{DC} is the resistance at DC, δ the skin depth and t the thickness of the Cu. The sheet resistance needs to be minimal to reduce ohmic losses at the Cu surface i.e. $R_s = R_{\mathrm{DC}}$ We infer $R_s \approx R_{\mathrm{DC}}$ if $t \approx \delta$. This condition becomes difficult to satisfy as δ gets smaller with frequency; for example δ = 1 μm at 6 GHz for Cu. Getting the thickness of Cu close to its skin depth intuitively means that charge carriers are not confined to move at the surface only but instead passes through the full cross-section, effectively attaining a resistance similar to R_{DC}. A second approach would be to use oxygen-free high purity copper (OFHC), because electrical resistance depends primarily on its purity and granularity of the material. OFHC has an RRR close to 50 and carefully annealing it many times can increase its RRR to 2000. Another option would be to replace the copper mounting box with a superconductor: this would offer no eddy-current loss, but is often avoided due to concerns of weaker thermalization provided by superconductors.

4.4. INCLUDING DIELECTRIC LOSSES ON LUMPED-ELEMENT DESIGNS IN THE SIMULATION

Dielectric losses are another source of loss which often dominate the internal loss rate of superconducting resonators. They come into play when electric fields generated in the resonators undergo dissipative interactions with a lossy dielectric film also known as two-level systems (TLS) [13, 39]. This lossy film is found between the substrate and metal and has a thickness of several nanometres with typical $\tan\delta \approx 1\times10^{-3}$ [40], many times larger than the loss tangent of bulk Sapphire. However, the exact $\tan\delta$ of the interface layer is usually unknown and depends on the fabrication process. Their presence is cannot be avoided due to uncontrollable contamination in the fabrication process, such as exposure to air or greasy handling tools. Mitigating this lossy interfacial film has been explored widely with different surface preparation techniques in fabrication processes [16, 32] and it should not be underestimated as it is time-consuming and challenging. Fortunately, reducing these losses is not only limited to improving fabrication procedures, but can also be achieved by optimizing the shape of the resonators, mainly of the capacitors, to prevent localized intense electric fields. Standard practice in designing low loss capacitors geometries are (1) circumventing sharp corners (90 ^{o} corners) that are known to possess high charge densities, resulting in intense localized electric fields; (2) Increasing conductor width w to reduce current density [32] and (3) removing or spacing the groundplane further away from the conductor [31]. When considering the last 2 design rules, one has to take into account the interplay between dielectric and radiation

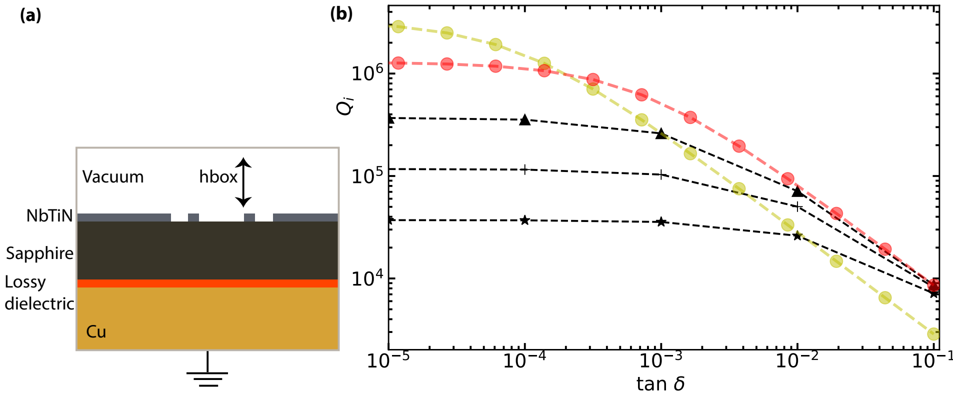

Figure 4.3: **Relevance of magnetic losses in presence of dielectric losses** **(a)** 2D cross-section of simulation box in Sonnet. Colour layers indicate materials used in the simulation. Bottom to top: Cu (orange), lossy dielectric film (red) and sapphire substrate with NbTiN (dark and light gray respectively). The device is enclosed in a lossless metal box to suppress radiation losses. **(b)** Simulation of internal loss by sweeping tan δ. The simulated loss of the LGR is shown for RRR_{CU} = 1, 10, 100 (black curves: star, plus, triangle markers). The loss of the LGR is limited by conductive losses below tan $\delta \approx 10^{-3}$, while the dielectric losses dominate at higher tan δ. The CPW (green circle, RRR_{CU}=1) is mainly affected by dielectric loss, as it shows a linear dependence (on log-log scale) over the whole interval. For the MGR (red circle), a higher conduction limited internal quality factor is estimated compared to the LGR, while the dielectric limited quality factor is the same.

loss, as large area conductor enchance coupling to free space. To investigate the effect of dielectric loss for our particular set of resonators (CPW, LGR, MGR), we add a lossy 10 nm dielectric film, with ϵ=10 [41] between the sapphire substrate and the NbTiN metal layer in our simulation as shown in Fig.4.3a. Here, tan δ is swept from 10^{-5} to 10^{-1} for different RRR_{Cu} and the loss dependence is shown in Fig.4.3b.

On log-log scale, the LGR (black: star, plus, triangle) exhibits a linear dependence starting at approximately tan $\delta \approx 10^{-2}$ for all RRR_{Cu}. At tan $\delta = 10^{-1}$, the dielectric loss dominates over the conductive losses and converges for all RRR_{Cu}. At tan $\delta < 10^{-3}$, the LGR performs better with increasing RRR_{Cu}, as the resonator is unaffected by the lossy dielectric film and eddy current losses get smaller. The loss of the CPW (green circle) is simulated by setting RRR_{Cu}=1 and we notice the loss to be conduction limited at tan δ $< 10^{-5}$. It sets a lower bound for the conductive losses because RRR_{Cu} increases above 1 at cryogenic temperatures. The CPW also appears to be more susceptible to dielectric losses in contrast to the LGR as seen by the linear dependence of the CPW over the whole simulated interval. The LGR shows higher Q_i than the CPW as tan δ increases above 5×10^{-3}. Relative high electric field in the CPW as a result of its small gap g between the conductor and the ground plane is the main reason for the relatively high dielectric losses, whereas the larger interdigitated capacitors of the LGR are spaced more widely.

We also investigated the influence of moving the groundplane closer to the MGR. Using an $\text{RRR}_{\text{Cu}} = 1$, we observe that the conduction limited Q_i of the MGR increases to above 1×10^6 and is consistent with the simulation in Fig.4.2. However, one has to be cautious because this comes with an increase in dielectric loss. The electric field intensity scales inversely with the distance between the conductor and groundplane. While the

MGR shows less conductive losses compared to the LGR, they are both affected equally by dielectric losses. In the supplementary note 4.6.2, we show that replacing the interdigitated capacitors with rectangular pads, we can further suppress dielectric loss of the lumped-element resonator.

4.5. CONCLUSION

Conductive losses are important to consider when designing superconducting high-Q and cannot always be neglected. Using simulations, we investigate conductive losses by designing a loop gap resonator (LGR) on a sapphire substrate with a Cu platform at the bottom. With a commercially available planar EM analysis software Sonnet EM, we simulate the frequency response of our device and by estimating the quality factors, we show that these losses are substantial in the LGR in contrast to CPW resonators. The conductive losses improve with increasing σ_{Cu}, which is the case after placing it in a cryogenic environment. This means that annealed oxygen-free high purity copper, with RRR>100, is preferable to be used in superconducting experiments to reduce ohmic losses induced by eddy currents. Next, we demonstrate that conductive losses can drastically be reduced by changing the geometry of the inductor i.e. replacing the loop with a meandering wire. We observe an almost tenfold reduction of the κ_i. At last, we study the importance of conductive losses in the presence of dielectric losses by adding a 10 nm dielectric thin film between the substrate and metal. The CPW is mainly limited by dielectric loss and only constrained by conduction loss at very small loss tangents i.e. $\tan\delta < 10^{-5}$. While the MGR has lower conduction losses compared to the LGR, the dielectric losses for both resonator are the same.

4.6. SUPPLEMENTARY INFORMATION

4.6.1. Q-FACTOR ESTIMATION IN SONNET

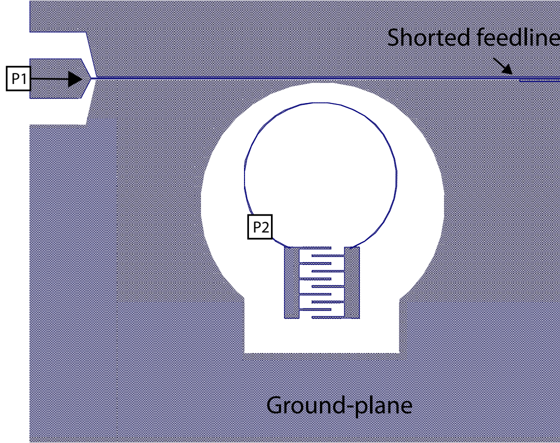

Figure 4.4: **Image of LGR created in Sonnet for estimating Q with internal port (a)**The feedline is connected to a 50 Ω source: P1, which is used for exciting and probing the resonator. A low impedance ($\approx 1 \times 10^{-7}$ Ω) port P2 is inserted at the inductor for estimating the total losses.

Running simulations in Sonnet is a time-consuming and memory intensive task, especially when a small grid size is chosen (≈ 1 μm) to ensure 50 Ω impedance of the feedline. When the resonance frequency of the resonator of interest is unknown, one can even miss the resonance, particularly for high-Q devices. We use Wisbey *et al.* [42] approach to determine Q-factor with a single frequency sweep. We start by (1) adding a second internal port as shown at the inductor of the resonator as shown in Fig. 4.4. This port should have a low impedance and need to be placed at a current maximum. (2) We short out this port by setting $Z_{o,2} = 10^{-7}$ Ω and hence we make sure that this port does not dissipate the resonators energy while probing the current that flows through it. To estimate the quality factor, we write the input impedance of the circuit as seen through the internal port P2

$$Z_{\text{in},2} = R\left[1 + \frac{j\omega L}{R} - \frac{j}{\omega CR}\right] \tag{4.4}$$

R, L and C are the resistance, inductance, and capacitance. In the high-Q limit, near $\omega \approx \omega_c$, we can Taylor expand Eq.4.4 into

$$Z_{\text{in},2} \approx R\left[1 + 2jQ(\frac{f - f_r}{f_r})\right]. \tag{4.5}$$

We can extract Q from the slope of the imaginary part of $Z_{\text{in},2}$ near $\omega \approx \omega_c$. We get

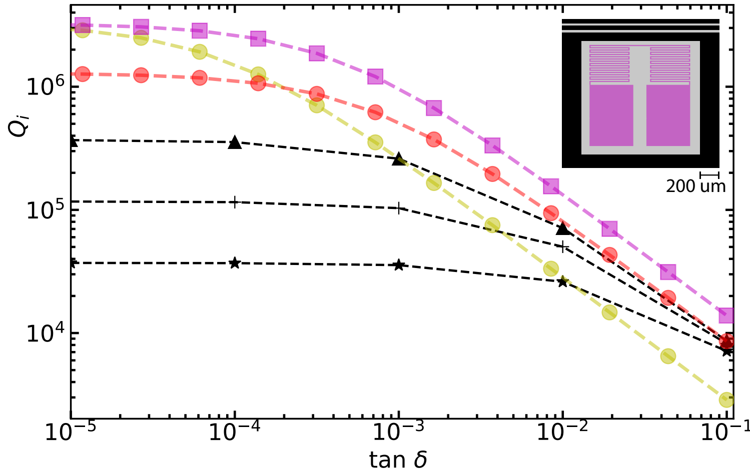

Figure 4.5: Loss simulation of improved MGR that has its interdigitated capacitors replaced with rectangular pads. Here, RRR_{Cu}=1 and the pink curve shows simulated loss with respect to loss tangent of lossy interfacial film.

$Z_{in,2}$ from the simulated resonator complex reflection response S_{11} at port 2:

$$S_{22} = \frac{Z_{\text{in},2} - Z_{o,2}}{Z_{\text{in},2} + Z_{o,2}} \tag{4.6}$$

The quality factor extracted here is the total Q including the external quality factor Q_e from the 50 Ω internal impedance of port P1. We infer the Q_i by setting the internal impedance of port 1 to $Z_{o,1} = 10^8$ Ω. This trick increases Q_e such that the $Q_{tot} \approx Q_i$. The advantage of this method is that it requires only one sweep over a wide frequency range, which drastically decreases the simulation time. An equation curve can be inserted in Sonnet so that the Q is calculated automatically.

4.6.2. REDUCING DIELECTRIC LOSS OF MGR

By abandoning the interdigitated capacitor design and replacing with rectangular pads, we increase the surface area [43]. An increased surface area of the capacitors results in lower surface charge density and thereby averting localized intense electric fields. Interdigitated capacitors are mainly used for achieving high capacitances while occupying relative little space and thus preserving chip area [44]. It is not an ideal component to be used in ultra-low loss superconducting microwave circuits. The new design is shown in the inset of Fig.4.3 and it shows similar loss as the CPW at $\tan\delta < 10^{-5}$. However, its Q_i is higher than the MGR, LGR and CPW above $\tan\delta > 10^{-5}$. Thus, the simulated loss of the lumped-element resonator with pads shows the lowest conductive and dielectric losses among the various resonators mentioned in this chapter.

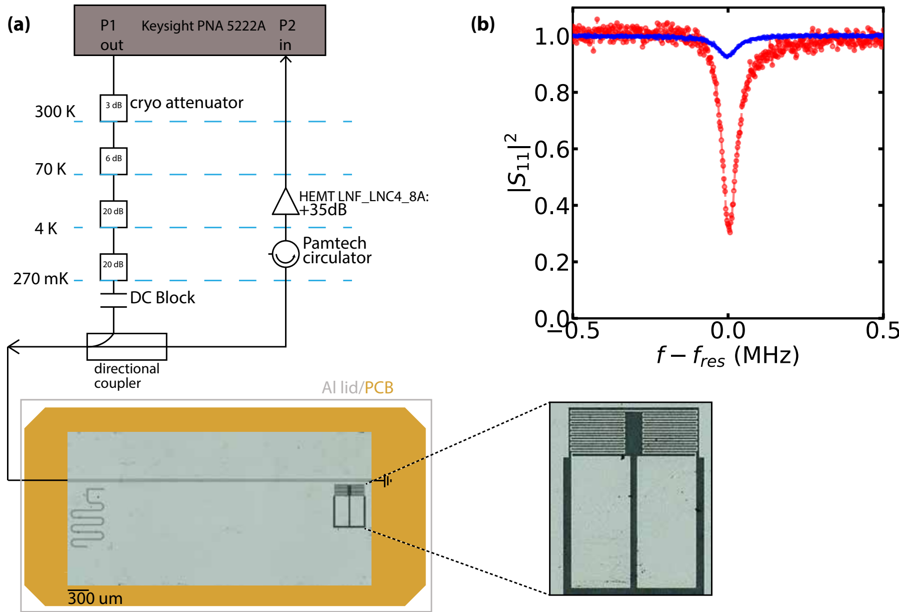

Figure 4.6: **Reflection measurement of fabricated MGR with pads and CPW at 15 mK (a)** Resonator sample shown in the optical image at the bottom is mounted on a Cu piece and thermally anchored to the 270 mK stage of a sorption cryostat (Entropy cryogenics: CRYO-H-0.4W-M-He-7). The input and output lines are connected to VNA ports (Keysight PNA 5222A). The input line consist of semi-rigid coaxial cables (CuNi) attenuated with cryo attenuators. In front of the resonator sample, a directional coupler (Pasternack PE2211-20) separates the input and output signal to circumvent input line cable reflection. The output signal is amplified with a HEMT low noise amplifier (LNF-LNC4_8C). To prevent the noise of the HEMT from leaking into the resonator, a circulator is placed before the HEMT. **(Inset)** An optical zoom of MGR with pad capacitors. **(b)**Reflection measurement of the CPW (blue) and lumped-element resonator (red) centred around their resonance frequency respectively 6.5 GHz and 7.4 GHz. Q_i is estimated to be 1.6×10^5 and 9×10^4 respectively for the MGR and CPW. This measurement is not taken at the single photon level but instead with $N > 10^6$.

4.6.3. MEASUREMENT OF CPW AND LUMPED-ELEMENT RESONATOR AT 15 MK

We have fabricated the MGR, but with pad capacitors and CPW NbTiN resonator (100 nm) on a 430 um thick sapphire substrate as shown in the optical image at the bottom of Fig.4.6a. The sample has a feedline shorted to ground with which we can probe the both resonators. The details of the fabrication process are explained in Chapter 3. The substrate is mounted on a thick Cu block and an aluminium lid is placed on top of the resonators to prevent radiation losses. Our device is cooled down to 270 mK using a sorption cryostat with 69 dB of cold attenuation between room temperature and input of the device. The output signal is transmitted lossless through a superconducting NbTiN coaxial wire to a low noise HEMT amplifier at 4K, where it is amplified and measured with a vector netwerk analyzer (VNA) at room temperature as shown in Fig.4.6. In Fig.4.6b we show the reflection response of the resonators centred around their resonance: 6.5 and 7.7 GHz for the CPW and MGR respectively. In order to compare internal losses between

resonators of different frequencies, we fit the S_{11} with [45, 46]

$$S_{11} = \alpha e^{i\phi} + (1-\alpha)\left(1 - \frac{\kappa_e}{i(\omega-\omega_r) + \frac{\kappa}{2}}\right) \tag{4.7}$$

This is the modified response of a single port reflection resonator that incorporates the finite isolation of the directional coupler and the cold circulator with parameter $\alpha e^{i\phi}$. To account for the observed weak asymmetry of the resonance profile [46], κ_e is considered to be complex i.e. $\kappa_e = |\kappa_e|e^{i\phi}$. After fitting we can deduce κ_e, κ_i and express it as Q factors ($Q = \omega/\kappa$). The internal quality factors Q_i are respectively 1.6×10^5 and 9×10^4 for the MGR resonator and CPW. Our simulation in the main text shows conduction limited Q_i of the CPW larger than 4×10^6 assuming $RRR_{Cu} > 1$. Hence, we establish that both resonators measured are by limited by dielectric losses. Our measurement shows $Q_{i_{MGR}} > Q_{i_{CPW}}$, a feature also predicted by our simulations at $\tan\delta > 1 \times 10^{-4}$ (Fig.4.5). Note that we have assumed a homogeneous 10 nm interfacial layer in our simulations with a position independent $\tan\delta$, which might not necessarily be the case for our fabricated sample.

REFERENCES

[1] F. Arute, K. Arya, R. Babbush, D. Bacon, J. C. Bardin, R. Barends, R. Biswas, S. Boixo, F. G. Brandao, D. A. Buell, *et al.*, *Quantum supremacy using a programmable superconducting processor,* Nature **574**, 505 (2019).

[2] C. Bultink, T. O'Brien, R. Vollmer, N. Muthusubramanian, M. Beekman, M. Rol, X. Fu, B. Tarasinski, V. Ostroukh, B. Varbanov, *et al.*, *Protecting quantum entanglement from leakage and qubit errors via repetitive parity measurements,* Science Advances **6**, eaay3050 (2020).

[3] J. D. Teufel, T. Donner, D. Li, J. W. Harlow, M. Allman, K. Cicak, A. J. Sirois, J. D. Whittaker, K. W. Lehnert, and R. W. Simmonds, *Sideband cooling of micromechanical motion to the quantum ground state,* Nature **475**, 359 (2011).

[4] A. Reed, K. Mayer, J. Teufel, L. Burkhart, W. Pfaff, M. Reagor, L. Sletten, X. Ma, R. Schoelkopf, E. Knill, *et al.*, *Faithful conversion of propagating quantum information to mechanical motion,* Nature Physics **13**, 1163 (2017).

[5] M. Castellanos-Beltran, K. Irwin, G. Hilton, L. Vale, and K. Lehnert, *Amplification and squeezing of quantum noise with a tunable josephson metamaterial,* Nature Physics **4**, 929 (2008).

[6] N. Bergeal, F. Schackert, M. Metcalfe, R. Vijay, V. Manucharyan, L. Frunzio, D. Prober, R. Schoelkopf, S. Girvin, and M. Devoret, *Phase-preserving amplification near the quantum limit with a josephson ring modulator,* Nature **465**, 64 (2010).

[7] P. K. Day, H. G. LeDuc, B. A. Mazin, A. Vayonakis, and J. Zmuidzinas, *A broadband superconducting detector suitable for use in large arrays,* Nature **425**, 817 (2003).

[8] A. Endo, K. Karatsu, Y. Tamura, T. Oshima, A. Taniguchi, T. Takekoshi, S. Asayama, T. J. Bakx, S. Bosma, J. Bueno, *et al.*, *First light demonstration of the integrated superconducting spectrometer,* Nature Astronomy **3**, 989 (2019).

[9] E. Flurin, N. Roch, J.-D. Pillet, F. Mallet, and B. Huard, *Superconducting quantum node for entanglement and storage of microwave radiation,* Physical review letters **114**, 090503 (2015).

[10] B. Vlastakis, G. Kirchmair, Z. Leghtas, S. E. Nigg, L. Frunzio, S. M. Girvin, M. Mirrahimi, M. H. Devoret, and R. J. Schoelkopf, *Deterministically encoding quantum information using 100-photon schrödinger cat states,* Science **342**, 607 (2013).

[11] L. Drabeck, K. Holczer, G. Grüner, and D. Scalapino, *Ohmic and radiation losses in superconducting films,* Journal of applied physics **68**, 892 (1990).

[12] B. A. Mazin, *Microwave kinetic inductance detectors,* Ph.D. thesis, California Institute of Technology (2004).

[13] J. Burnett, L. Faoro, I. Wisby, V. Gurtovoi, A. Chernykh, G. Mikhailov, V. Tulin, R. Shaikhaidarov, V. Antonov, P. Meeson, *et al.*, *Evidence for interacting two-level

systems from the 1/f noise of a superconducting resonator, Nature Communications **5**, 1 (2014).

[14] J. Lisenfeld, A. Bilmes, A. Megrant, R. Barends, J. Kelly, P. Klimov, G. Weiss, J. M. Martinis, and A. V. Ustinov, *Electric field spectroscopy of material defects in transmon qubits,* npj Quantum Information **5**, 1 (2019).

[15] R. Barends, N. Vercruyssen, A. Endo, P. De Visser, T. Zijlstra, T. Klapwijk, P. Diener, S. Yates, and J. Baselmans, *Minimal resonator loss for circuit quantum electrodynamics,* Applied Physics Letters **97**, 023508 (2010).

[16] A. Bruno, G. De Lange, S. Asaad, K. Van Der Enden, N. Langford, and L. DiCarlo, *Reducing intrinsic loss in superconducting resonators by surface treatment and deep etching of silicon substrates,* Applied Physics Letters **106**, 182601 (2015).

4

[17] M. Sandberg, M. R. Vissers, J. S. Kline, M. Weides, J. Gao, D. S. Wisbey, and D. P. Pappas, *Etch induced microwave losses in titanium nitride superconducting resonators,* Applied Physics Letters **100**, 262605 (2012).

[18] I. Rodrigues, D. Bothner, and G. Steele, *Coupling microwave photons to a mechanical resonator using quantum interference,* Nature communications **10**, 1 (2019).

[19] G. Via, G. Kirchmair, and O. Romero-Isart, *Strong single-photon coupling in superconducting quantum magnetomechanics,* Physical review letters **114**, 143602 (2015).

[20] M. F. Gely, M. Kounalakis, C. Dickel, J. Dalle, R. Vatré, B. Baker, M. D. Jenkins, and G. A. Steele, *Observation and stabilization of photonic fock states in a hot radio-frequency resonator,* Science **363**, 1072 (2019).

[21] M. Grajcar, A. Izmalkov, S. Van Der Ploeg, S. Linzen, E. Il'Ichev, T. Wagner, U. Hübner, H.-G. Meyer, A. M. Van Den Brink, S. Uchaikin, *et al.*, *Direct josephson coupling between superconducting flux qubits,* Physical Review B **72**, 020503 (2005).

[22] C. H. Van Der Wal, A. Ter Haar, F. Wilhelm, R. Schouten, C. Harmans, T. Orlando, S. Lloyd, and J. Mooij, *Quantum superposition of macroscopic persistent-current states,* Science **290**, 773 (2000).

[23] M. R. Vissers, M. P. Weides, J. S. Kline, M. Sandberg, and D. P. Pappas, *Identifying capacitive and inductive loss in lumped element superconducting hybrid titanium nitride/aluminum resonators,* Applied Physics Letters **101**, 022601 (2012).

[24] S. S. Inc., *Sonnet precision electromagnetics,* (1983).

[25] S. Meier, *Loss reduction of superconducting coplanar microwave resonators on sapphire substrates,* Bachelor Thesis (2014).

[26] H. Zou, H. Zhang, C. Song, H. Wang, and P. Wang, *Characterisation and modelling of mitered coplanar waveguide bends on silicon substrate,* International Journal of Electronics **97**, 715 (2010).

[27] R. Simons, *Coplanar waveguide circuits, components, and systems new york john wiley & sons,* (2001).

[28] V. Lahtinen and M. Möttönen, *Effects of device geometry and material properties on dielectric losses in superconducting coplanar-waveguide resonators,* Journal of Physics: Condensed Matter **32**, 405702 (2020).

[29] M. Rösch, *Development of lumped element kinetic inductance detectors for mm-wave astronomy at the IRAM 30 m telescope*, Vol. 12 (KIT Scientific Publishing, 2014).

[30] D. J. Thoen, B. G. C. Bos, E. Haalebos, T. Klapwijk, J. Baselmans, and A. Endo, *Superconducting nbtin thin films with highly uniform properties over a ∅ 100 mm wafer,* IEEE Transactions on Applied Superconductivity **27**, 1 (2016).

[31] C. Wang, C. Axline, Y. Y. Gao, T. Brecht, Y. Chu, L. Frunzio, M. Devoret, and R. J. Schoelkopf, *Surface participation and dielectric loss in superconducting qubits,* Applied Physics Letters **107**, 162601 (2015).

[32] J. M. Sage, V. Bolkhovsky, W. D. Oliver, B. Turek, and P. B. Welander, *Study of loss in superconducting coplanar waveguide resonators,* Journal of Applied Physics **109**, 063915 (2011).

[33] M. Sandberg, M. R. Vissers, T. A. Ohki, J. Gao, J. Aumentado, M. Weides, and D. P. Pappas, *Radiation-suppressed superconducting quantum bit in a planar geometry,* Applied Physics Letters **102**, 072601 (2013).

[34] A. D. Córcoles, J. M. Chow, J. M. Gambetta, C. Rigetti, J. R. Rozen, G. A. Keefe, M. Beth Rothwell, M. B. Ketchen, and M. Steffen, *Protecting superconducting qubits from radiation,* Applied Physics Letters **99**, 181906 (2011).

[35] J. Wenner, M. Neeley, R. C. Bialczak, M. Lenander, E. Lucero, A. D. O'Connell, D. Sank, H. Wang, M. Weides, A. N. Cleland, *et al.*, *Wirebond crosstalk and cavity modes in large chip mounts for superconducting qubits,* Superconductor Science and Technology **24**, 065001 (2011).

[36] D. Rosenberg, S. J. Weber, D. Conway, D.-R. W. Yost, J. Mallek, G. Calusine, R. Das, D. Kim, M. E. Schwartz, W. Woods, *et al.*, *Solid-state qubits: 3d integration and packaging,* IEEE Microwave Magazine **21**, 72 (2020).

[37] *Common cryogenic copper confusions | hydrogen properties for energy research (hyper) laboratory | washington state university,* https://hydrogen.wsu.edu/2018/03/08/common-cryogenic-copper-confusions/, (Accessed on 08/18/2021).

[38] S. Ahyoune, J. Sieiro, M. N. Vidal, and J. M. López-Villegas, *Skin effect formula for metal strips in laminated substrates,* in *2017 32nd Conference on Design of Circuits and Integrated Systems (DCIS)* (IEEE, 2017) pp. 1–4.

[39] D. P. Pappas, M. R. Vissers, D. S. Wisbey, J. S. Kline, and J. Gao, *Two level system loss in superconducting microwave resonators,* IEEE Transactions on Applied Superconductivity **21**, 871 (2011).

4

[40] C. R. H. McRae, R. Lake, J. Long, M. Bal, X. Wu, B. Jugdersuren, T. Metcalf, X. Liu, and D. P. Pappas, *Dielectric loss extraction for superconducting microwave resonators,* Applied Physics Letters **116**, 194003 (2020).

[41] G. Calusine, A. Melville, W. Woods, R. Das, C. Stull, V. Bolkhovsky, D. Braje, D. Hover, D. K. Kim, X. Miloshi, *et al.*, *Analysis and mitigation of interface losses in trenched superconducting coplanar waveguide resonators,* Applied Physics Letters **112**, 062601 (2018).

[42] D. Wisbey, A. Martin, A. Reinisch, and J. Gao, *New method for determining the quality factor and resonance frequency of superconducting micro-resonators from sonnet simulations,* Journal of Low Temperature Physics **176**, 538 (2014).

[43] Y. Chu, C. Axline, C. Wang, T. Brecht, Y. Y. Gao, L. Frunzio, and R. J. Schoelkopf, *Suspending superconducting qubits by silicon micromachining,* Applied Physics Letters **109**, 112601 (2016).

[44] J. Koch, M. Y. Terri, J. Gambetta, A. A. Houck, D. I. Schuster, J. Majer, A. Blais, M. H. Devoret, S. M. Girvin, and R. J. Schoelkopf, *Charge-insensitive qubit design derived from the cooper pair box,* Physical Review A **76**, 042319 (2007).

[45] V. Singh, S. Bosman, B. Schneider, Y. M. Blanter, A. Castellanos-Gomez, and G. Steele, *Optomechanical coupling between a multilayer graphene mechanical resonator and a superconducting microwave cavity,* Nature nanotechnology **9**, 820 (2014).

[46] M. Khalil, M. Stoutimore, F. Wellstood, and K. Osborn, *An analysis method for asymmetric resonator transmission applied to superconducting devices,* Journal of Applied Physics **111**, 054510 (2012).

5

A cryogenic accelerometer from Hz to MHz using a membrane electromechanical cavity

Technology for millikelvin cooling is crucial for the rapidly expanding field of research and applications of quantum technologies, particularly those based on recently developed cryogen-free systems. While enabling new possibilities, these systems are known to generate significant vibrational noise that can impact sensitive measurements and experiments. For quantifying this vibrational noise, it is desirable to have a sensitive broadband cryogenic accelerometer. Here, we present a cavity electromechanical device which is used as an accelerometer in a millikelvin environment with high resolution of acceleration noise. Using a heavy, high-frequency mechanical membrane, we achieve a bandwidth of up to 1 MHz and a broadband sensitivity on the order of 1 to 10 $\mathrm{mg}/\sqrt{\mathrm{Hz}}$*. We use the accelerometer to characterize the acceleration noise at the 10 mK stage of a dilution refrigerator, and to study the influence of the pulse-tube cooler on the vibrations transmitted to the sample stage. We expect that with optimizations, this technique should be capable of sub-*$\mu g/\sqrt{\mathrm{Hz}}$*, offering a unique tool for characterizing vibrations in cryogenic environments.*

This chapter is being prepared for publication as *A cyrogenic accelerometer from Hz to MHz using a membrane electromechanical cavity.* A.Sanz Mora*, S.R.Peiter* and G.A.Steele

5.1. INTRODUCTION

Advances in cryogenic systems, such as the development of cryogen-free coolers [1], have fundamentally transformed research at millikelvin temperatures. Breakthroughs and progress in for example quantum computing [2, 3], optical to microwave transducers [4, 5], cavity electromechanical devices [6, 7] and radio astronomy [8–10] would not continue at this rapid pace were it not for the reliable operation of properly designed crycoolers, capable of reaching temperatures below 4 K. Another advantage of these cryogen-free systems is that we are hedged against the scarcity and increasing liquid helium prices and are therefore able to reach liquid helium temperature in an economical manner.

However, one of the major drawbacks is that cryocoolers generate mechanical vibrations (~ 1-2 Hz) due to their internal gas pressure oscillations [11] which then can interfere with sensitive measurements [12, 13]. For example, triboelectric effects in coaxial cables can lead to voltage or current noises that can affect gates and flux biasing [14]. Furthermore, vibration in these cables can also cause the capacitance to fluctuate, resulting in unwanted phase noise in microwave signals. Mechanically compliant devices will suffer directly from any acceleration noise they experience. Measuring, characterizing, and understanding vibrational noise in millikelvin systems is therefore important for future cryogenic technological applications.

5

An attractive tool for cryogenic accelerometry is cavity electromechanics (EM) [15], where a mechanical oscillator is capacitively or inductively coupled to a superconducting microwave (MW) circuit. High-Q mechanical devices have shown to be excellent force sensor at millikelvin temperatures [16, 17], with sensitivities at resonance reaching below the standard quantum limit. In addition, they also provide a high degree of off-resonance sensitivity for frequencies below resonance, making them suitable as broadband detectors. Increasing the mass of the resonators provide higher acceleration sensitivity as the acceleration results in larger force. A heavy, high frequency cavity EM device is therefore desirable for such a cryo accelerometer.

Here, we present an electromechanical device that maintains high sensitivity over a large bandwidth and is capable of operating in a millikelvin environment. Fig.5.1 shows the electromechanical device that consists of high stress Si_3N_4 membrane capacitively coupled to a lumped-element resonator. The analysis is performed in the large cavity noise limit, where we infer an acceleration sensitivity on the order of 1 to 10 mg/$\sqrt{\text{Hz}}$ over a bandwidth of 1 MHz. When mounted on the millikelvin stage of a Bluefors dilution refrigerator, we are able to map the acceleration noise that is transmitted to the sample by the pulse-tube cryocooler. We observe many mechanical resonances within a frequency span of 200 kHz with pulse-tube on.

We can further optimize our device to increase acceleration sensitivity. For example increasing mass M, g_0, drive photons N and using a parametric amplifier will boost the sensitivity by approximately 5 order of magnitude i.e. 1 μg/$\sqrt{\text{Hz}}$. This will be useful for getting crucial sensitive, broadband vibration measurements in these extreme cryogenic environments.

5.2. DEVICE DETAILS

The electromechanical device combines a superconducting microwave resonator with a mechanical MHz resonator and is fixed with a flipchip tool, as shown in Fig.5.1a. The electrical circuit consists of a lumped-element resonator (LER) with a bare frequency $\omega_c = 2\pi\times$ 12.4 GHz and is coupled to a shorted feedline. The design approach of the microwave resonator is elaborated in Chapter 4.

Device fabrication starts with the sputtering of a 100 nm thick NbTiN film on top of a c-plane sapphire substrate. The feedline and LER are defined in a single step with electron beam lithography using positive e-beam resist (ARP-6200.13 [18]) followed by an SF_6/O_2 reactive-ion plasma etch. The sputtered NbTiN kinetic inductance is measured to be 1.2 pH/□ [19]. The mechanical resonator is a high tensile stress ($\sigma \approx 1$ GPa) stochiometric Si_3N_4 film that is suspended and clamped to a 200 μm thick silicon (Si) substrate. The Si substrate is a monocrystal with its crystal plane oriented along the <100>-direction that has a high resistivity (> 3500 Ω.cm). The film is 50 nm thin and is grown on both sides of the double side polished (DSP) Si substrate inside a low-pressure chemical deposition (LPCVD) oven. On the backside of Si substrate, a square window is etched into SiN before the whole sample is immersed in a 40% KOH solution at elevated temperature (80 ^{o}C) to etch away the Si. Depending on the etch rate, typically around 1 μm/min, we end up with a 350×350 μm square window on the front side of the Si substrate. These devices are fabricated by Norcada Inc. [20] and mass-produced on a 4" Si wafer and afterwards cleaved into 10x10 mm pieces. To enhance coupling to the electrical circuit, we coat the suspended SiN membrane with 25 nm Al+1%Si metal, and it covers an area of 300×300 μm. Details of the fabrication process of both devices are provided in chapter 3.2.

The devices are assembled using our new flipchip tool, of which we provide the details in supplementary note 5.7.2. The advantage of this flipchip tool is its modularity. It allows for swapping of the membrane device quite easily in case it cracks without the need of also replacing the microwave cavity. This tool makes the use of epoxy for clamping unnecessary, which is also unpleasant to work with and can also be a source of energy dissipation for both devices if not applied correctly. The ease of adjusting the gap distance between the two devices by turning the screws is also worth to mention. We can systematically reach sub-μm gaps between the microwave and mechanical resonator. This is confirmed optically through the observation of interference rings that start to appear after the two devices are aligned and pressed against each other. The flipchip device is mounted upside down on the mK-plate of a BlueFors (BF-LD250) dilution refrigerator and cooled down to 10 mK.

In this electromechanical configuration, the membrane is capacitively coupled to the LER. Since the effective capacitance of the circuit is increased, the cavity resonance frequency shifts down. Besides this static frequency shift, the thermal induced mechanical displacement also modulates the capacitance of the resonator and thus its resonance frequency ω_c. Below, we describe the characterization of the electromechanical circuit.

Characterization of the electromechanical device first starts with a measurement of the frequency response S_{11} of the LER with a vector network analyzer (VNA). To probe the mechanical resonator, we use optomechanical sideband pumping that leads to backaction and allows us to readout and control the mechanical response [21, 22]. This mea-

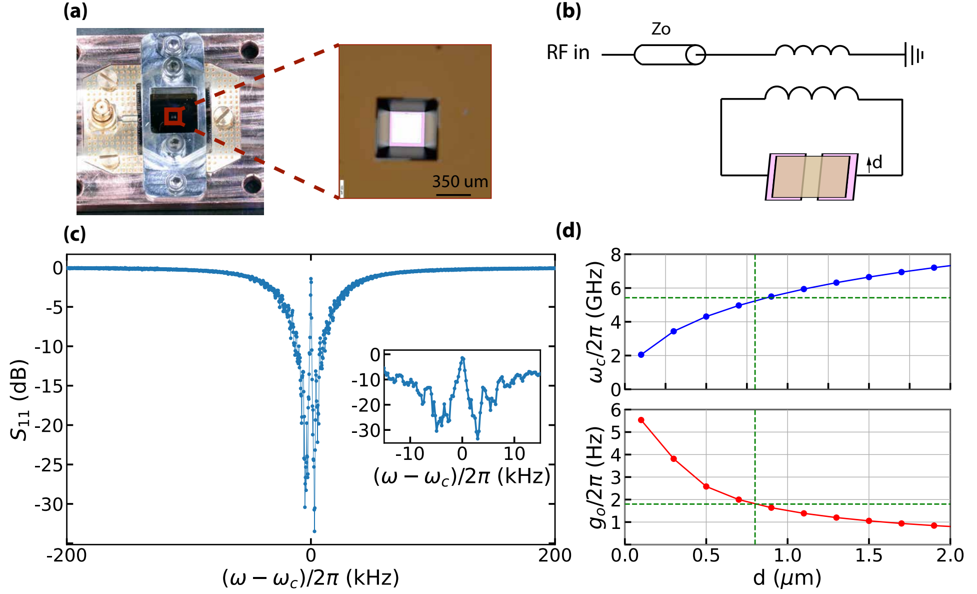

Figure 5.1: **Flipchip device characterization with fridge pulse-tube off.** **(a)** Flipchip assembled device with LER at the bottom and Al+1%Si metalized SiN square membrane flipped on top. The resonator sample is glued with GE varnish onto the Cu holder and is wire-bonded to a PCB (gold octagon). **(Zoom in)** The square membrane is aligned with the rectangular capacitor pads of the LER, before it is pressed at all its edges. In this geometry, the mechanical resonator is capacitively coupled to the LER. **(b)** Circuit equivalent of the device. The LER is inductively coupled to the feedline to increase the mechanical capacitance participation ratio, hence enhancing electromechanical coupling. We control g_o indirectly by turning the top screws of the flipchip tool and thereby altering the gap d. **(c)** OMIT response of the electromechanical device centred at $\omega_c = 2\pi\times 5.425$ GHz. We turn off the pulse-tube of the dilution refrigerator and choose a high power such that the transparency window is clearly visible. The response at low powers is noisy, which makes C estimation rather challenging. **(Inset)** A zoom-in of the optomechanical transparency window around the cavity resonance. The window rises to 0 dB and can therefore be determined that $C > 1$. **(d)** Sonnet simulation of the cavity resonance as the gap d between the metalized membrane and LER is swept. Based on the resonance frequency obtained in **(c)**, we estimate the $d \approx 800$ nm (horizontal green dashed line). **(e)** Single photon-phonon coupling g_o given by the gradient of the curve in **(d)** and multiplied by the zero-point amplitude fluctuation x_{zpf}. We estimate $g_o \approx 2\pi\times$ 2 Hz.

surement involves a strong red detuned pump at $\omega_d = \omega_c - \omega_m$, while sweeping the MW cavity with a weak probe tone. Here, ω_m is the mechanical fundamental mode and as result, a transparency window with a Lorentzian shape centred around LER resonance ω_c emerges. The full width half maximum (FWHM) and height of the Lorentzian scale linearly with the redpump strength. This phenomenon is known as optomechanical induced transparency (OMIT) [23, 24] and is caused by interference between the probe and redpump field mediated by the mechanics. A snapshot of the device OMIT response is shown in Fig.5.1c. The LER measured resonance frequency $\omega_c = 2\pi\times$ 5.425 GHz in this flipchip configuration, while the fundamental mode of mechanical resonator $\omega_m = 2\pi\times$ 953.3 kHz. For this OMIT measurement, we have chosen a high redpump strength such that the Lorentzian is clearly visible above the noisy S_{11}. On the resonance, the S_{11}

reflection of microwave cavity is given by [25]

$$S_{11}(\omega_c) = 1 - \frac{2\eta}{1+C} \tag{5.1}$$

Here, C is the coorperativity and quantifies the electromechanical coupling strength with respect to mechanical and electrical dissipation. As the height of the OMIT peak in Fig.5.1c reaches above 3 dB, we establish that the multi-photon $C > 1$. With the OMIT measurement provided, we turn to simulation to estimate the gap d and hence the single-photon electromechanical coupling. We use a commercial planar electromagnetic software Sonnet EM [26] and simulate the response of the LER in presence of a lossless metal on top of its pad capacitors. The simulation setup is explained and shown in supplementary note 5.7.1. We sweep the gap distance d from 100 nm to 2 μm and show the ω_c dependence in Fig.5.1d. For $d > 2\,\mu$m, $\omega_c/2\pi$ converges to the 12.4 GHz, which is the bare frequency of the microwave cavity shown in supplementary note 5.7.4. With the electromechanical ω_c measured, we infer $d \approx 0.8$ μm. The sub-μm gap we have obtained with the flipchip tool is remarkable considering no use of spacers and/or epoxy [27, 28]. The single phonon-photon coupling g_o is derived from the gradient of the resonance curve i.e. $(\partial\omega_c/\partial x)x_{zpf}$ (x, the mechanical displacement; and x_{zpf} the amplitude zero-point fluctuation) and is shown in Fig.5.1e. Assuming an effective mass density of 3.0 g/cm^3 of the metallized SiN membrane, we estimate x_{zpf}= 0.5 fm ($\sqrt{\frac{\hbar}{2m_{\text{eff}}\omega_m}}$) and we infer $g_o \approx 2\pi\times$ 2 Hz, almost an order of magnitude higher than Refs. [27, 29].

5.3. CAVITY NOISE

Experimentally estimating electromechanical parameters of the device requires careful calibration of C with respect to input pump power and bath temperature. However, in the presence of cavity frequency and amplitude fluctuations as noticeable near ω_c, shown in the inset of Fig.5.1c, this becomes extremely challenging. If the noise contains frequency components larger than our measurement bandwidth, the response curve of the cavity is broadened and does not follow a Lorentzian profile anymore. Therefore, it is important to characterize the properties of the noise that is impinging our device. Cavity noise in this case is a manifestation of mechanical noise that excite the mechanical resonator, hence modifying the cavity transmission and resonance frequency. To model this effect, we assume that the cavity fluctuates around its mean value. Here, we let $x \to \overline{x} + \delta x$, where $\overline{x}$ is the mean value of x and δx are random fluctuations. We assume δx to be Gaussian with zero mean and variance σ_{ω_x}. We expand the cavity resonance to lowest order and obtain[30]

$$\omega_c(x+\delta x) \approx \omega_c(\overline{x}) + \delta\omega_c(\overline{x}) \tag{5.2}$$

with the second term

$$\delta\omega_c(\overline{x}) = \frac{\partial\omega_c(\overline{x})}{\partial x}\delta x \tag{5.3}$$

is itself a Gaussian random variable with zero mean and variance, given by

$$\sigma^2_{\omega_c} = \left|\frac{\partial\omega_c(\overline{x})}{\partial x}\right|^2 \sigma_x^2 \tag{5.4}$$

The probability distribution function associated with the random variable $\delta\omega_c$ is given by

$$P(\Omega) = \frac{1}{\sqrt{2\pi\sigma^2_{\omega_c}}} e^{-\Omega^2/2\sigma^2_{\omega c}} \tag{5.5}$$

with Ω, the drawing value.

Mechanical noise in our setup is generated by the pulse-tube that comes with the dilution refrigerator and essential to keep the cooldown process running. Mechanical vibrations due to the pumps and compressor also contribute to cavity noise, but to a lesser extent. To investigate the scope of the noise introduced by the pulse-tube experimentally, we first measure 110 S_{11} traces with the pulse-tube switched off. We then repeat the same measurement with the pulse back on again. The IF-bandwidth (IFBW) of the VNA is configured to its maximum of 100 kHz, but this does not correspond to a measurement time of 10 μs per frequency point. Internal machine initialization and data recording introduces additional overhead, resulting in measurement time slightly above 10 μs per point. In Fig.5.2, we show 30 S_{11} response curves with each trace containing 5000 points. An instable microwave cavity with frequency fluctuations is observed in both cases, but manifests to greater extent with the pulse-tube on. In case of the pulse-tube is off, we find the cavity to preserve its Lorentzian response with above-mentioned measurement settings, but the cavity resonance is shifted in frequency for each trace. The resonance shift is to first order linearly proportional to the amplitude deflection of the mechanical resonator σ_x as given by Eq. (5.3). The lowest detectable frequency component of the noise is set by the total measurement bandwidth $1/\tau_m$, with τ_m the measurement time of a single trace. The upper frequency limit is given by the cavity total linewidth κ such that

$$\sigma^2_{\omega_c} = \int_{1/\tau_m}^{\kappa/2\pi} S_{\omega_c\omega_c}(f)df \tag{5.6}$$

Here, $S_{\omega_c\omega_c}$ is the frequency noise power spectral density and is simple the frequency variance per unit frequency. We quantify the frequency fluctuations for the measurement with pulse-tube off, by fitting each trace with a Lorentzian function to extract ω_c and calculate the standard deviation σ_{ω_c}. We plot a normalized histogram with the different realizations of ω_c in the inset of Fig.5.2a and show that the noise posses Gaussian distribution with $\sigma_{\omega_c} \approx 2\pi\times$ 20 kHz. From the fits, we extract coupling rates i.e. $\kappa_i/2\pi$, $\kappa_e/2\pi$ to be respectively 24 kHz and 26 kHz i.e. a critical coupled cavity with $\eta(=\kappa_e/\kappa) = 0.46$. The fitting procedure is described in supplementary note 4.6.3 of chapter 4. Averaging all the S_{11} realizations with different ω_c is essentially equivalent to the convolution of the true cavity Lorentzian reflection function with a Gaussian noise distribution and is given by

$$\overline{S_{11}(\omega)} = \int_{-\infty}^{\infty} S_{11}(\omega-\Omega)P(\Omega)d\Omega. \tag{5.7}$$

This can be thought of as inhomogeneous broadening and effectively we are averaging the response of an ensemble of cavities with different resonant frequencies. The averaged response is the black curve also shown in Fig.5.2 and is described with a Voigt function [31] that has also been reported in a diverse range of fields [32, 33].

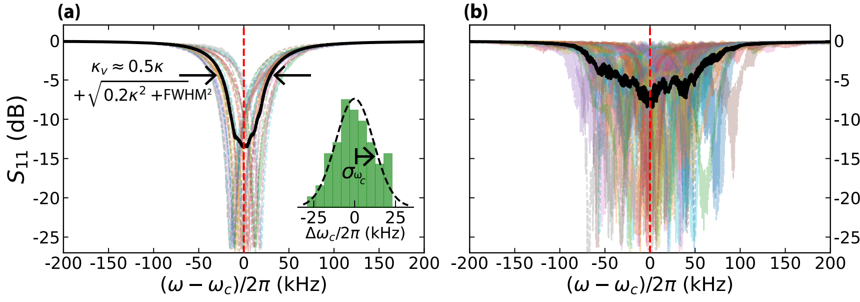

Figure 5.2: **S_{11} in the presence of cavity noise.** **(a)** Reflection response S_{11} as measured with a VNA and the pulse-tube off centred around the average cavity resonance $\overline{\omega_c} = 2\pi\times$ 5.425 GHz (red vertical dashed line). The IFBW of the VNA is set to 100 kHz and the region where the cavity resonance is located contains approximately 500 points resulting in an effective $\tau_m \approx 5$ ms. Averaging of over all S_{11} responses broadens the device response profile (black trace), with a total linewidth of 83 kHz and is expressed in κ and the FWHM of a Gaussian i.e. $\sqrt{2\ln(2)}\cdot 2\sigma_{\omega_c}$. **(Inset)** Normalised Gaussian distribution of cavity fluctuations with a corresponding fit (black). **(b)** Reflection response S_{11} with pulse-tube on. Mechanical noise introduced by the pulse-tube makes calibrating device parameters extremely difficult. The frequency components of the noise that contribute significantly fall outside measurement bandwidth $1/\tau_m$ which is then observed as a very distorted and broadened (non-Lorentzian) response.

With the pulse-tube on, the S_{11} curves of the LER gets distorted to the point where we are not able to recognize the intrinsic Lorentzian response, making it difficult to exactly pinpoint ω_c. Not only is σ_{ω_c} larger in this case, but we also find the frequency components of the noise exciting the mechanical resonator to be greater than $1/\tau_m$. Upon visually inspecting, we estimate the FWHM of the averaged trace to increase to approximately $2\pi\times$ 150 kHz, almost twice compared when the pulse-tube is off. The averaged response in both case have the centre frequency at $\overline{\omega_c} = 2\pi\times$ 5.425 GHz. It is evident that the electromechanical device is sensitive to vibrations from the environment, i.e. the mechanical resonator is susceptible to the mechanical noise mainly coming from the pulse-tube. This noise is imprinted in the cavity response profile. Hence, we use this device to quantify acceleration properties of the mechanical noise sources from the environment. In the next sections, we quantify its accelerometric parameters such as sensitivity, noise equivalent acceleration and bandwidth.

5.4. DISPLACEMENT SENSITIVITY

Typically, the acceleration and displacement of the mechanics are related by

$$\frac{X(\omega)}{a(\omega)} = -\frac{1}{\omega_m^2 - \omega^2 + i\omega\gamma_m} \tag{5.8}$$

with γ_m, the mechanical damping rate. The reflection power spectrum of the microwave cavity is exquisitely sensitive to motion-driven cavity resonance fluctuations induced by the mechanical oscillator. By using the power spectrum, we can thus calibrate the displacement spectrum of the mechanical resonator. We first record the noise power spectrum of the cavity while the pulse-tube is off. The noise power spectral density (*PSD*) S_{pp} is acquired by driving the coupled system on resonance with a microwave drive at

$\omega_\mathrm{d} = \omega_\mathrm{c}$ and measuring the reflected microwave field. The reflected signal is monitored with a spectrum analyser and averaged internally (n = 256), shown in Fig.5.3a. The measurement setup we to use to carry out this measurement is shown in supplementary note 5.7.3. We find the thermoelectrical sideband caused by thermal noise of the mechanics appearing at both side with offset 953.5 kHz from the drive. This offset corresponds to the mechanical fundamental mode ω_m, which is consistent with the OMIT measurement in Fig.5.1. We do however observe an asymmetry in the thermal sidebands which should not occur when driving on resonance as there is no dynamical backaction involved. We attribute this asymmetry to the fact that the injected microwave drive might slightly be detuned from the microwave cavity by approximately a few kHz since targeting the exact cavity resonance can be challenging in the presence of cavity noise. Alongside the thermal response, we find spurious asymmetric noise peaks spaced with an offset of 45 kHz at both side from the drive. We suspect this to be a mechanical resonance originating from one of the mechanical elements belonging to the flipchip tool.

We convert the measured powerspectrum to displacement spectral density (*DSD*) using the following expression,

$$\begin{aligned}
\frac{S_\mathrm{pp}(\omega)}{P(\omega_d)} &= \delta(\omega-\omega_d) + F(\omega-\omega_d,\Delta)\left[S^\mathrm{th}_\mathrm{xx}(\omega-\omega_d) + \frac{n'_\mathrm{add}+\frac{1}{2}}{8\kappa_e g^2|\chi_c(\omega-\omega_d,\Delta)|^2}\right] \text{ where}\\
F(\omega-\omega_d,\Delta) &= 16\kappa_e^2 g_o^2 \frac{|\chi_c(0,\Delta)|^2}{|\Gamma_c(\omega_d)|^2}|\chi_c(\omega-\omega_d,\Delta)|^2\\
\chi_c(\omega,\Delta) &= \frac{1/2}{-\mathrm{i}(\omega-\Delta)+\kappa/2}\\
\Gamma_c(\omega) &= \frac{\kappa_i-\kappa_e+2\mathrm{i}(\omega-\omega_c)}{\kappa_i+\kappa_e+2\mathrm{i}(\omega-\omega_c)}\\
n'_\mathrm{add} &= \left(\frac{1}{\eta_l}-1\right)\frac{1}{2}+\frac{1}{\eta_l}\left(\bar{n}_\mathrm{A}+\frac{1}{2}\right)
\end{aligned} \tag{5.9}$$

Here, $\Delta = \omega_\mathrm{d} - \omega_\mathrm{c}$. The δ-function in the first term on the right represents the drive tone. The second term contains the displacement amplitude $S^\mathrm{th}_\mathrm{xx}$ of the mechanical oscillator due to thermal noise and the imprecision noise $S^\mathrm{imp}_\mathrm{xx}$ added by the readout chain. Here, χ_c, Γ_c are the cavity susceptibility and reflection coefficient, respectively. The thermal photon noise quanta n'_add arise from the input noise ($\bar{n}_\mathrm{A}$) inherent to the LNA and the finite loss (η_l) between the sample and LNA. We obtain Eq. (5.9) by solving the quantum Heisenberg-Langevin equations of motions for field and displacement amplitude of the mechanical oscillator and cavity, respectively and subsequently computing the magnitude in the Fourier domain. By normalising the *PSD* with the measured drive power $\mathrm{P}(\omega_\mathrm{d})$ at the spectrum analyser, the conversion term $\mathrm{F}(\omega-\omega_\mathrm{d},\Delta)$ becomes independent of the intracavity photon number N and therefore a rigorous input power calibration is not necessary. The full derivation is provided in chapter 2.

In the presence of cavity noise, the measurement bandwidth determines whether Eq. (5.9) can be used to obtain $S^\mathrm{tot}_\mathrm{xx}$ from measured powerspectrum directly, considering $\chi_c(\omega,\Delta)$ and $\Gamma_c(\omega_d)$ become time dependent. Here, the spectral measurements are taken

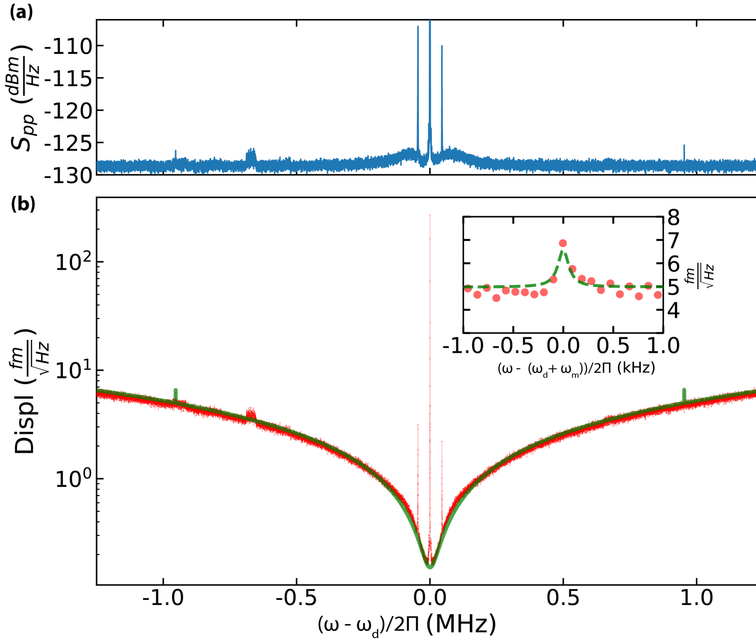

Figure 5.3: **Calibrating broadband sensitivity with pulse-tube off.** (a) Measured power spectral density S_{pp} internally averaged with the spectrum analyser (n = 256), after injection of a microwave tone at the cavity resonance $\omega_d = \omega_c$. The measurements are taken with a resolution bandwidth of 100 Hz. The thermal sidebands of the mechanics appear at $\omega_m = 2\pi \times$ 953.5 kHz with its mechanical linewidth $\gamma_m = 2\pi \times$ 120 Hz. The exact origins of the spurious speaks spaced at offset 45 kHz are yet unknown, but we suspect the mechanical resonance of the flipchip tool to be responsible. The step-like noise added on the background located to the left of the drive comes from low noise amplifier (LNA) located on the 4K stage. (b) Broadband displacement sensitivity $\sqrt{S_{xx}}$ (red) obtained by converting S_{pp} accordingly and taking the cavity frequency noise into account. We reproduce $\sqrt{S_{xx}}$ (green) with a Monte Carlo simulation of the cavity noise and estimated g_o and N. We calculate a average intracavity photons $\langle N \rangle = 1.6 \times 10^6$ for this measurement and obtain the mechanical mode temperature T_m = 300 mK. Displacement sensitivity increases as we move closer to ω_c and is limited by the imprecision noise $S_{xx}^{imp}(\omega)$ that is proportional to $(\omega/\kappa)^2$. **(Inset)** Zoom-in of the electrothermal sideband on the right (blueside) of the drive.

with a measurement bandwidth of 100 Hz which is twice the total measurement time of the VNA in Fig.5.2. We assume that the noise also falls within spectrum analyser bandwidth as it did in our VNA response measurements considering the minor difference in total measurement time τ_m. To determine the total displacement density S_{xx}^{tot} from the measured power spectrum while taking into account cavity noise, we adopt a numerical approach based on Monte Carlo simulations. We create an ensemble of different realisations of $F(\omega, \Delta)$ by randomly drawing ω_c from a Gaussian distribution $P(\sigma_{\omega_c}, \Omega)$. We obtain $\langle S_{xx}^{tot} \rangle_{256}$ by normalizing the measured $[\langle S_{pp}(\omega)\rangle / \langle P(\omega_d)\rangle]_{256}$ with the simulated ensemble average of $\langle F(\omega - \omega_d, \Delta)\rangle_{256}$, as shown in Fig.5.3b. As expected, the displacement sensitivity increases (low S_{xx}) as we approach ω_c. Here, the microwave cavity acts as a low pass filter with its attenuation proportional to $(\omega/\kappa)^2$

We then perform a fit with no free parameters using Eq.(5.9) to estimate the mechan-

ical mode temperature T_m. The fit requires the external coupling κ_e, mechanical decay rate γ_m, single phonon-photon coupling g_0, the intra cavity photon number N, T_m and the imprecision noise. Unfortunately, the last three parameters are unknown and we thus need to make a considered estimate. The LNA input noise is the biggest contributor to the imprecision noise in this measurement scheme. The imprecision noise is then calculated by assuming an LNA input noise temperature T_N = 2.5 K [34] and 3 dB loss between the sample and LNA. Notice that the fit also requires the multi phonon-photon coupling g that depend on the number of intracavity photons N. We determine N by estimating the input drive power at the device P_{in} using the measured drive power P_d at the spectrum analyser, LNA input noise temperature T_N and the cavity reflection response $\Gamma_c(\omega)$. This is detailed in supplementary note 5.7.5. For a reflection cavity, N is given by

$$N = \frac{\kappa_e}{\Delta^2 + \frac{\kappa^2}{4}} \frac{P_{in}}{\hbar\omega_d} \tag{5.10}$$

5

with $\Delta = \omega_d - \omega_c$. We repeat the calculation of N and subsequently S_{xx}^{tot} for randomly drawn ω_c to imitate the noise that the cavity experiences and show the computed ensemble average in Fig.5.3 with the green curve. It follows the measured displacement spectral density and, for T_m = 300 mK, the simulated thermal peak matches the measured electrothermal response. We point out that our calculation of T_m depend strongly on our estimation of σ_{ω_c}. Cavity noise alters the cavity susceptibility $\chi(\omega, \Delta)$ and reflection function $\Gamma_c(\omega)$ and results in a fluctuating internal photon occupation N. Because the reflection measurements with the VNA were fast enough to resolve the true response of the cavity with the pulse-tube off, we assume that our estimates of κ, κ_e and σ_{ω_c} are reliable. Our claim of the mode temperature is thus well contemplated.

5.5. ACCELEROMETRIC SENSING

With our flipchip device, we are also able to measure the acceleration of mechanical structures that are excited by the pulse-tube while it is on. Now that we have calibrated the displacement sensitivity of the mechanical oscillator, we can proceed by estimating the input acceleration to the device caused by the pulse-tube. The extent to which we can quantify this parameter, depend on the sensitivity, bandwidth and imprecision noise of our device. The sensitivity is quantified by the noise equivalent acceleration (NEA) is given by [35]

$$\text{NEA} = \sqrt{a_{th}^2 + a_{det}^2 + a_{ba}^2} \tag{5.11}$$

The first term is the thermal induced motion of the mass and is the most sensitive on mechanical resonance ω_m with

$$a_{th} = \sqrt{\frac{4k_b T_m \omega_m}{m_{eff} Q_m}} \tag{5.12}$$

The two remaining terms arise from the readout displacement noise and the backaction from the measurement itself. We deduce the NEA by first monitoring the power spectrum with pulse-tube on and extract S_{xx}^{tot} using the same procedure described in

the previous section. Note that this measurement is performed by driving the cavity on resonance and therefore the term a_{ba} that comes from dynamical backaction noise is neglegible. Also, the same measurement setup and input pumppower P_{in} are used to drive the device as in the scenario with the pulse-tube off. With the pulse-tube on, we measure a 3 dB higher pumppower P_{d} at the spectrum analyser. This is expected because the pulse-tube causes σ_{ω_c} to increase, confirmed by our measurement shown in Fig.5.2b. This effectively makes the cavity appear more reflective. Based on the difference in P_{d}, we deduce an increase of σ_{ω_c} to approximately 50 kHz consistent with our estimate in section 5.3. We show and compare the displacement noise in Fig.5.4a and notice sharp resonances emerging close to ω_{d} in case the pulse-tube is on. We also witness an increase of the noisefloor up to 100 kHz and it is within this interval where most of the spikes are located. Here, the pulse-tube is most likely able to excite modes beyond its 1.4 Hz step-like excitation. The spikes decrease in amplitude as we move away from the drive and completely diminish at frequencies above 160 kHz. These are mechanical resonances of either the stiff flipchip components or mK-plate given the kHz range they appear at. Another candidate for causing these mechanical resonances, is the semi-rigid coaxial cable attached to the device at one end and the mK-plate at the other. We also observe an increase in thermal amplitude of the mechanical resonator by approximately an order of magnitude, effectively making the mechanical mode appear hotter.

The NEA of the electromechanical device is obtained by normalising the displacement noise with the mutual susceptibility $\epsilon_{\mathrm{m}}(\omega)$. The relation is given by

$$\begin{aligned} S_{\mathrm{aa}}(\omega) &= \frac{\hbar\omega_m}{m_{\mathrm{eff}}|\epsilon_m(\omega)|^2} S_{\mathrm{xx}}^{\mathrm{tot}}(\omega) \quad \text{with} \\ \epsilon_m(\omega) &= \frac{\chi_{\mathrm{m}}(\omega)}{1-4g^2\chi_{\mathrm{m}}(\omega)[\chi_{\mathrm{c}}(\omega;\Delta)-\chi_{\mathrm{c}}^*(-\omega;\Delta)]} \end{aligned} \tag{5.13}$$

The mutual susceptibility reduces to the mechanical susceptibility in case of resonant driving and no cavity noise. The NEA is shown in Fig.5.4b. It is limited by a_{det} up to 800 kHz, as a result of the input noise T_N of the LNA and is identified by the almost flat acceleration noise density. Close to the mechanical resonance as shown in Fig.5.4d, the device is limited by thermal noise of the mechanical resonator with maximum sensitivity $a_{\mathrm{th}} = 4\ \mu g/\sqrt{\mathrm{Hz}}$ with the pulse-tube off. As expected, a_{th} increases when the pulse-tube is on due to the added mechanical noise. At lower frequencies, as shown in Fig.5.4c, the spurious mechanical resonances show strikingly large acceleration, in particular at 45 kHz. This sharp resonance is present even with the pulse-tube off, where it is excited via vibrations of the surrounding. By the addition of pulse-tube vibrations, it gets enhanced.

We investigate the NEA also at lower frequencies, i.e. < 1 kHz. At these frequencies, we use a higher frequency resolution than the measurements shown above, resulting in a longer measurement time τ_m. We carry out a time domain measurement, where the measurement time and sampling rate is set such that we obtain a resolution bandwidth of 1.4 Hz. In Fig.5.5, we show the averaged NEA of 2000 time domain traces and immediately notice a series of sharp peaks that are larger in acceleration than the mechanical resonances located at the kHz range. The highest peak is located around 30 Hz as shown in the inset of Fig.5.5 and is consistent with mechanical resonance of fridge frame reported by Bluefors [36]. They observed similar mechanical resonances below 200 Hz,

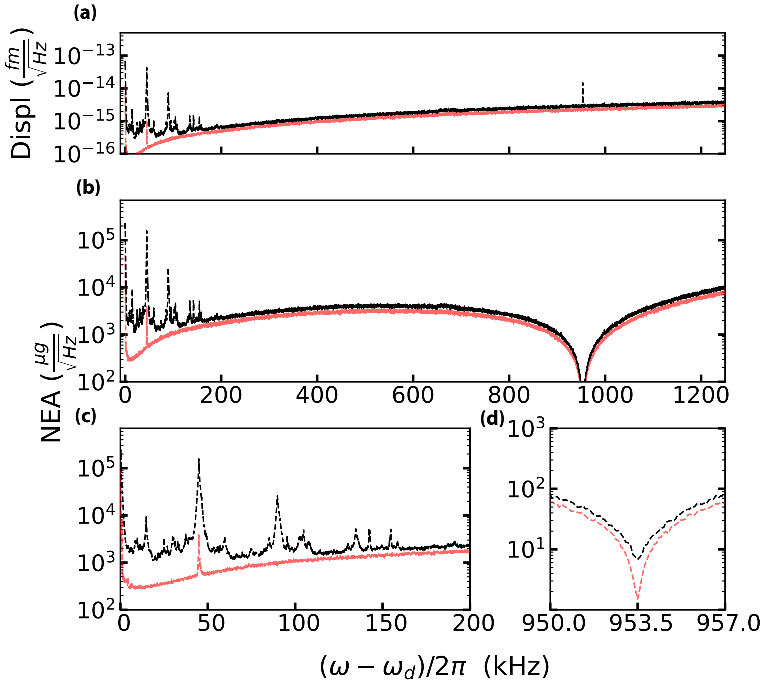

Figure 5.4: **Broadband accelerometric performance of electromechical device (a)** Broadband displacement spectral density with pulse-tube off (red) and on (black) centred at drive $\omega_{\mathrm{d}} = \omega_{\mathrm{c}}$. Alongside an increase of the thermal sideband amplitude at offset ω_{m} from the drive, the pulse-tube also causes many mechanical resonances to emerge close to ω_{d} . **(b)** Noise equivalent acceleration (NEA) with zoom in near ω_{d} and $\Delta = \omega_{\mathrm{m}}$ in **(c)** and **(d)**, respectively. Sharp peaks are clearly visible within $\Delta = \omega_{\mathrm{m}}$ interval from the centre. Regarding acceleration, the device is the most sensitive at a mechanical resonance from the drive as seen by sharp drop in amplitude.

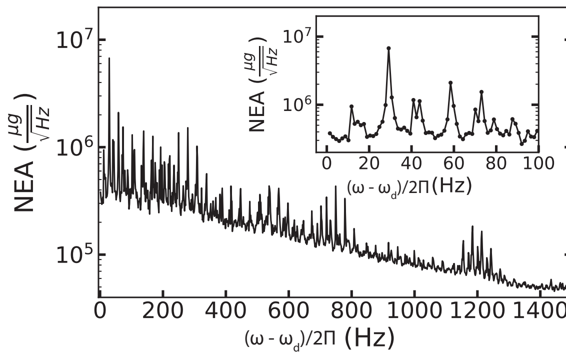

Figure 5.5: **sub-kHz NEA of electromechanical device.** NEA with < 2 Hz frequency resolution obtained with time domain measurement. Sharp spikes appearing below 200 Hz are due to the mechanical resonances of the fridge support. **(Inset)** A zoom-in of the NEA below 100 Hz with the highest resonance located at 30 Hz.

which they have attributed to the fridge supports.

5.6. DISCUSSION

We have fabricated a cryogenic accelerometer which combines a superconducting lumped-element resonator and a high-tensile stress Si_3N_4 square membrane, using a custom-made flipchip tool. We found this new flipchip tool to be favourable compared to other techniques [27, 28] as it makes use of the epoxy and spacers redundant, and allows us to consistently reach sub-micron gaps. It is very modular, as it allows for exchanging damaged mechanical or microwave devices fast and gently, and therefore increases fabrication to measurement throughput.

We have cooled down this device to 15 mK after which we then measured OMIT through red sideband pumping and found that we operate in the resolved sideband regime ($\omega_m/\kappa \approx 40$). In the frequency response measurements of the electromechanical cavity, we observe fluctuations in cavity resonance frequency, which makes it difficult to calibrate electromechanical parameters accurately. This cavity noise is a result of vibrations from the environment that is transferred to the sample and couples to the mechanical resonator. With the pulse-tube off and recording many successive S_{11} measurements, we find that the averaged response is broadened and accurately described by the Voigt function, with the full width half maximum (FWHM) given by $\kappa_v = 0.5\kappa + \sqrt{0.2\kappa^2 + 2\ln(2)\cdot(2\sigma_{\omega_c})^2}$. The cavity noise posses a Gaussian distribution with $\sigma_{\omega_c} \approx 2\pi\times$ 20 kHz, which more than doubles when the pulse-tube is switched on.

The calibration of the displacement spectrum is performed with the measured noise power spectrum upon resonantly driving the cavity with the pulse-tube switched off. Using Monte Carlo sampling, we simulate cavity noise by generating an ensemble of cavity susceptibilities $\chi_c(\omega,\Delta)$ with random ω_c. The ensemble average is used to convert the measured $\langle S_{\mathrm{pp}}\rangle$ into $\langle S_{\mathrm{xx}}\rangle$. Subsequently, normalising $\langle S_{\mathrm{xx}}\rangle$ by the susceptibility of the mechanical oscillator, we find the noise equivalent acceleration (NEA) for our electromechanical device. At the mechanical resonance ω_{m} the device has the highest sensitivity (low NEA) of 4 μg/$\sqrt{\mathrm{Hz}}$ and is limited by thermal noise. At frequencies below ω_{m}, we find acceleration sensitivities in the range of 1 and 10 mg/$\sqrt{\mathrm{Hz}}$. Since the microwave cavity acts as a filter, the NEA decreases (high sensitivy) as we move closer to the cavity resonance ω_{c}. Here, we are limited by the input noise of the low noise amplifier.

With the pulse-tube on, sharp mechanical resonances appear within a 200 kHz interval from the resonant drive. We believe these kHz mechanical noise to be originating from the stiff flipchip metal components, semi-rigid coaxial cable attached to the device or the chip itself. The mechanical thermal noise amplitude also increases, making the mechanical mode to appear hotter at cost of the acceleration sensitivity. We also investigate the scope of mechanical noise below 1 kHz with frequency resolution of 1.4 Hz by performing time-domain IQ measurements. By computing the *PSD* of the IQ traces, we find yet a collection of sharp mechanical spikes, with the highest located at 30 Hz. The mechanical noise peaks visible below 200 Hz are consistent with the mechanical resonances of the support structures of the fridge as reported also by BlueFors.

The calibration of the mechanical mode temperature, displacement and acceleration noise spectra done in this chapter depend on the intracavity photon number N.

Correctly calibrating N relies on our estimation of cavity parameters and σ_{ω_c}. In our case, we have used a single noise power spectral measurement that is averaged for 256 times. We then simulate an ensemble of cavity susceptibilities and responses with random ω_c to calibrate N from the measured drive power. Hence, we emphasize that this method is as good as our characterization and knowledge of the cavity noise. Regardless of this issue, the analytical equations used to describe to derive the broadband displacement and acceleration noise agrees with our expectation of an electromechanical device operating in the resolved sideband regime.

5.7. SUPPLEMENTARY INFORMATION

5.7.1. SONNET g_o SIMULATION

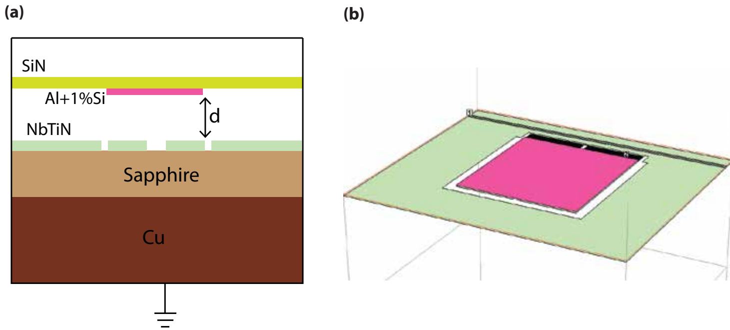

Figure 5.6: **Sonnet simulation model. (a)** Colour layering indicate material and device is enclosed in grounded lossless metal box. Here, internal losses are omitted and d is swept in order to determine g_o. **(b)** 3D schematic device model in Sonnet EM.

5

We use a commercial electromagnetic software Sonnet EM [26] to simulate and estimate the single photon-phonon coupling g_o. The Sonnet simulations starts by designing the lumped-element resonator that we already discussed in chapter 4. We assign NbTiN superconducting properties to the metal of LER and groundplane i.e. L_s=1.3pH/□ and R_s=0. The LER sits on a 430 μm sapphire substrate with ϵ_r = 10. We place a 50 nm SiN layer metallized with 25 nm Al+1%Si at a distance d above the pad capacitors of the LER. At this thickness of the Al+1%Si, we assume a kinetic inductance of 2 pH/□ [37]. It now mimics the assembled electromechanical device. The device enclosed in a grounded lossless metallic box and the feedline is connected to a port with its internal impedance set to 50 Ω. A cross-section of the material composition in the simulation domain is shown in Fig.5.6. We exclude internal losses from this simulation, since we are only interested in detecting the resonance frequency of the device with respect to gap distance d. However, no internal losses result in the LER being overcoupled and, as a consequence, detection of the cavity resonance can be problematic if the frequency steps are not chosen small enough. Fine frequency sweeps, on the other hand, are time-consuming and memory intensive. To circumvent this, we use the approach discussed in Ref. [38] and chapter 4 by inserting a low impedance port 2 in the meandered inductor of the LER. This allows for performing a coarse frequency sweep without missing the resonance of the overcoupled electromechanical device. We vary d and plot the resonance frequencies in Fig.5.1d. At large d, the participation ratio of the mechanical capacitance is small and the LER natural resonance converges to its bare resonance $\omega_c = 2\pi\times$ 12.4 GHz.

5.7.2. FLIPCHIP SCHEMATIC

The flipchip tool, as shown in Fig.5.7, is placed on a thick Copper piece that is machined to hold the PCB and the sapphire substrate. The PCB is anchored via screws to the Cu holder, while the sapphire substrate is fixed with GE Varnish. Next, we flip the SiN membrane device on top of the resonator sample, which is wirebonded to the PCB. A po-

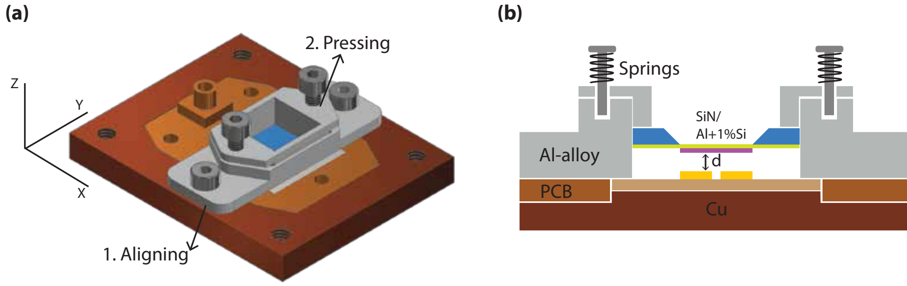

Figure 5.7: **3D Design layout of flipchip tool.** **(a)** flipchip tool used for assembling the electromechanical device. The alignment and clamping are carried out with the tools indicated arrow 1 and 2. **(b)** 2D Cross-section taken at the middle of the flipchip. By turning the screws, we can change d, hence g_o.

sitioner indicated with arrow 1 is used to align the square membrane to the capacitor pads of the LER. We are able to inspect the alignment through the opening in the middle of the positioner that has the same lateral dimensions as the flipped Si chip i.e. 10×10 mm. After a coarse alignment, we proceed with finer alignment by loosely fixing the positioner with screws to the Cu holder. Here, we are still able to move the membrane window ± 250 μm over the x−y plane after which we then completely tighten the screws to fix its position with respect to the microwave device. Note that we make use of an optical microscope in the alignment process while the positioner, containing the membrane device, is moved with tweezers. For z-control, we use a presser that has the shape of a hollow square cage as indicated with arrow 2. It fits precisely in the opening of the positioner, and has a 1 mm wide contact area that applies pressure to all 4 edges Si frame, as shown in Fig.5.7b. By turning the screws attached to it, we are able to consistently reach gap spacings d below a micron. We confirm this visually through the appearance of interference fringes as it is difficult to accurately measure d due to geometrical limitations of our optical setup. We also insert springs around the thread of the screws to prevent it from getting stuck due to thermal contraction during a cooldown cycle. Although it is tempting to fully tighten the screws to reach smaller gaps of several hundred nanometres, we remark that one should proceed with caution. We noticed that this causes the membrane to break within one cooldown cycle. Whether this happens during loading or the cooldown itself, is yet unclear. Therefore, we do not fully tighten both screws (≈ 2.5 turns) and ensure that the springs are not fully compressed before cooling down.

5.7.3. MEASUREMENT SETUP

All the experiments reported in this chapter were performed in a dilution refrigerator operating at a base temperature close to T_b = 7 mK. A schematic of the experimental setup and external configurations used in the different measurements is shown in Fig.5.8. The flipchip tool containing our PCB and the fabricated electromechanical device is mounted upside down on the mK-plate of a Bluefors dilution refrigerator (LD250) and its input line connected to a semi-rigid coaxial line. The device is measured in a reflection geometry, and therefore the input and output signals were split via a directional coupler. The output signal went into a cryogenic low noise amplifier for their particu-

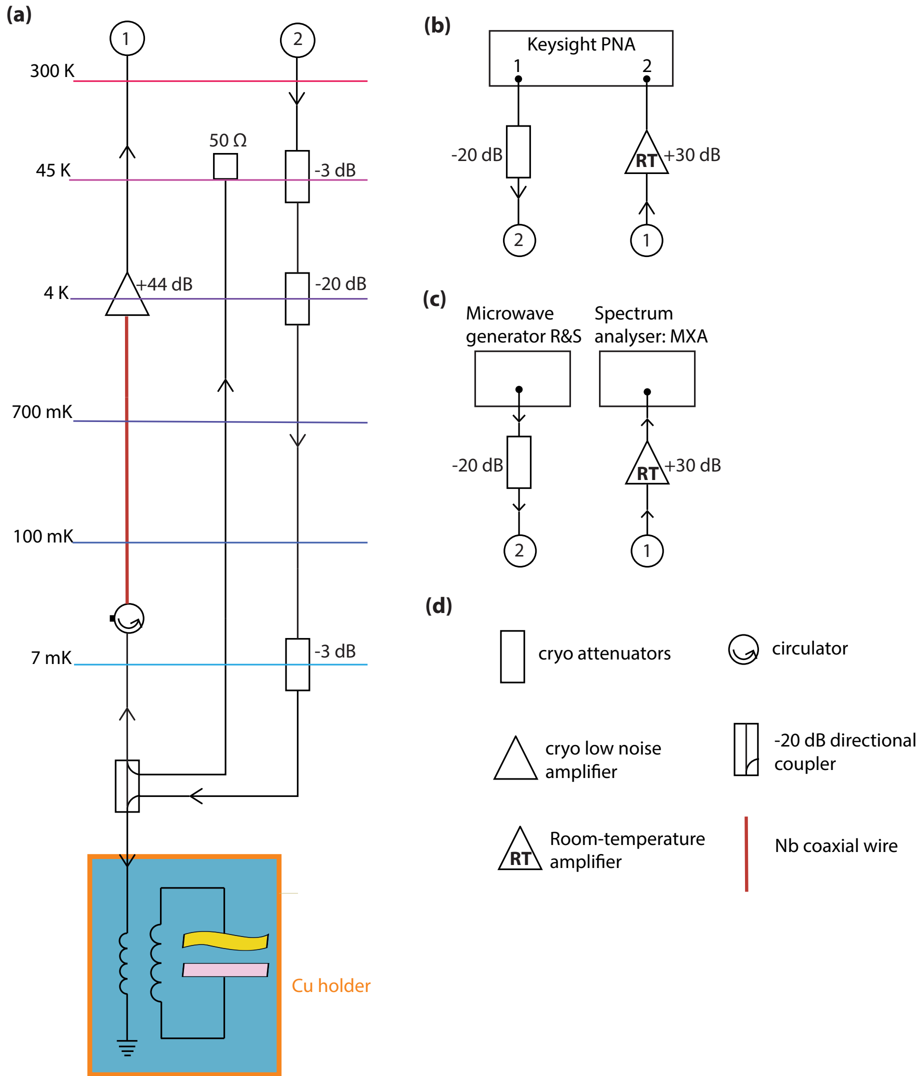

Figure 5.8: **Schematics of the measurement setup used for monitoring OMIT (b) and power spectral densities (c).**

lar frequency range. The input lines were attenuated in order to balance the thermal radiation from the line to the base temperature of the fridge.

5.7.4. BARE CAVITY MEASUREMENT

Before placing the SiN membrane device on the resonator sample, we first performed a S_{11} reflection measurement of the standalone LER. This measurement provides us the

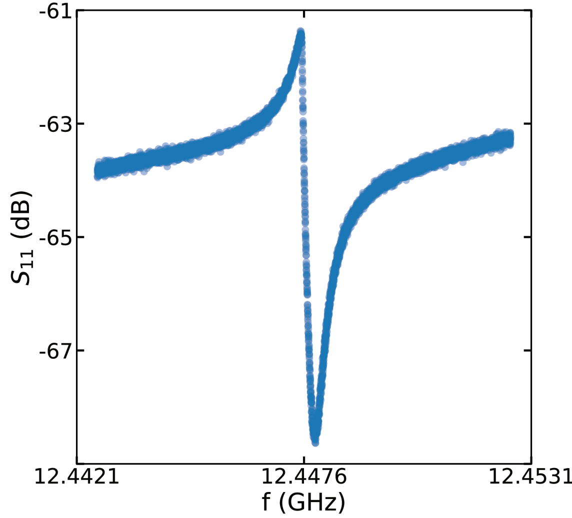

Figure 5.9: **Reflection response of bare LER.** The response has a Fano shape characterised by an asymmetric profile with resonance frequency located at 12.4 GHz. Fitting and estimating cavity parameters in case of Fano requires the careful calibration of S_{11} with an open and load.

bare ω_c that is used to calibrate the Sonnet simulations for estimating the gap d in presence of a flipped membrane. The observed LER has a resonance frequency of 12.4 GHz as shown in Fig.5.9 and agrees within 5% with the Sonnet simulations. This measurement however, shows an asymmetric S_{11} response, and therefore we are not able to reliably extract the internal and external losses of the LER. In literature [39], this is known as a Fano response and is a result of interference between microwave field reflected of the cavity and cable resonances originating from input and output coaxial lines.

5.7.5. ESTIMATING INTRA CAVITY PHOTONS N

Estimating the intra cavity photons N in presence of cavity noise requires a non-standard approach. In our measurement, we drive the cavity on resonance and the power of the reflected field is then amplified and measured with a spectrum analyser. For convenience, we name this power $\mathrm{P_d}$. The measurement is repeated for 256 times and averaged. Since the cavity is subjected to frequency noise, N also fluctuates. To get an estimate of N, we need to determine the power $\mathrm{P_{in}}$ at the input of the device. By offsetting the effective gain of the output line from the averaged drive power $\mathrm{P_d}$, we obtain the power $\mathrm{P_{out}}$ right after the output of the device. We use the convoluted cavity response function $\overline{S_{11}(\omega)}$ as expressed in Eq.(5.7) to obtain $\mathrm{P_{in}}$ from $\mathrm{P_{out}}$. So $\mathrm{P_{in}}$ can be calculated by

$$P_{\mathrm{in}} = \frac{1}{\overline{\overline{S_{11}(\omega)}}} \frac{P_d}{A} \tag{5.14}$$

where, A is the effective gain of the output line. The method for estimating A is highlighted in the supplementary note of chapter 6.

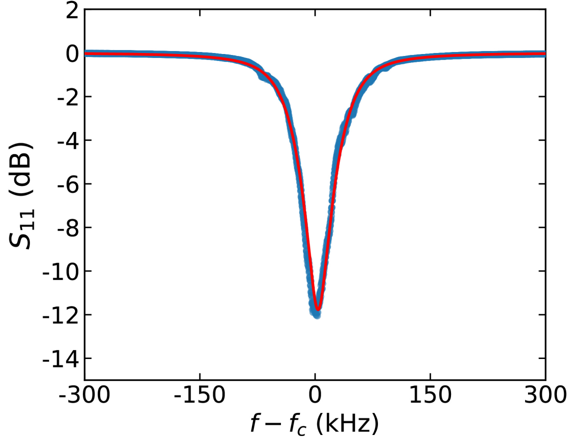

Figure 5.10: $\overline{S_{11}(\omega)}$ (blue) that is the average reflection response from the electromechanical device taken over 90 measured S11 traces and fitted with a Voigt function (red).

5

We attain $\overline{S_{11}(\omega)}$ through the measurement discussed in Fig.5.2. The average response is fitted to a Voigt function given by

$$\begin{aligned}\overline{S_{11}(\omega)}' &= \frac{B\,\mathrm{Re}\left[\mathrm{w(z)}\right]}{2\pi\sigma_{\omega_c}} \quad \text{where} \\ z &= \frac{\omega + \mathrm{i}\kappa/2}{\sigma_{\omega_c}\sqrt{2}} \\ w(z) &= e^{-z^2}\mathrm{erfc}(-\mathrm{iz})\end{aligned} \tag{5.15}$$

and is shown in Fig.5.10. With P_{in} known, the intracavity photons N is estimated with Eq.(5.7.5).

REFERENCES

[1] R. Radebaugh, *Cryocoolers: the state of the art and recent developments,* Journal of Physics: Condensed Matter **21**, 164219 (2009).

[2] F. Arute, K. Arya, R. Babbush, D. Bacon, J. C. Bardin, R. Barends, R. Biswas, S. Boixo, F. G. Brandao, D. A. Buell, *et al.*, *Quantum supremacy using a programmable superconducting processor,* Nature **574**, 505 (2019).

[3] A. Kandala, A. Mezzacapo, K. Temme, M. Takita, M. Brink, J. M. Chow, and J. M. Gambetta, *Hardware-efficient variational quantum eigensolver for small molecules and quantum magnets,* Nature **549**, 242 (2017).

[4] R. W. Andrews, R. W. Peterson, T. P. Purdy, K. Cicak, R. W. Simmonds, C. A. Regal, and K. W. Lehnert, *Bidirectional and efficient conversion between microwave and optical light,* Nature physics **10**, 321 (2014).

[5] M. Forsch, R. Stockill, A. Wallucks, I. Marinković, C. Gärtner, R. A. Norte, F. van Otten, A. Fiore, K. Srinivasan, and S. Gröblacher, *Microwave-to-optics conversion using a mechanical oscillator in its quantum ground state,* Nature Physics **16**, 69 (2020).

[6] A. Reed, K. Mayer, J. Teufel, L. Burkhart, W. Pfaff, M. Reagor, L. Sletten, X. Ma, R. Schoelkopf, E. Knill, *et al.*, *Faithful conversion of propagating quantum information to mechanical motion,* Nature Physics **13**, 1163 (2017).

[7] J. D. Teufel, T. Donner, D. Li, J. W. Harlow, M. Allman, K. Cicak, A. J. Sirois, J. D. Whittaker, K. W. Lehnert, and R. W. Simmonds, *Sideband cooling of micromechanical motion to the quantum ground state,* Nature **475**, 359 (2011).

[8] A. Endo, K. Karatsu, Y. Tamura, T. Oshima, A. Taniguchi, T. Takekoshi, S. Asayama, T. J. Bakx, S. Bosma, J. Bueno, *et al.*, *First light demonstration of the integrated superconducting spectrometer,* Nature Astronomy **3**, 989 (2019).

[9] P. Ade, M. Aravena, E. Barria, A. Beelen, A. Benoit, M. Béthermin, J. Bounmy, O. Bourrion, G. Bres, C. De Breuck, *et al.*, *A wide field-of-view low-resolution spectrometer at apex: Instrument design and scientific forecast,* Astronomy & Astrophysics **642**, A60 (2020).

[10] E. Taralli, C. Pobes, P. Khosropanah, L. Fàbrega, A. Camón, L. Gottardi, K. Nagayoshi, M. Ridder, M. Bruijn, and J. Gao, *Ac/dc characterization of a ti/au tes with au/bi absorber for x-ray detection,* Journal of Low Temperature Physics **199**, 102 (2020).

[11] T. Tomaru, T. Suzuki, T. Haruyama, T. Shintomi, A. Yamamoto, T. Koyama, and R. Li, *Vibration analysis of cryocoolers,* Cryogenics **44**, 309 (2004).

[12] E. Olivieri, J. Billard, M. De Jesus, A. Juillard, and A. Leder, *Vibrations on pulse tube based dry dilution refrigerators for low noise measurements,* Nuclear Instruments and Methods in Physics Research Section A: Accelerators, Spectrometers, Detectors and Associated Equipment **858**, 73 (2017).

[13] A. Den Haan, G. Wijts, F. Galli, O. Usenko, G. Van Baarle, D. Van Der Zalm, and T. Oosterkamp, *Atomic resolution scanning tunneling microscopy in a cryogen free dilution refrigerator at 15 mk,* Review of Scientific Instruments **85**, 035112 (2014).

[14] R. Kalra, A. Laucht, J. P. Dehollain, D. Bar, S. Freer, S. Simmons, J. T. Muhonen, and A. Morello, *Vibration-induced electrical noise in a cryogen-free dilution refrigerator: Characterization, mitigation, and impact on qubit coherence,* Review of Scientific Instruments **87**, 073905 (2016).

[15] T. J. Kippenberg and K. J. Vahala, *Cavity optomechanics: back-action at the mesoscale,* science **321**, 1172 (2008).

[16] E. Gavartin, P. Verlot, and T. J. Kippenberg, *A hybrid on-chip optomechanical transducer for ultrasensitive force measurements,* Nature nanotechnology **7**, 509 (2012).

[17] J. D. Teufel, T. Donner, M. Castellanos-Beltran, J. W. Harlow, and K. W. Lehnert, *Nanomechanical motion measured with an imprecision below that at the standard quantum limit,* Nature nanotechnology **4**, 820 (2009).

[18] *Ar-p6200_csar62english_allresist_product-information.pdf,* https://www.allresist.com/wp-content/uploads/sites/2/2020/03/AR-P6200_CSAR62english_Allresist_product-information.pdf, (Accessed on 08/20/2021).

[19] D. J. Thoen, B. G. C. Bos, E. Haalebos, T. Klapwijk, J. Baselmans, and A. Endo, *Superconducting nbtin thin films with highly uniform properties over a ∅ 100 mm wafer,* IEEE Transactions on Applied Superconductivity **27**, 1 (2016).

[20] *Mems chips and lasers for industrial and scientific applications |norcada,* https://www.norcada.com/, (Accessed on 07/26/2021).

[21] A. Schliesser, P. Del'Haye, N. Nooshi, K. Vahala, and T. J. Kippenberg, *Radiation pressure cooling of a micromechanical oscillator using dynamical backaction,* Physical Review Letters **97**, 243905 (2006).

[22] J. B. Clark, F. Lecocq, R. W. Simmonds, J. Aumentado, and J. D. Teufel, *Sideband cooling beyond the quantum backaction limit with squeezed light,* Nature **541**, 191 (2017).

[23] S. Weis, R. Rivière, S. Deléglise, E. Gavartin, O. Arcizet, A. Schliesser, and T. J. Kippenberg, *Optomechanically induced transparency,* Science **330**, 1520 (2010).

[24] J. D. Teufel, D. Li, M. Allman, K. Cicak, A. Sirois, J. Whittaker, and R. Simmonds, *Circuit cavity electromechanics in the strong-coupling regime,* Nature **471**, 204 (2011).

[25] V. Singh, S. Bosman, B. Schneider, Y. M. Blanter, A. Castellanos-Gomez, and G. Steele, *Optomechanical coupling between a multilayer graphene mechanical resonator and a superconducting microwave cavity,* Nature nanotechnology **9**, 820 (2014).

[26] S. S. Inc., *Sonnet precision electromagnetics,* (1983).

[27] M. Yuan, V. Singh, Y. M. Blanter, and G. A. Steele, *Large cooperativity and microkelvin cooling with a three-dimensional optomechanical cavity,* Nature communications **6**, 1 (2015).

[28] A. Noguchi, R. Yamazaki, M. Ataka, H. Fujita, Y. Tabuchi, T. Ishikawa, K. Usami, and Y. Nakamura, *Ground state cooling of a quantum electromechanical system with a silicon nitride membrane in a 3d loop-gap cavity,* New Journal of Physics **18**, 103036 (2016).

[29] M. Yuan, M. A. Cohen, and G. A. Steele, *Silicon nitride membrane resonators at millikelvin temperatures with quality factors exceeding 108,* Applied Physics Letters **107**, 263501 (2015).

[30] B. Brock, M. Blencowe, and A. Rimberg, *Frequency fluctuations in tunable and nonlinear microwave cavities,* Physical Review Applied **14**, 054026 (2020).

[31] B. Armstrong, *Spectrum line profiles: the voigt function,* Journal of Quantitative Spectroscopy and Radiative Transfer **7**, 61 (1967).

[32] P. Siddons, C. S. Adams, and I. G. Hughes, *Off-resonance absorption and dispersion in vapours of hot alkali-metal atoms,* Journal of Physics B: Atomic, Molecular and Optical Physics **42**, 175004 (2009).

[33] I. Diniz, S. Portolan, R. Ferreira, J. Gérard, P. Bertet, and A. Auffeves, *Strongly coupling a cavity to inhomogeneous ensembles of emitters: Potential for long-lived solid-state quantum memories,* Physical Review A **84**, 063810 (2011).

[34] *lownoisefactory.com :: 4-8 ghz single junction,* https://www.lownoisefactory.com/products/iso/lnf-isc4_8a/, (Accessed on 08/25/2021).

[35] A. G. Krause, M. Winger, T. D. Blasius, Q. Lin, and O. Painter, *A high-resolution microchip optomechanical accelerometer,* Nature Photonics **6**, 768 (2012).

[36] *Ld dilution refrigerator measurement system - bluefors,* https://bluefors.com/products/ld-dilution-refrigerator/, (Accessed on 08/25/2021).

[37] M. Rösch, *Development of lumped element kinetic inductance detectors for mm-wave astronomy at the IRAM 30 m telescope,* Vol. 12 (KIT Scientific Publishing, 2014).

[38] D. Wisbey, A. Martin, A. Reinisch, and J. Gao, *New method for determining the quality factor and resonance frequency of superconducting micro-resonators from sonnet simulations,* Journal of Low Temperature Physics **176**, 538 (2014).

[39] M. Khalil, M. Stoutimore, F. Wellstood, and K. Osborn, *An analysis method for asymmetric resonator transmission applied to superconducting devices,* Journal of Applied Physics **111**, 054510 (2012).

5

6

High cooperativity and high-Q mechanics in a flip-chip membrane cavity electromechanical device

High stress stoichiometric silicon nitride membranes have emerged as promising candidates in a wide range optomechanical experiments due to their high-Q. Combining these high-Q membranes with superconducting microwave platforms allows for macroscopic quantum state engineering with large decoherence times. Their relative high mass can therefore enable the exploration of quantum mechanics and gravity simultaneously. Initial demonstrations using simple flip-chip techniques showed great promise, but proved to be difficult to implement. Here, we present a platform and device for flip-chip cavity electromechanics which enables a new generation of high-Q, high cooperativity membrane devices. Our platform combines a new clamping method and holder with a phononic shield built into the silicon frame. For flip-chip electromechanics, the phononic shield is crucial, as it allows us to maintain high Q while still clamping the chip tightly on all sides to provide a reliable flip-chip assembly. We observe ringdown times up to 37 seconds, corresponding to mechanical Q-factor of 3.7×10^7, and cooperativities up to 12000. We observe mechanical noise sidebands with resonant drive, but find that these are fluctuating significantly in amplitude, which we attribute to effects arsing from large cavity frequency noise we believe are induced from vibrations in the cryostat. Combining the new developments in this device with cryogenic vibration isolation and cavity locking, will enable ground state cooling and future experiments engineering quantum superpositions of massive objects.

This chapter is being prepared for publication as *High cooperativity and high-Q mechanics in a flip-chip membrane cavity electromechanical device.* S.R.Peiter*, A.Sanz Mora*, J.P. van Soest, Claus Gaertner and G.A.Steele

6.1. INTRODUCTION

High-Q and high coorperativity (C) optomechanics have provided a platform for a wide range of applications such as force sensing [1, 2], microwave to optical transduction [3, 4] and memory elements in combination with quantum communication and computing devices [5–7]. For example, they enable force sensing with sensitivities below the standard quantum limit, have auspicious conversion efficiency in transducers and relative long information storage time due to their high Q. In addition, this platform in combination with a large mass mechanical oscillator has been proposed as a very promising candidate for exploring quantum mechanics and gravity simultaneously. [8–10]. Therefore, highly stressed stoichiometric SiN membranes in a cavity electromechanical architecture are favourable, since their high Q-factor and mass [11, 12] can be exploited to create and sustain massive macroscopic quantum states. Here, gravity is suspected to be a decoherence mechanism for these massive mechanical quantum states [13].

The simple flipchip technique was primarily considered for interfacing these highly stress membranes with electrical cavities [14, 15], but eventually turned out to be difficult to realize, due to clamping induced losses [16]. This is especially noticeable in the work of Ref.[17], where they discovered a trend whereby the lower order membrane modes, particularly the fundamental, exhibited significantly deteriorated Q-values relative to higher-order membrane modes. In addition, the quality factor of the lower order modes varied widely from chip to chip. Another major drawback of this flipping routine is that the membranes break inconsistently for reasons unknown yet [12, 18].

Here, we present a mechanical device in a robust and modular platform that facilitates high-Q and high coorperativity electromechanical experiments. Fig.6.1 shows the electromechanical device that combines a superconducting lumped-element resonator with a SiN membrane surrounded by a phononic shield micromachined into the silicon substrate and fixated by our custom designed flipping tool. With this tool, we introduce a new clamping method, where contact and varying pressure can be applied to all 4 edges of the mechanical device. This allows us to systematically reach sub-μm gaps without damaging or breaking of the membrane. In this tightly held assembly, the phononic shield is essential in overcoming clamping induced losses and therefore the SiN membrane preserves its high mechanical Q.

With time domain ringdown measurements, we extract a mechanical quality factor $Q_m = 3.7 \times 10^7$ or decay time $\tau_m = 37$ seconds. At the highest redpump strength, limited by the compression point of the low noise amplifier, we estimate a coorperativity $C \sim 12000$. Furthermore, the device is affected by vibration noise generated by the pulse-tube cryocooler and manifests as cavity frequency noise. As a result, the mechanical thermal sidebands upon resonant driving fluctuate in amplitude during consecutive measurements, making the estimation of the mechanical mode temperature extremely challenging.

Current internal efforts in cryogenic vibration isolation [19] and cavity noise locking [20] will pave the way to performing more advanced experiments such as groundstate cooling and eventually quantum state engineering with these massive macroscopic objects. This enables the creation of macroscopic quantum superpositions and will serve as a valuable asset for quantum gravity research [21].

6.2. DEVICE DETAILS

Our electromechanical device consists of a lumped-element resonator and is coupled capacitively to a high stress stoichiometric Si_3N_4 square membrane with area 350×350 μm, as shown in the zoom-in in Fig.6.1b. The inductor and capacitor of the lumped element resonator are meandering wires and rectangular pads, respectively. This is detailed and shown in chapter 4. To induce optomechanical coupling of the device, we coat the 50 nm thin membrane with 25 nm Al+1%Si. The metallized SiN membrane is clamped onto a 200 μm thick Si substrate that is etched through entirely such that we are left with freestanding Si structures. This resembles a crystal lattice that functions as an acoustic bandpass filter between the environment and the membrane, also called a phononic shield. It has shown to suppress clamping losses from the Si support structures and increase mechanical Q_m of the SiN membrane [22–24]. The phononic shield consists of an array of square blocks with chamfered edges and connected by tethers that have high aspect ratios. By choosing its lateral dimension carefully, we create a bandgap in the acoustic mode spectrum of the substrate that is centred around the SiN membrane fundamental mode, thus effectively suppressing the coupling of the fundamental mode to the substrate modes. The detailed design and fabrication methodology of the phononic shield is provided respectively in supplementary note 6.7.1 and chapter 3. The membrane device is flipped onto the microwave sample, then fixed and pressed with a custom-made flipchip tool, as shown in Fig.6.1a. The device is placed in a cylindrical cage and thereafter loaded, using a loading arm, onto the mK plate of an Oxford Triton 200 dilution refrigerator. With coaxial lines that pass from room temperature down to the device at 15 mK, we are able to probe our device with a microwave tone. The reflected signal is amplified with a low noise amplifier (LNA), located at the 4K-stage, before it is measured with a vector network analyser (VNA) at room temperature. All the measurements in this chapter, unless explicitly stated, are taken with the pulse tube off to avoid mechanical noise as much as possible. The layout and optical images of the measurement setup are shown in supplementary note 6.7.2.

Fig.6.1c shows the reflection response of the electromechanical device after performing a frequency sweep with VNA. The microwave cavity mode is detected at $\omega_c = 2\pi\times$ 5.806 GHz and allows us to estimate g_o considering the bare cavity mode is 12.4 GHz. With Sonnet EM [25], we use the bare and shifted resonance as a method to calibrate the gap d between the membrane and cavity. We extract $d \approx 0.9$ μm and estimate single phonon-photon coupling $g_o \approx 2\pi\times$ 2 Hz assuming $x_{zpf} = 0.5$ fm ($x_{zpf} = \sqrt{\frac{\hbar}{2m_{eff}\omega_m}}$). In the supplementary note 5.7.1 of chapter 5 explains the details of the simulation routine to estimate g_o. We fit the S_{11} response to a complex Lorentzian function and extract external and internal losses (κ_e, κ_i) of respectively $2\pi\times$ 32 and $2\pi\times$195 kHz. The cavity is thus undercoupled since $\kappa_i > \kappa_e$ with $\eta = 0.13$ ($\eta = \kappa_e/\kappa$). In the fitting procedure, we have also accounted for the slightly asymmetric shape of the response, known as Fano [26].

In addition, the reflection response curve contains oscillations in the amplitude that get larger as we move closer to the resonance frequency ω_c. The manifestation of these amplitude fluctuations in the response are a result of spurious acoustic noise that excite the membrane. The frequency of these oscillations is given by the difference (beating) between the VNA IFBW bandwidth and the frequency component of the noise responsible for the cavity resonance fluctuations. Beside amplitude fluctuations, the mechanical

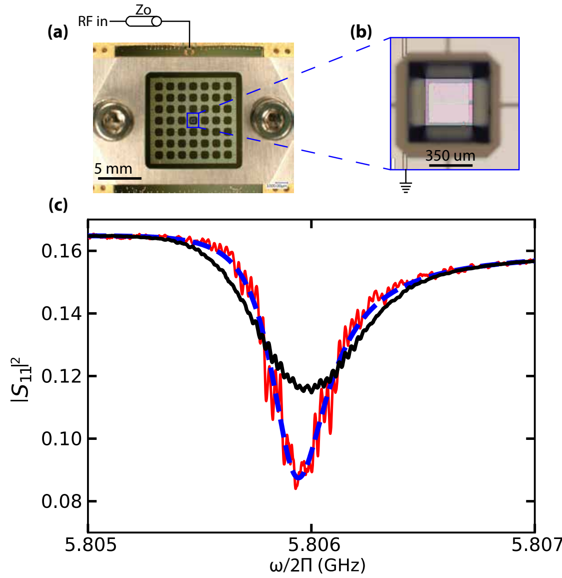

Figure 6.1: **Device characterization with pulse tube off.** **(a)** Top view of flipchip device consisting of Si phononic crystal with square metallized Si_3N_4 membrane in the middle. The membrane is capacitively coupled to the lumped-element resonator that is situated at the bottom, on a Copper (Cu) holder. **(b)** Zoom-in of the centre where the metallized membrane is aligned with the big pad capacitors of the lumped-element resonator, hence inducing an electromechanical coupling. **(c)** Reflection measurement S_{11} (red) and Lorentzian fit (blue) of the electromechanical device as measured directly with a vector network analyser (VNA). The IF-bandwidth (IFBW) of the VNA is set to 10 kHz and taken with 3300 sweeppoints. The response has an asymmetric lineshape also known as Fano and contains mechanical induced cavity noise visible close to its resonance. The average $\overline{S_{11}}$ (black) taken over 100 separate S_{11} measurements is used to estimate the cavity noise σ_{ω_c}.

noise also causes the resonance frequency of the cavity change, i.e. $\omega_c \rightarrow \omega_c(x(t))$. The cavity frequency noise σ_{ω_c} is then given by

$$\sigma_{\omega_c} = \int_{1/\tau_{\mathrm{m}}}^{\kappa/2\pi} S_{\omega_c\omega_c}(f)df \tag{6.1}$$

with $1/\tau_m$, the measurement bandwidth.

To determine σ_{ω_c}, we start by recording 100 consecutive S_{11} traces, of which we show the average response in Fig.6.1c. We notice that the average response is broader and the oscillations in amplitude close to ω_c, due to mechanical noise, get reduced. The average response does not follow a Lorentzian function any more, but is instead convoluted with the cavity noise distribution and is given by

$$\overline{S_{11}(\omega)} = \int_{\infty}^{\infty} S_{11}(\omega)P(\omega-\Omega)d\Omega \tag{6.2}$$

Here, P(Ω) is the cavity noisy probability distribution function. By assuming a Gaussian distribution [27], $\overline{S_{11}(\omega)}$ becomes a Voigt function [28]. By fitting the average response using a Voigt profile, we deduce that the cavity is broadened by $\sigma_{\omega_c} \approx 2\times$ 276 kHz. The fit

is performed after correcting for the Fano effects in the individual S_{11} responses. We outline the fitting procedure in supplementary note 6.7.3. Due to large vibration present in the cryogenic environment, the cavity frequency noise σ_{ω_c} is comparable to κ. This can form an obstacle that limits us from performing more advanced experiments which require a stable cavity, such as red-sideband cooling or coherent photon-to-phonon conversion [29, 30].

6.3. OMIT

To probe the mechanical resonator, we inject a strong microwave pump at the red-side of the coupled system i.e. $\omega_\mathrm{d} = \omega_\mathrm{c} - \omega_\mathrm{m}$, while probing the cavity with a drive much weaker than the redpump. Mixing of these two drives mediated by the mechanics results in a ω_m beating that give rise to a time-varying radiation pressure force. This force resonantly excites the mechanical resonator when ω_m matches the mechanical fundamental mode. The mechanics on its turn create sidebands of the redpump of which the higher harmonic matches ω_c. It destructively interferes with the probe field, resulting in the appearance of a Lorentzian transparency window that is centred at ω_c. This phenomenon is known as optomechanical induced transparency (OMIT) [31, 32] and through dynamical back-action [33], we get an increase of the overall mechanical damping rate i.e. $\gamma_\mathrm{eff} = \gamma_\mathrm{m} + \gamma_\mathrm{opt}$ [34]. The optomechanical damping rate γ_opt in case of OMIT is positive and proportional to the coupling strength between the mechanical and microwave mode given by the cooperativity $C = 4g_0^2 N/\kappa\gamma_\mathrm{m}$ [35] with N, the intracavity photon number. To obtain the power at the input of the device $\mathrm{P_{in}}$ and hence N, we subtract the total input line attenuation of 55 dB from the power applied at room temperature. In supplementary note 6.7.4, we provide the details and assumptions made for calibrating N, while also accounting for cavity noise.

In Fig.6.2, we show OMIT responses that are averaged 3 times for each redpump power $\mathrm{P_{red}}$ to increase signal-to-noise ratio (SNR). In the plots, $|S_{11}|^2 = 1$ corresponds to maximum reflection and $\mathrm{P_{red}}$ is referenced at the output of the VNA. We witness OMIT occurring for $\omega_\mathrm{m} = 2\pi\times$ 1.01 MHz, the mechanical fundamental mode, and thereby not located deep in the resolved sideband regime where the criterion $\kappa/\omega_m \gg 1$ holds [36]. By increasing $\mathrm{P_{red}}$, we do notice an increase in the area of the Lorentzian and the overall mechanical damping rate γ_eff. The height of the OMIT window is given by [37]

$$S_{11}(\omega_c) = 1 - \frac{2\eta}{1+C} \tag{6.3}$$

We are only able to resolve the mechanical linewidth down to 0.7 Hz with the VNA as shown in Fig.6.2a. The height of the Lorentzians almost reach unity in Fig.6.2b,c with increasing power and considering Eq.(6.3), we deduct that the cooperatively satisfies $C >$ 1. We are not able to increase $\mathrm{P_{red}}$ above 5 dBm to explore the lower limit of γ_eff. At these pump powers, the LNA start to saturate and at this point the input noise temperature and gain of the LNA start to deteriorate [38] causing the noisefloor to increase.

Note that we cannot yet accurately quantify C with the current OMIT measurements because the intrinsic mechanical linewidth γ_m is unknown. In the next section, We determine γ_m by recording the mechanical decay in time domain.

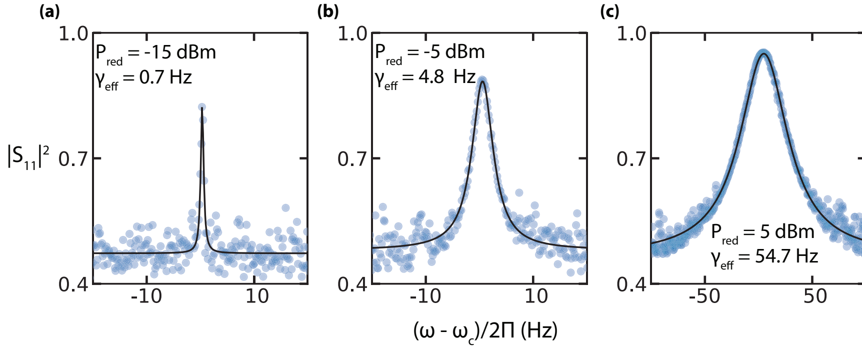

Figure 6.2: OMIT response with increasing red pump power P_{red} (left to right: **a, b, c**) centred around ω_c. γ_{eff} is resolved down to approximately 2 × 0.7 Hz, limited by the IF bandwidth of the VNA. The highest P_{red} = 5 dBm corresponds to an intracavity photons $N \approx 4 \times 10^6$. Increasing P_{red} above 5 dBm saturates the LNA causing the noisefloor to increase.

6.4. MECHANICAL RINGDOWN

To resolve the narrow intrinsic mechanical linewidth γ_m, we turn to time domain measurements. We utilize the mechanical sidebands of the cavity to drive and readout the mechanical resonators, as demonstrated in the measurement scheme shown in Fig.6.3a. The measurement protocol is follows: we first excite the mechanical resonator using a blue detuned pump. We notice that the mechanics exhibits non-linear behaviour after some time because bluepumping causes γ_{opt} to become negative and results in anti-damping. While this causes amplification [39, 40], it can also lead to an instability that give rise to self-induced oscillations [41, 42] when $|\gamma_{opt}| > |\gamma_m|$. We then switch on a red-pump a few seconds after the bluepump and record the reflected signal at ω_c. We sweep P_{red} and track the mechanical decay rate γ_{eff} dependence on the intracavity photons N.

In Fig.6.3b, the mechanical ringdown monitored at ω_c is shown for P_{red} = -60, -40 dBm, almost 4 orders of magnitude smaller compared to the powers used with the VNA. After an initial settling time $t_{u,s}$ at which the mechanical resonator relaxes out of the limit cycle oscillations, we observe an exponential decay of the energy from the cavity and is related to the decay of mechanical energy. Performing a linear fit of the initial decay in log-scale, we are able to extract the mechanical decay time and plot the mechanical Q_m ($Q_m = \omega_m/\gamma_m$) for various P_{red} in Fig.6.3c. We witness a flattening of the curve below P_{red} = -40 dBm. Here, $C \ll 1$ and thus radiation pressure force is negligibly small such that the effects of dynamical back-action can be disregarded, and no broadening occurs i.e. $\gamma_{eff} \simeq \gamma_m$. Therefore, we extract an intrinsic $Q_m = 37 \times 10^6$, which corresponds to a natural mechanical decay time τ_{mech} = 37 s. Reducing P_{red} to lower powers become challenging as we are limited by the short time span of a couple of minutes that the pulse-tube can stay off. However, it is also not crucial since Q_m already flattens at the low P_{red} and reducing it further would not reveal any new information. The full time domain traces for all P_{red} powers, including the time interval where nonlinear behaviour is observed, are provided in supplementary note 6.7.6.

The relative high intrinsic Q_m is expected [43] since the mechanical impedance mis-

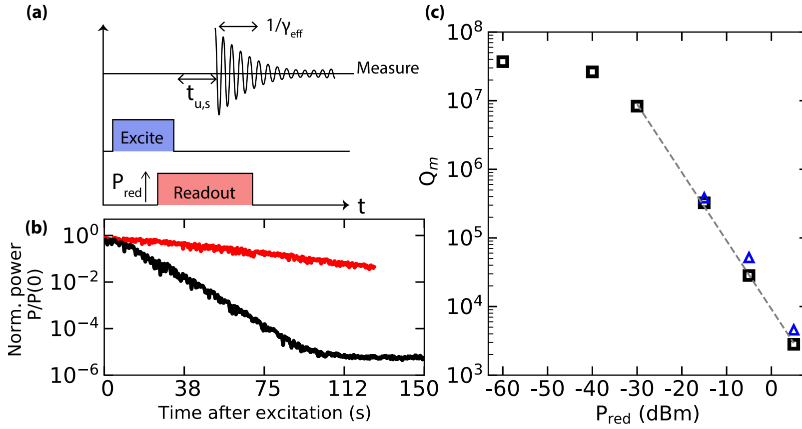

Figure 6.3: **Determining mechanical ringdown time through blue and redside pumping for excitation and readout.** **(a)** Scheme used to measure mechanical ringdown. After blue side-pumping, we switch on the red pump to dampen the mechanical oscillations. The damping strength depends on the intra cavity photons N from the redpump. A spectrum analyser is used to monitor the output signal at ω_c. **(b)** Time domain trace for 2 powers of the redpump i.e. P_{red} = -60 dBm (black) and -40 dBm (red) and the decay time is obtained by fitting curves with a linear function. **(c)** Mechanical Q_m for increasing P_{red} estimated through time domain ringdown of the mechanics(black square) and via OMIT (blue triangles). Q flattens at low powers to its intrinsic $Q_m = 37 \times 10^6$. A guide to the eye (gray dashed) reveals the expected linear dependence between C and γ_{eff} . At the highest P_{red}, C reaches 12000 corresponding to $N \approx 4 \times 10^6$.

match introduced by the lattice-like structure of the phononic shield suppresses radiation energy loss of the membrane [23]. The losses in this context come from the clamping of the mechanical device at all of its 4 edges in our flipchip setup. Clamping however is necessary in an electromechanical architecture, but can result in low mechanical Q due to coupling to low Q substrate modes that lose energy via the clamping points of the chip [44]. Q_m start to decrease linearly when P_{red} is increased, which translates to an increase in damping of the mechanics and confirms that γ_{opt} depend linearly on N. The mechanical quality factors we estimate from the OMIT measurements agrees with its ringdown counterpart to the extent that they have the same order of magnitude. With the ringdown measurement able to resolve γ_m, it paves way for determining $C = \frac{\gamma_{eff}}{\gamma_m} - 1$. Here, C reaches 12000 at P_{red} = 5 dBm, corresponding to $N \approx 4 \times 10^6$. With this measurement setup it is not straightforward to increase P_{red} to reach higher C, since we exceed the LNA compression point of -45 dBm (at its input). this is detrimental to our measurement due to an increase of the noisefloor and a reduction in gain.

6.5. THERMAL NOISE

We have already discussed that the presence of dynamical backaction can alter the overall damping rate of the mechanics with γ_{opt} being either positive or negative. Now it becomes apparent that we can also employ this effect to cool the mechanical resonator into its quantum groundstate [29]. Ground-state cooling proceeds by driving the electromechanical system parametrically with a negative detuned drive $\omega_d = \omega_c - \omega_m$, such

that $\Delta = \omega_\mathrm{d} - \omega_\mathrm{c} = \omega_\mathrm{m}$. The time-varying radiation pressure force damps the amplitude of the mechanical oscillations close to x_zpf. To determine if red sideband cooling can be utilized to reach groundstate of the mechanics, which is characterized by mechanical mode occupation $n_\mathrm{m} < 1$, a classical description is not enough. We need a quantum description [45] that summarizes three criteria that need to be satisfied. First, the electromechanical device need to be sideband resolved i.e. $\kappa \ll \omega_m$. In the mechanical picture, this means that the cavity does not respond instantaneously to the displacement of the mechanical resonator. There is a finite delay that causes the radiation pressure force to be out of phase with the mechanical displacement, which for negative detuning lead to cooling. If not sideband resolved i.e. $\kappa \gg \omega_m$, cooling is still possible, but cooling to the groundstate is not possible [35]. Second, is the weak coupling criterion, i.e. $g \ll \kappa$. If this condition is not satisfied, energy transfer between the cavity and mechanics occurs faster than the cavity dissipation rate κ. This leads to energy being put back in the mechanical resonator without dissipation. The third condition is $C + 1 > n_\mathrm{th}$. Here n_th is the thermal occupation of the mechanical mode and need to be estimated by monitoring the thermal noise of the mechanical resonator. Next, we make an attempt to verify whether our system meets the third condition, since it already satisfies the first two.

We measure the thermal noise of the mechanical mode by driving the coupled system on resonance with a signal generator at $\Delta = 0$ and thereby monitoring the reflected signal with a spectrum analyser. The phase and amplitude of the reflected signal is modulated by the mechanical frequency, resulting in sidebands in the power spectrum located at an offset $\Delta = \pm\omega_\mathrm{m}$ from the drive. The spectrum analyser is configured to record the I and Q quadratures of the redsideband for a duration of 360 s, at $\omega_\mathrm{c} - \omega_\mathrm{m}$. We repeat this measurement 4 times, using the same initial condition each time i.e. turn on the resonant drive, set pulse tube off and immediately start capturing the quadratures. We split the recorded time traces in 32 segments of 45 s, larger than $\tau_\mathrm{mech} = 37$ s, after which we apply a Fast Fourier Transform (FFT) to get the noise power spectral density S_pp. We show S_pp for 3 arbitrary segments in Fig.6.4(a,b,c) where we detect an inconstancy in amplitude. To investigate this further, we extract the thermal peak amplitude for each segment as shown in Fig.6.4d. The first 45 s of each measured time trace is highlighted with thick crosses, as these still contains noise related to the pulse tube. Now, it is evident that the mechanical thermal noise is not constant and fluctuates over a 20 dB range, hinting that our mechanical mode is not thermalized within its mechanical decay time $\tau_\mathrm{mech} = 37$ s. There also does not seem to be some degree of consistency that allows us to estimate the properties of this amplitude variation. The mechanical mode does not reach a thermal equilibrium as a result of the continuous presence of cavity noise. We determine the average mechanical mode temperature $\langle \mathrm{T_m} \rangle$ assuming a Gaussian distribution of the cavity noise and show that it also fluctuates accordingly between 3 and 300 mK. The analytic expression used to determine $\langle \mathrm{T_m} \rangle$ is provided in supplementary note 6.7.7. It is challenging to calibrate $\mathrm{T_m}$ precisely, since a time varying detuning $\Delta(t)$ of the drive with respect to the cavity gives rise to a radiation pressure force responsible for either damping (cooling) and amplifying (heating) of the mechanical resonator. This corresponds to a changing γ_eff, which can also become negative when blue detuned. We then we no longer have amplification, but instead an instability [46]. Here, the amplitude of the mechanical oscillations grows exponentially and then saturates to a steady

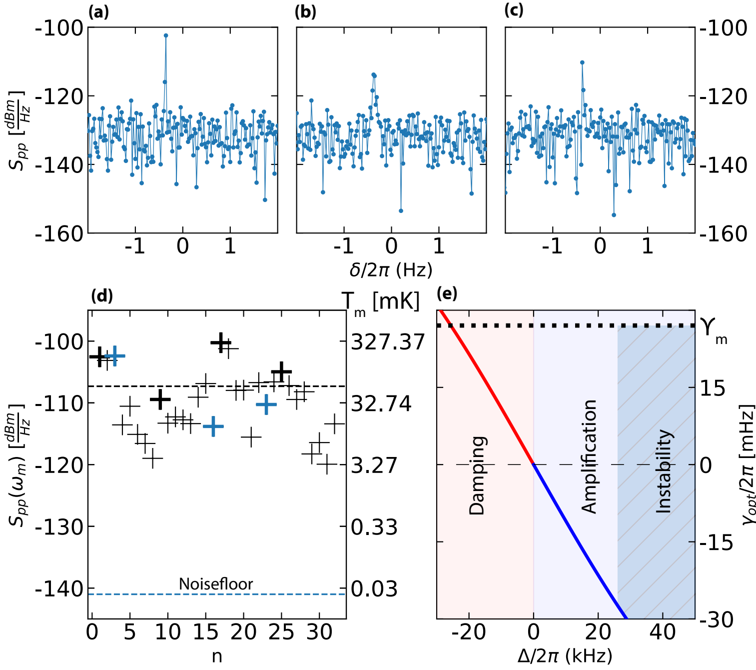

Figure 6.4: **(a,b,c)** The power spectral density S_{pp} calculated by acquiring four 360 s IQ time traces measured at $\delta = \omega - (\omega_{\mathrm{c}} - \omega_{\mathrm{m}})$ with sampling rate $\mathrm{F_s}$ = 1 kHz. We calculate $S_{\mathrm{pp}}(\delta)$ by splitting the data into n = 32 segments, each 45 s long. Variation of mechanical thermal noise amplitude is visible across 3 arbitrary segments and is over 10 dB. **(d)** max($S_{\mathrm{pp}}(\delta)$) calculated and extracted for all the 32 segments. The first 45 s, right after the pulsetube is off is shown with black crosses for each of the 4 datasets. The HEMT limited noise floor (blue dash) is shown as reference, while the black corresponds to the ensemble average. **(e)** The optomechanical damping rate γ_{opt} with detuning ($\Delta = \omega_{\mathrm{d}} - \omega_{\mathrm{c}}$). Here, Δ=0 separates the regions of damping and amplification highlighted with respectively red and blue. At $\Delta = 2\pi\times$ 24 kHz, the intersection (hatched blue area) between intrinsic γ_{m} (horizontal black line) with γ_{opt} marks the point where the mechanical resonator reaches an instability. At $\Delta > 2\pi\times$ 24 kHz, the mechanical resonator attains a negative linewidth and exhibits non-linear dynamics.

state value also known as self-induced oscillations. To explore and quantify this region for our device, we provide the expression for the optomechanical mechanical damping γ_{opt} with respect to the detuning [47]:

$$\gamma_{\mathrm{opt}}(t) = g(t)^2\kappa\left[\frac{1}{(\omega_m + \Delta(t))^2 + (\frac{\kappa}{2})^2} - \frac{1}{(\omega_m - \Delta(t))^2 + (\frac{\kappa}{2})^2}\right] \tag{6.4}$$

assuming that the weak coupling $g \ll \kappa$ criterion and $\kappa \gg \gamma_{\mathrm{eff}}$ holds. Both conditions are satisfied for our device. If $\Delta = 0$, dynamical back-action is absent resulting in $\gamma_{\mathrm{opt}} = 0$ and the mechanical resonator is left unchanged i.e. $\gamma_{\mathrm{eff}} = \gamma_{\mathrm{m}}$. In Fig.6.4e, we show γ_{opt} dependence on Δ for our device parameters. The mechanical mode attains a negative γ_{eff} for $\Delta > 2\pi\times$ 24 kHz, since it intersects and increases above the γ_{m}. This is shown by the blue hatched area. As our device suffers from noise with $\sigma_{\omega_c} \approx 2\pi\times$ 276 kHz, it is obvious that we are (occasionally) located deep in this domain where the trajectory

mechanical resonator evolves around an instability and exhibiting the self-induced oscillations. The concept of a mode temperature is therefore not valid, as our device never reaches a thermal steady state and is constantly displaced from equilibrium by either radiation pressure induced damping or self-induced oscillations.

6.6. Discussion

We have used a custom-made flipchip tool to assemble an electromechanical device consisting of a lumped-element resonator capacitively coupled to a high stress stoichiometric Si_3N_4 membrane. The SiN membrane is surrounded by a Si phononic shield with the aim to minimize clamping losses. Upon characterizing the device at cryogenic temperatures (T = 15 mK), we notice a strinkingly unstable cavity that is shifting around its resonance with $\sigma_{\omega_c} = 2\pi\times$ 276 kHz, larger than its linewidth $\kappa = 2\pi\times$ 228 kHz. This cavity noise arises from the mechanical resonator, which is subjected to acoustic excitations from it surrounding. Upon monitoring the sidebands of a resonant drive in the noise power spectrum of the cavity, we find that the spurious mechanical resonances span up to 100 kHz. Also, does the noisefloor in the powerspectrum appear to increase with the pulse-tube on. Furthermore, we succeed in performing OMIT measurements, which allow us to extract the effective mechanical linewidth γ_{eff}. We are not able to extract the intrinsic linewidth γ_{m} in the OMIT measurement by using low redpump power such that $C \ll 1$ due to low signal-to-noise and limited time that the pulse-tube can stay off. We use time domain measurement to measure the mechanical decay rate on longer timescales and find a strikingly large intrinsic $\gamma_{\text{m}} = 2\pi\times 27$ mHz or $Q_{\text{m}} = 37\times 10^6$. The use of a SiN membrane surrounded by a phononic shield has proven to have superior mechanical quality factor compared to no shield and using the same flipchip configuration as in Chapter 5. With this device, we have shown to reach a multiphoton cooperativity $C \approx 12000$ without saturating the microwave cavity or the LNA with the powers used. Upon estimating the mechanical mode temperature, we observe fluctuations of the thermal peak amplitude which makes it difficult to draw conclusions about the mode temperature. We attribute the dynamic behaviour of the thermal peak to be a result of cavity noise that plagues our electromechanical system. Cavity noise causes the mechanical resonator to spontaneously cool or self-oscillate upon resonant driving, hence always preventing the mechanical resonator from thermalizing to its environment.

In prospect, phase locking of the cavity to the mechanical noise and actively moving the drive to follow the cavity will eliminate most of the noise induced dynamical backaction. It will then be possible to obtain a static Lorentzian thermal response at the sidebands, from which we can estimate the mode temperature. With current FPGA based PID controllers, we should be able to phaselock the microwave drive to cavity noise frequencies spanning from DC up to 50 kHz. This feedback scheme should not be confused to experiments which also employ feedback circuitry to achieve active cooling of mechanical oscillators. In the latter, the displacement of the mechanical oscillators itself is monitored and controlled [48–50], while in our case the shift in cavity resonance frequency is used as error feedback signal [20].

6.7. SUPPLEMENTARY INFORMATION

6.7.1. PHONONIC SHIELD DESIGN

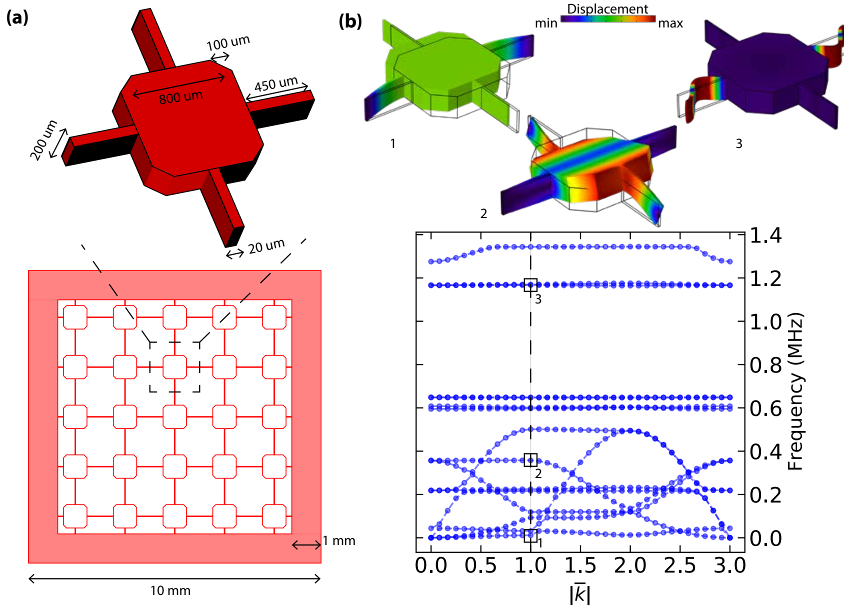

Figure 6.5: **Schematic layout of phononic shield with simulated band diagram.** **(a)** Full layout of phononic shield device that is a 200 μm thick Si-chip and has dimensions of 10×10 mm. There is a 1 mm margin at the edge such that it is possible for the flipchip presser tool to make contact and apply pressure. We isolate an unitcell of the phononic shield and provide the dimensions in the **zoom-in** i.e. a total length l_{UC} = 1700 μm **(b)** Bandgap diagram obtained with COMSOL eigenfrequency simulation for infinite unitcells in 2D, joined together via periodic boundary conditions. By sweeping the wave vector $|\bar{k}|$, we witness 3 full in-plane bandgaps appearing, of which the largest located between 600 and 1100 kHz. We show the several eigenmode shapes of the unit cell for $|\bar{k}|$ = 1 labelled with 1-3.

The phononic crystal is used to supress the coupling between the Si_3N_4 membrane and the Si support structure. The coupling is disadvantageous because this results in (1) clamping or radiation loss [16], in which the mechanical energy is radiated into the substrate and (2) substrate noise, in which the presence of mechanical modes of the substrate can limit optomechanical cooling [43]. The crystal is composed of square blocks joined together by narrow tethers and has a 2D square lattice structure, as shown in Fig.6.5. Each square with 4 tethers is known as a unit cell (zoom in) and by tailoring its dimension, we can modify the energy banddiagram of the lattice. In the banddiagram of this square lattice, there will be a bandgap due to the mechanical impedance mismatch that is introduced by the presence of the thin tethers connected to the square blocks. The full device is 10×10 mm and fits a total of 5 unit cells in each direction. We leave a margin of 1 mm at the edges that is used for applying pressure with the flipchip tool. A crystal thickness of 200 μm is chosen for its relative short etch-through time.

Considering that the Si_3N_4 membrane discrete modes are given by $f_{mn} = \sqrt{\sigma(m^2+n^2)/4\rho w^2}$ [51], we obtain a mechanical fundamental mode f_{11} = 1.01 MHz for the membranes used

in this thesis. Here, σ is the tensile stress, (m, n) are the integer indices of the anti nodes, ρ is the mass density and w is the window sidelength of the membrane.

We can now make a proximate estimation of the total length of a unit cell, l_{UC} such that a bandgap is centred around f_{11}. Using the speed of sound in silicon $v = 2200$ m/s, we determine $l_{UC} = \lambda/2 = v/2f \approx 1.1$ mm. We choose a unit cell length $l_{UC} = 1700$ μm in our design to compensate for the decrease in mechanical mode frequency due to the applied coating of the membrane with Al+1%Si. We perform an eigenfrequency analysis using a finite element software COMSOL to obtain the banddiagram as shown in Fig.6.5b. The boundaries are subjected to Bloch-Floquet boundary conditions [52] and the eigenfrequencies are calculated for the wavevectors $\overline{k}$ that span the Brillouine zone of the 2D square lattice in reciprocal space. We notice the largest bandgap appearing between 600 and 1100 kHz and the mechanical fundamental mode f_{11} is situated well within the bandgap. Note that the length, width, thickness, chamfer of the square block and tether length and width are all variables that can be tuned to alter the bandgap width and position in frequency. We did not study this in very much details and the interested reader is referred to Ref. [53].

6.7.2. MEASUREMENT SETUP

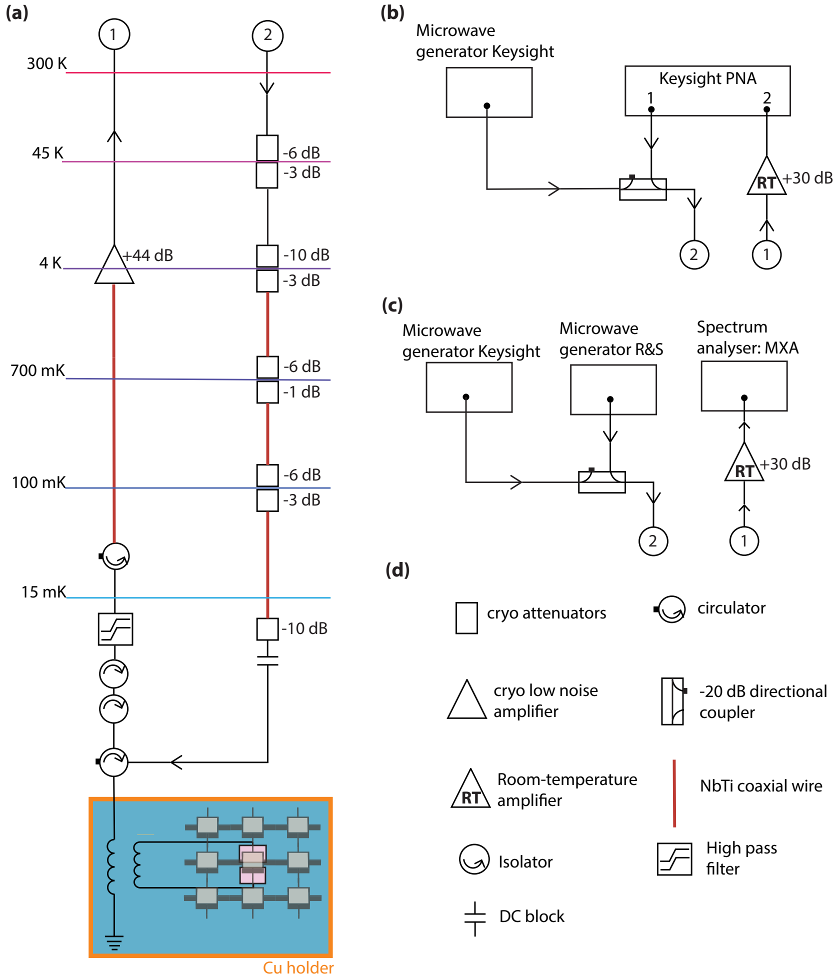

Figure 6.6: **(a)**Experimental setup used for performing the measurements carried out in this chapter. Experimental configurations for: **(b)** reflection response and OMIT measurements, **(c)** ringdown and spectral density measurements. **(d)** Microwave components symbols in experimental setup.

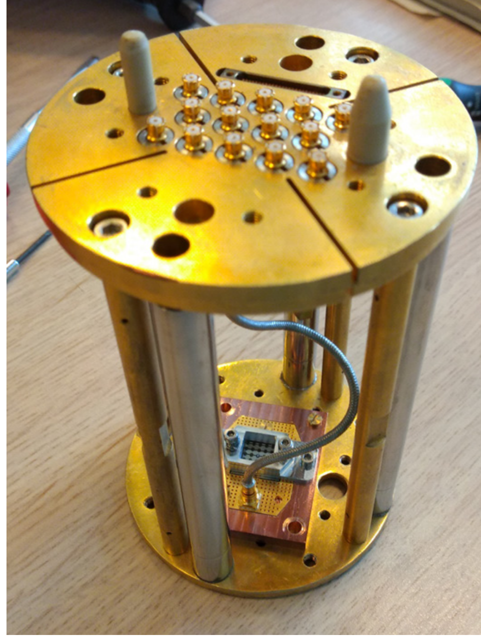

6

Figure 6.7: Optical image of electromechanical device mounted in puck before loading with loading arm into the Oxford Triton dilution refrigerator.

6.7.3. Voigt fit of cavity response

In this section, we first show the procedure used to correct Fano effects in the S_{11} response such that we can make an accurate estimation of the cavity parameters. Secondly, we show that the contribution of cavity noise also has to be taken into account, as this modulates the underlying S_{11} response of the cavity. By fitting the measured reflection response, which is a convolution of the noise and intrinsic response, we can estimate the broadening of the cavity σ_{ω_c}.

The ideal S_{11} of a microwave cavity in a reflection geometry is given by

$$\Gamma(\omega) = \frac{\kappa_e - \kappa_i - 2i\Delta\omega}{\kappa_e + \kappa_i + 2i\Delta\omega} \tag{6.5}$$

Here, $\Gamma(\omega)$ traces a circle in the complex-plane when $\Delta\omega = \omega - \omega_\mathrm{c}$ is swept. For frequencies far from resonance, $\Gamma(\omega) = -1$ and remains on the real axis. We call this the anchor point. In this case, the circle is also symmetric around the real axis, with its centre located on the real axis. Now, the asymmetric cavity response can be now understood by drawing a network diagram of the measurement setup as shown in Fig.6.8.

The connecting circuit consists of attenuators, coaxial cables, amplifiers and a directional coupler located between the source (VNA) and cavity. It alters the reflection response from the ideal case and is modelled as a black box of which the scattering matrix elements are unknown. We derive the modified reflection response $\Gamma'(\omega)$ as measured

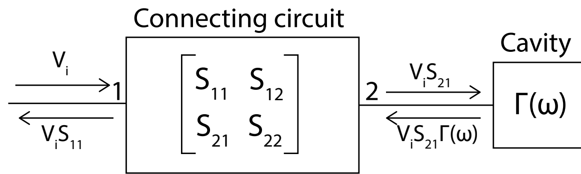

Figure 6.8: Network diagram of measurement setup. The connecting circuit is modelled as a black box with an unknown scattering matrix.

with the VNA:

$$\begin{aligned}\Gamma'(\omega) &= s_{11} + \left[s_{21}\Gamma(\omega)s_{12} + s_{21}\Gamma(\omega)^2 s_{22}s_{12} + s_{21}\Gamma(\omega)^3 s_{22}^2 s_{12} + \ldots\right] \\ &= s_{11} + \frac{s_{21}s_{12}\Gamma(\omega)}{1-\Gamma(\omega)s_{22}}\end{aligned} \tag{6.6}$$

Note that for any given $\Gamma(\omega)$, we are left with a (complex) offset s_{11} and scaling factor $s_{21}s_{12}/(1-\Gamma(\omega)s_{22})$. The latter is frequency dependent because of $\Gamma(\omega)$. This translates in a scaled and rotated circle with its centre displaced. This action is responsible for the asymmetric reflection response observed in the VNA measurements, as shown in Fig.6.9.

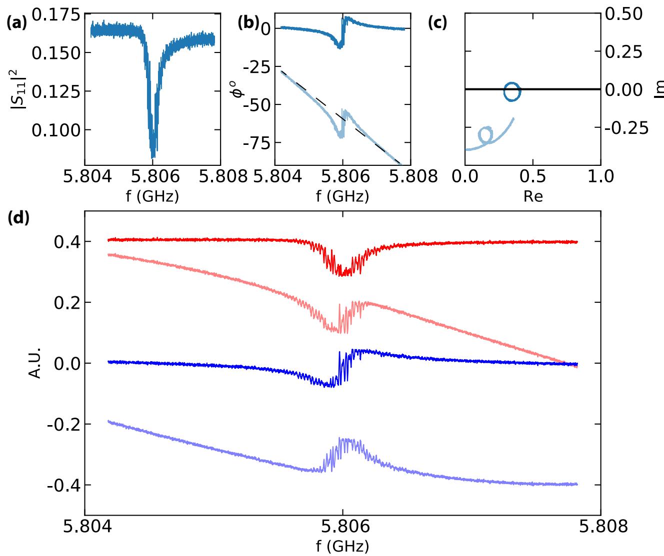

Figure 6.9: Reflection response S_{11} as measured with the VNA and represented in the following order with transparent lines: **(a)** magnitude, **(b)** phase, **(c)** phase space, **(d)** real (red) and imaginary (blue) part. Non-transparent lines represent response data after subtraction of the slope (black dashed line) from the phase in **(b)**. Magnitude in **(a)** does not change after this operation.

The skewness of the magnitude in Fig.6.9a is clearly visible and is a result of irregular

cable resonance (connecting circuit) i.e. matrix daig(S) $\neq 0$ The phase response in **(b)** is tilted because the electrical length of the coaxial cable is linearly dependent on the frequency. This all contributes to a circle in **(c)** that is displaced from the real axis and does not close on itself. We assume that $\Gamma s_{22} \ll 1$ and s_{11} is a (complex) constant offset with no frequency dependence.

The procedure is as follows:

- We first subtract the tilt from the phase with a linear line that is fitted to the background, shown in Fig.6.9b. This operation places the anchor point back on the real axis of the complex-plane. The phase away from resonance (background) now is zero, but the circle is not symmetric around the real axis (Fig.6.9c). This can also be seen by the slight offset of the resonance phase jump from $\phi = 0$ in Fig.6.10b. The magnitude is not affected by this operation.

- Next, we centre the resonance phase jump along $\phi = 0$ by subtracting an offset ϕ_s from the phase. This effectively corresponds to a rotation in the complex plane. After this operation, the skewness in the real and imaginary quadrature vanishes, and we obtain respectively $1 - L(\omega)$ and $\omega L(\omega)$ but displaces the anchor point from the real axis.

- At last, we subtract an offset Q_o from the imaginary quadrature such that its amplitude is symmetric around $Q = 0$. This corresponds to placing the anchor point back on the real axis of the complex-plane in **(c)**.

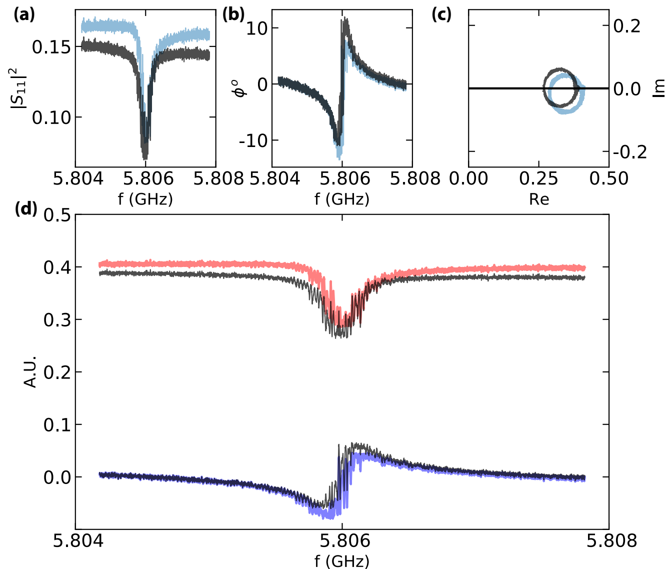

Figure 6.10: Reflection response S_{11} before (transparent coloured lines) and after (solid black) offsetting the phase and imaginary quadrature to undo Fano. S_{11} represented in the following order: (a) magnitude, (b) phase, (c) complex plane, (d) real (red) and imaginary (blue) part.

To study the broadening of the cavity due to noise, we calculated the average $\overline{S_{11}}$ taken over 100 single S_{11} measurements. The analytical expression is the convolution of a Gaussian distribution with the cavity Lorentzian profile resulting in a Voigt function [28] i.e.

$$\overline{S_{11}(\omega)} = \int_{\infty}^{\infty} S_{11}(\omega)P(\omega-\Omega)d\Omega \tag{6.7}$$

After removing the asymmetry from the single S_{11} responses using the procedure described above, the average response $\overline{S_{11}}$ is symmetric around its resonance, as shown in Fig.6.11. Note that $\overline{S_{11}(\omega)}$ is shallower and broader than a response of the cavity taken with a fast measurement.

By fitting $\overline{S_{11}(\omega)}$, we extract $\kappa = 2\pi\times$ 228 kHz and $\sigma_{\omega_c} = 2\pi\times$ 276 kHz.

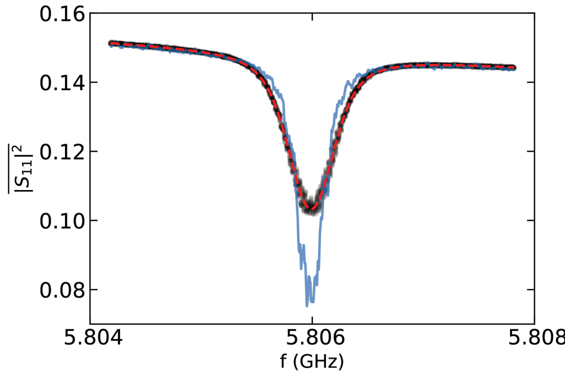

Figure 6.11: Single reflection response S_{11} (blue) next to an average $\overline{S_{11}}$ (black) taken over 100 fast reflection measurements. $\overline{S_{11}}$ is fitted with a Voigt profile (red dash) that is a convolution of a Lorentzian response with a Gaussian noise distribution function.

6.7.4. PHOTON NUMBER CALIBRATION

In this section, we present a method of estimating the intracavity photons by based on the input noise temperature of the LNA.

The number of photons N inside an ideal single port microwave cavity is calculated with,

$$N = \frac{\kappa_e}{\Delta^2 + (\kappa/2)^2}\frac{P_{\text{in}}}{\hbar\omega_d} \tag{6.8}$$

Here, P_{in} represent the power at the input of the cavity and $\Delta = \omega_{\text{d}} - \omega_{\text{c}}$. Estimating P_{in} is straightforward if the total input line attenuation (up to device) is known, but in practice that turns out to be more intricate. The total input line attenuation is determined by the cryo attenuators and the coaxial line attenuation. The first are manually placed onto the input line and have a stable attenuation which is known, whereas the latter is temperature dependent and unknown. We estimate residual coaxial line attenuation using the input noise temperature of the LNA i.e. T_{LNA} = 2 K as reported by [38]. By assuming that LNA noise contribution is dominant over all other noise components in the measurement chain, we can deduce the signal power at the input of the LNA based on the

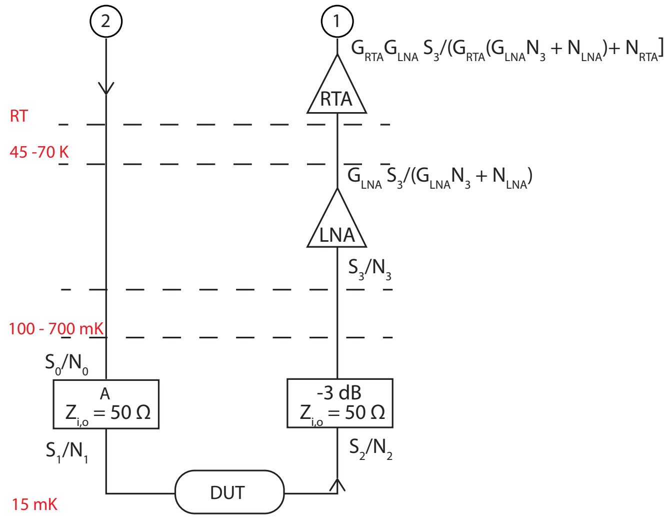

Figure 6.12: Signal-to-noise ratio (SNR) calculated at different stages and locations of the measurement chain. Measuring SNR with spectrum analyser of VNA allows for determining intracavity photons N. The device under test (DUT) is our electromechanical device.

measured signal-to-noise ratio (SNR). In Fig.6.12, we show the measurement chain corresponding to our experimental setup and show the SNR at different stages in the chain.

Whenever we inject a signal with power S_0 into the input line, we unwittingly add thermal noise coming internally from the signal generator and coaxial lines that have finite impedance $\mathrm{Z}_o = 50\,\Omega$. The integrated power of the noise is given by N_0 and as the signal propagates along the coaxial line down to our device, we record the signal-to-noise ratio S/N after it passes through the microwave components. The total input line attenuation is given with an effective single attenuator with attenuation A and its input and output impedance equal to $Z = 50\,\Omega$. S_0 and N_0 are equally attenuated by the attenuators, but the SNR at the output of the attenuator is higher than its input. The reason is that the attenuators contain internal resistors that also generate their own noise $\mathrm{N}_{\mathrm{att}} = \mathrm{k_b T \Delta f}$, with Δf the measurement bandwidth and added onto the signal. Noticeable is that $\mathrm{N}_{\mathrm{att}}$ depends on the temperature at which the attenuator is thermalized and not its resistance. As in our case, where the input and output impedance $Z = 50\ \Omega$, $\mathrm{N}_{\mathrm{att}}$ is transferred completely to the remaining circuit such that $\mathrm{N}_1 = \mathrm{N}_0 + \mathrm{N}_{\mathrm{att}}$. In the measurement setup, attenuators are placed strategically at each temperature stage to reduce the thermal noise originating from the higher temperature stages above. With total cry attenuation of 48 dB distributed over 5 stages, we reduce room temperature thermal noise to 5 mK at the lowest stage.

After the signal interacts with our sample, S_1 becomes S_2 and is related by the reflection coefficient of the cavity. It continues to propagate through a coaxial line from the sample to LNA. This results in an additional attenuation of S_2 of approximately 3 dB. At this stage, the total noise $\mathrm{N}_2 \approx \mathrm{N}_3$ is dominated by thermal noise originating from the 15 mK environment. Thermal noise from the higher stages have already been attenuated to

noise temperatures below 15 mK and therefore do not contribute. At the 4K stage S_3 is amplified once with the LNA and again at room temperature. Internal generated noise by the LNA with noise power temperature $k_b T_{LNA}$ added to the singal. Here, $T_{LNA} \gg 15$ mK and $G_{RTA} T_{LNA} \gg T_{RTA}, T_{SA}$. This means that the noise of the LNA dominates over all other noise components added after the LNA in the measurement chain i.e. RT amplifier and spectrum analyser. From this follows that the noise figure F= $\frac{SNR_o}{SNR_i}$ between the input of the LNA and input of the spectrum analyser is approximately 1. By measuring the SNR with the spectrum analyser at room temperature, we can derive the S_3 at the input of the LNA. We calculate the power at the output of the sample S_2 by offsetting S_3 by the attenuation between sample and LNA. In case the signal sent is off-resonant with the microwave cavity i.e. $\Delta \gg \kappa$, S_2 is equal to that of S_1 because the reflection coefficient is 1. Otherwise, the reflection response is needed to relate S_2 to S_1.

We show the calibration of the input line attenuation by driving the cavity on resonance and using the procedure described above. The frequency and power of the signal generator is set to respectively ω_c and -30 dBm.

- We measure SNR at spectrum analyser by subtracting noisefloor NF = -159 dBm (Δf = 0.015 Hz) from drive power P_d = -29 dBm, and we obtain SNR = 130. With F between LNA and spectrum analyser approximately 1, we get SNR at input of LNA.
- We estimate S_3 = -89 dBm at input of LNA since T_{LNA} = 2 K. We offset S_3 by the sample-LNA attenuation of 3 dB and obtain S_2 = -86 dBm.
- We obtain the power at the input of the sample S_1 by dividing the S_2 with the response function of the cavity. In presence of cavity noise, the cavity response is given by the Voigt function (Eq.(6.7)): $S_1 = \frac{S_2}{|S_{11}(\omega)|^2}$ = -85 dBm.
- With total -48 dB of cry attenuators, we derive 7 dB for attenuation of the input coaxial lines. This is reasonable considering, we have coaxial cables of several meters and cannot fully rule out the possibility of connectors that might not be properly tightened.

6.7.5. CAVITY NOISE SPECTRUM

To determine the frequencies of the mechanical noise sources responsible for the fluctuating cavity resonance, we have measured the cavity power spectrum. The cavity noise spectral density is obtained by driving the cavity on resonance i.e. $\omega_d = \omega_c$ and recording the fluctuations of the power that is reflected of the cavity with a spectrum analyser. This measurement is repeated n = 256 times with the pulse tube on and off and the average spectral densities normalized by the drive power S_{pp}/P_d are shown in Fig.6.13.

It is clear that with pulse-tube on, the noisefloor increases over the complete frequency interval. With the pulsetube off, the noisefloor drops, but we still observe a sharp resonance spaced periodically at 12.4 kHz from the drive. We attribute these to the mechanical resonances of the flipchip structure or the resonances of the Si shield itself. Low frequency noise peaks present within 100 Hz band from the drive originate from the supports of the fridge on which it is resting [54]. Note that we do not observe a change of the location of the noise peaks with the pulse tube on or off. Surprisingly, we do notice higher noise peaks up to 75 kHz from the drive when the pulse tube off. The

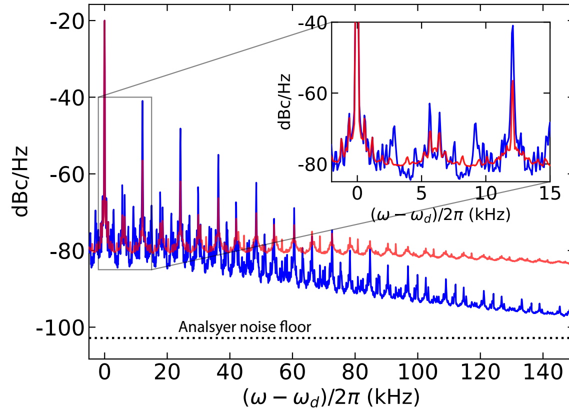

Figure 6.13: **Cavity noise spectroscopy comparison with pulse tube on and off.** Sharp noise sidebands appear when injecting a microwave drive on resonance with the cavity and monitoring the noise power of the reflected signal a spectrum analyser.The curve is an average taken over 256 measured traces with a resolution bandwidth of 100 Hz. The background of both curves converge to the analyser noise floor (black dash) for $\omega - \omega_d \gg \kappa$. **(Inset)** Zoom in on the region close to the drive where the highest noise peak (12.4 kHz) is located.

first sharp and highest sideband peak that is spaced at 12.4 kHz away from the drive also has higher harmonics. These decrease in amplitude as we move further from the drive. The appearance of higher harmonics is explained by the non-linear dynamics of the mechanical resonator. As mentioned in the main text, cavity noise results in uncontrollable detuning to both sides of the drive. When blue detuned by more than 24 kHz, the mechanical resonator obtains a negative linewidth where its dynamics becomes instable. Here, the mechanical fundamental mode depends on the large mechanical amplitudes and gives rise to higher-order electromechanical mixing (coupling) terms.

6.7.6. FULL RINGDOWN MEASUREMENTS

In Fig.6.14, we present the complete ringdown trace of the mechanical resonator, including its dynamics while the bluepump is on. The measurements are normalized to P_{blue}. Here, the redpump is switched on from t = 5 s, while the bluepump starts at t = 15 s. As the latter takes place, the amplitude of the mechanical oscillations increase and start to oscillate for the whole duration of t_b. We noticed that the amplitude of these oscillations depend on the strength P_{red} and P_{blue} and time duration of the bluepump t_b. The oscillations become more pronounced when P_{blue} = 0 dBm and t_b = 7 s, while P_{red} is increased from -15 to -5 dBm. While the oscillations stop immediately when the blue pump is off, the mechanical resonator does not start to ring down instantly. Instead, we notice an increase in amplitude for a time duration t_u that is dependent on P_{red}. Right after, a sharp jump occurs where the amplitude goes up for time duration t_s before the linear decay starts (log-scale). This settling time $t_{u,s} = t_u + t_s$ gets shorter as P_{red} is increased. Lastly, the mechanical resonator decays exponentially as expected, and its decay time decreases linearly with increasing P_{red}.

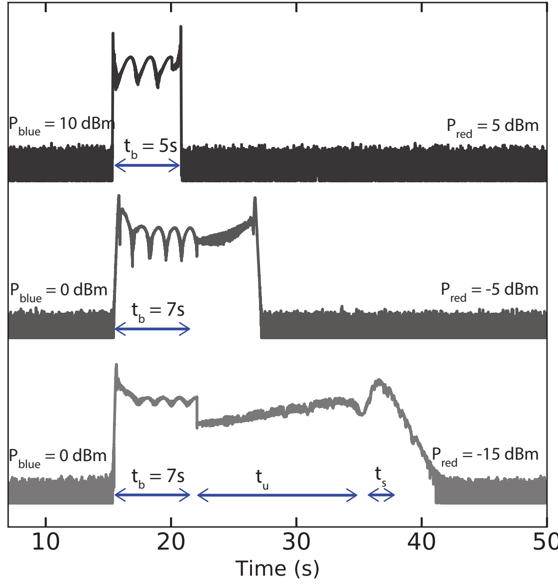

Figure 6.14: Mechanical ringdown with increasing redpump power P_{red} in log-scale. All measurements are normalized by the bluepump drive power P_{blue} that is switched on for a time duration of t_b.

6.7.7. MECHANICAL MODE TEMPERATURE ESTIMATION

The mechanical mode temperature shown in Fig.6.4d is estimated by first measuring the thermal-induced mechanical noise power upon resonantly driving the cavity. The analytical expression for the noise power spectral density at a mechanical frequency ω_{m} from the drive is given by

$$\begin{aligned}\frac{S_{\mathrm{pp}}(\omega=\omega_d\pm\omega_m)}{P_{\mathrm{d}}} &= \frac{16g_0^2\kappa_e^2}{\Delta^2+(\kappa/2)^2}\frac{1}{|\Gamma(\omega_d)|^2}|\chi_c(\omega=\pm\omega_m;\Delta=0)|^2\\ &\times\left[S_{\mathrm{xx}}^{\mathrm{th}}(\mp\omega_m)+\frac{n'_{\mathrm{add}}+1/2}{8\kappa_e g^2|\chi_c(\omega=\pm\omega_m;\Delta=0)|^2}\right]\\ &= F\times\left[S_{\mathrm{xx}}^{\mathrm{th}}(\mp\omega_m)+S_{\mathrm{xx}}^{\mathrm{imp}}(\mp\omega_m)\right]\end{aligned} \tag{6.9}$$

Here, n'_{add} is the noise added by the readout measurement chain and Γ and χ_c are the cavity reflection coefficient (Eq.(6.5)) and susceptibility, respectively. These are defined as:

$$\begin{aligned}n'_{\mathrm{add}} &= \left(\frac{1}{\eta_l}-1\right)\frac{1}{2}+\frac{1}{\eta_l}\left(n_{\mathrm{A}}+\frac{1}{2}\right)\\ \chi_{\mathrm{c}}(\omega;\Delta) &= \frac{-\mathrm{i}/2}{-\mathrm{i}(\omega-\Delta)+\kappa/2}\end{aligned} \tag{6.10}$$

with n_{A} is the photon noise quanta as a result of the input noise of the LNA and eta_l, the attenuation between sample and LNA. Note that the units of S_{xx} are given in mechanical

quanta n_m per Hertz (n_m/Hz). The equation above relates the measured noise power with the displacement spectral density of the mechanics. However, it does not account for the fluctuations (noise) in cavity resonance that our device experiences. Since the cavity resonance noise falls outside the 100 Hz measurement bandwidth of the spectrum analyser, the expectation value $\langle\cdot\rangle$ of Eq.(6.9) is used to correctly describe the measurement. By only considering the thermal noise at the redside of the drive, we get

$$\frac{\langle S_{\text{pp}}(\omega_d - \omega_m)\rangle}{\langle P_d\rangle} = \langle F \times \left[S_{\text{xx}}^{\text{th}}(\omega_m) + S_{\text{xx}}^{\text{imp}}(\omega_m) \right] \rangle \tag{6.11}$$

In case of resonantly driving the cavity, we assume that $\langle F S_{\text{xx}}^{\text{tot}}\rangle \rightarrow \langle F\rangle\langle S_{\text{xx}}^{\text{tot}}\rangle$ to first order. The mode temperature can then be calculated with

$$\begin{aligned} \langle T_m\rangle &= \frac{\hbar\omega_m}{k_b}\int_{-\infty}^{\infty}\langle S_{\text{xx}}^{\text{th}}(\omega)\rangle \mathrm{d}\omega \\ &\simeq \frac{\hbar\omega_m}{k_b}\langle S_{\text{xx}}^{\text{th}}(\omega_m)\rangle\gamma_m/2 \end{aligned} \tag{6.12}$$

The last step in Eq.(6.12) is justified since the measurement bandwidth is much larger than γ_m and therefore we can omit the integral and only use the thermal noise amplitude at $\pm\omega_m$ from the drive.

6

REFERENCES

[1] R. A. Norte, M. Forsch, A. Wallucks, I. Marinković, and S. Gröblacher, *Platform for measurements of the casimir force between two superconductors,* Physical review letters **121**, 030405 (2018).

[2] C. Reinhardt, T. Müller, A. Bourassa, and J. C. Sankey, *Ultralow-noise sin trampoline resonators for sensing and optomechanics,* Physical Review X **6**, 021001 (2016).

[3] M. Forsch, R. Stockill, A. Wallucks, I. Marinković, C. Gärtner, R. A. Norte, F. van Otten, A. Fiore, K. Srinivasan, and S. Gröblacher, *Microwave-to-optics conversion using a mechanical oscillator in its quantum ground state,* Nature Physics **16**, 69 (2020).

[4] R. W. Andrews, R. W. Peterson, T. P. Purdy, K. Cicak, R. W. Simmonds, C. A. Regal, and K. W. Lehnert, *Bidirectional and efficient conversion between microwave and optical light,* Nature physics **10**, 321 (2014).

[5] A. Wallucks, I. Marinković, B. Hensen, R. Stockill, and S. Gröblacher, *A quantum memory at telecom wavelengths,* Nature Physics **16**, 772 (2020).

[6] E. A. Sete and H. Eleuch, *High-efficiency quantum state transfer and quantum memory using a mechanical oscillator,* Physical Review A **91**, 032309 (2015).

[7] C. Simon, *Towards a global quantum network,* Nature Photonics **11**, 678 (2017).

[8] M. F. Gely and G. A. Steele, *Superconducting electro-mechanics to explore the effect of general relativity in massive superpositions,* arXiv preprint arXiv:2103.12729 (2021).

[9] R. Penrose, *On the gravitization of quantum mechanics 1: Quantum state reduction,* Foundations of Physics **44**, 557 (2014).

[10] C. Marletto and V. Vedral, *Gravitationally induced entanglement between two massive particles is sufficient evidence of quantum effects in gravity,* Physical review letters **119**, 240402 (2017).

[11] B. Zwickl, W. Shanks, A. Jayich, C. Yang, A. Bleszynski Jayich, J. Thompson, and J. Harris, *High quality mechanical and optical properties of commercial silicon nitride membranes,* Applied Physics Letters **92**, 103125 (2008).

[12] M. Yuan, M. A. Cohen, and G. A. Steele, *Silicon nitride membrane resonators at millikelvin temperatures with quality factors exceeding 108,* Applied Physics Letters **107**, 263501 (2015).

[13] R. Penrose, *On gravity's role in quantum state reduction,* General relativity and gravitation **28**, 581 (1996).

[14] A. Noguchi, R. Yamazaki, M. Ataka, H. Fujita, Y. Tabuchi, T. Ishikawa, K. Usami, and Y. Nakamura, *Ground state cooling of a quantum electromechanical system with a silicon nitride membrane in a 3d loop-gap cavity,* New Journal of Physics **18**, 103036 (2016).

[15] M. Yuan, V. Singh, Y. M. Blanter, and G. A. Steele, *Large cooperativity and microkelvin cooling with a three-dimensional optomechanical cavity,* Nature communications **6**, 1 (2015).

[16] I. Wilson-Rae, *Intrinsic dissipation in nanomechanical resonators due to phonon tunneling,* Physical Review B **77**, 245418 (2008).

[17] D. J. Wilson, *Cavity optomechanics with high-stress silicon nitride films* (California Institute of Technology, 2012).

[18] M. Cohen, *Optomechanics in a 3D microwave cavity*, Ph.D. thesis, Delft University of Technology (2019), casimir PhD Series, Delft-Leiden 2018-18.

[19] M. de Wit, G. Welker, K. Heeck, F. M. Buters, H. J. Eerkens, G. Koning, H. van der Meer, D. Bouwmeester, and T. H. Oosterkamp, *Vibration isolation with high thermal conductance for a cryogen-free dilution refrigerator,* Review of Scientific Instruments **90**, 015112 (2019).

[20] E. D. Black, *An introduction to pound–drever–hall laser frequency stabilization,* American journal of physics **69**, 79 (2001).

[21] W. Marshall, C. Simon, R. Penrose, and D. Bouwmeester, *Towards quantum superpositions of a mirror,* Physical Review Letters **91**, 130401 (2003).

[22] P.-L. Yu, T. Purdy, and C. Regal, *Control of material damping in high-q membrane microresonators,* Physical review letters **108**, 083603 (2012).

[23] A. H. Safavi-Naeini and O. Painter, *Design of optomechanical cavities and waveguides on a simultaneous bandgap phononic-photonic crystal slab,* Optics express **18**, 14926 (2010).

[24] A. H. Ghadimi, S. A. Fedorov, N. J. Engelsen, M. J. Bereyhi, R. Schilling, D. J. Wilson, and T. J. Kippenberg, *Elastic strain engineering for ultralow mechanical dissipation,* Science **360**, 764 (2018).

[25] S. S. Inc., *Sonnet precision electromagnetics,* (1983).

[26] M. Khalil, M. Stoutimore, F. Wellstood, and K. Osborn, *An analysis method for asymmetric resonator transmission applied to superconducting devices,* Journal of Applied Physics **111**, 054510 (2012).

[27] B. Brock, M. Blencowe, and A. Rimberg, *Frequency fluctuations in tunable and nonlinear microwave cavities,* Physical Review Applied **14**, 054026 (2020).

[28] B. Armstrong, *Spectrum line profiles: the voigt function,* Journal of Quantitative Spectroscopy and Radiative Transfer **7**, 61 (1967).

[29] J. D. Teufel, T. Donner, D. Li, J. W. Harlow, M. Allman, K. Cicak, A. J. Sirois, J. D. Whittaker, K. W. Lehnert, and R. W. Simmonds, *Sideband cooling of micromechanical motion to the quantum ground state,* Nature **475**, 359 (2011).

[30] A. Reed, K. Mayer, J. Teufel, L. Burkhart, W. Pfaff, M. Reagor, L. Sletten, X. Ma, R. Schoelkopf, E. Knill, *et al.*, *Faithful conversion of propagating quantum information to mechanical motion,* Nature Physics **13**, 1163 (2017).

[31] S. Weis, R. Rivière, S. Deléglise, E. Gavartin, O. Arcizet, A. Schliesser, and T. J. Kippenberg, *Optomechanically induced transparency,* Science **330**, 1520 (2010).

[32] A. H. Safavi-Naeini, T. M. Alegre, J. Chan, M. Eichenfield, M. Winger, Q. Lin, J. T. Hill, D. E. Chang, and O. Painter, *Electromagnetically induced transparency and slow light with optomechanics,* Nature **472**, 69 (2011).

[33] T. J. Kippenberg and K. J. Vahala, *Cavity optomechanics: back-action at the mesoscale,* science **321**, 1172 (2008).

[34] A. Schliesser and T. J. Kippenberg, *Cavity optomechanics with whispering-gallery mode optical micro-resonators,* Advances In Atomic, Molecular, and Optical Physics **58**, 207 (2010).

[35] M. Aspelmeyer, T. J. Kippenberg, and F. Marquardt, *Cavity optomechanics: nano- and micromechanical resonators interacting with light* (Springer, 2014).

[36] A. Schliesser, R. Rivière, G. Anetsberger, O. Arcizet, and T. J. Kippenberg, *Resolved-sideband cooling of a micromechanical oscillator,* Nature Physics **4**, 415 (2008).

[37] V. Singh, S. Bosman, B. Schneider, Y. M. Blanter, A. Castellanos-Gomez, and G. Steele, *Optomechanical coupling between a multilayer graphene mechanical resonator and a superconducting microwave cavity,* Nature nanotechnology **9**, 820 (2014).

[38] *lownoisefactory.com :: 4-8 ghz single junction,* https://www.lownoisefactory.com/products/iso/lnf-isc4_8a/, (Accessed on 08/25/2021).

[39] F. Massel, T. T. Heikkilä, J.-M. Pirkkalainen, S.-U. Cho, H. Saloniemi, P. J. Hakonen, and M. A. Sillanpää, *Microwave amplification with nanomechanical resonators,* Nature **480**, 351 (2011).

[40] T. Kippenberg, H. Rokhsari, T. Carmon, A. Scherer, and K. Vahala, *Analysis of radiation-pressure induced mechanical oscillation of an optical microcavity,* Physical Review Letters **95**, 033901 (2005).

[41] R. Ma, A. Schliesser, P. Del'Haye, A. Dabirian, G. Anetsberger, and T. J. Kippenberg, *Radiation-pressure-driven vibrational modes in ultrahigh-q silica microspheres,* Optics letters **32**, 2200 (2007).

[42] T. Carmon and K. J. Vahala, *Modal spectroscopy of optoexcited vibrations of a micron-scale on-chip resonator at greater than 1 ghz frequency,* Physical review letters **98**, 123901 (2007).

[43] P.-L. Yu, K. Cicak, N. Kampel, Y. Tsaturyan, T. Purdy, R. Simmonds, and C. Regal, *A phononic bandgap shield for high-q membrane microresonators,* Applied Physics Letters **104**, 023510 (2014).

[44] J. Rieger, A. Isacsson, M. J. Seitner, J. P. Kotthaus, and E. M. Weig, *Energy losses of nanomechanical resonators induced by atomic force microscopy-controlled mechanical impedance mismatching,* Nature communications **5**, 1 (2014).

[45] I. Wilson-Rae, N. Nooshi, W. Zwerger, and T. J. Kippenberg, *Theory of ground state cooling of a mechanical oscillator using dynamical backaction,* Physical review letters **99**, 093901 (2007).

[46] F. Marquardt, J. Harris, and S. M. Girvin, *Dynamical multistability induced by radiation pressure in high-finesse micromechanical optical cavities,* Physical review letters **96**, 103901 (2006).

[47] A. Clerk and F. Marquardt, *Basic theory of cavity optomechanics,* (2014) pp. 5–23.

[48] S. Mancini, D. Vitali, and P. Tombesi, *Optomechanical cooling of a macroscopic oscillator by homodyne feedback,* Physical Review Letters **80**, 688 (1998).

[49] M. Poggio, C. Degen, H. Mamin, and D. Rugar, *Feedback cooling of a cantilever's fundamental mode below 5 mk,* Physical Review Letters **99**, 017201 (2007).

[50] H. M. Wiseman and G. J. Milburn, *Quantum measurement and control* (Cambridge university press, 2009).

[51] S. Chakram, Y. Patil, L. Chang, and M. Vengalattore, *Dissipation in ultrahigh quality factor sin membrane resonators,* Physical review letters **112**, 127201 (2014).

[52] P. Moradi and A. Bahrami, *Design of an optomechanical filter based on solid/solid phoxonic crystals,* Journal of Applied Physics **123**, 115113 (2018).

[53] C.-M. Gärtner, *Advanced membrane architectures for multimode optomechanics* (Wien, 2020).

[54] *Ld dilution refrigerator measurement system - bluefors,* https://bluefors.com/products/ld-dilution-refrigerator/, (Accessed on 08/25/2021).

7

Conclusion and Outlook

7.1. LOW LOSS LUMPED ELEMENT RESONATOR

In **chapter 4**, we have investigated the effect of resonator geometry on its conductive losses in a cryogenic environment. Using Sonnet electromagnetic (EM) simulations [1], we design a lumped element resonator that consists of a big loop with its diameter $D \sim$ 1.2 mm and is shunted with finger capacitors. These represent the inductor and the capacitor of the circuit, respectively, and is made of a 100 nm thick superconducting NbTiN film on a sapphire substrate. On the same substrate, we have also added a CPW resonator since these are mainly limited by dielectric losses at cryogenic temperatures [2, 3]. Hence, it serves as an excellent insight into the dielectric losses of the device. Both resonators are coupled to a transmission line that is shorted to ground. This is known as reflection architecture, where the reflected signal contains information about the frequency response of the resonators. The substrate sits on top of a copper (Cu) surface and is enclosed in a lossless aluminium (Al) box. We first investigate the resonators losses that arise to the finite conductivity of Cu. By assuming $\mathrm{RRR_{Cu}} = 1$, we perform a frequency sweep to probe the response of the resonators. By fitting the response to a Lorentzian profile, we extract 100× difference in loss between the CPW and LGR, with the LGR having superior losses with $\mathrm{Q}_i \approx 6 \times 10^4$. The loss here arises from the large stray magnetic fields generated by the big loop that induces eddy currents on the lossy Cu surface.

Upon replacing the loop inductor of the LGR with a meandering inductor and sweeping $\mathrm{RRR_{Cu}}$ from 1 to 100, we witness 10× reduction in loss across the full simulated range. For clarity, we call this design the meandered gap resonator (MGR).

At last, we also study the effect of dielectric loss on MGR design by assuming a lossy dielectric film of 10 nm between the substrate and metal. By sweeping the loss tangent $10^{-5} < \tan\delta < 10^{-1}$, we observe that the MGR has lower dielectric loss than the CPW for $\tan\delta > 10^{-4}$, while still limited by conductive losses for loss tangent $\tan\delta < 10^{-4}$.

Note that in our simulations with dielectric loss comes only from the interfacial layer between the substrate and metal. We have neglected losses that come from substrate-air and metal-air, as these are generally negligible [4]. For convenience, we have also assumed a homogenous layer, which might not necessarily be the case as reported by Ref. [5]. Our simulation nevertheless provides a good picture of the interplay between the magnetic and dielectric loss in superconducting lumped element resonators.

To reduce dielectric losses of the MGR further, one can replace the finger capacitors of the MGR with rectangular pads. The reason is that the pads have larger mode volume and results in a smaller electric field participation ratio at the substrate-metal interface. We have shown that it has a higher quality factor than the LGR and MGR for all $\mathrm{RRR_{Cu}}$ and $\tan\delta$.

Another type of loss we have neglected is radiation losses, as most resonators used in superconducting experiments are electrically shielded from the environment with a metal lid [6] and therefore this type of loss becomes irrelavant.

7.2. BROADBAND CRYOGENIC ACCELEROMETER

In **chapter 5**, we have assembled an electromechanical device consisting of a superconducting lumped-element resonator and high tensile stress SiN square membrane and

have it to function as a cryogenic accelerometer. The device is placed in a cryogenic environment (Bluefors LD-250) and by comparing characterization measurements with Sonnet EM simulations, we calibrate a single photon-phonon coupling $g_0 \approx 2\pi\times$ 2 Hz, which corresponds to a gap distance d = 800 nm. We used a new flipping technique such that we can omit using epoxy to fix both devices, which generally give greater gap distances [7, 8]. It is also very modular by nature, as it also allows us to swap membrane devices easily in case the SiN film is damaged or fractured. This is not possible when using epoxy to fixate the devices.

The reflection response S_{11} of the cavity shows fluctuations of the cavity resonance frequency and amplitude. We believe that this noise originates from vibrational noise of the environment as a result of the mechanical freedom in our system. Specifically, the crycooler (pulse-tube) of the dilution refrigerator is the main source of mechanical noise, which is confirmed by switching off the pulse-tube. Here, the fluctuations in resonance frequency of the cavity response decrease by half to $\sigma_{\omega_c} \approx 2\pi\times$ 20 kHz, similar to the cavity total linewidth κ. Since the electromechanical device is sensitive to mechanical noise, it is used as a cryogenic accelerometer to quantify the acceleration of the vibrations transferred to the sample. This is a useful insight since pulse-tube vibrational noise is known to interfere with the sensitive measurements involved in quantum experiments and can cause all sorts of electrical noise.

We characterize the noise by driving the cavity on resonance and measuring the noise power spectral density. Here, we observe many mechanical resonances within 200 kHz from the drive. We believe that the high frequency (~ kHz) spikes can be attributed to resonances of the flipchip structures and cable mechanical resonances, whereas the lower frequencies (< 200 Hz) to the supports of the fridge. We calibrate the displacement sensitivity of the accelerometer with an analytic expression of the power spectrum that we have derived using the solutions of quantum Heisenberg-Langevin equations of motion. In the calibration procedure, we account for the effects of cavity noise using Monte Carlo sampling of the analytical power spectral density. Based on this, we estimate a mode temperature T_m = 300 mK.

Furthermore, we obtain the acceleration sensitivity by normalizing the displacement sensitivity with mechanical susceptibility. We extract an acceleration sensitivity in the range of 1 mg/$\sqrt{\text{Hz}}$ from DC to 10 kHz and 10 mg/$\sqrt{\text{Hz}}$ at higher frequencies. At the mechanical resonance, the accelerometer is the most sensitive, reaching sensitivity 4 μg/$\sqrt{\text{Hz}}$. Our calibration relies on the intra cavity photon number N. Determining the internal photon number is not so straightforward in presence of cavity noise and depends on the measurement bandwidth. Using a small bandwidth, we observe that cavity frequency response does not follow a Lorentzian profile, but instead is convoluted with the cavity noise distribution into a Voigt function. A Voigt model need to be used in order to correctly determine N, because assuming a Lorentzian cavity response will result in overestimating N and therefore underestimating T_m and the acceleration sensitivity (unjustly high resolution).

7.3. HIGH-Q CAVITY ELECTROMECHANICS WITH SIN MEMBRANE AND PHONONIC SHIELD

In **chapter 6**, we make use of a new flipping technique in combination with a phononic shield surrounding the SiN membrane and thereby realizing a high-Q and high coorperativity electromechanical device. With this technique, we are able to tightly clamp the mechanical device and systematically reach sub-μm gaps.

As in chapter 5, we have used a custom-built flipchip tool to assemble an electromechanical device consisting of a superconducting lumped-element resonator and a SiN membrane within a phononic shield [9]. Here, the phononic shield suppresses the radiation losses of the membrane that is introduced by the tight clamping of the flipchip tool [10]. We realize the phononic shield through DRIE etching with a total of 2 unit cells on each side.

The device is placed in a cryogenic environment (Oxford Triton 200) and upon characterizing the electromechanical device, we witness an instable cavity resonance frequency. We believe that the noise comes from vibrations of the environment i.e. pulse-tube, vacuum pumps etc. With the pulse-tube switched off, the cavity noise $\sigma_{\omega_c} \approx 2\pi\times$ 276 kHz and is greater than $\kappa \approx 2\pi\times$ 228 kHz. The cavity noise is also substantial compared to the device measured in chapter 5. We have nevertheless been able to record OMIT and ringdown measurements, where we extract intrinsic $Q_\mathrm{m} = 3.3 \times 10^7$. We find multiphoton coorperativity $C \sim 12000$ at maximum redpump power limited by the compression point of the 4K low noise amplifier. We estimate the intra cavity photons N that corresponds to the redpump drive to be approximately 4×10^6.

Furthermore, we measure the mechanical thermal noise of the device to determine the mode temperature. We inject a microwave tone on resonance with the cavity and record the I and Q traces at the redside of the cavity for 45 seconds, repeated 32 times. The thermal sideband amplitude fluctuates and the values are scattered over a range of 20 dB, corresponding to mode temperatures between 3 and 300 mK. The reason is that cavity noise, in presence of a static drive on cavity resonance, effectively results in cooling and amplification. With our current estimated C and γ_m, we find that the cavity need to be shifted by only 24 kHz to the red side, such that the drive is blue detuned at which the mechanics enters an instability regime. Here the mechanical resonator start to exhibit non-linear dynamics resulting in limit cycle oscillations [11].

7.4. THE NEXT STEPS...

We currently have all the ingredients device-wise to take this research into the next phase, which is to cool the mechanical SiN resonator to its quantum groundstate. However, we are constrained by the challenging conditions of the environment in which the device is placed, i.e. dilution refrigerator. Although the cryocooler (pulse-tube) of the fridge is an essential piece of equipment that has enabled all the experiments discussed in the thesis, it also generates ~ 1-2 Hz acoustic pulses (like a hammer) due to its internal gas pressure oscillations. The pulse-tube noise can subsequently cause large amplitude vibrations of a wide range of resonant structures in the fridge, sample mounting system, or even the chip itself, resulting in flicker and fluctuations of the electromechanical cavity frequency. This is very undesirable for us as experimentalists because the mechanical

degree of freedom in the electromechanical system can couple easily to vibrational noise of the environment and limits our ability to probe and control the mechanics. Cavity noise poses a problem in attempting to cool the mechanical resonator to its quantum groundstate. Groundstate cooling requires a stable cavity because maximum cooling takes place if the drive tone ω_d is resonant with mode $\omega_c - \omega_m$. In this case, phonons are scattered into photons with maximum rate of $\gamma_{opt} = 4g_0^2 N/\kappa$. As in our case, the cavity suffers from mechanical induced noise and therefore the cooling mode becomes time dependent, i.e. $\omega_c(t) - \omega_m$. Since reddrive that is outputted from the microwave generator is fixed in frequency, the cooling rate will also become be time dependent, with the average cooling rate $\overline{\gamma_{opt}}$ lower than the maximum obtainable rate γ_{opt}.

Groundstate cooling of the mechanics suddenly becomes more difficult than just simply red sideband pumping of the cavity. Switching off the pulse-tube is not an optimal solution because we lose cryogenic cooling power and this can damage other equipment required to keep the fridge working. We, therefore, discuss some other approaches that can be useful in future experiments in limiting and mitigating vibrational noise generated by the pulse-tube.

General solutions that suppress vibrational noise outside the cryostat involve placing the pumps in a separate room or using sand to dampen vibration transfer via vacuum lines. In addition, our cryostat supports a large mass aluminum plate, with an added mass of 500 kg. This added mass helps to absorb vibrations that couple through the floor (connecting the frames) and thermal links (copper braids) between cold head and cryostat flanges (4K and 50 K flanges). An extra feature that our cryostat possesses is a helium battery. Cryogenic systems manufacturer Bluefors offers a battery option with their standard dilution systems. This feature allows for a temporary elimination of cooling with the pulse-tube and therefore no vibration noise from the pulse-tube. The battery is basically an external cylinder that contains helium gas which can be pumped to a container located at the 4K stage, where it is liquified by the pulse-tube. Subsequently, the pulse can be switched off and cooling power is provided by the liquified helium, with a hold time of approximately 3 to 4 hours. By turning off the pulse-tube, we have seen a reduction of the number of mechanical resonances, but as witnessed in Fig.5.3 of chapter 5, there are still spurious resonances spaced at 45 kHz. Although the exact source of this resonance is unknown, we believe it to be vibration induced. These could be the vibration levels of the building (the support frame is rigidly mounted to the lab floor) or the vibrations of the vacuum lines. Therefore, eliminating the pulse-tube is not enough, and we need to further reduce the mechanical noise transferred to our sample.

We propose a technique used by the scanning probe community that is to decouple the sample space from the mixing chamber stage of the fridge by suspending it with springs [12], as shown in Fig.7.1a,c. Here, they have designed a mechanical low-pass filter that is a network of masses and springs connected together and is able to suppress vibrations between 50 Hz up to 100 kHz at the sample space. We have designed a simpler mechanical low-pass filter consisting of one mass suspended by 3 springs (Fig.7.1b,d), which we have not characterized yet.

In designing this filter, we are constrained by the limited space of approximately $\Delta L =$ 30 cm beneath the mixing chamber plate , which also sets a lower limit for the resonance frequency of the mass-spring $\omega_{ms} = \sqrt{g/\Delta L} \approx 6$ Hz. We have a mass of 7 kg and

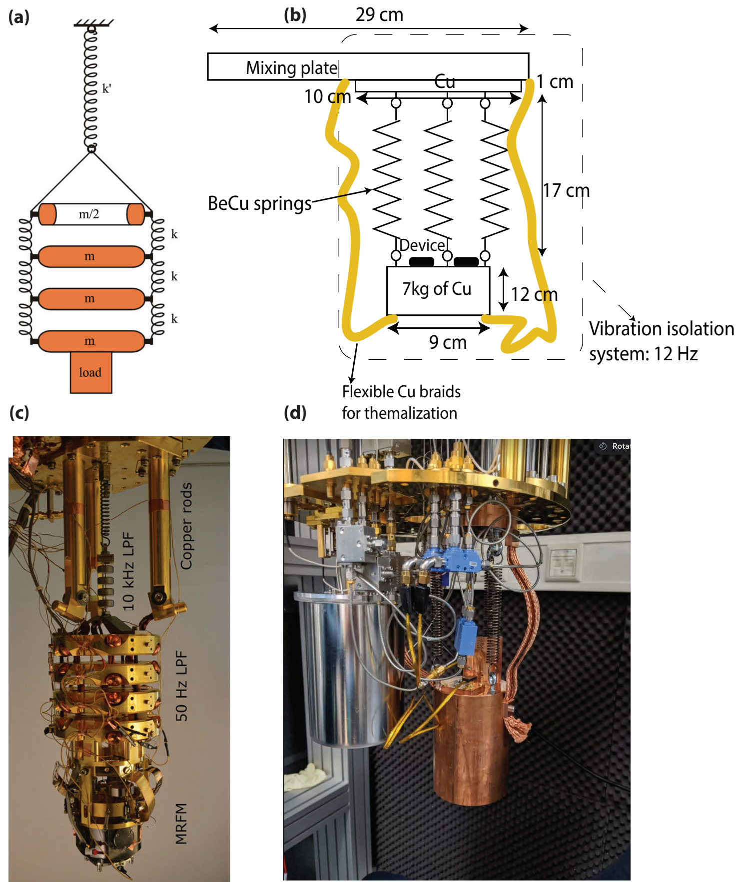

Figure 7.1: **Vibration isolation systems for cryogenic systems.** **(a)** A network of masses connected to springs which suppress vibration between 50 Hz and 100 kHz at sample space [12]. **(b)** Simple vibration isolation systems designed for our experimental setup with resonance at 12 Hz. **(c)** and **(d)** are physical realization of **(a)** and **(b)**, respectively.

3 beryllium copper (BeCu) springs, each with a spring constant of 333 N/m and totals to 1000 N/m. In equilibrium, the springs are elongated by 7 cm and the cut-off frequency is approximately 12 Hz. We have not been able to fully characterize this filter in a cryogenic environment yet, and might be a useful piece of equipment to integrate into future experiments to further suppress vibrational noise. We have attached flexible copper braids to improve thermalization of the Cu mass. A weak thermal link can increase cooldown times significantly and prevent the sample from being thermalized with the mixing chamber plate. A few test cooldowns with this 7 kg mass-spring isolation system have revealed a roughly 40% increase in cooldown time. In addition, we also suggest replacing standard coaxial cables with Delft Circuit [13] flexible coaxial cables for measuring the device. The latter have shown to have less phase noise in presence of

mechanical vibrations.

Another approach to tackle cavity noise is to frequency lock the measurement to the cavity noise. One method to achieve this objective and also frequently employed in for example optical communication [14], atomics clock [15] and gravitational-wave observatories [16], is called the Pound-Drever-Hall (PDH) frequency stabilization [17]. In the above-mentioned applications, a highly frequency-stable laser source is very much desirable. The frequency of even the most advanced laser sources are not stable and drift over time. To counter this effect, the PDH stabilization technique is used. The general concept is that the laser light is sent to a Fabry-Perot cavity and the intensity of the reflected signal is monitored in the phase quadrature, where the response is antisymmetric. A drift in frequency results in a change in intensity, which is measured, and the error signal is used to adjust the output frequency of the laser. The measurement is made using a form of nulled lock-in detection, which decouples the frequency measurement from the laser's intensity.

In our case, the stability of the microwave source is not a problem, but it is the cavity resonance frequency that is fluctuating. It is not practical to obtain control over the cavity resonance frequency in our setup. Instead, the PDH frequency stabilization technique is applied to the microwave source to follow the fluctuations in cavity resonance. The microwave implementation of the PDH scheme is shown in Fig.7.2 and is currently being integrated in our measurement setup.

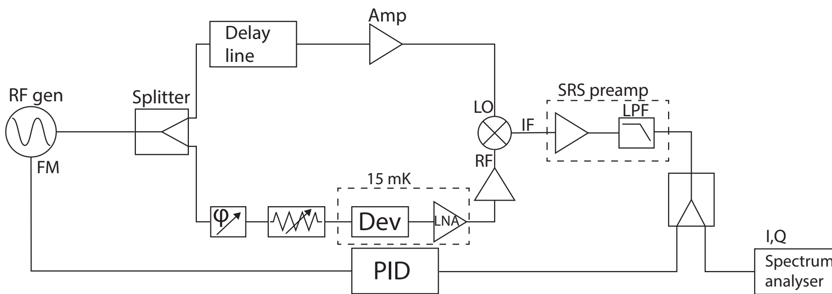

Figure 7.2: Block diagram of PDH scheme in microwave domain for locking microwave drive to the cavity noise.

With the efforts mentioned above to overcome vibrational noise, we believe that groundstate cooling of the mechanical resonator and even mechanical quantum state engineering can be realized in the near future.

REFERENCES

[1] S. S. Inc., *Sonnet precision electromagnetics,* (1983).

[2] A. Bruno, G. De Lange, S. Asaad, K. Van Der Enden, N. Langford, and L. DiCarlo, *Reducing intrinsic loss in superconducting resonators by surface treatment and deep etching of silicon substrates,* Applied Physics Letters **106**, 182601 (2015).

[3] D. P. Pappas, M. R. Vissers, D. S. Wisbey, J. S. Kline, and J. Gao, *Two level system loss in superconducting microwave resonators,* IEEE Transactions on Applied Superconductivity **21**, 871 (2011).

[4] V. Lahtinen and M. Möttönen, *Effects of device geometry and material properties on dielectric losses in superconducting coplanar-waveguide resonators,* Journal of Physics: Condensed Matter **32**, 405702 (2020).

[5] B. Chiaro, A. Megrant, A. Dunsworth, Z. Chen, R. Barends, B. Campbell, Y. Chen, A. Fowler, I. Hoi, E. Jeffrey, *et al.*, *Dielectric surface loss in superconducting resonators with flux-trapping holes,* Superconductor Science and Technology **29**, 104006 (2016).

[6] D. Rosenberg, S. J. Weber, D. Conway, D.-R. W. Yost, J. Mallek, G. Calusine, R. Das, D. Kim, M. E. Schwartz, W. Woods, *et al.*, *Solid-state qubits: 3d integration and packaging,* IEEE Microwave Magazine **21**, 72 (2020).

[7] A. Noguchi, R. Yamazaki, M. Ataka, H. Fujita, Y. Tabuchi, T. Ishikawa, K. Usami, and Y. Nakamura, *Ground state cooling of a quantum electromechanical system with a silicon nitride membrane in a 3d loop-gap cavity,* New Journal of Physics **18**, 103036 (2016).

[8] M. Yuan, V. Singh, Y. M. Blanter, and G. A. Steele, *Large cooperativity and microkelvin cooling with a three-dimensional optomechanical cavity,* Nature communications **6**, 1 (2015).

[9] P.-L. Yu, K. Cicak, N. Kampel, Y. Tsaturyan, T. Purdy, R. Simmonds, and C. Regal, *A phononic bandgap shield for high-q membrane microresonators,* Applied Physics Letters **104**, 023510 (2014).

[10] D. J. Wilson, *Cavity optomechanics with high-stress silicon nitride films* (California Institute of Technology, 2012).

[11] M. Ludwig, B. Kubala, and F. Marquardt, *The optomechanical instability in the quantum regime,* New Journal of Physics **10**, 095013 (2008).

[12] M. de Wit, G. Welker, K. Heeck, F. M. Buters, H. J. Eerkens, G. Koning, H. van der Meer, D. Bouwmeester, and T. H. Oosterkamp, *Vibration isolation with high thermal conductance for a cryogen-free dilution refrigerator,* Review of Scientific Instruments **90**, 015112 (2019).

[13] *Delft circuits | flexible cryogenic cables | quantum hardware provider,* `https://delft-circuits.com/`, (Accessed on 09/23/2021).

7

[14] H. Al-Taiy, N. Wenzel, S. Preußler, J. Klinger, and T. Schneider, *Ultra-narrow linewidth, stable and tunable laser source for optical communication systems and spectroscopy,* Optics Letters **39**, 5826 (2014).

[15] Y. Jiang, A. Ludlow, N. D. Lemke, R. W. Fox, J. A. Sherman, L.-S. Ma, and C. W. Oates, *Making optical atomic clocks more stable with 10- 16-level laser stabilization,* Nature Photonics **5**, 158 (2011).

[16] B. Abbott, R. Abbott, R. Adhikari, P. Ajith, B. Allen, G. Allen, R. Amin, S. Anderson, W. Anderson, M. Arain, *et al.*, *Ligo: the laser interferometer gravitational-wave observatory,* Reports on Progress in Physics **72**, 076901 (2009).

[17] E. D. Black, *An introduction to pound–drever–hall laser frequency stabilization,* American journal of physics **69**, 79 (2001).

ACKNOWLEDGEMENTS

The work in this PhD thesis would not have come about if I did not have the right people around me. Sometimes I wonder what would have happened if I had to do this alone. I get anxious about that thought and prefer not to think about it. That is why I want to express my gratitude here to everyone who has been supportive and encouraged me when things were not going as expected.

First of all, I would like to express my deepest thanks to **Gary** for offering me a PhD position 5 years ago. During this PhD journey, we had lots of ups and downs and not everything went as planned, but nevertheless, you were always optimistic and positive. Although you were a very busy person, I could always walk into your office for a quick chat. Your enthusiasm for physics is really on another level and your ability to communicate difficult topics is impressive. Therefore I did not hesitate to use of your strong intuition of various subjects, whether it was fabrication, hardware/software or physics. With your supervision and guidance, I have grown as a researcher and more importantly, I learned how to ask the right questions that lead to interesting data.

2 years into my PhD, there came **Adrian**, the new postdoc to strengthen the membrane team. You were eager to learn everything: fabrication, experiments, design, simulations and measurements. And you did. I am honestly impressed that this happened really fast considering that you have been a theorist your whole academic career. With your critical attitude and your attention to detail, you have been a valuable asset to the team. Therefore, without your presence and expertise, this project would have progressed at a far slower pace. Our time was not only limited within the lab. I enjoyed our cooking session together where I would often eat all your dried mango, our trips to the market in The Hague and our frequent grocery shopping trips. Our coffee and lunch breaks often revolved around topics such as social inequalities, politics and the essence of life. I admire you as a person because you have strong values and morals and you act according to those without compromise. Soon your time in the group will come to an end, and I wish you all the best in taking the next step.

Jean-Paul, I am entertained by your ingenuity and enthusiasm, especially where you once used your phone to measure the frequency of the cryocooler. And of course, your sense of humor needs to be mentioned and I cannot remember one joke that you made where I did not laugh. I am sure that in the coming years of your PhD you will have lots of new and interesting things to dig into with your devices

Jasper, thanks for looking out for the fridges, especially when we forgot to fill the nitrogen traps. I must also thank you for keeping the labs organised because it saved us a lot of time from running back and forth to look for parts. You are a go-getter but

unfortunately the cleanroom does not always cooperate. Nevertheless, this should not demotivate you and soon you will reap the benefits.

Jacob, you are always very open and helpful and I am amazed by your general knowledge on almost every subject. When talking to you I got to learn more about music, North American politics and Japan. **Robin**, I am thankful to have you as an office mate, because you guys never complained when I had my spotify playlist running on the background. It is nice to see that you grow each day and get more confident about your project.

I am the last one of the previous generation of PhD students in Steelelab to graduate. All of my old fellow PhD students have already left the group to find another challenge in life. That is why I also want say a few words about the fun and educational times we went through.

When I started, **Martijn** you showed me the way in cleanroom and I could not ask for a better mentor. We were not only colleagues, but also good friends outside work. You got me into crypto and looking back now, I do not regret it. It is nice to see that you have made a successful transition to industry.

Mark, you were one of the group's microwave gurus. You introduced me to the labs and all the equipment and instruments. You have also taught me the art of microwave measurements and debugging. At lunch, I enjoyed your outspoken opinions and your passion for gaming. I could always walk into your office and you would be available to help. So thanks again for your extensive guidance and help throughout the first years of my PhD. I hope you like working in industry and wonder whether your view of cooperates has changed.

Daniel, the other microwave guru. It was as if you had been sent to earth by the optomechanical gods. You knew the answer to most of the issues that came up during my experiments. Thanks for all the constructive discussions and feedback that helped tremendously in giving me direction during my PhD. I wish you all the best and hope you yourself can start your own lab in the near future.

Mario, I have known you since the master program. You are one of the most relaxed persons I know and have never seen you stressing. We were not only colleagues, but we are also good friends outside work, whom I could share everything with. I will never forget the great times we had together at parties and hope we can relive those good old times in the near future. Good luck with pursuing ion trap based quantum computers in the UK.

Ines, your project started with lots of fabrication and experimental setbacks and was considered extremely difficult by your peers. However, you did not let that demotivate you and continued working hard. In the end, all the extra long hours paid off and resulted in amazing results. You and Daniel are a prime example of what a great team can achieve when working efficiently. I have no doubt that you will also be successful as a postdoc in Zurich.

Byoung-Moo, from very early on, we became best mates in and outside the Lab. I now already miss the moments where you would enter my office to have a chat. I am happy for you went back to South Korea to become a senior scientist.

Marios, I did not know you very well outside of work, but that changed after our trip to US for the march meeting. We had a great time and will cherish the moments at the pubs. I noticed that you get disappointed when you start thinking about life and society as a whole, but I hope you do not take it too seriously.

Yildiz, we have had great times together for example in the US, where we often could not resist the temptation of all the sweet delicious pastries. Thanks to you I got to know Thrive and other great people. You are a very social person and connecting people with different backgrounds is your strength. Now that you have transitioned into industry, I hope you found the right place that you feel home at.

Felix, I admire your level of planning, precision, documentation and organisation. Together with Mark, you made a great team and achieved much success. I liked the fact that you were active physically and challenged me to take part in a mud runs. Life after PhD has changed for you since you moved back to Germany and became a dad. Since I have not spoken to you for a long time, I hope all is well with you and your family.

Nikos, while you mostly worked alone, your presence in the group could not be unnoticed. I liked that I could spar with you about the gym, health, eating diets and fashion. We could level very easily, because you are outspoken and honest.

Hadi, you are a graphene researcher at heart and hope you are enjoying your new challenge at mechanical engineering. I am extremely grateful that I could use your help and expertise in the cleanroom when fabricating the membranes.

Fatimeh, unfortunately we did not collaborate as much as I would have liked to since you had very interesting ideas of what we could do with 3D cavities, membranes and magnetic particles. Goodluck in continuing your scientific career in Canada. By the way, the safran from Iran you brought me once, is amazing.

Hossein, it was pleasant to have you here in Delft for a few months. I thank you for making a start to the optical setup in our lab. Your company and patience made my work in the cleanroom more bearable.

Hiresh, you were the first bachelor student I supervised. Although the project did not go as expected, I applaud your courage for taking up the challenge. I congratulate you on obtaining your master degree recently.

My time as a PhD in QN department would not have been fun were it not for the working environment created by its members. I cannot begin to express my thanks to **Claus** for sharing and demonstrating his phononic shield recipe with me and also letting me use his tools in the cleanroom. With your devices we have been able to bring our experiments to new heights. **Moritz**, due to you I got into digital 3D drawing with blender. **Joao** and **Matthijs**, I would like to thank you for letting us use your optical setup

to characterise our membrane quality factors. **Rob**, **Bas**, **Jingkun**, **Irina**, **Brecht**, **Luigi**, **Rasa**, **Robby**, **Samer**, **Lacopo**, **Sonakshi**, **Fellipe**, **Yuvan**, **Andreas**, **Igor**, **Fred**, **Martin**, **Thierry**, **duardo**, **Sabena**, **Allard**, **Hristo**, **Adrian Rol (QT)**, **Niels Bultink** (QT), **Ramiro sagastizabal** (QT), **Christian Dickel** (QT), **Alessandro Bruno** (QT), **Nandini** (QT) (and everyone else I forgot) for the occasional small talks in the coffee area or the cleanroom.

My PhD project involved lots of cleanroom work and I received great support from the Kavli cleanroom staff. So special thanks to **Charles** and **Marc** for helping with LPCVD and etching, **Arnold** and **Anja** for E-beam support, **Marco** for deposition advice, **Eugene** and **Pauline** for wet processing, **Marco** and **Ron** for repairing the machines in case they malfunctioned, **Hozanna** for SEM support and **Ewan** for making sure I had clean equipment and accessories to work with. A PhD project involves lots and lots of administration and I would like to express my gratitude to the secretaries: **Etty**, **Maria**, **Marijke**, **Heleen** and **Lizzy**. I also want to thank the technicians who made sure we had all the infrastructure in place to keep our experiments running day and night. **Tino**, for maintaining the vacuum pumps and guaranteeing a safe working environment in our labs. **Tom** for helping me each time in the workshop. No matter what issue I had, you always had a smart solution. **Ronald**, you are born a mechanical genius and I appreciate that I could always walk into your office for advice or questions. The mechanical parts that you made for us have been crucial for the success of our experiments.

Also family and friends have played a big role during my PhD. I could always turn to them if something was bothering me. First I would like my **mom** and **dad** for their unconditional support throughout my PhD. My holidays to Suriname, where I grew up, felt like an all-inclusive trip and my parents did everything in their power to make me feel at home. I could always count on my brother **Raynel**, who came here a few years after me. I am proud of you that you graduated recently and I was invited to your final project where you prepared a delicious 3 course dinner for us. My aunts and Uncle in the Netherlands (**Maltie mousi**, **Sine mousi**, **Tante Truus**, **Oom Stas**, **Oom Bob**, **Oom Him**) made it possible that I could enjoy authentic Surinamese food whenever I asked them nicely. They acted as my parents and made me feel at home here in the Netherlands. **Akash** and **Kaviradj**, the relationship we have as cousins is quite rare. You guys have provided me safe environment where I could express myself in any way I wanted. My nieces **Shania** and **Shuraja** who always thought of me when it was Raksha Badhan. I am so grateful to see your children, my niece **Anaya** and nephew **Ayan** grow up so fast. **Aswin**, I am grateful to have you as a brother-in-law. I could always count on your help and I thankful that you have repaired my car several times and helped me with moving. **Prya**, I could not wish for a better sister-in-law. You are sharp, ambitious and never let someone walk over you. I sincerely believe that you will secure yourself a position as a lawyer intern in the near future.

Jeff, you introduced me to performance art. By taking part in your performance, I got to explore another side of me which I did not know even existed. **Kadhim**, **Francis**, **Alex Misdorp**, **Zege**, **Jelle**, **Niek**, **Sadiq**, **Theo**, **Vincent**, **Jan**, **Berend**, **Stijn**, **Alexander**, **Stefanos** and **Daan** are some of my best friends whom I could always count on and had lots of fun with.

Farisch, we became friends because our parents knew each other. Quite on accident, you also studied applied physics and our friendship grew even stronger. I admire you, because you are smart, entrepreneurial and honest. It was a honor to work with you and **Masoed** to build up BlancoBlauw and I will always remember our first trip to Groningen.

During my PhD, I participated in extracurricular activities that got me out of the science bubble and I had the pleasure to meet, work and learn from great people. **Theresa**, I admire you for your ability to communicate precise and clearly and was impressed by the website you had built for the project. **Dilnoza**, your project planning and organisational skills immediately stood out. **Oscar**, your concrete and analytical thinking was crucial and motivating. I could not wish for better teammates. I had fun at each session when we came together to brainstorm. In the end, we came up with a great proposal and we all should be very proud of ourselves. **Han**, **Maud**, **Jim** and **Julliete** thanks for making me a member of the Thrive community, connecting us with interesting people and the 24/7 support you provided throughout this project. The West Wing think tank is the second project I participated in. **Isabelle**, you were a great team leader and I applaud you for being sharp and steering this project in the right direction. I had the honor to work with **Sander**, **Abdul**, **Nana**, **Lotte**, **Veerle**, **Cars**, **Pim**, **Jens**, **Madelief** and **Winne**. We all had different background and we complemented each other well. While I learn a lot from you guys in the arena of policy making, international relations and public speaking, I will cherish the informal moments we had and I hope the relationships we've built throughout the project, never gets lost.

At last, I would like to thank my comité members for accepting my invitation, their willingness to serve on my doctoral comité and taking the time to examine my thesis.

Coming together is a beginning.
Keeping together is progress.
Working together is success.

Henry Ford

Curriculum Vitæ

Sarwan Ruben Peiter

18-12-1992	Born in Rotterdam, Netherlands.

Education

2003–2010 Anton Resida Mulo school, Wanica (2003–2007)
VWO Lyceum 1, Paramaribo (2007–2010)

2010–2013 Bachelor in Applied Physics
Delft University of Technology
Thesis: Simulating the performance of DESHIMA detector
Advisor: Prof. dr. A. Endo and Dr. T. Bakx

2013–2017 Master in Applied Physics
Delft University of Technology
Thesis: Deterministic entanglement of two remote transmon qubits
Advisor: Prof. dr. L. Di Carlo and Dr. C. Dickel

Internship: (SRON) Characterizing X-ray TES calorimeters
Advisor: Prof. dr. J.R. Gao and Dr. P. Koshropanah

2017 PhD. Applied Physics
Delft University of Technology
Thesis: Cavity electromechanics using flipped silicon nitride membranes
Promotors: Prof. dr. G.A. Steele and Prof. dr. L. Kuipers

List of Publications

3. **S.R. Peiter***, A. Sanz Mora*, J.P. van Soest, C. Gaertner and G.A. Steele, *High cooperativity and high-Q mechanics in a flip-chip membrane cavity electromechanical device* (under review) (2021).

2. A. Sanz Mora*, **S.R. Peiter***, and G.A. Steele, *A cyrogenic accelerometer from* Hz *to* MHz *using a membrane electromechanical cavity* (in preparation) (2022).

1. **S.R. Peiter**, G.A. Steele, *Magnetic losses in planar lumped-element superconducting microwave resonators* (in preparation) (2022).